CARBON STRUCTURES AND Mg-BASED MATERIALS FOR GAS SORPTION

Mi Tian

Submitted for the Degree of Doctor of Philosophy

School of Environmental Sciences

University of East Anglia

April 2014

Abstract

Hydrogen is an alternative energy carrier for both mobile and stationary applications, which can effectively alleviate greenhouse gas emissions and reduce dependence on fossil fuels. The other promising approach in reducing greenhouse gas emissions is carbon capture. Mg-based materials have been considered as a promising hydrogen storage system due to their high hydrogen capacity (up to 7.6 wt.%), high abundance, low cost and lightweight. Different carbon structures have also drawn considerable interests for hydrogen storage and carbon capture.

In this research, the nanostructured carbon was produced in a cold plasma reactor designed in-house as additives for improving hydrogen storage properties of Mg-based materials and CO_2 storage of MgO. The effects of the plasma reactor's flow rate, temperature and power were evaluated for the formation of the carbon structures. TEM shows that the carbon consists of spherical particles of 40.8±8.7 nm in diameter and graphene sheets.

Further thermal treatment of the plasma carbon was carried out to enhance the surface area. The treatment conditions were optimized through response surface methodology (RSM). The effects of the treatment temperature, time and pressure on BET surface area and yield were studied. The predicted BET surface area and yield by RSM were found to agree with the experimental values. The optimum treatment conditions for the plasma carbon (PC) were found to be: temperature = 950°C and time = 120 min, pressure = 100 kPaCO_2 gas flow.

The optimized PC was mixed as an additive with 20h-milled MgH_2/TiC for improvement of hydrogen storage properties. RSM optimized the mixing time and the content of PC in the (MgH_2/TiC + PC) composite. The results demonstrated that both mixing time and the content of plasma carbon (PC) significantly affected the hydrogen storage properties. The effects of the PC, activated carbon (AC) and carbon nanotubes (CNTs) on hydrogen storage properties of MgH_2/TiC were studied. PC, AC and CNTs showed positive effects on reducing hydrogen desorption temperature and improving the adsorption kinetics of the 20h-milled MgH_2/TiC. PC shows the best effect due to its unique structure. The mechanism of the effects of the three carbon structures on hydrogen storage was discussed.

I

The optimized PC was also mixed with MgO, both by ball milling and chemical co-precipitation methods to form porous carbon supported MgO for CO_2 storage and separation. The results indicated that the chemically synthesized MgO+PC calcined at 800 °C (referred to as MgO/PC-800) showed the most promising CO_2 storage capacity up to 6.16 mmol/g at 25 °C and 1500 kPa CO_2 pressure. The introduction of PC improves the CO_2 adsorption capacity of the chemical synthesized MgO due to improved surface area. The dual-site Langmuir (DSL) model was employed to predict adsorption equilibria of CO_2/H_2 gas mixtures, which well simulated the behaviors of pure CO_2 adsorption and H_2 adsorption, and can be used to predict the binary CO_2/H_2 gas mixture separation.

Acknowledgements

I take this opportunity to express my profound gratitude and deep regards to my supervisor Dr. Congxiao Shang for her exemplary guidance, constant encouragement and invaluable contribution to this thesis. I am deeply thankful to Dr. Alex Baker for being my supervisor and helping me with many complicated issues at the final stage of my study as well as for his encouragement to maintain my progress in track. Many thanks to Prof. Zheng Xiao Guo for allowing me to use the lab instruments in UCL, guiding my research, correcting my thesis and sharing his knowledge with me.

I am very grateful to my supervisory team Prof. Peter Brimblecombe and Dr. Simon Batty for supporting my study. I would like to express my immense gratitude to the financial support of Research Council of Norway and the technical assistance of GasPLas team.

I would also like to acknowledge with much appreciation the help of Dr. Iain Lake for his help in the progress of my study. I am very grateful to the laboratory support staff, Mr. Bertrand Leze, Mr. Christopher Barkway and Mr Simon Ellis. I would like to thank to the research technician Dr. John Brindle for all his support and understanding. A very special thank you goes to my teammate, Dr. Chris Roberts, who helped me with my English and shared lab work and ideas with me.

I cannot express enough thanks to my dear friends María Martínez de Álvaro and Andrew Kerr for their sincere friendship and for supporting me emotionally through the very difficult personal and academic times during my PhD. I am deeply grateful to Dr. Alessia Freddo, Dr. Alina Mihailova and Dr. Maribel Velasco Pérez for their friendship and for many enriching discussions, both academic and personal, that we always enjoyed. Many thanks to my friends Dr. Qingwen Tian, Dr. Ping Jiang, Johanna Scheidegger, Maira Benchimol and Lisha Li.

Finally, I would love to thank my parents for supporting me to pursue my dreams without which this assignment would not be possible. Many thanks to my husband for his unconditional love, patience and support for being with me in spite of the distance.

To my son, I love you.

List of Contents

List of Figures

List of Tables

1

INTRODUCTION

There is a growing consensus that a major cause of global climate change is the anthropogenic emission of greenhouse gases (GHGs) into the atmosphere. Fossil fuels currently supply over 85% of the energy needs of the U.S. and a similar percentage of the energy used worldwide [1]. The U.S. Department of Energy estimates that consumption of fossil fuels will increase by 27% over the next 20 years, thereby increasing U.S. CO_2 emissions from the current 6000 million tons per year to 8000 million tons per year by 2030. The U.S. Department of Energy also estimates that the combined CO_2 emissions from China and India in 2030 from coal use will be three times that of the U.S. [2].

Hydrogen is an ideal energy carrier for both mobile and stationary applications while alleviating greenhouse gas emissions and reducing dependence on fossil fuels. Hydrogen is non-toxic and extremely environmentally energy since water is the only exhaust product when hydrogen is converted into energy. Hydrogen can be produced from a variety of sources including fossil fuels, renewables and water (by means of nuclear, wind or solar energy). Despite obvious benefits, an immediate incorporation of hydrogen into the world economy faces a number of challenges. Unlike oil and natural gas, hydrogen has no large-scale infrastructure supporting its transportation. Although it is routinely used by chemical and refining industries, the cost of hydrogen storage and delivery is too high for practiced

applications, thus hydrogen storage is one of the key challenges in developing hydrogen economy. The U.S. Department of Energy has produced a series of performance targets for hydrogen storage system [2], shown in Table 1-1.

Table 1-1 The U.S. Department of Energy targets for on-board hydrogen storage systems for light-duty vehicles [2].

Storage system parameter	Original 2010 target	Revised 2010 target	2017 target	Ultimate target
Gravimetric capacity kgH$_2$/kg system	6%	4.50%	5.50%	7.50%
Volumetric capacity g H$_2$/L system	45	28	40	70
Operational cycle life	1000	1000	1500	1500
Fill time (min, for 5 kg)	3	4.2	3.3	2.5
Minimum full flow rate (gH$_2$/s/kW)	0.02	0.02	0.02	0.02
Min. delivery pressure @ 85 °C PEMFC (atm)	8	5	4	3
Fuel purity	99.99%	99.97%	99.97%	99.97%

The common hydrogen storage methods, such as high-pressure gas or liquid, cannot fulfill future storage targets. Chemical or physically combined hydrogen storage in solid materials has potential advantages from safety perspective and high efficiency. Hydrogen forms metal hydrides with some metals and alloys leading to solid-state storage under moderate temperature and pressure that gives them the important safety advantage over the gas and liquid storage methods. Metal hydrides have higher hydrogen storage density (such as 110 g/L for MgH$_2$) than hydrogen gas (0.08988 g/L at 273 K and 101.325 kPa) or liquid hydrogen (70.99 g/L at 20 K).

Metal hydrides as hydrogen storage systems have been reported in numerous studies [3-8]. Light metals such as Li, Be, Na, Mg, B and Al, form a large variety of metal hydrogen compounds. A group of Mg-based hydrides stands as promising candidate for competitive hydrogen storage due to its reversible hydrogen capacity up to 7.6 wt% for on-board applications and low cost [4, 9, 10]. However, slow kinetics and high dehydrogenation temperature of > 300°C limit its practical applications [9]. Many efforts have focused on Mg-based hydrides in recent years to reduce the dehydrogenation temperature and to speed-up the re/dehydrogenation reactions. These can be accomplished to some extent by changing the microstructure of the hydride by mechanical milling with elements which reduce the stability of the hydrides and also by using proper catalyst to improve the kinetics [11]. It was found that mixing Mg with catalytic transition elements, such as Ni, Co, Ti, Fe or intermetallic

compounds, e.g. $LaNi_5$, $FeTi_{1.2}$, $ZrFe_{1.4}$, could improve the hydriding and dehydriding kinetics of Mg efficiently at high temperatures (>300 °C) [12-16]. Hanada et al. reported that the hydrogen absorption of Mg-mesoporous Nb_2O_5 reached up to about 4.5 wt.% at room temperature within 15 s [17]. However, the state-of-art materials are still far from meeting the aimed target for their transport applications.

Recently, carbon materials are used to enhance the hydrogen storage performance of Mg-based systems. Imamura et al. [18-20] correlated the observed property/structure difference between the Mg/graphite composites that were prepared by dry milling or wet milling in presence of organic additives. Shang and Guo [21] indicated that graphite posed little influence on the desorption properties of MgH_2 by investigating the effect of graphite on dehydrogenation/rehydrogenation performance of milled (MgH_2+ graphite) mixtures. In addition to the traditional carbon materials, novel carbon nanostructures, such as carbon nanotubes (CNTs), have drawn considerable interest in the catalytic effectiveness of the hydrogen storage of Mg because of their stability, low weight, and good porosity, which provides large specific surface areas [22]. The combination of carbon nanoparticles and transition metals has been found to lead to an especially great enhancement of hydrogen dissociation and diffusion into Mg nanoparticles [23].

The other promising approach to reduce GHGs emissions is carbon capture. Carbon capture and storage (CCS) is considered to play a crucial role to attain the required GHG emissions reduction [24]. CCS is defined as a method for the separation and capture of CO_2 produced at stationary sources, followed by transport and storage in geological reservoirs or in the ocean. There are three major approaches for CCS: post-combustion capture, pre-combustion capture and oxyfuel process. The main challenges for all these technologies are the reliability, stability and removal efficiency. There is a great need for improving the performance, and reducing the cost and energy required for CO_2 capture and separation.

Many carbon structures, such as activated carbons, carbon black, carbon membranes, graphene and carbon nanotubes, have been widely used for gas separation, water purification, catalyst supports, electrodes for batteries and fuel cells, and flexible energy storage and conversion devices [25-32], due to their stable physicochemical properties, good conductivity, low cost, and high surface area or porosity [29-33]. One of the attractive

methods of producing hydrogen and high value-added carbon is plasma-reforming of hydrocarbons. Moreover, carbon modification methods are employed to get different carbon structures for the desired applications.

For post CO_2 capture/adsorption techniques, various amines compounds, metal oxides, hydrotalcites, amine containing polymers and zeolites are identified as efficient post CO_2 capture sorbents. Among the various metal oxide and hydrotalcites that have been examined for CO_2 adsorption, MgO and/or $Mg(OH)_2$ have been recognized as efficient sorbents due to their high CO_2 adsorption capacity of 3-4 mol of CO_2/kg (132-176 mg of CO_2/g). Other MgO-based sorbents are prepared by modification of dolomite for CO_2 removal in syngas at high temperature (300–450 °C) and high pressure (20 atm), and their capacity achieves 102–117 mg/g. Synthesis of mesoporous MgO with a high surface area is an important issue for CO_2 capture/adsorption. The carbon materials with high surface area are usually used as supports or templates for synthesis of mesoporous MgO [34, 35]. Bhagiyalakshmi et al. reported an adsorption capacity of 92 mg of CO_2/g over ordered mesoporous carbon supported MgO at 25 °C and regenerated at 200 °C [35].

The purpose of this thesis is to investigate the carbon structures produced by a plasma reactor, as a joint project with GasPlas AS Company, and to examine the hydrogen storage properties of the synthesized Mg-based materials. The plasma reactor was developed by GasPlas AS Company and improved upon according to my experimental work on plasma carbon structures and plasma process. Subsequently, the carbon products by the plasma reactor were modified and applied to improve hydrogen storage performance of MgH_2 and CO_2 storage/separation of MgO.

The main challenge of this research was to control the experimental error and to understand the experimental process and the underlying theory when a large amount of experimental work need to be carried out. Statistical design of experiments (DOE) is commonly seen as an effective and essential solution. The general objective of DOE is to guarantee that the dependency between experimental conditions and the outcome of the experiments (the responses) can be estimated reliably at minimal cost, i.e. with the minimal number of experiments. DOE can be divided into several subtopics: (i) to determine the most important variables from a large set of variables (screening designs), (ii) to understand the effect of a

mixture composition on the response variables (mixture designs), (iii) to identify sources of error (variance component analysis) in a measurement system, (iv) to design experiments for optimal parameter estimation in mathematical models (response surface methodology, RSM).

This research includes a comprehensive literature review of carbon products by a plasma reactor, CO_2 capture and storage, hydrogen storage of Mg-based materials, and experimental design in *Chapter 2* and the description of experimental facilities and the process of sample preparation in *Chapter 3*. *Chapter 4* reports the synthesis of nanostructured carbons by the microwave plasma cracking of methane. Surface area and microstructure of the carbon samples collected at different positions were characterized by BET surface area analysis, X-ray diffraction and transmission electron microscopy. The effects of flow rate, temperature and power were evaluated for the formation of the carbon structures. *Chapter 5* centers on the methodology used for the optimization of the modification conditions of plasma carbon. *Chapter 6* describes the investigation of the effects of plasma carbon on hydrogen storage properties of the Mg-based composites by means of a central composite design. In *Chapter 7*, a porous carbon supported MgO was studied for CO_2 storage. The dual-site Langmuir model was employed to predict adsorption equilibria of CO_2/H_2 gas mixture according to the experimental results of CO_2 and H_2 adsorption. Main conclusions from the research are drawn and recommendations for future work are presented in *Chapter 9*.

2

LITERATURE REVIEW

2.1   Hydrogen storage of Mg-based materials

Hydrogen is the ideal candidate as an energy carrier for both mobile and stationary applications as it is clean and inexhaustible. Nowadays, the challenge for hydrogen technology is the lack of safe and efficient hydrogen carriers especially for onboard applications. Hydrogen storage can be stored as pressurized gas, cryogenic liquid, solid fuel as chemical or physical combination with materials, such as metal hydrides, complex hydrides and carbon materials.

Different kinds of hydrogen storage materials have been developed, such as metal hydrides, complex hydrides, carbon nanotubes and metal organic frameworks (MOF) [36]. Consideration based on cost, weight, storage capacity and material availability reveal that reversible hydriding of Mg according to the following reaction:
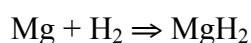
$$Mg + H_2 \Rightarrow MgH_2$$

is the most practical option for hydrogen storage.

Moreover, MgH_2 offers a low reactivity towards air and makes it a very safe energy carrier candidate for mobile applications. Indeed, MgH_2 meets the minimum requirements described

by the US Department of Energy: 6.5% of gravimetric capacity and 62 kg/m^3 H$_2$ of volumetric capacity at the decomposition temperature between 60 and 120 °C for onboard applications. However, there are still many barriers that make it very difficult to be used for practical applications, such as the slow hydrogen sorption kinetics and the high operation temperature.

2.1.1 Magnesium as a hydrogen storage medium

Mg has shown a promising property for onboard hydrogen storage system due to its high hydrogen capacity 7.6% high volumetric density and low cost. MgH$_2$ possesses good quality functional properties, such as heat resistance, vibration absorbing, reversibility and recyclability. MgH$_2$ has the highest energy density of 9 MJ/kg Mg among all reversible hydrides applicable for hydrogen storage [37]. MgH$_2$ is different to other metal hydrides according to the type of Mg-H bonds and crystal structure and properties, which is similar to ionic hydrides of alkali and alkaline earth metals.

The main advantages of MgH$_2$ as a hydrogen storage medium is the high desorption temperature, slow desorption kinetics and a high reactivity toward air and oxygen. There are several factors that significantly hinder the rate of hydrogenation e.g. surface oxidation of Mg exposed to air is one of them and hence to initiate hydrogen absorption, the oxide layer should be broken down by activation process. The activation may consist in the cyclic heating and cooling in a vacuum or hydrogen atmosphere. Another reason of the slow rate of hydrogenation is low dissociation rate of hydrogen molecules on the metal surface [38]. A clean surface of pure Mg needs a high energy for dissociation. In addition the diffusion of dissociated hydrogen atoms within metal hydride is very difficult [39].

Recently many efforts have focused on reducing the desorption temperature and accelerating the re/dehydrogenation reactions of Mg-based hydrides. These can be accomplished to some extent by changing the microstructure of the hydride by ball-milling with elements which reduce the stability of the hydrides and also by using proper catalysts to improve the kinetics [40].

2.1.2 Approaches to optimise sorption properties of MgH₂

Mg-based materials can be modified to improve the sorption characteristics. The efforts have been made to reduce the desorption temperature and to speed up the re/dehydrogenation reactions which are influenced by: 1) improving surface and kinetics properties by ball milling; 2) combining with other transition metal and their oxides; 3) using catalysts; and 4) carbon as additives.

2.1.2.1 Ball milling

The surface of Mg is a critical factor for hydrogen adsorption, which activates dissociation of hydrogen molecules and allows easy diffusion of hydrogen into the bulk. With hydrogen diffusion taking place during the hydrogenation of Mg, The hydride layer grows, which produces a nearly impermeable layer. Diffusion through this hydride layer becomes the rate-limiting step in the hydride formation process [41].

The ball milling/mechanical milling has shown a path to overcome this problem which relies on mechanical impact and friction to refine and alloy powder materials [40]. The main effects of milling are increased surface area, formation of micro/nanostructures and creation of defects on the surface and in the interior of the material. The induced lattice defects may aid the diffusion of hydrogen in materials by providing many sites with low activation energy of diffusion. The induced microstrain assists diffusion by reducing the hysteresis of hydrogen absorption and desorption [42]. The increased surface contact with catalyst during ball-milling leads to fast kinetics of hydrogen transformations. The nanocrystalline Mg produced by milling gives remarkable improvement of kinetics and surface activity for hydrogenation [43]. It has been reported that with the decrease in crystal grain size, the desorption energy decreases drastically, reducing the desorption temperature up to 200 °C [44]. Another method is milling under hydrogen atmosphere, which provides an easy way to diffuse hydrogen into the material. Thus, nanostructured materials can provide much better results for storing hydrogen with fast kinetics [43]. The method is based on infiltration of nanoporous carbon with molten Mg, The size of this prepared Mg crystallites has been reported from 2-5 nm to less than 2 nm. The microstructure refinement and increase in the density of crystal lattice defects caused by enthalpy, change the slope of the pressure plateau in pressure-composition

isotherms, decrease the pressure hysteresis, and accelerate the hydrogen desorption kinetics. [45]

2.1.2.2 Alloying with other transition metal and their oxides

Alloying Mg with other transition metal and their oxides has shown a way to reduce the desorption temperature and to remove other thermodynamic constraints. Zhu et al. [46] reported that the hydrogen sorption properties of Mg and Mg-Ni-based alloys can significantly be improved by forming composites having proper microstructural feature. Mg_2NiH_4 attracts wide interest for being a promising hydrogen store material due to its relatively high capacity, low cost, light weight and low-toxicity [47] and for its unusual structural and bonding properties [47]. Mg_2Ni react with hydrogen as following reaction at 470-500 K:

$$Mg_2Ni + 2\ H_2 \rightleftharpoons Mg_2NiH_4$$
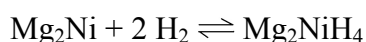
Mg_2Ni reacts with 3.6 wt% of H_2 and transforms into the hydride phase, Mg_2NiH_4. The dehydrogenation temperature is 250-300 °C at desorption pressure of 2.1-3 bar [47]. High hydrogen capacity of four hydrogen atoms per Mg_2Ni, combined with the small specific weight of the alloy is the most important advantage of Mg_2Ni over MgH_2 [48].

Mg_2FeH_6 with highest volumetric capacity of hydrogen (150 kg/m^3) but the hydride phase is very difficult to synthesize. However, hydrogen can act as binding component to form Mg_2FeH_6.[49]. Another example is Mg-Ti alloy synthesized by using a high pressure anvil cell at 8 GPa and 873 K. Recently Mg-Al alloys has attracted worldwide attention as an alternative for hydrogen storage applications. Al is considered to destabilize MgH_2 and forms Mg/Al alloys after dehydrogenation. Bouaricha et al. reported favourable kinetics at 400 °C for $Mg_{0.9}Al_{0.1}$ and $Mg_{0.75}Al_{0.25}$ alloys. Mg and Al were found to alloy upon desorption to form $Mg_{17}Al_{12}$ [50]. A nanocrystalline $Mg_{1.9}Ti_{0.1}Ni$ alloy shows good absorption kinetics at room temperature. The Ti decreases the kinetic barriers of absorption while the Ni protects the alloy from deactivation due to oxide layer formation.

Except these well known Mg based alloys there are several other contenders which may be useful for hydrogen storage in future e.g. Mg_2CoH_5, Mg_3IrH_5, Mg_3RuH_6, Mg_3ReH_7,

Mg$_3$MnH$_7$ Mg$_3$CrH$_6$, Mg$_3$Pr etc. These are having very good hydrogen content but the synthesis process is still very complicated to be used in practical applications [39]. A nanocrystalline Mg$_{1.9}$Ti$_{0.1}$Ni alloy shows good absorption kinetics at room temperature [51]. Ti decreases the kinetic barriers of absorption while Ni protects the alloy from deactivation due to oxide layer formation.

2.1.2.3 Catalysis

The use of catalysts has been proved an important pathway to enhance surface kinetics of Mg/MgH$_2$. The catalysts are often used such as transition metals [17, 52, 53], metal oxides [17, 52, 53], intermetallic compounds [54-56] and carbon materials [57]. Hydrogen molecules have a strong affinity for nickel and readily dissociate and adsorb onto surface-layer nickel clusters [58]. Holtz and [59] have investigated that through the addition of 1 at.% of nickel to Mg, a decrease in the temperature of the onset hydrogenation from 275 to 175 °C, and a lowering of the dehydrogenation onset temperature from 350 to 275 °C. Ti and V block the oxidation of alloy surface and increase the discharge capacity over multi cycles [60]. Walker et al. has also reported that MgH$_2$ ball-milled with Ge leads to a thermodynamic destabilisation of >50 kJ mol^{-1} (H$_2$), which has dramatically reduced the temperature of dehydrogenation to 130 °C [61]. It has been found that the poor kinetics of MgH$_2$ can be greatly improved by addition of different oxide catalysts that enhance hydriding properties at relatively low temperature, such as V$_2$O$_5$ [62] and Cr$_2$O$_3$ [63]. Oelerich et al. [64] investigated the oxide catalysts (Sc$_2$O$_3$, TiO$_2$, V$_2$O$_5$, Cr$_2$O$_3$, Mn$_2$O$_3$, Fe$_3$O$_4$, CuO, Al$_2$O$_3$, and SiO$_2$) effects on hydrogen storage of MgH$_2$. In absorption, the catalytic effect of TiO$_2$, V$_2$O$_5$, Cr$_2$O$_3$, Mn$_2$O$_3$, Fe$_3$O$_4$, and CuO is comparable. Concerning desorption, the composite material containing Fe$_3$O$_4$ shows the fastest kinetics followed by V$_2$O$_5$, Mn$_2$O$_3$, Cr$_2$O$_3$, and TiO$_2$. Only 0.2 mole% of the catalysts is sufficient to provide a fast sorption kinetics. Croston et al. [65] investigated that TiO$_2$-based additives result in significantly reduced onset temperature of dehydrogenation and increased hydrogenation and dehydrogenation rates of MgH$_2$. The Ti based oxide additives were found to change the mechanism of dehydrogenation from the milled MgH$_2$ from one of surface control followed by contracting volume, to a 2D Johnson-Mehl-Avrami nucleation and growth mechanism.

Recently the use of a new catalyst SiC has been reported to improve the hydrogenation properties of MgH_2 by Ranjbar et al. [23]. They found improved hydrogen absorption/desorption kinetics by adding SiC and capacity of MgH_2 is also found to be increased by increasing the surface area and defect concentration. Another processing material for making compound with Mg is Zr based alloys. Such as, MgH_2 + 10 wt% ZrNi composite could absorbed about 5 wt% in less than 3 mins and desorb the same amount in 7 mins at 300 °C. FeTi has also been reported as an exciting material to improve the kinetics of MgH_2, The maximum capacity was found to be 5.8% at 300 °C and 5.12 wt% at 200 °C for Mg-5% FeTi. The effect of chromium and vanadium transition metal catalysts on the cycling properties of the controlled multilayer thin films of Mg/Cr and Mg/V coated by the physical vapour deposition (PVD) system has been studied by Christopher et al. [66, 67]. They found that the chromium-catalysed coating had the most favourable hydrogen storage kinetics with an activation energy for the dehydrogenation reaction of 65.7 ± 2.5 kJ mol^{-1} and a hydrogen capacity of 6.1 ± 0.3 wt.%.

2.1.2.4 *The effects of carbon structures on hydrogen storage properties of Mg*

The most recent effects are to make the composite of Mg-based materials with carbon. Due to its high specific area and unique adsorbing properties, nanostructured carbon has been shown to have a high catalytic activity. Wu et al. has shown significant increase in the hydrogen storage capacity with the decrease in temperature. Imamura et al. [18-20] correlated the observed property/structure difference between the Mg/graphite composites that were prepared by dry milling and wet milling in the presence of organic additives, respectively. They suggested that the highly dispersed cleaved lamellae of graphite with nanocrystal sizes, which only existed in the composites milled with organic additives, acted as active sites. Shang and Guo [16] investigated the effect of graphite on hydrogen desorption performance of milled (MgH_2 + G) mixtures and rehydrogenated (MgH_2 + G) mixtures using simultaneous thermogravimetry (TG) and diffraction scanning calorimetry (DSC), respectively. The results showed that peak positions of the pure MgH_2 and (MgH_2 + 10G) milled for the same length of time were more or less the same, which indicated that graphite posed little influence on the desorption properties of MgH_2.

In comparison with that on the traditional carbon materials, the investigation on the catalytic effectiveness of novel nanostructural carbons, for example, carbon nanotubes (CNTs), on hydrogen storage of Mg is quite limited. Reyhani [22] investigated the influence of Mg doping to the multi-walled carbon nanotubes (MWCNTs) on its hydrogen storage property. The electrochemical discharging curves of the MWCNTs and Mg-MWCNTs revealed that the hydrogen storage capacity was 363 and 450 mAh g^{-1}, respectively. Volumetric technique determined that the hydrogen storage capacity of the MWCNTs and Mg-MWCNTs was 0.7 and 1.5 wt%, respectively. There are likely a couple of mechanism for Mg metal that used as dopants to pure MWCNs, one involves increasing of absorption binding energy and desorption temperature due to increasing defect sites, while the second explains by electron transfer from metal atoms to carbon atoms resulting in a considerable increase in both the adsorption binding energy and desorption temperature.

Ranjbar [23] et al. reported the effects of CNTs on the hydrogen storage properties of MgH_2. The sample with CNTs showed considerable improvement in hydrogen sorption properties. Its temperature of desorption was 125 °C lower than for the pure Mg. In addition, the gravimetric capacity of the ternary sample was 6 wt% at 300 °C and 5.6 wt% at 250 °C, and it absorbed 90% of this amount at 150 s and 516 s at 300 °C and 250 °C, respectively. It can be hypothesised from the results that CNTs facilitate access of H-atoms into the interior of Mg grains.

Various Mg/carbon and Mg/noncarbon composite systems were prepared by mechanical milling and their hydrogen storage behaviours were investigated by Wu et al. [11]. They found that all the carbon additives exhibited prominent advantage over the noncarbon additives in improving the hydrogen capacity and dehydriding/hydriding kinetics of Mg. And among the various carbon additives, purified single-walled carbon nanotubes (SWNTs) exhibited the most prominent 'catalytic' effect on the hydrogen storage properties of Mg, followed by amorphous carbon, fullerene and graphite.

The proposed reasons for this prominent effect can be: (1) segregation of carbon at grain boundary thus resulting the increment in hydrogen diffusion along the boundaries. (2) the dispersive feature of carbon assists to obtain Mg particles that shorten the diffusion path [39].

Furthermore, the high ductility of Mg impedes its high-degree dispersion. This problem could be overcome by adding carbon as anti-sticking agent and for activation purpose [68]. Some researchers investigated using carbon as solid milling aid, e.g. graphite, CNTs, carbon black, and coal [69]. The results indicated the crystallitic carbon is an effective milling aid for the milling of Mg with roles of dispersive agent, milling media and lubricant.

2.2 CO_2 capture and storage technologies

Excessive greenhouse gasses (GHG) in the atmosphere are responsible for various environmental problems, such as, continuous rise of water level in sea, the increasing number of ocean storms, floods, etc. [70]. Among the GHGs, CO_2 is the major contributor for global warming and it has the greatest adverse impact, which accounts approximately 55 % of the observed global warming. CO_2 alone is responsible for about 64 % of the enhanced greenhouse effect [71]. The capture of CO_2 from power plant flue gas accounts three quarter of the total cost of carbon capture and storage. It has become an important research issue of global perspectives as more international attention is focused on global warming [72]. Various processes, such as liquid solvent absorption, cryogenic techniques, membrane separation, solid sorbent, and pressure (and/or temperature) swing adsorption have been proposed for the separation and capture of CO_2 emitted by power plants.

Depending on different plant configurations, CO_2 emissions from thermal power plant flue gas can be reduced by three methods: pre-combustion capture, post-combustion capture and oxyfuel combustion. The difference between pre- and post- combustion depends whether carbon (in the form of CO_2) is removed before or after a fuel is burned. The oxyfuel combustion does not require a CO_2 capture device. This concept is still under development and is not yet commercial. Different plant configurations will require different CO_2 strategies as shown in Figure 2-1.

```
                    ┌─────────────────────────┐
                    │  CO₂ capture and storage │
                    └─────────────────────────┘
```
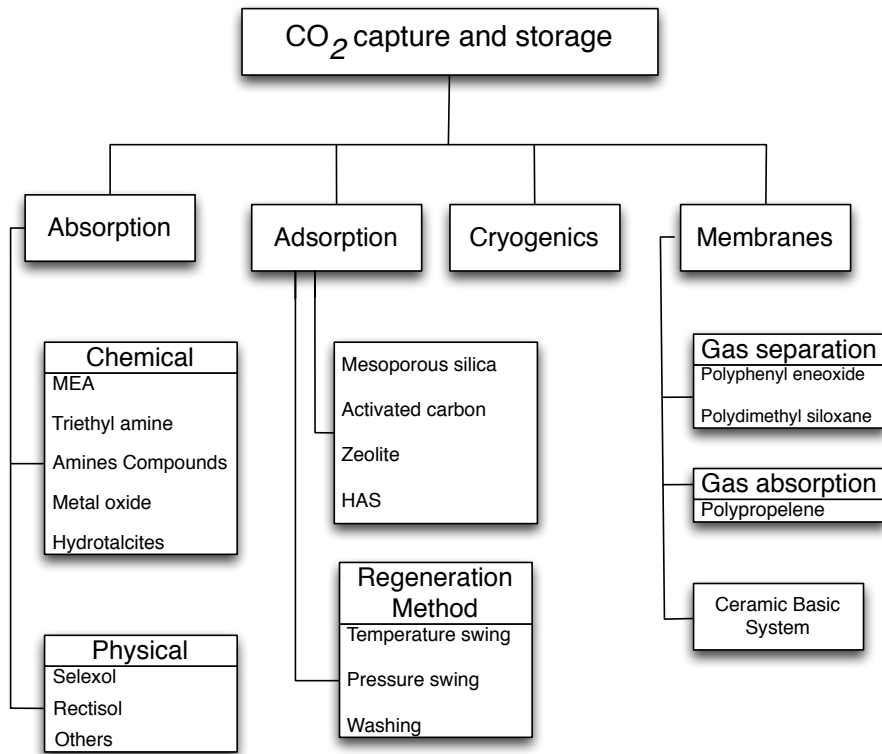
Figure 2-1 Technologies for CO_2 capture [73].

2.2.1 Absorption

Chemical or physical absorption are widely used in the petroleum, natural gas and coal fired power plants as well as chemical industries for separation of CO_2. It is based on the reaction between CO_2 and chemical solvent such as aqueous solution of mono-. di-, and tri-amine, di-isopropanol amine, etc. [72]. Generally, absorber and regenerator are working continuously. Flue gas steam containing CO_2 is introduced at the bottom of the absorber. Absorbent is introduced from top of the column that leads counter current contact between flue gas and solvent and a selective absorption of CO_2 takes place. Then CO_2 rich steam is fed to the regenerator, where desorption of CO_2 occurs and regenerated solvent is recycled for further use, desorbed CO_2 is compressed and sent to storage. Chemical absorbents such as monoethanol amine (MEA), diethanol amine (DEA), N-methyldiethanolamine (MDEA), and di-2-propanolamine (DIPA) are commonly used [74]. Other absorbents such as, diglycolamine (DGA), 2-(2-aminoethylamino) ethanol (AEE), 2-amino 2-methyl 1-propanol (AMP), N-2-aminoethyl 1,3-propanediamine (AEPDNH$_2$), triethanol amine (TEA), triethylene tetra amine (TETA), piperazine (PZ), glucosamine (GA), NaOH, NH$_3$, K$_2$CO$_3$,

etc. were also tested for CO_2 removal, however their individual limitations make them less suitable for large scale industrial CO_2 removal. Recently blended solvents provide an enhancement in overall efficiency than individual solvent [72]. However, these methods are carried out at relative low temperature, generally below 100 °C, while the temperature of flue gas vent is usually in the range of 150-400 °C [75, 76]. Thus, it is crucial to develop materials and techniques to trap CO_2 from flue gas at high temperature.

Recently, adsorbents based on metal oxide with considerable CO_2 uptake and reversibility have been developed [77, 78]. Among them Li-based adsorbent is able to trap; however, decomposition of Li_2CO_3 needs high temperature of 800-900 °C to release CO_2. Moreover, they are expensive [79]. Ca-based sorbents can capture CO_2 at 600-700 °C, but temperature above 900 °C is required for their regeneration [80]. MgO and/or $Mg(OH)_2$ have been recognized as efficient sorbents due to their high CO_2 adsorption capacity of 3-4 mol of CO_2/kg (132-176 mg of CO_2/g) at relative high temperature. MgO loaded on Al_2O_3 sorbents can be prepared by impregnation method, and their CO_2 adsorption capacities reach 42 and 60 mg/g in the absence and presence of water vapor, respectively [81]. Other MgO-based sorbents are prepared by modification of dolomite for CO_2 removal in syngas at high temperature (300-150 °C) and high pressure of 20 atm, and their capacity achieves 102-117mg/g. Bhagiyalakshmi reported the ordered mesoporous carbon supported MgO can absorb 92 mg/g at 25 °C and be regenerated at 200 °C [35].

2.2.2 Adsorption

Adsorption is a process for removal of one or more components of a mixture with the help of a solid surface. Solid sorbents have the potential for significant energy savings over liquid solvents, because they avoid the need for the large quantities of water that must be repeatedly heated and cooled to regenerate the solvent solution. The adsorption processes are based on significant intermolecular forces between gases (including CO_2) and the surfaces of certain solid materials. Depending on the temperature, partial pressure, surface force and adsorbent pore size, single or multiple layers of gases can be adsorbed [82]. As the adsorption is an exothermic process, the regeneration of the adsorbents through desorption can be performed by rising the temperature. Numerous CO_2 adsorbents like zeolites [83-85] and carbons [86-

89] are used commercially for the removal of CO_2. In addition, considerable research effort has been made in recent years to develop novel CO_2 adsorbents such as basic oxides [81, 90-95], metal-organic frameworks (MOFs) [84], organosilicans and surface-modified silicas [96]. However, zeolites, silica and MOFs often are limited in their widespread utilizing due to their structural instability and inefficiency. Recently, porous carbon materials have been used in gas storage due to their highly developed porosity, extended surface area, surface chemistry, and thermal stability. Previous studies have been carried out on the use of activated carbons, activated carbon fibers, carbon molecular sieves, carbon nanotubes, and graphite nanofibers as adsorbents for CO_2 capture.

Adsorption of CO_2 from a gas stream is a dry process and hence it has no by-product such as wastewater in conventional absorption process. And it requires low energy as compared to that of cryogenic and absorption process. However, low selectivity and capacity of adsorbed CO_2 on adsorbent and lower removal efficiency limits its applications. The adsorbents need to be regenerated for further use.

In CO_2 capture by adsorption technology, a packed column is mainly filled by spherical adsorbent and CO_2-bearing stream is passed through the column. CO_2 is attracted towards the adsorbent and adhere on the surface of adsorbent, as shown in Figure 2-2. After achieving the equilibrium, desorption takes place to get CO_2 in pure form and regenerated adsorbent can be utilized for further cycle.

CO_2-bearing stream   Adsorbent column   Gas without CO_2
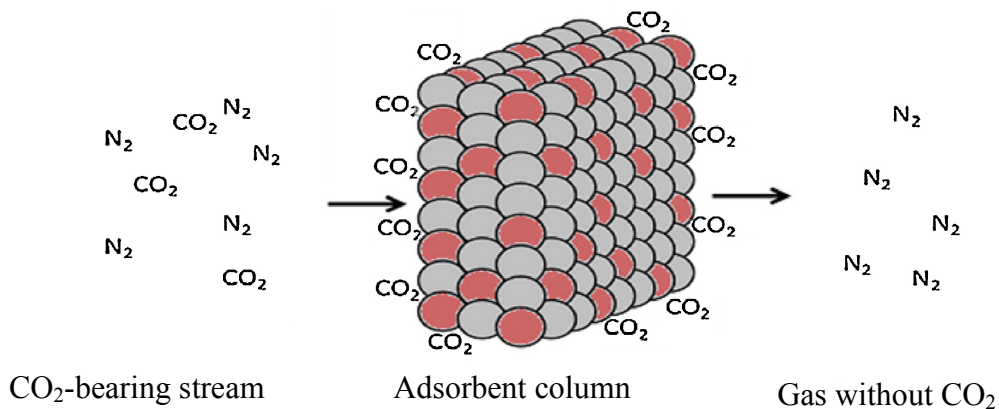
Figure 2-2 Schematic of CO_2 adsorption process [97].

16

2.2.3 Cryogenics

Cryogenic separation method is widely used commercially for separation of CO_2 from streams having high CO_2 concentrations (typically more than 50 %). It is not normally used for dilute CO_2 streams such as flue gas from coal/natural gas fired boilers as the amount of energy required for refrigeration is uneconomical for the plant. The main advantage of cryogenic CO_2 capture is that no absorbent is required and the process can operate at atmospheric pressure. The main disadvantage of this system is that the water content in the feed stream to the cooling units should be minimal in order to avoid the producing of ice. In addition the layer of solid CO_2 on heat exchanger surfaces could increase during the capture cycle, which has an adverse effect on the heat transfer.

2.2.4 Membranes

Membranes are specially manufactured materials that allow the selective permeation of a gas through them. The selectively of the membrane to different gas is intimately related to the nature of the material, but the flow of gas through the membrane is usually driven by the pressure difference across the membrane. Therefore, high-pressure streams are usually preferred for membrane process. There are many different types of membrane materials that can be either organic (polymeric) or inorganic (carbon, zeolite, ceramic or metallic) and can be either porous or non-porous. The selective membranes can be used to separate certain components from a gas stream, such as CO_2 from flue gas (post-combustion system), CO_2 from natural gas (natural gas processing), and CO_2 from hydrogen (pre-combustion systems) or oxygen from nitrogen (oxyfuel combustion system).

The membrane systems can be considered highly effective only when the CO_2 concentration is higher than 20%. For CO_2 concentration lower than 20% the membrane system offer a very low efficiency [98]. A further reduction in CO_2 concentration, in fact, produces reduction of the driving force with a consequent decrease in CO_2 recovery and in product purity. The main problem that limits the applications of membrane technology is lower concentration of CO_2 in flue gases. For high temperature application, membrane technology needs additional pre-treatment, e.g. cooling for reduced temperature.

2.3 Synthesis of carbon nanoparticles by a plasma reactor

Many carbon structures, such as activated carbon, carbon black, carbon membranes, graphene and carbon nanotubes, have been widely used or considered for gas separation, water purification, catalyst support, electrodes for batteries and fuel cells, and flexible energy storage and conversion devices [99]. This is due to their stable physicochemical properties, good conductivity, low cost, and high surface area or porosity [100-102]. Recently, graphitic carbons with highly crystalline structure and large surface area have attracted extensive attention as catalyst supports. Graphitic carbons are usually prepared by two methods: 1) conventional high temperature (>2500 °C) graphitization to form carbons with well-developed graphitic order [103]; and 2) relatively low temperature (<1000 °C) heterogeneous graphitization with the aid of catalysts, e.g. Fe, Co and Ni [104, 105]. Although exhibiting graphitic structure, these materials possess relatively low BET surface areas [106]. In addition, the synthesis procedures employed to produce such materials are rather complicated: it requires a high processing temperature between 500 and 1800 °C, and the corresponding aerogels used in the process need to be prepared by the sol−gel method from polymerization of resorcinol with formaldehyde [107].

Recently high-energy plasma has become an attractive method for reforming hydrocarbons into hydrogen and carbon. This is a single-stage and non-catalytic reaction, $C_nH_m \rightarrow nC + 0.5mH_2$ [107-110]. It is reported that plasma reforming overcomes many limitations of conventional techniques in terms of cost and deterioration of the catalysts, slow reaction rate, and restrictions on hydrogen production from heavy hydrocarbons [111-113]. In general, plasma is an ionized gas that can be generated by a number of methods, such as combustion, flame, electrically heated furnaces, electric discharge and shock [114]. The plasma contains reactive radicals, ions and high-energy electrons.

2.3.1 Thermal plasma and non-thermal plasma

Plasma technologies include a wide range of applications across many industrial sectors. Examples of such important applications are briefly reviewed as follows:

- Surface modification - physical and/or chemical modification of the first few molecular layers of the surface, while maintaining the properties of the bulk [115] etching of semiconductors, plasma hardening of metallic components for cars and aircrafts, and plasma deposited films in biomaterial applications [116].

- Thin film deposition - including carbon and fullerene film deposition, zirconate titanate grains deposition, surface nitriding or carbon implantation, anti-reflective coatings for lenses, hydrophilic and hydrophobic coatings for textiles, and deposition of diamond for cutting tools [117].

- Pollutant control - Removal of NOx and SO_2 from a stationary source or a mobile source, decomposition of hazardous air pollutants (HAPs) and volatile organic compounds (VOCs) and flue-gas cleaning [118].

- Chemical synthesis - natural gas reforming, methane reforming, O_3 generation, or/and synthesis of acetylene.

- Lighting - e.g. plasma lamps - a type of electrodeless lamp energized by radio frequency (RF) power, including Ceravision, Luxim, Plasma International, i-Giant and Topanga Technologies.

- Biomedical techniques - used for sterilisation or as therapeutic techniques, such as wound sterilization and cancer treatment.

Depending on their energy level, temperature and electron density, plasma state is usually classified as a high temperature (or thermal) plasma and a cold (or non-thermal or non-equilibrium) plasma [119]. Plasma contains reactive radicals, ions and high-energy electrons. Because of the large difference in mass, the electrons reach to thermodynamic equilibrium much faster amongst themselves than they become equilibrium with the ions or neutral

atoms. Therefore, the temperatures of the electrons, ions and neutrals may be very different. Based on temperature differences, plasma technologies can be generally classified as thermal and non-thermal. In thermal plasma electrons and heavy particles (neutrals, ions) have the same temperature [120]. For non-thermal plasma, the temperature of heavy particles can be much lower than those of electrons [121]. For example, Jesinski et al. [107] generated a cold plasma with the electron temperatures of 4000 – 10000 K, and the heavy particle temperatures of 2000 – 6000 K.

2.3.1.1 *Thermal plasma*

Thermal plasma are currently under development for powder densification [122] and fine particle synthesis [123]. Fabry etc.[124] reported a thermal plasma process for carbon black produced at temperatures between 1300-1600 K and then annealed in the region of electric arcs. Three thermal plasma carbon black populations were identified: graphitized spherical particles, amorphous particles and acetylene black aggregates [125]. The reactor geometries have been shown a significant influence on the product morphology. Pristavita et al. [126] found that using a cylindrical shape reactor the obtained powders were composed mainly of spherical particles, with irregular particles sizes with diameters between 30 and 150 nm. Changing the reactor to a conical geometry resulted in a crystalline and flake-like morphology made of sheets having 6-16 graphitic planes. Okuno et al. [127] exploited the thermal plasma produced by an electric arc between three graphite electrodes to treat solid powders of carbonaceous and catalytic precursors in the form of carbon black coated with nickel and cobalt. The structure of their product was shown to be strongly linked to the nature of the plasma gas and the resulting temperature fields in the reactor. The position of the product collection plate was varied, providing various levels of quench rates and sampling temperatures. High sampling temperatures proved important for the growth of multiwall carbon nanotubes (MWNT) [128]. In their study on the effect of the operating conditions in arc-jet thermal plasma synthesis of nanotubes, Choi et al. [129, 130] used methane as the carbon precursor and Ni powders as the catalyst, both being injected in the tailflame of the plasma torch. They indicate that the higher temperatures of the jet obtained from hydrogen addition is important to have proper metal catalyst evaporation.

Table 2-1 Different types thermal plasma reactor and parameters

Reactor	Temperature (K)	Carbon source	Buffer gas	Production	Reference
a thermal plasma jet	1000	alcohols or hydrocarbons		CNT	[131]
an arc plasma jet	3700 K	Coal	H_2, Ar	CNT	[106]
A thermal plasma reactor		CH_4	H_2	carbon nanoclusters such as multi-walled carbon nanotubes (MWCNTs) or carbon nanofibers (CNFs)	[132]
a novel DC-thermal plasma process	773 or 1173	Polyethylene	N_2	spherical CB with a high degree of turbostratic organization	[133]
a constrained thermal plasma jet		CH_4	N_2	Single-wall and cup-stacked carbon nanotubes	[134]

Thermal plasma based methods also have been used for the synthesis of carbon nanotubes. High purity (~80%) CNTs were produced with a continuous process by using a thermal plasma jet with helical extension reactor equipment [135]. A thermal plasma torch technology was used to the supersonic expansion of the plasma to generate in situ the nanoparticles of metal catalyst and simultaneously treat large amounts of carbon-containing gas for conversion into CNTs [128]. Harbec et al.[136] showed carbon nanotube production in a thermal plasma torch device using a chlorine-containing precursor, and the metal vapors generated by the electrode erosion process in the plasma torch. In another paper by Harbec et al.[128], they present CNTs catalytically produced using tetrachloroethylene (TCE) as the carbon raw material injected in the nozzle of a DC thermal plasma torch operating in the supersonic flow regime. The high temperature zone of thermal plasma often reaches above 10,000 K at the position of reactant injection.

2.3.1.2 *Non-thermal plasma*

Non-thermal plasma has been applied for fuel gas treatment and has been considered very promising for carbon powder synthesis because of the process's non-equilibrium properties, low power requirement and its capacity to induce physical and chemical reactions within

gases at relatively low temperatures. It has been shown, by Bromberg [137] et al., that methane reforming and diesel reforming could be attained with both kinds of plasma, but at significantly lower energy consumption in the case of non-thermal plasma (see Figure 2-3).

Based on mechanisms of plasma generation, system pressure and the electrode geometry, non-thermal plasma can be categorized into several types: glow discharge, corona discharge, silent discharge, dielectric barrier discharge (DBD), microwave discharge and radio frequency discharge. The pressure of glow discharge plasma generator is usually less than 1000 Pa, operating between flat electrodes[138]. Electrons in the glow discharge are highly energetic. The excited neutral atoms and molecules generate a typical glow. Due to its low pressure characteristics, the glow discharge is not very suitable for chemical synthesis. The corona discharge is an inhomogeneous discharge and can be initiated at atmospheric pressure using inhomogeneous electrode geometries. Corona discharge usually forms at highly curved regions on electrodes, such as sharp corners, projecting points, edges of metal surfaces or small diameter wires. The high curvature causes a high potential gradient at these locations so that the air breaks down and forms plasma there first. In order to suppress corona formation, terminals on high voltage equipment are frequently designed with smooth, large diameter rounded shapes like balls or toruses, and corona rings are often added to insulators of high voltage transmission lines [139]. The silent discharge or DBD combines the large volume excitation of the glow discharge with the high-pressure characteristics of the corona discharge [140]. DBD plasmas are generated by applying a high voltage to a pair of electrodes where at least one of them is coated with a dielectric made of quartz, glass or ceramic. These discharges are used in the treatment of air, contaminated with VOCs (volatile organic compounds). The DBD technique was also been successfully applied in ozone generation, which is used in water purification. The RF discharge operates at high frequencies (several MHz) and very low pressure to achieve the non-equilibrium conditions. This discharge is also not suitable for chemical synthesis. The microwave discharge is far from local thermodynamic equilibrium and can be operated in a wide pressure range. More recently, gliding arc discharge, a combination of high power equilibrium arc discharge and better selectivity of non-thermal plasmas, have also been reported to be used for reforming application.

H$_2$ yield vs. energy consumption CH$_4$

H$_2$ yield vs. energy consumption for diesel reforming
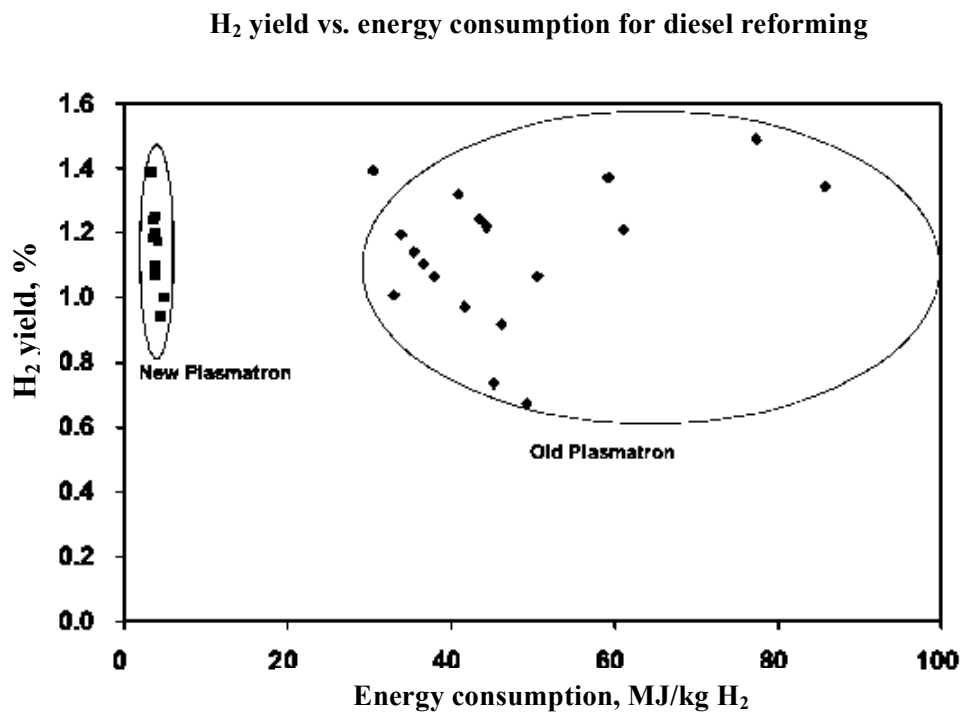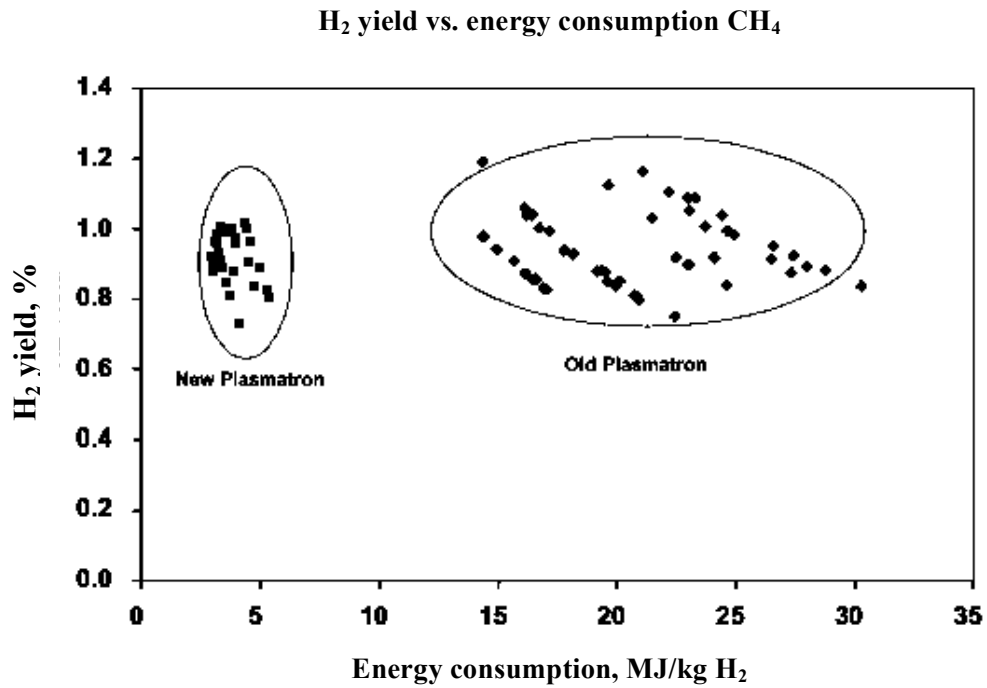
Figure 2-3 Hydrogen yield for methane as function of the specific energy consumption, for both the thermal plasmatron and the non-thermal plasmatron, left figure for methane reforming and right figure for diesel reforming. "New plasmatron" and "old plasmatron" refer to a non-thermal and thermal plasma assisted reformers, respectively [137].

2.3.2 Methane reforming for carbon product by plasma reactor

Several different types of plasma have been investigated for reforming of methane over the last 15 years. The most notable examples include DBDs, atmospheric pressure plasma jets, gliding arc discharges, coronas and a microwave discharge. The use of plasma discharge alone has shown that hydrogen and carbon products can be generated at low temperature and atmospheric pressure. This is a single-stage and non-catalytic reaction, $C_nH_m \rightarrow nC + 0.5m$ H_2 [107-110]. It is reported that plasma reforming overcomes many limitations of conventional techniques in terms of cost and deterioration of the catalysts, slow reaction rate, and restrictions on hydrogen production from heavy hydrocarbons [111-113]. In addition of hydrogen and carbon, significant amounts of hydrocarbons, oxygenates, liquid hydrocarbons and polymers can be formed [141, 142].

Carbon produced can be sold as a co-product with hydrogen into the carbon black market (ink, paints, tires, batteries, etc.). Several processes for carbon black production are currently used to produce furnace black, lampblack, channel black, thermal black and acetylene black. Their output represent 95% of world production and consume primarily petroleum by-products [143]. Cho et al. [143] presented an environment-friendly process for hydrogen and carbon black from natural gas and methane by microwave plasma and catalytic reaction. The plasma carbon produced has almost the same electronic resistivity with that of acetylene black. A non-thermal plasma process, based on low current–high voltage discharges has been developed by Moreno-Couranjou et al.[121] for gas phase synthesis of carbon nanoparticles at atmospheric pressure. This process can produce a broad range of products such as furnace-type carbon blacks, acetylene-type carbon blacks and nanoparticles with a peculiar morphology called "crumpled paper sheets". Some correlations between the operating conditions and the characteristics of carbon nanostructures highlight temperature as a key parameter for controlling the growth, formation, and type of the nanoparticles obtained. Kim et al.[144] synthesized carbon powder by an atmospheric microwave plasma torch. The synthesized carbon productions showed thorn bush-shaped, fingerprint like and onion like structures. Using methane as a source of carbon atoms, injected directly into the microwave plasma torch, it was identified from FTIR data that the samples contain functional groups of C-N, C=N, and C≡N.

Synthesis of carbon nanostructure was closely related to plasma processes. Carbon nanotubes (CNTs), similarly to fullerenes, can be synthesized by arc discharge [145], laser ablation [146] and chemical vapor deposition (CVD) methods [147]. For the CNT growth it is necessary to obtain nano scaled catalytic particles. Sufian et al. [148] synthesized graphitic nanofibres using the CVD method with ethylene (C_2H_4) as the carbon feedstock and iron (III) oxide as the catalyst. Smiljanic et al.[149] reported a method for producing single wall carbon nanotubes (SWNT) based on the atomization of a gaseous mixture by an atmospheric-pressure microwave plasma torch, using iron as the catalyst, which provides results comparable to laser ablation and arc discharge techniques. Recently more attentions referring to the production of CNTs have been paid on plasma enhanced CVD (PECVD) where CVD is combined with plasma processes. Atmospheric pressure discharges have been studied by some research groups because of their relatively simple set-up without vacuum systems. Some publications with the synthesis of CNTs using DC plasma arc jet or torch are close to arc discharge method [150]. The catalyst can be integrated into a graphite electrode or introduced into the gas phase. Generally, these methods produce soot with certain portion of unaligned single and multiwall CNTs. Microwave plasma reactors usually focus on the floating catalyst approach (ferrocene, iron pentacarbonyl) and bulk production of unaligned CNTs [151]. However recently one research group has successfully set up a microwave plasma reactor for high speed synthesis of vertically aligned supported CNTs [152, 153] and another group outlined a method for producing graphene sheets in an atmospheric pressure microwave reactor by decomposition of ethanol without the need of a substrate [154].

2.3.3 Morphologies of carbon materials synthesized by plasma

A large range of carbons with different morphologies were synthesized and classified according to their texture: (1) nanoparticles with an overall concentric texture such as furnace-type carbon black, acetylene-type carbon black and carbon shells filled with metal; (2) nanoparticles with an overall isotropic texture such as the "crumpled paper sheet" texture and other with the micro-porous texture; (3) other morphologies and/or textures, e.g. carbon rods and carbon deposits.

2.3.3.1 *Furnace type carbon black (CB)*

Furnace-type CB can be widely synthesized by either a thermal plasma or a non-thermal plasma reactor. It appears as a homogeneous product made of aggregates of small spherical particles (average size ~ 70nm) (Figure 2-4a). The TEM image of Figure 2-4b confirms the low level of organization of this nano-texture.
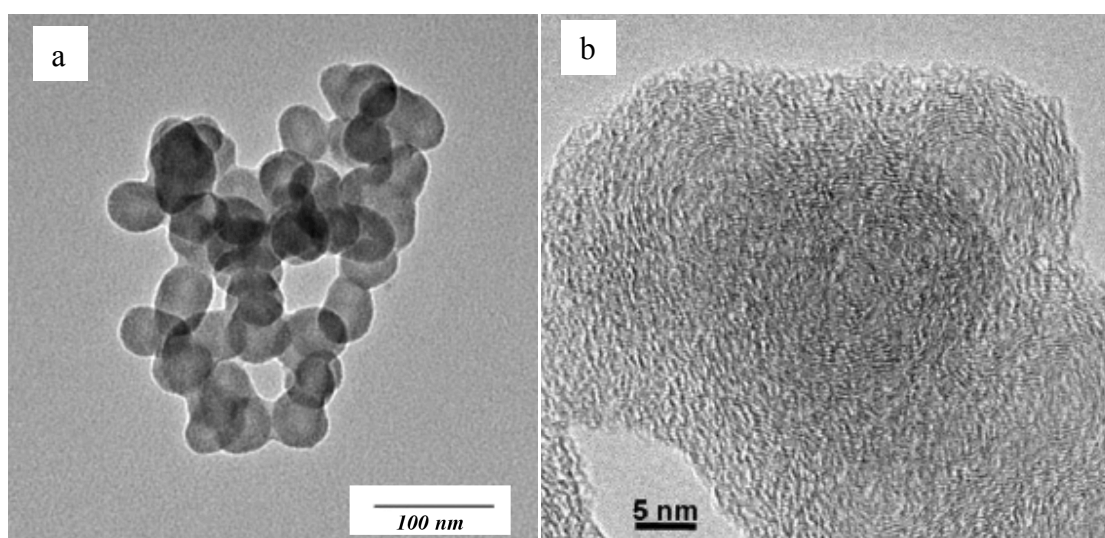
Figure 2-4 TEM image of the carbon black produced by an atmospheric pressure microwave plasma reactor [121, 155]

2.3.3.2 *Acetylene-type carbon black (CB)*

Acetylene black can be produced from methane decomposition in a plasma reactor [121, 143]. Figure 2-5 shows a heterogeneous carbon structure, including population 1 of acetylene-type CB, population 2 corresponding of furnace-type CB and population 3 relevant to carbon nanoparticles with a microporous structure.
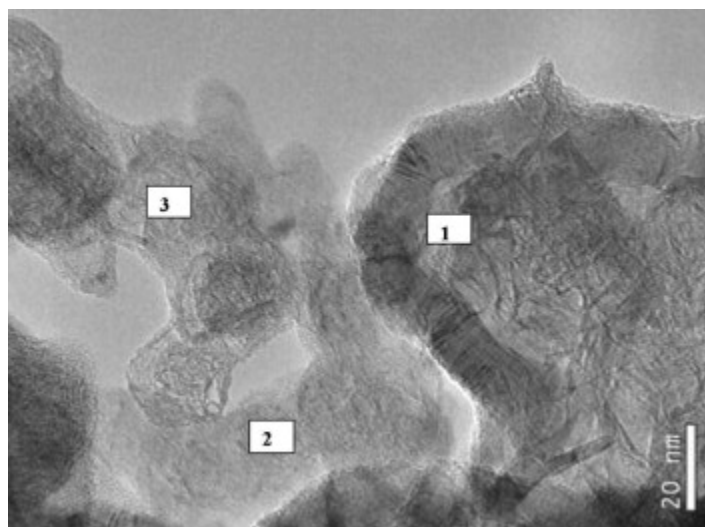
Figure 2-5 TEM image of a heterogeneous, three-phase material: (1) acetylene-type carbon black, (2) furnace-type carbon black and (3) microporous carbon nanoparticles [121].

2.3.3.3 *Carbon shells filled with metal nanoparticles- carbon nanocapsules.*

The graphitic carbon shell protects effectively against environmental degradation and has excellent adhesive bonding with the surface of the metal particles. Such graphitic carbon shells are airtight and protect the entrapped materials from oxidation, and they are generally known as "carbon nanocapsules" (CNCs). Carbon-encapsulated metal carbide (Fe3C, χ-Fe2.5C, Co3C,CoCx) nanocapsules can be synthesized by low-current plasma processing [156]. TEM measurements showed that the cores of the as-prepared carbon nanocapsules were composed of metal carbides with different size. Such as in Figure 2-6a and b show the TEM image and corresponding selected area electron diffraction pattern of a typical metallic iron nanoparticle covered with graphitic carbon.
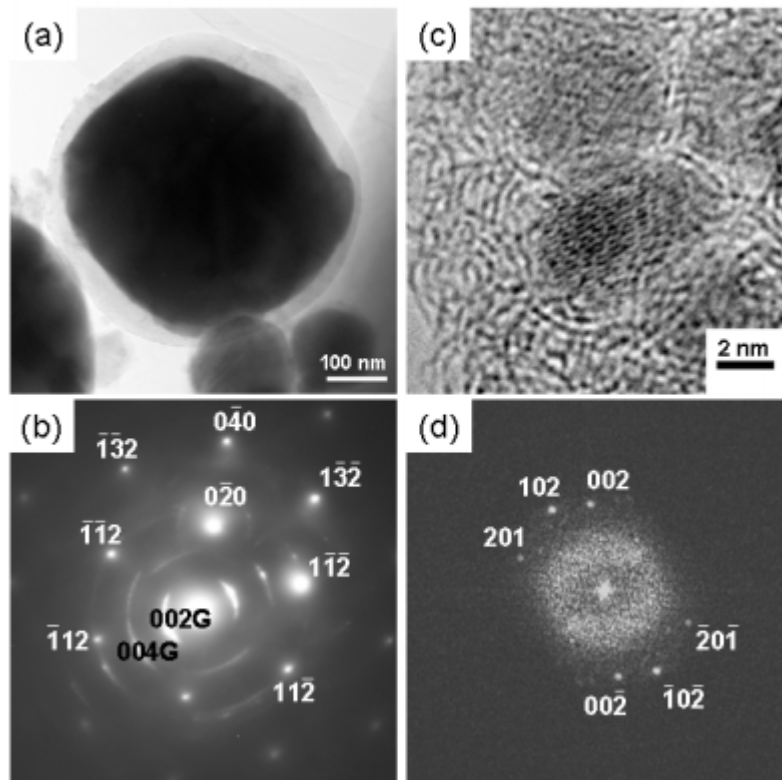
Figure 2-6 (a) TEM image of an Fe particle and (b) the corresponding SAED from the core of Fe; (c) HRTEM image and (d) the corresponding digital diffractogram computed by FFT of the cementite nanoparticles[156].

2.3.3.4 Carbon rods

In different reaction position, the different carbon structures can be produced. Moreno et al. [121] reported when the hydrocarbon gas was injected at the base of the plasma torch, carbon rods and carbon deposits were obtained. The rod is rigid, with a length ranging from 0.5 to 4cm and a nearly constant diameter (~1 mm), somewhat equal to that of the electrode (Figure 2-7). Another example is that nitrogen incorporated hydrogenated carbon nanorods (CNx:H) were synthesized by radio-frequency plasma-enhanced chemical vapor deposition (PE-CVD) without the use of catalyst (Figure 2-8). These nanorods grew irregularly both in distribution and length. The density of the nanorods and the vertical alignment were enhanced with the increase of the deposition duration.
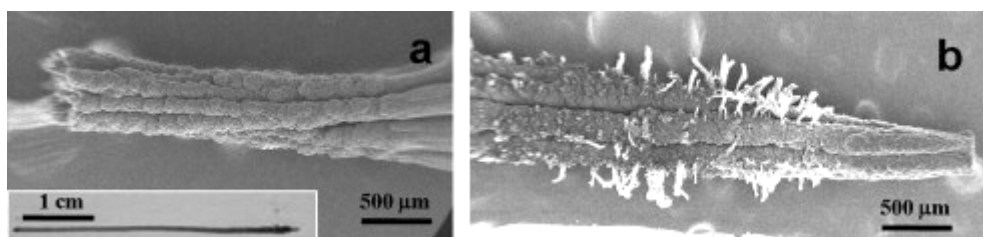
Figure 2-7 Example of carbon rod collected in the discharge zone of the plasma reactor. (a) SEM image of the rod base. (b) SEM image of the rod tip.
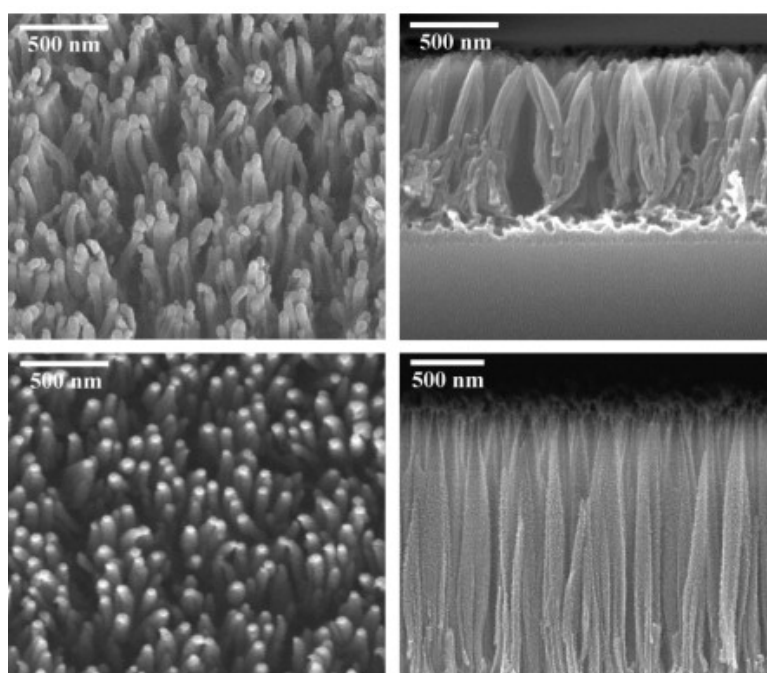
Figure 2-8 Top (left column) and cross-section (right column) views of CNx:H nanorods obtained at varied deposition duration in a plasma-enhanced chemical vapor deposition (PE-CVD)[157]

2.3.3.5 Turbostratic carbon

Carbon deposits with no peculiar morphology were generally formed in the hottest zone of the plasma reactor. From XRD analysis the ground carbon deposits is typical of a less-ordered turbostratic structure (Figure 2-9).
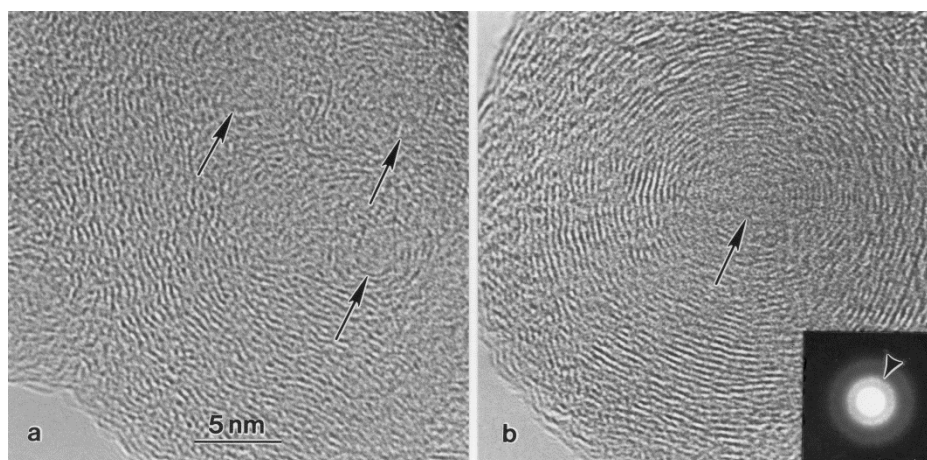
Figure 2-9 TEM micrographs showing the turbostratic microstructures, consisting of concentric carbon layers surrounding a) several nuclei in vehicle exhaust (arrows), or b) a single nucleus in wood smoke (arrow). The inset shows a SAED pattern from a wood smoke particle. The arrowhead points at the ring corresponding to the 002 spacings in the turbostratic microstructure[158].

2.3.3.6 Carbon nanotube (CNT)

Arc discharge, laser ablation and chemical vapor deposition (CVD) methods are mainly used for preparation of carbon nanoclusters [159, 160]. CNTs prepared by the arc discharge method have a higher degree of crystallinity and a lower number of defects than those prepared by CVD [132]. The synthesis of carbon nanoclusters or CNTs using a plasma jet was studied by some authors [132, 161-163]. Usually, catalysts, for example Fe, CO and Ni, are needed and the reactor is operated with high power for CNTs production. Ohishi [132] et al. have applied the thermal plasma reactor for continuous synthesis of CNTs by using CH_4 as an material gas, and that production of CNTs are enhanced with the injection of H_2 gas as an assist gas and Ni as substrate. Harbec et al. [128] produced CNT using a DC non-transferred plasma torch operated at a power of 30 kW in argon and producing a supersonic jet. Tethrachloroethylene (TCE) is used as the carbon raw material and the morphology of CNTs is shown in Figure 2-10. Smiljanic et al. [164] use a microwave plasma for the decomposition of methane to produce single wall carbon nanotubes. Hahn et al. [163] and Tian et al. [165], respectively, decompose CO and coal using a DC thermal plasma torch. Hahn et al. [131] further developed the thermal plasma jet using alcohols or hydrocarbons in a stagnation point flow geometry on a plate acting as a surface for the nucleation and growth of the nanotubes. Solid carbon powders and metal catalyst powders were also used by Watanabe et al. [166] in a RF inductively coupled thermal device. The position of the product collection plate was varied, providing various levels of quench rates and sampling temperatures. High sampling temperatures proved important effect on the growth of CNTs, while high quench rates in the

order of 105-106 k/s were generated in the process in a way similar to Smiljanic et al. [164] for the non-thermal plasma process. Choi et al. [129, 130] used methane as the carbon precursor and Ni powder as the catalyst, both being injected in the tail flame of the plasma torch. They indicate that the higher temperatures of the jet obtained from hydrogen addition is important to have proper metal catalyst evaporation. Figure 2-11 shows CNTs synthesized by decomposition of methane using an arc-jet plasma.
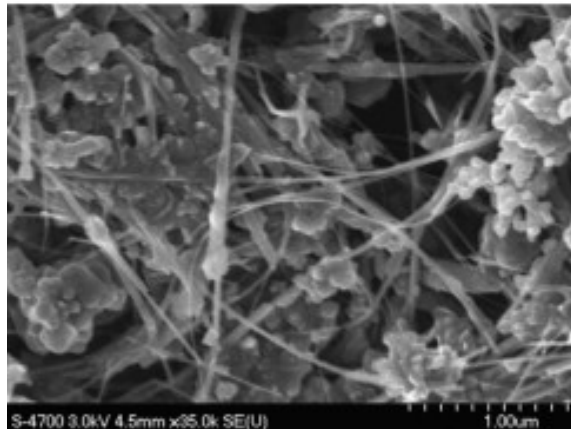
Figure 2-10 FE-SEM micrograph of nozzle deposits including CNT and carbon soot using a DC non-transferred plasma torch [128] .
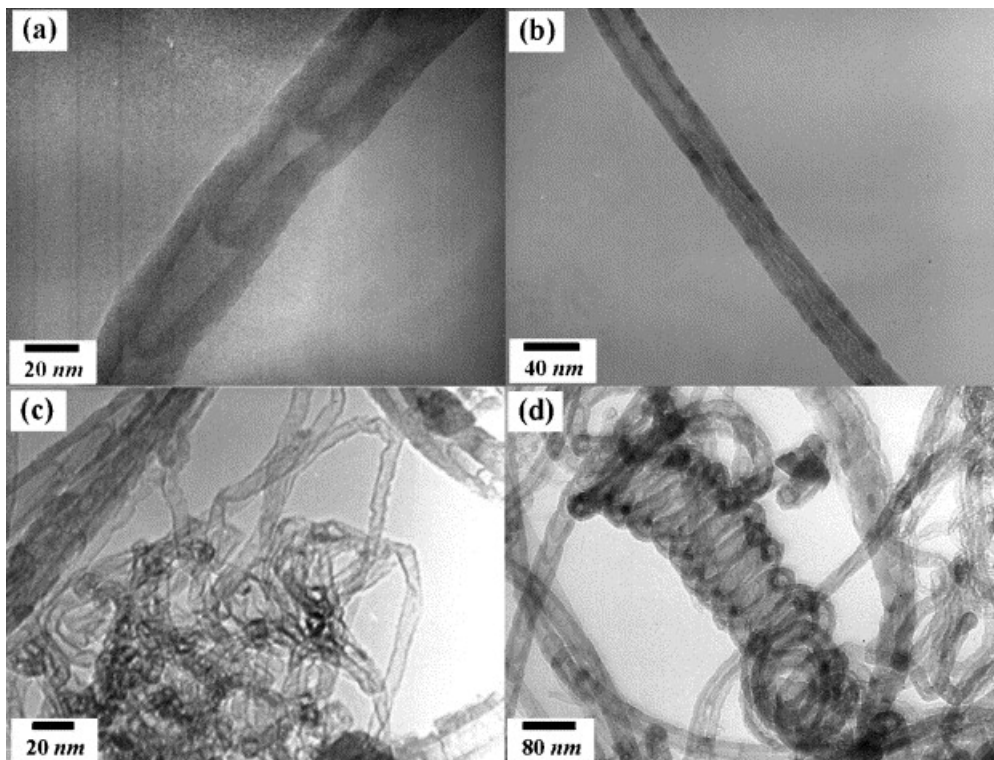
Figure 2-11 TEM images show the CNTs of different structures produced by the arc-jet plasma method: (a) bamboo-like muti-walled CNT, (b) multi-walled CNT, (c) CNTs with very thin wall, and (d) coiled CNTs. [130]

2.3.3.7 Graphene

Graphene is an atomically thin sheet of carbon atoms tightly packed in a two-dimensional (2D) honeycomb lattice. Graphene possesses many extraordinary properties, and its potential applications have recently been the subject of intense scientific interest. However, producing graphene sheets is a challenge. Methods developed thus far rely on three-dimensional (3D) crystals [167-174] or substrates to obtain 2D graphene [175-179]. These techniques include the micromechanical cleavage of graphite [167-171], the chemical reduction of exfoliated graphite oxide [172-174], the vacuum graphitization of silicon carbide substrates [175, 176], and the growth of graphene on metal substrates [177, 178].

Homogeneous carbon nanoparticles exhibiting graphene sheets overall morphology were synthesised by nano-thermal plasma reactor by using C_2H_4 as carbon source and the mixture gas of argon and CO_2 as plasma gas. A more or less pronounced crumpling effect were observed and modelled in Figure 2-12a and b. This texture is similar to that already proposed by Oberlin [180] and de Fonton et al. to describe polyaromatic carbon fragments making the pore wall in cokes.

Bragg fringes are frequently seen in TEM images as shown in Figure 2-12a. Comparing with the outer sheath of the acetylene-type CB where Bragg fringe lengths tend to be shorter than the graphene stack thickness, Bragg fringe lengths in paper sheet-like carbon nanoparticles are as long as the whole sheet thickness, revealing the high coherence of the graphene stacks making the sheets. Electron diffraction patterns Figure 2-13b are again typical of the turbostratic structure, thus the local texture is highly anisotropic at the nanoscale. It is worth noting that these carbon morphologies are similar to referenced in the literature as a DC thermal plasma torch [181] and a gliding discharge under non-equilibrium plasma conditions [182].
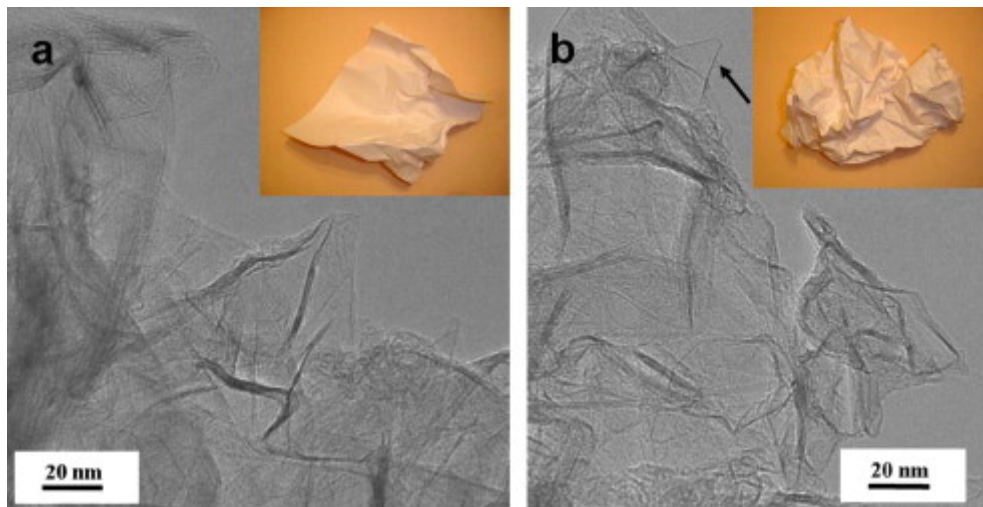
Figure 2-12 TEM images of graphene sheets, (a) low crumpling; (b) high crumpling. Insets: paper sheet models [121].
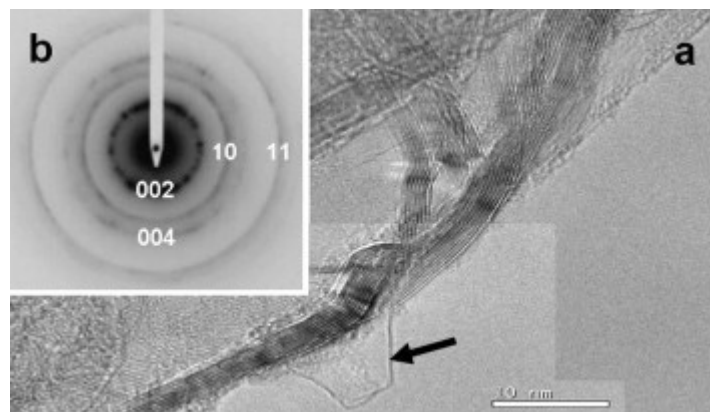
Figure 2-13 (a) HRTEM image of graphene sheets. A single graphene is arrowed: (b) related SAED pattern.
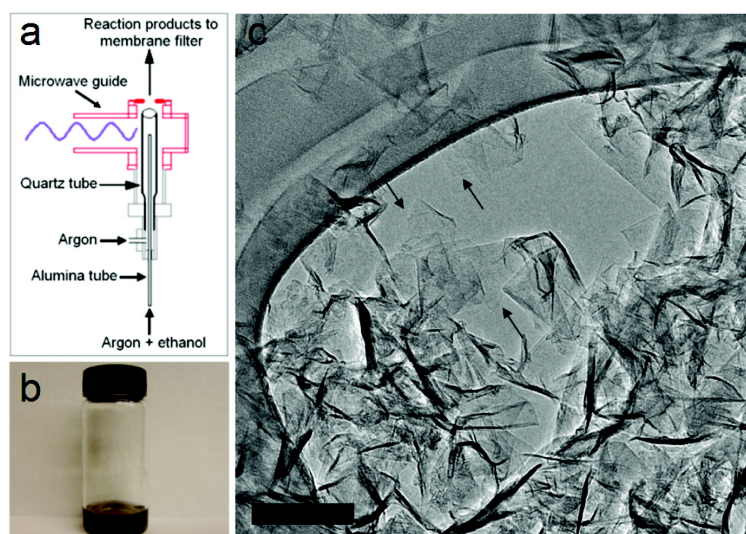
Figure 2-14 Synthesis of graphene sheets. (a) Schematic of the atmospheric pressure microwave plasma reactor used to synthesize graphene. (b) Photograph of graphene sheets dispersed in methanol. (c) A TEM image of graphene sheets freely suspended on a lacey carbon TEM grid [154].

33

Dato et al. [154] synthesized graphene sheets in the gas phase using a substrate-free, atmospheric-pressure microwave plasma reactor. Graphene sheets (as shown in Figure 2-14) were synthesized by passing liquid ethanol droplets into argon plasma. They proved that graphene can be created without three-dimensional materials or substrates and demonstrated a possible avenue to the large-scale synthesis of graphene.

2.3.4 Plasma reactor

The most widely used method for plasma generation utilizes the electrical breakdown of a neutral gas in the presence of an external electric field. Charge carriers accelerated in the electromagnetic field couple their energy into the plasma via collisions with other particles. Electrons retain most of their energy in elastic collisions with atoms and molecules because of their small mass and transfer their energy primarily in inelastic collisions.

Several different types of non-thermal plasma can be formed depending on the type of applied electric field used to drive the plasma formation. These include a continuous or pulsed direct current (DC) [28, 183, 184] [184-186] [187] [188-190] [191], dielectric barrier discharges (DBD) [118, 188, 192-197], an alternating current (AC) utilizing radio frequencies (kHz-MHz) [198] [199], atmospheric pressure plasma jet (APPJ) [128, 131, 151, 200, 201] and microwave frequencies (GHz) [108, 143] [155, 183, 202-208] [209] [210] etc.

2.3.5 Carbon modification

Activated carbon (AC) has been used in many applications, usually in purification of gases or water, or in gas separation processes. It is a widely used adsorbent in the treatment of wastewaters due to its exceptionally high surface areas which range from 500 to 1500 m^2/g, well-developed internal microporosity structure as well as the presence of a wide spectrum of surface functional groups [211]. Activated carbon with large surface area and porous structure is able to distribute chemicals on its large hydrophobic surface that makes them accessible to reactants. Hence of late research on ACs has focused on their modification and characterisation for gases sorption. There are three main methods to modify carbon: physical,

chemical and biological methods. (Figure 2-15) [212]. Table 2-2 lists and compares the advantages and disadvantages of existing modification techniques.
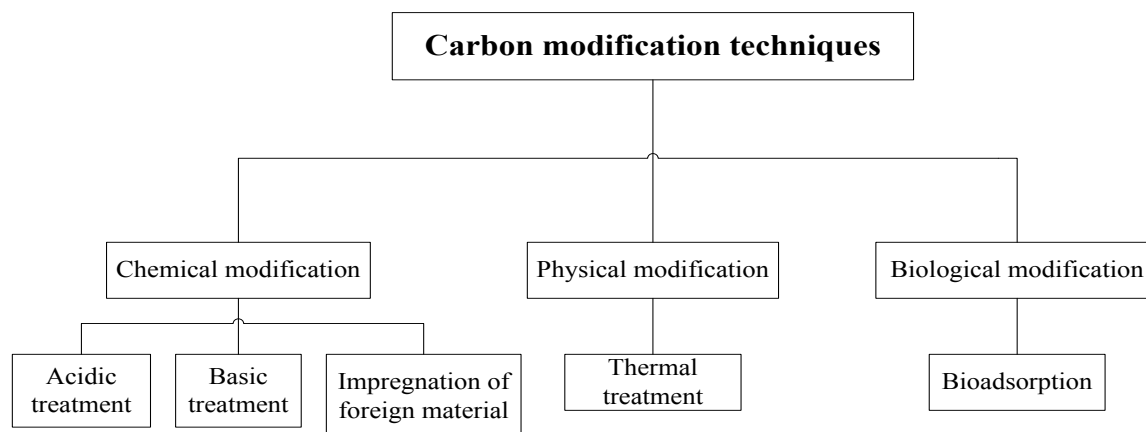
Figure 2-15 Categories of activated carbon modification techniques.

Table 2-2 Technical advantages and disadvantages of existing modification techniques

Modification	Treatment	Advantages	Disadvantages
Chemical characteristics	Acidic	Increases acidic functional groups on AC surface. Enhances chelation ability with metal species.	May decrease BET surface area and pore volume.
			Has adverse effect on uptake of organics.
			May give off undesired SO_2 (treatment with H_2SO_4) or NO_2 (treatment with HNO_3) gases.
	Basic	Enhances uptake of organics	May, in some cases, decrease the uptake of metal ions.
	Impregnation of foreign material	Enhances in-built catalytic oxidation capability.	May decrease BET surface area and pore volume.
Physical characteristics	Heat	Increases BET surface area and pore volume.	Decreases oxygen surface functional groups.
Biological characteristics	Bioadsorption	Prolongs AC bed life by rapid oxidation of organics by bacteria before the material can occupy adsorption sites.	Thick bio-film encapsulating AC may impede diffusion of adsorbate species.

35

2.3.5.1 Chemical modification

Chemical modification may be further divided into two broad groups, those resulting in acidic and basic surface [213-215]. The third type of chemical modification is the surface impregnation of carbon with active metals and their oxides. Many applications, with emphasis on metal removal from aqueous solutions, are directed towards modifying carbon surfaces to increase their acidic surface functional groups, which are types of oxygen complexes, such as carboxyl, quinine, carbonyl, lactone, hydroxyl and carboxylic anhydride [212], as shown in Figure 2-16.

The most commonly used methods to introduce oxygen containing acidic groups are oxidation by gases and aqueous oxidant [89, 216]. Nitric acid or nitric and sulphuric acid mixture have also been shown to be very effective oxidizing agents due to introduction of a significant number of oxygenated acidic functionalities onto the carbon surface that mainly include carboxylic, lactone, and phenolic hydroxyl groups [217, 218]. It has been demonstrated that oxidation of activated carbon in the gas phase increases mainly the concentration of hydroxyl and carbonyl surface groups while oxidation in liquid phase can incorporate a higher amount of oxygen in the form of carbonxylic and phenolic hydroxyl groups.
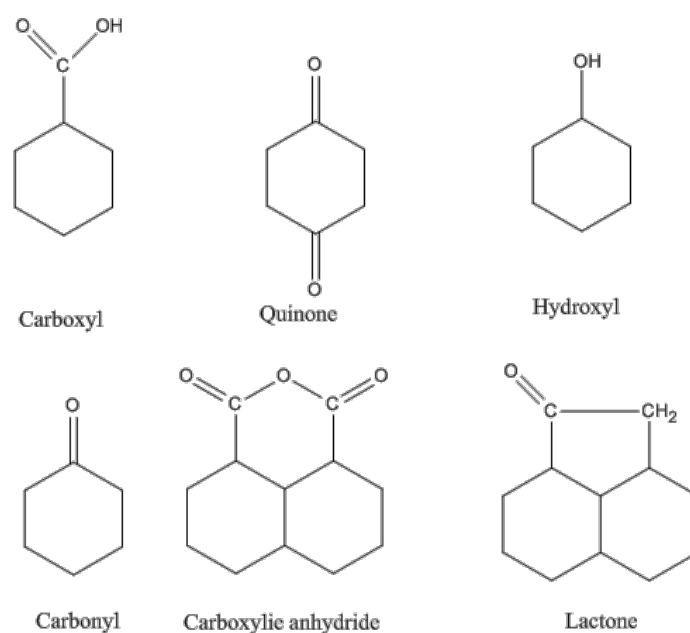
Figure 2-16 Simplified schematic of acidic surface groups bonded to aromatic rings on AC [212].

Basic surfaces of AC can be associated with: (1) resonating π-electrons of carbon aromatic rings that attract protons, and (2) basic surface functionalities (e.g. nitrogen containing groups) that are capable of binding with protons. In the presence of a large number of oxygen containing acidic groups on carbon surface, the contribution of π-electrons to carbon basicity is very limited. Therefore, one method of increasing basicity is to remove or neutralize the acidic functionalities, and other way is to replace acidic groups with proper basic groups (e.g., basic nitrogen functionalities).

2.3.5.2 *Physical modification*

Physical activation involves the carbonization of a carbonaceous precursor followed by the gasification of the resulting char in the presence of suitable oxidizing gasifying agents such as CO_2 and steam at high temperatures (e.g., 1073 -1373 K) [219, 220]. After physical thermal treatment, the physical characteristics such as BET surface area and pore volume can be increased.

Physical activation permits better control over the creation of a desired micro porous structure. Activation at higher temperatures (>700°C) enlarges the diameter of the pores, where by the pore volume increases significantly. Steam activation has shown the best potential for producing activated carbons with high surface area and good pore ratio [221]. The main advantage of physical activation over chemical activation is that it avoids the incorporation of impurities coming from the activating agent. Because of the activation step, a certain mass of the carbonized material is lost due to the formation of gaseous carbon oxides. The burn-off percent influences the textural properties of the activated carbons although, in general, the materials produced in this manner usually show a well-developed surface area and porous texture [222]. A drawback of heat treatment of AC is that oxygen surface functional groups can be destroyed at high temperatures [223]. As such, destruction of these groups may indicate lesser capacity to form chelats with metal species and thus reduces their uptakes onto the modified AC. Table 2-3 lists research works on physical activation methods and their effects on carbon structure.

Table 2-3 Techniques used to significantly modify physical characteristics of AC

Technique(s) used	Physical characteristic(s) improved	Changes in physical characteristic(s)	Chemical species removed as enhanced by modification	Reference
Heat treatment at 400 and 600 °C	Specific surface area and total pore volume	Bet surface area (+7.2% for 400 °C; +6.6% for 600 °C), total pore volume (+ 6.8% for 400 °C; +8.6% for 600 °C)	Acid dyes (acid red 73 and acid yellow 23)	[223]
Ozonation	Specific surface area (micropore size) and total pore volume, total pore volume (+9.0%)	Bet surface area (+8.7%)	Methylethylketone and benzene	[224]
Heat treatment via annealing at 1173 K in a quartz reactor	Specific surface area (micropore size)	Bet surface area (+21.5%)	Herbicides (2,4-dichlorophenoxyacetic acid and benzolin)	[211]
Heat treatment by steam or methane and stream at 1000 °C	Micropore and mesopore volumes	Micropore volume (+50–70%), mesopore volume (+65-90%)	2-Methylisoborneol	[225]
Heat treatment at 350 °C	Specific surface area (micropore size) and total pore volume	Bet surface area (+ up to 19.4%), total pore volume (+ up to 19.2%)	Maltooligosaccharide (carbohydrate)	[226]
H_2O-CO_2 heat treatment at 850 °C	Specific surface area (micropore size) and total pore volume	BET surface area up to 1779 m^2/g		[227]
CO2 heat treatment at 900 °	Specific surface area and total pore volume	BET surface area up to 604 m^2/g		[228]

2.3.5.3 Biological modification

Biological treatment is used to remove the microorganisms in water by giving rise to the formation of bacteria colonies by the adsorption of bacteria/ microorganisms on the activated carbons. The porous structure of activated carbon particles provides bacteria with a protective environment, and the presence of a large variety of surface functional groups on carbon particles enhances the adhesion of the microorganisms of activated carbon [229, 230]. In biological AC process, carbon-bed life can be prolonged by converting a portion of recalcitrant organics to biodegradable organics by preozonation. The attached

microorganisms then convert the biodegradable portion to biomass, carbon dioxide and waste products before this material can occupy adsorption sites on the AC [230]. Moreover, the biofilm formed on AC can change the surface charge density of the AC, mainly increasing its negative value, which could enhance its adsorption capacity against some positively charged pollutant species, such as most of the heavy metals [230]. The investigation by Moreno-Castilla et al. supported this theory, in which they found out that pH of the point of zero charge of AC-bacterial complex of coli was decreased due to the lower pH of the bacteria. The disadvantage of Bioadsorption is that the formation of biofilm that may have an encapsulating effect on AC. If this biofilm becomes too thick, the adsorbate species may encounter difficulty in diffusing through the biofilm and thus reduces adsorption [212].

2.4 Design of Experiments - Response Surface Methodology

Design of experiments, referred to as DOE, is a systematic approach to understand how process and product parameters affect response variables such as processability, physical properties, or product performance [231]. This method was first developed in the 1920s and 1930, by Sir Ronald A. Fisher. It is a strategy to design experiment in order to get most efficiently proper information to satisfy the purpose of experiment from minimum number of experiments. In a traditional DOE, screening experiments are performed in the early stages of the procedures, when it is likely that many of the design variables initially considered have little or no effect on the response. The purpose is to identify the design variables that have large effects for further investigation. A detailed description of the DOE theory can be found in Box et. al.[232], Myers et.al. [233], and Montgomery [234]. The application of DOE to structural optimization has been reviewed by Schoofs [235].

Response surface methodology, or RSM is a collection of mathematical and statistical techniques that are useful for the modeling and analysis of problems in which a response of interest is influenced by several variables and the objective is to optimize this response. An important aspect of RSM is the design of experiments. Before applying the RSM, it is first

necessary to choose an experimental design that will define which experiments should be carried out in the experimental region being studied [232]. RSM has been widely used to optimise products and processes in manufacturing, chemical industries and material science [101, 102, 236-238].

The steps of RSM as an optimization technique are as follows: 1) the selection of independent variables of major effects on the system through screening studies and the delimitation of the experimental region, according to the objective of the study and the experience of the researcher; 2) the choice of the experimental design and carrying out the experiments according to the selected experimental matrix; 3) the mathematic and statistical treatment of the obtained data through the fit of a polynomial function; 4) the evaluation of the model's fitness; 5) the verification of the necessity and possibility of performing a displacement in direction to the optimal region; and 6) obtaining the optimum values for each studied variable.

2.4.1 Screening of variables

Screening designs should be carried out to determine the variables that present more significant effects on the experimental results since numerous variables may affect the response of the system and it is practically impossible to control the small contributions from each one. Generally, full or fractional two-level factorial designs may be used for this objective because they are efficient and economical [239].

2.4.2 Design of Experiments

The simplest model, Equation 1, which can be used in RSM is based on a linear function.

$$y = \beta_0 + \sum_{i=1}^{k} \beta_i x_i + \varepsilon \qquad \text{Equation 1}$$

where k is the number of variables, β_0 is the constant term, β_i represents the coefficients of the linear parameters, x_i represents the variables, and ε is the residual associated to the experiments. Residual is the difference between the calculated and experimental result for a

determinate set of conditions. A good mathematical model fitted to experimental data must present low residuals values.

To evaluate curvature, a second-order model must be applied. Two-level factorial designs are used in the estimation of first-order effects, but they fail when additional effects, such as second-order effects are significant. So, a central point in two-level factorial designs can be used for evaluation curvature. A model for a second-order interaction presents the following

$$y = \beta_0 + \sum_{i=1}^{k} \beta_i x_i + \sum_{1 \le i \le j}^{k} \beta_{ij} x_i x_j + \varepsilon \qquad \text{Equation 2}$$

where β_{ij} represents the coefficients of the interaction parameters.

In order to determine a critical point (such as, maximum, minimum, or saddle), it is necessary for the polynomial function to contain quadratic terms according to the equation presented below:

$$y = \beta_0 + \sum_{i=1}^{k} \beta_i x_i + \sum_{i=1}^{k} \beta_{ii} x_i^2 + \sum_{1 \le i \le j}^{k} \beta_{ij} x_i x_j + \varepsilon \qquad \text{Equation 3}$$

where β_{ii} represents the coefficients of the quadratic parameters.

To estimate the parameters in Equation 3, the experimental design has to assure that all studied variables are carried out in at least three factor levels. Among the more known second-order symmetrical designs are the three-level factorial design, Box–Behnken design, central composite design, and Doehlert design. These symmetrical designs differ from one another with respect to their selection of experimental points, number of levels for variables, and number of runs and blocks.

2.4.2.1 Full factorial design

To construct an approximation model that can capture interactions between N design variables, a full factorial approach [240] may be necessary to investigate all possible combinations. A factorial experiment is an experimental strategy in which design variables are varied together, instead of one at a time.

The lower and upper bounds of each of N variables in the optimization problem needs to be defined. The allowable range is then discretized at different levels. If each of the variables is defined at only the lower and upper bounds (two levels), the experimental design is called 2^N full factorial. Similarly, if the midpoints are included, the design is called 3^N full factorial and shown in Figure 2-17a and b. Figure 2-17 (a and b) shows the three levels factorial designs for the optimization of two and three variables, respectively.
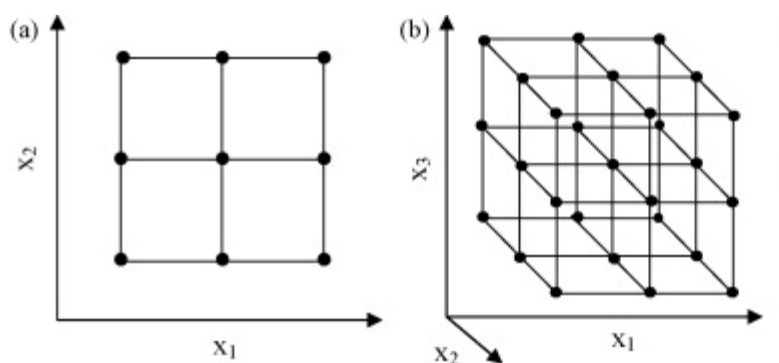
Figure 2-17 Experimental designs based on the study of all variables in three levels: (a) two variables and (b) three variables.

Full factorial design is limited in RSM when the factor number is higher than 2 because the number of experiments required for this design is very large, thereby losing its efficiency in the modeling. Thus designs that present a smaller number of experimental points, such as Box-and Behnken, central composite are more used [241].

2.4.2.2 Central Composite Design

CCD has been widely used for fitting a second-order model and to come out with a minimum number of experiments for a complex experimental process [102, 242, 243]. CCD presents an alternative to 3^N designs in the construction of second-order models because the number of experiments is reduced as compared to a full factorial design. Such as, for a three factors experiment, the number of experiments runs is 15 in the case of CCD compared to 27 for a full-factorial design. The CCD consists of a two-level (±1) factorial design with center points and axial points, which are a distance of -alpha & +alpha from the centre of the design (Figure 2-18a). The regular CCD can be modified by choosing alpha = 1.0, which is named as a face centered CCD (Figure 2-18b). It has been reported that CCD can optimize ACs production [236, 244] in order to get maximum dyes adsorption [238, 245, 246] or to study the variation of their physicochemical characteristics as a function of the activation

conditions [247]. CCD has also been used to optimize activated carbon (ACs) for hydrogen storage [237] to achieve hydrogen storage capacities.
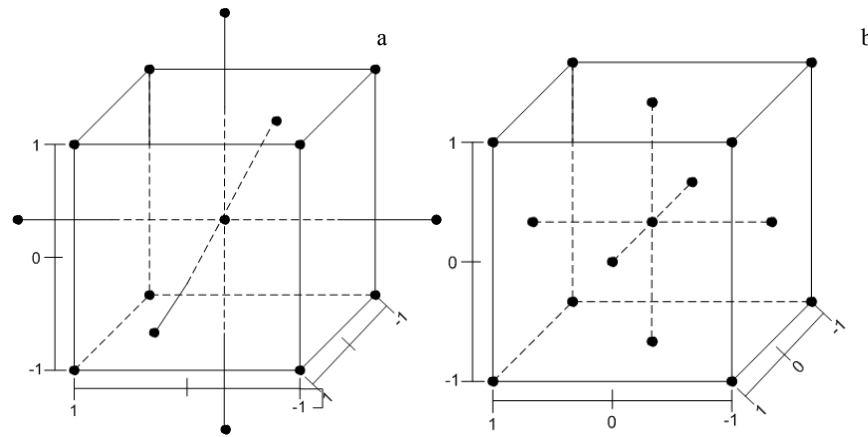
Figure 2-18 Orientation of points at design space (a) CCD and (b) face centered CCD.

2.4.2.3 Box-Behnken Design

Box-Behnken design (BBD) is used to calibrate full quadratic models. A Box-Behnken design has points at the center and the midpoint of each side, as exemplified for a three-factor design in Figure 2-19. There are no corner points and the design is spherical so it is rotatable and, for a small number of factors (four or less), require fewer runs than Central Composite Designs [240, 248, 249]. Its principal characteristics are:

(1) requires an experiment number according to N-2k(k-1)+C_p, where k is the number of factors and C_p is the number of the central points;

(2) all factor levels have to be adjusted only at three levels (-1, 0, 1) with equally spaced intervals between these levels. This experimental design has been applied for the optimization of chemical and physical processes.
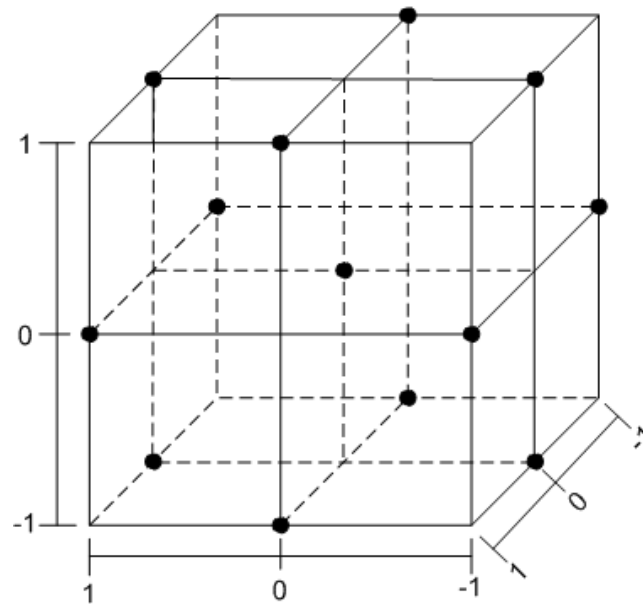
Figure 2-19 The positions of the data points for BBD.

2.4.3 Evaluation of the fitted model

After fitting the function to the experimental data, the quality of the model fitted is evaluated by the application of analysis of variance (ANOVA) [101]. In the typical application of ANOVA, the null hypothesis is that all groups are simply random samples of the same population. This implies that all treatments have the same effect (perhaps none). Rejecting the null hypothesis implies that different treatments result in altered effects. The central idea of ANOVA is to compare the variance due to the treatment with the variation due to random errors inherent to the measurements of the generated responses [240].

In ANOVA, the evaluation of data set variation is made by studying its dispersion. The evaluation of deviation (d_i) that each observation (y_i) or its replicates (y_{ij}) present in relation to the media ($\bar{y}$), or, more precisely, the square of this deviation, is presented in Equation 4.

$$d_i^2 = \left(y_{ij} - \bar{y}\right)^2 \qquad \text{Equation 4}$$

The sum of the square for all observation deviations in relation to the media is called the total sum of the square (SS_{tot}); it can be dismembered in the sum of the square due to the fitted

mathematical model, that is, due to regression (SS$_{reg}$), and in the sum of the square due to residuals generated by the model (SS$_{res}$), as shown below:

$$SS_{tot} = SS_{reg} + SS_{res}$$

Equation 5

As replicate of the central point are made, it is possible to estimate the pure error associated with repetitions. Thus, the sum of the square for residuals can be dismembered into two more parcels: the sum of the square due to pure error (SS$_{pe}$) and the sum of the square due the lack of fit (SS$_{lof}$), as shown below:

$$SS_{res} = SS_{pe} + SS_{lof}$$

Equation 6

when the division of the sum of the square for each source of variation (total, regression, residual, lack of fit, and pure error) is made by its respective numbers of degrees of freedom (d.f.), the media of the square (MS) are obtained. The numbers of degree of freedom for these sources of variation are calculated by the expressions presented in the third column of Table 2-4. Table 2-4 also presents equations related to the source of variations for the calculation of SSs and MSs [235, 240].

Table 2-4 Analysis of variance for fitted mathematical model to an experimental data set using multiple regressions

Variation source	Sum of the square	Degree of freedom	Media of the square
Regression	$SS_{reg} = \sum_i^m \sum_j^{n_i} (\hat{y}_i - \bar{y})^2$	p - 1	$MS_{reg} = \dfrac{SS_{reg}}{p - 1}$
Residuals	$SS_{res} = \sum_i^m \sum_j^{n_i} (y_{ij} - \hat{y}_i)^2$	n - p	$MS_{res} = \dfrac{SS_{res}}{n - p}$
Lack of fit	$SS_{lof} = \sum_i^m \sum_j^{n_i} (\hat{y}_i - \bar{y}_i)^2$	m - p	$MS_{lof} = \dfrac{SS_{lof}}{m - p}$
Pure error	$SS_{pe} = \sum_i^m \sum_j^{n_i} (y_{ij} - \bar{y}_i)^2$	n - m	$MS_{pe} = \dfrac{SS_{pe}}{n - m}$
Total	$SS_{tot} = \sum_i^m \sum_j^{n_i} (y_{ij} - \bar{y})^2$	n - 1	

n_i, number of observations; m, total number of levels in the design; p, number of parameter of model; $\hat{y}_i$, estimated value by the model for the level i; $\bar{y}$, overall media; y_{ij}, replicates performed in each individual levels; $\hat{y}_i$, media of replicates performed in the same set of experimental conditions.

The significance of regression can be evaluated by the ratio between MS_{reg} and MS_{res} and by comparing these variation sources using the F test, taking into account its respective degrees of freedom associated to regression (v_{reg}) and to residual (v_{res}) variances:

$$\frac{MS_{reg}}{MS_{res}} \approx F_{v_{reg}, v_{res}}$$

Equation 7

Thus, if a statistically significant value for this ratio is higher than the tabulated value for F, it indicates that the model is well fitted to the experimental data. Another way to evaluate the model is the lack of fit test. If the model is well fitted to the experimental data, MS_{lof} should reflect only the random errors inherent to the system. Additionally, MS_{pe} is also an estimate of these random errors, and it is assumed that these two values are not statistically different. This is the main idea of the lack of fit test. It is possible to use the F distribution to evaluate if there is some statistical difference between these two media, in the same way that the significance of regression was verified:

$$\frac{MS_{lof}}{MS_{pe}} \approx F_{v_{lof}, v_{pe}}$$

Equation 8

where, v_{lof} and v_{pe} are, respectively, the degree of freedom associated with the lack of fit and the pure error variances. If this ratio is higher than the tabulated value of F, it is conclude that there is evidence of a lack of fit and that model needs to be improved. However, if the value is lower than the tabulated value, the model fitness can be considered satisfactory. In order to apply a lack of fit test, DOE must be performed with authentic repetitions at least in its central point.

In short, a model will be well fitted to the experimental data if it presents a significant regression and a non-significant lack of fit. Most variation related to residuals is due to pure error (random fluctuation of measurements) and not to the lack of fit, which is directly related to the model quality [233]. The visual inspection of the residual graphs can also generate valuable information about the model suitability. If the model is well fitted, its graph of residuals presents a behavior that suggests a normal distribution. If the model generates larger residuals, it is not adequate to make precise inferences about the data behavior in the studied

experimental area. Moreover, if the model needs other terms, the residual graph will present a behavior that indicates the kind of term that needs to be added to the model [101].

2.4.4 Multiple responses optimization in analytical chemistry by using RSM

It is relatively simple to find the optimal conditions for a single response using RSM. However, the researchers may be interested in more than one response simultaneously. If the amount of significant factors allows the graphical visualization of adjusted models, and if the numbers of response are not very large, the surfaces can be overlapped to enable finding experimental region that can satisfy all the responses [104].

If the optimal values for each response are localized in different regions, it will be more difficult to find the conditions that simultaneously satisfy all responses. The level of difficulty increases as these optimum regions become more distant from each other and do not intersect. Changes in the level of a factor can improve one specific response and have a very negative effect on another.

Myers and Montgomery [233] describe a multiple response method called desirability that is the most important and most currently used method to solve the problem of the optimization of several responses. The method makes use of an objective function, D(X), called the desirability function. It reflects the desirable ranges for each response (d_i). The desirable ranges are from zero to one (least to most desirable, respectively). The simultaneous objective function is a geometric mean of all transformed responses:

$$D = \sqrt[n]{(d_1 \times d_2 \times ... \times d_n)}$$

Equation 9

where n is the number of responses. If any of the responses of factors fall outside their desirability range, the overall function becomes zero.

There are five types of transformations for obtaining individual desirability, as listed below:

if the target value for the response y is maximum:

$$d_i = \begin{cases} 0, & \text{if } y < L \\ \left(\dfrac{y - L}{T - L}\right)^s, & \text{if } L \le y \le T \\ 1, & \text{if } y > T \end{cases}$$

Equation 10

where L is the lower acceptable value to the response, y is response, T is target value and s is the weight. s is applied for t to attribute levels of importance to the T.

if the target value for the response y is minimum:

$$d_i = \begin{cases} 0, & \text{if } T < y \\ \left(\dfrac{U - y}{U - T}\right)^s, & \text{if } T \le y \le U \\ 1, & \text{if } y > U \end{cases}$$

Equation 11

where U is the upper acceptable value to the response, y is response, T is target value and s is the weight.

If T is located between L and U, then, a bilateral desirability function will be used:

$$d_i = \begin{cases} 0, & \text{if } y < L \\ \left(\dfrac{y-L}{T-L}\right)^s, & \text{if } L \le y \le T \\ \left(\dfrac{U-y}{U-T}\right)^s, & \text{if } T \le y \le U \\ 0, & \text{if } y > U \end{cases}$$

Equation 12

As demonstrated, s control the variation rate of the desirability functions. The desirability function can be used for any number responses, factors and/or components provided at least one response is included in the target set. And it is feasible to attribute different desirability to the response and, consequently, to increase or decrease the range of acceptable values during the optimization process.

From the above review, it is clear that an ideal sorbent for either hydrogen storage or CO_2 capture has not yet been developed. As carbon is a versatile and low-cost material and can exist in many structural forms, from graphene, nanotubes, to high-surface porous structures, it was selected here for further study. Particularly, a novel non-thermal plasma technique was under development. There exist great potential of using the technology to generate a variety of carbon-based nanostructures. In addition, Mg is also a low-cost system with a relatively

large capacity for hydrogen and there are still opportunities for further development. Hence, the objectives of this study are focused on: 1) the preparation of nanostructured carbon by methane cracking in a relatively low-energy cold plasma reactor designed in-house; 2) optimization of thermal treatment conditions for carbon materials produced by the microwave plasma route; 3) the effects of carbon structures on hydrogen storage properties of MgH_2; 4) CO_2 capture and CO_2/H_2 separation of MgO and MgO/plasma carbon.

3

CHARACTERISATION METHODS

In this chapter, various characterisation methods and the relevant facilities used in the following chapters are described, including X-ray diffraction (XRD), scanning electron microscopy (SEM) and transmission electron microscopy (TEM), surface area and porosity analysis system, thermogravimetric analysis, and Raman spectroscopy. The synthesis methods will be described in following Chapters, along with the specific materials.

3.1   X-ray diffraction (XRD)

X-ray diffraction (XRD) is a versatile technique that reveals detailed information about the chemical composition and crystallographic structure of materials. X-ray powder diffraction is usually used for the identification of crystalline compounds by their diffraction patterns. Some specific uses are listed below:

- Crystallographic structural analysis and unit-cell calculations for crystalline materials

- Quantitative determination of crystalline phases in multi-phase mixtures by peak-ratio calculations.

- Quantitative determination of phases by whole-pattern refinement.

- Determination of crystallite size from analysis of peak broadening.

- Determination of crystallite shape from study of peak symmetry.

The angle of the diffraction is related to the interplanar spacing, d, by the Bragg's Law [250], and the intensity of the diffraction maximum is related to the strength of those diffractions in the specimen. X-ray data are recorded in terms of 2θ (x-axis) vs. intensity (y-axis).

XRD used in this study was mainly for detecting the phase transformation of the materials during mechanical milling, dehydrogenation, and carbon structure, and for the analysis of crystallite size. An XTra diffractometer (Thermo ARL, the United States) was used for powder X-ray diffraction. The source was Cu K_α (λ=1.554056 Å) radiation from a conventional water-cooled X-ray tube. The scan range was from 2θ= 10° to 80° and the scan rate was 1.2°/min with a step size of 0.02°. In order to avoid exposure to air, the Mg-based samples were prepared in the glove box and a sample holder covered with an airtight plastic dome which had a negligible effect on diffraction patterns was used. The nanograin (crystallite) size of phases was calculated from the broadening of their respective XRD peaks. Since the Bragg peak broadening in an XRD pattern is due to a combination of grain refinement (nanograin/crystallite) and lattice strains, it is customary to use computing techniques by means of which one can separate these two contributions. The crystallite size was obtained from Scherrer formula:

$$D = K\lambda/(B\cos\theta) \qquad\qquad \text{Equation 13}$$

where D is the averaged dimension of crystallites; K is the Scherrer constant, a somewhat arbitrary value that falls in the range 0.87-1.0 (it is usually assumed to be 1); λ is the wavelength of X-ray; and B is the integral breadth of a reflection (in radians 2θ) located at 2θ. B is often calculated relative to a reference solid (with crystallite size >500 nm) added to the sample: $B^2=B_s^2-B_r^2$. The program JADE 5.0 was used to evaluate the diffraction patterns.

3.2 Scanning Electron Microscopy (SEM) and Transmission Electron Microscopy (TEM)

The scanning electron microscope (SEM) uses a focused beam of high-energy electrons to generate a variety of signals at the surface of solid specimens. The signals that derive from electron-sample interactions reveal information about the sample including external morphology, chemical composition, and crystalline structure and orientation of materials making up the sample. All the samples were coated with an ultrathin coating of gold by vacuum sputter coating. The coating of gold increases signal and surface resolution, especially with samples of low atomic number. The improvement in resolution arises because backscattering and secondary electron emission near the surface are enhanced and thus an image of the surface is formed.

Backscattered electrons (BSE) consist of high-energy electrons originating in the electron beam, which are reflected, or back-scattered, out of the specimen interaction volume by elastic scattering interactions with specimen atoms. Since heavy elements (high atomic number) backscatter electrons more strongly than light elements (low atomic number), they appear brighter in the image. BSE were used to detect contrast between areas with different chemical compositions in this study. A JEOL (Japan) thermionic SEM was used for the image analyses.

Transmission Electron Microscopy (TEM) was employed to further examine the particle size and particle distribution of samples. It exploits the very small wavelengths of high-energy electrons to probe solids at the atomic scale. A Jeol JEM 2100 TEM in the 200kV class analysis has been developed to achieve the highest image quality and analytical performance with a probe size under 0.2 nm. For TEM observation, a dilute suspension of sample powder was dropped onto a TEM grid, and dried.

The particle sizes of the powder mixtures were calculated from the SEM and TEM images as the equivalent circle diameter, $ECD = \frac{1}{2}\left(\frac{4A}{\pi}\right)$, where A represents the projected particle area, using the *Image Tool v.3.00 software*.

3.3   BET Surface Area and Porosity

The surface areas of samples have been measured by nitrogen/argon equilibrium at liquid nitrogen temperature using a Quantachrome AUTOSORB-1 (shown in Figure 3-1). The cleaned samples were degassed for 8 h at 573 K to remove any moisture or adsorbed contaminants that may be presented on their surfaces. The BET surface area of the carbons was determined by applying the BET equation imbedded in the manufacturer-supplied software to the adsorption data. The pore size distribution was evaluated by the density functional theory (DFT) method [251, 252]. DFT method bridges the gap between the molecular level and macroscopic approaches and provides a more accurate approach for pore size analysis, comparing with the classical macroscopic theories, such as the Dubinin-Radushkevich approach, the BJH method, and Horvath and Kawazoe (HK).

Figure 3-1 An image of AUTOSORB AS-1

3.3.1 Adsorption isotherms

An understanding of the surface area and porosity of an adsorbent can be achieved by the construction of an adsorption isotherm. When the quantity of adsorbate on a surface is measured over a wide range of relative pressures at constant temperature, the result is an adsorption isotherm. The adsorption isotherm is obtained point-by-point on the AUTOSORB AS-1 by admitting to the adsorbent successive known volumes of nitrogen and measuring the equilibrium pressure. Similarly, desorption isotherms can be obtained by measuring the quantities of gas removed from the sample as the relative pressure is lowered. All adsorption isotherms may be grouped into one of the six types shown below:
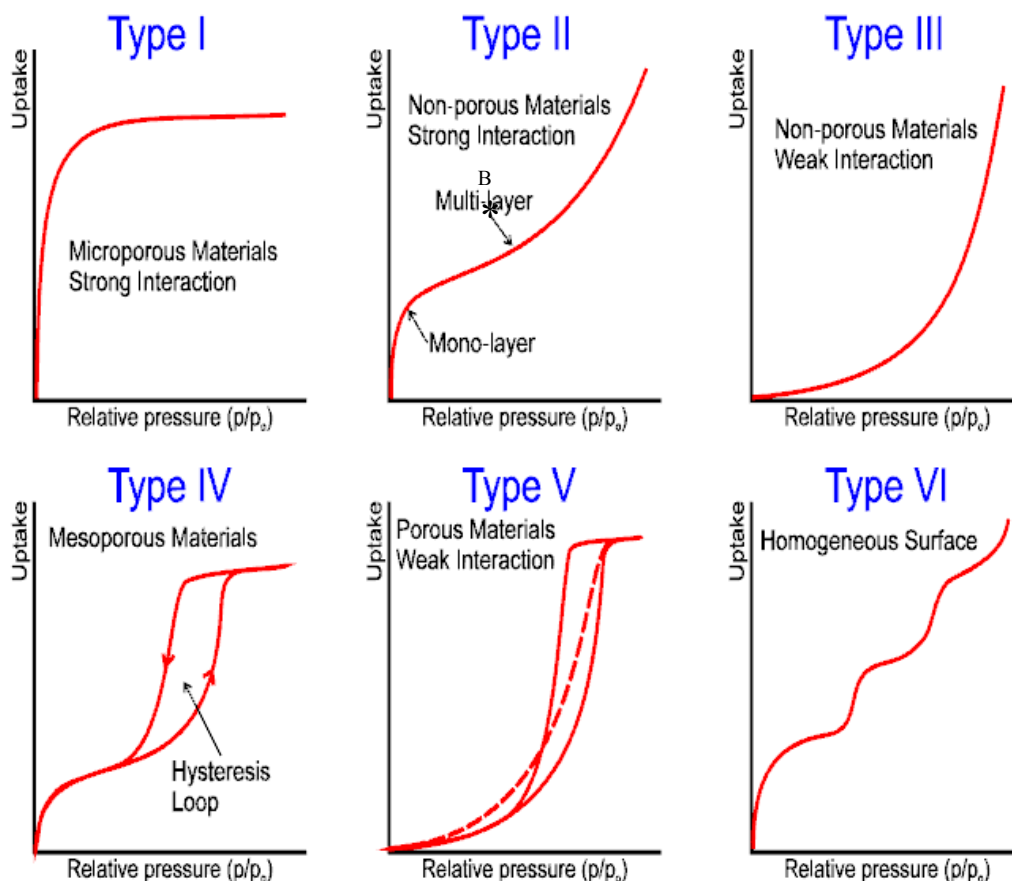
Figure 3-2 The IUPAC classification for adsorption isotherms [253].

This isotherm type is also a guide to the type and analysis of porosity.

1) Pores with dimension greater than 50 nm are called macrospore.

2) Pores with dimension less than 2 nm are called micropore and have Type I isotherm

3) Pores with dimension intermediate between 2 and 50 nm are called mesopore and have Type IV or Type V isotherms.

Type I or Langmuir isotherms are concave to the P/P_0 axis and the amount of adsorbate approaches a limiting value as P/P_0 approaches 1. Type I physisorption isotherms are exhibited by microporous solids having relatively small external surfaces, for example, activated carbons and molecular sieve zeolites. The limiting uptake of adsorbate is governed by the accessible micropore volume rather than by the internal surface area.

Type II isotherms are the normal form of isotherm obtained with a nonporous or macroporous adsorbent. It describes a system, which shows multi layer adsorption after reaching the monomolecular adsorbate layer at point B up to the setting in of condensation at P/P_0.

Type III isotherms are convex to the P/P_0 axis over its entire range. A well-known example is the adsorption of water vapor on nonporous carbons.

Type IV isotherms are associated with capillary condensation in mesopores, indicated by the steep slope at higher relative pressure. Also mesopores cause a hysteresis (Type IV and Type V).

Type V isotherms are uncommon, corresponding to the type III, except that pores in the mesopores range are present.

Type VI shows the gradual formation of individual adsorbate layers, which stem from a multimodal pore distribution.

Types I, II and III isotherms are generally reversible, but microporous materials having type I isotherms can exhibit hysteresis. Types IV and V, associated with mesoporosity, usually exhibit hysteresis between the adsorption and desorption isotherms. The pore morphology could be inferred using the de Boer work [254]. De Boer has identified five types of hysteresis loops and correlated them with various pore shapes, as shown in Table 3-1.

Table 3-1 Five hysteresis types and the corresponding pore shapes, according to de Boer [254].

Hysteresis	Geometric shape	Examples
Type A	Cylindrical pores open at both ends	
Type B	Slit-shaped pores or the space between parallel plates	
Type C	Wedge-shaped pores with open ends	
Type D	Wedge-shaped pores with narrow necks at one or both open ends	
Type E	'ink-bottle' pores	
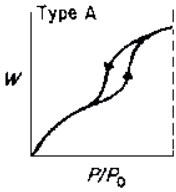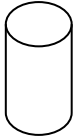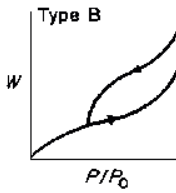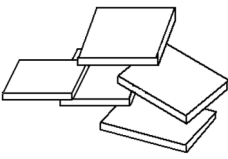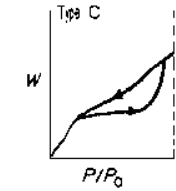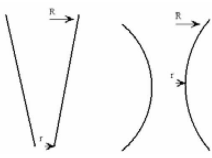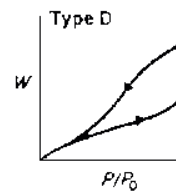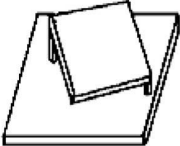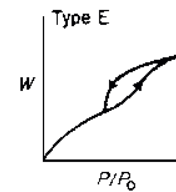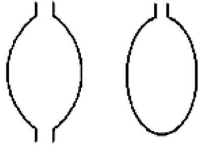
Type A is attributed to cylindrical pores: type B is associated with slit-shaped pores; type C is produced by wedge-shaped pores with open ends; type D results from wedge-shaped pores with narrow necks at one or both open ends. Type E has been attributed to 'ink-bottle' pores. Characteristically, the hysteresis in all isotherms close before reaching a relative pressure of 0.3 in the desorption process except when microporosity is present.

3.3.2 BET surface area

The Brunauer-Emmett-Teller (BET) method [251] is the most widely used procedure for the determination of the surface area of solid materials and involves the use of BET equation (Equation 14)

$$\frac{1}{W(\frac{P_0}{P} - 1)} = \frac{1}{W_m C} + \frac{C - 1}{W_m C}(\frac{P}{P_0})$$

Equation 14

where, W is the weight of gas adsorbed at a relative pressure, P/P_0, and W_m is the weight of adsorbate constituting a monolayer of surface coverage. The term C, the BET C constant, is related to the energy of adsorption in the first adsorbed layer and consequently its value is an indication of the magnitude of the adsorbent/adsorbate interactions.

The Equation 14 predicts a linear plot between the experimental $\frac{1}{W(\frac{P_0}{P}-1)}$ and P/P_0 values with slop equal to $\frac{C-1}{W_m C}$ and y-intercept equal to $\frac{1}{W_m C}$. From the slope and intercept, W_m can be calculated. The surface area S of the sample can be expressed as:

$$S = \frac{W_m N A_{cs}}{Mw}$$

Equation 15

where N is Avogadro's number (6.023×10^{23} molecules/mol) and M is the molecular weight of the adsorbate. Adsorption of nitrogen gas at its boiling point is generally used for surface area measurements using BET methods, A_{cs} is molecular cross-sectional area for N_2 of 0.162 nm^2. The linearity of BET plot is severely restricted to within the P/P_0 range of 0.05-0.30. A very high or very low C value will create considerable error in calculating the effective adsorbate cross-sectional area. High C values are likely to be associated either with localised monolayer adsorption or with micropore filling. Best results are obtained if the C values are within the approximate range 80-120 [255].

3.3.3 Total pore volume and average pore width

The total pore volume is derived from the amount of vapor adsorbed at a relative pressure close to unity, by assuming that the pores are then filled with liquid adsorbate. The total

volume of nitrogen (V_{ads}) can be converted to the volume of liquid nitrogen contained in the pores using Equation 16.

$$V_{liq} = \frac{P_a V_{ads} V_m}{RT}$$ Equation 16

where, P_a and T are ambient pressure and temperature, respectively, and V_m is the molar volume of the liquid adsorbate (34.7 cm^3/mol for nitrogen).

Since pores which would not be filled below a relative pressure of 1 have a negligible contribution to the total pore volume and the surface area, the average pore size can be estimated from the pore volume. For example, assuming cylindrical pore geometry (type A hysteresis), the average pore width r_p can be expressed as:

$$r_p = \frac{2V_{liq}}{S}$$ Equation 17

where Vliq I obtained from Equation 18 and S is the BET surface area. For other pore geometries a knowledge of the shape of the hysteresis in the adsorption/desorption isotherm is required.

BET surface area and porosity of each sample were determined from N_2 or Ar adsorption at 77 K using two independent surface area/pore size analyzers, a Quantachrome AUTOSORB-1 and a TRISTAR II 3020. The cleaned carbon samples were degassed for 8 h at 573 K to remove any moisture or adsorbed contaminants that may be presented on their surfaces. The BET surface area of the carbons was determined by applying the BET equation imbedded in the manufacture supplied software to the adsorption data. The pore size distribution was evaluated by the density functional theory (DFT) method, which has largely been applied to the characterization of micro- and mesoporous carbons, silica's and zeolites [251, 252].

3.4 Thermogravimetric Analysis and Gases sorption

3.4.1 Thermogravimetry and hydrogen sorption

Thermogravimetry (TG) using the IGA-003 measures the amount of weight change of samples, either as a function of increasing temperature, or isothermally as a function of time, in an atmosphere of helium or in vacuum. Intelligent Gravimetric Analyzer (IGA) supplied by Hidden Analytical Ltd (Figure 3-3) was used for experimental applications where it is necessary to have a flow of gas passed the sample including thermal analysis experiments and muti-component sorption. Sorption processes including physisorption, chemisorption, capillary condensation and absorption can be investigated. Densitometry analysis of the sample or gas phase is also provided.

Figure 3-3 An image of Intelligent Gravimetric Analyzer (IGA-003).

The method of differential thermogravimetry (DTG) analysis, which was calculated from TG data, was used for thermal investigations of analytical precipitates. There is good agreement of the onset temperature and the peak temperature of the materials between the DTG and Differential Thermal Analysis (DTA) [256, 257]. This simply means that the maximum rate of weight loss occurs at the greatest temperature differential recorded by DTA [256, 257]. The TG analysis was applied in Chapter 6 and 7. The experimental conditions of TG have been listed in the corresponding chapters.

Hydrogen adsorption of Mg-based material, which is considered as the chemical adsorption process, was measured under a flow mode within high pressure hydrogen flow (usually 1000 kPa hydrogen pressure) till reaching equilibrium. By analysis of IGA results, the hydrogen sorption kinetics and storage capacities of the materials at different temperatures can be obtained.

3.4.2 CO_2 sorption and buoyancy correction

The sorption behaviors of CO_2 and CO_2-containing gas mixtures, which are considered as the physisorption, were also performed using the thermogravimetric analyses by IGA. Gravimetric analysis of sorption processes uses a sensitive balance to record changes in weight of a sample. Typically, a solid sample is held at a fixed temperature, and a sorption isotherm is measured, by varying the partial pressure of the sorbate. The gravimetric measurement of weight gives a continuous direct indication of the amount of sorbate interacting with the sample. For each value of pressure, the weight of the sample is monitored until the sample reaches equilibrium with the gas. This weight value, at equilibrium, gives a point on the sorption isotherm. It is important to note that the measured weight includes contributions from various effects, in addition to the amount of sorption, such as

- The buoyancy force, due to the displaced mass of gas.

- Forces due to the movement of the gases around the sample, which may be due to deliberate use of a flowing gas environment, or to thermal effects.

- Interactions between the sample and ambient magnetic fields.

Thus, to obtain the quantity of interest, the mass of adsorbate (m), from the measured data, a buoyancy correction has to be performed:

Concentration$=m_a/Mm_s$ Equation 19

Mass % $= 100\ m_a/m_s$ Equation 20

$$m_a = \frac{\left\{\Phi_s - \Phi_U + \sum_{i=1,4}\frac{w_i(\rho_{gi} - \rho_{air})}{(\rho_i - \rho_{air})} - \sum_{j=1,4}\frac{w_j(\rho_{gj} - \rho_{air})}{(\rho_j - \rho_{air})} - m_s\left(1 - \frac{\rho_{gs}}{\rho_s}\right)\right\}}{\left(1 - \frac{\rho_{gs}}{\rho_a}\right)}$$ Equation 21

$m_s = \Phi_D - \Phi_U$ Equation 22

where m_a is the calculation of mass uptake after gas sorption, m_s is the dry mass, M is gas molar mass, Φ_s is the reading of the balance after reaction with gas, Φ_U is unload reading, Φ_D is dry reading, ρ_{air} is air density, ρ_{gs} is sample gas density, ρ_s is sample density.

Description	Weight (g)	Density (g/ml)	Gas density (mg/ml)	Temperature (K)
Sample container	$W_{i=1}$	$\rho_{i=1}$	$\rho_{gi=1}$	$T_{gi=1}$
Sample Ballast	$W_{i=2}$	$\rho_{i=2}$	$\rho_{gi=2}$	$T_{gi=2}$
Lower Sample Hangdown	$W_{i=3}$	$\rho_{i=3}$	$\rho_{gi=3}$	$T_{gi=3}$
Upper Sample Hangdown	$W_{i=4}$	$\rho_{i=4}$	$\rho_{gi=4}$	$T_{gi=4}$
Counterweight Container	$W_{j=1}$	$\rho_{j=1}$	$\rho_{gj=1}$	$T_{gj=1}$
Counterweight	$W_{j=2}$	$\rho_{j=2}$	$\rho_{gj=2}$	$T_{gj=2}$
Lower C/W Hangdown	$W_{j=3}$	$\rho_{j=3}$	$\rho_{gj=3}$	$T_{gj=3}$
Upper C/W Hangdown	$W_{j=4}$	$\rho_{j=4}$	$\rho_{gj=4}$	$T_{gj=4}$

In order to obtain the sample density ρ_s, Equation 23, the so-called helium volume was determined. Accordingly, we performed blank measurements with He as the "adsorbed" gas. Applying Equation 19, assuming He is not adsorbed, the volume of the adsorbent can be calculated from the measured data.

$\rho_s = m_s / V_s$ Equation 23

where V_s is helium volume.

3.5 Raman Spectroscopy

Raman spectroscopy is a vibrational spectroscopy technique used to collect a unique chemical fingerprint of molecules [258]. Each molecule has a different set of vibrational energy levels, and the photons emitted have unique wavelength shifts. Vibrational spectroscopy involves collecting and examining these wavelength shifts and using them to identify what is in a sample. Different peaks in the spectrum correspond to different Raman excitations.

When light interacts with matter, the photons which make up the light may be absorbed or scattered, or may not interact with the material and may pass straight through it. If the energy of an incident photon corresponds to the energy gap between the ground state of a molecule and an excited state, the photon may be absorbed and the molecule promoted to the higher energy excited state. It is also possible for the photon to interact with the molecule and scatter from it. The scattered photons can be observed by collecting light at an angle to the incident light beam, and provided there is no absorption from any electronic transitions which have similar energies to that of the incident light, the efficiency increases as the fourth power of the frequency of the incident light. The process of absorption is used in a wide range of spectroscopic techniques. For example, it is used in acoustic spectroscopy where there is a very small energy difference between the ground and excited states and in X-ray absorption spectroscopy where there is a very large difference. In between these absorption ranges are many of the common techniques such as NMR, EPR, IR, electronic absorption and fluorescence emission and UV spectroscopy. Figure 3-4 indicates the wavelength ranges of some commonly used types of radiation.

Gamma X-rays	UV-visible	Near IR	Mid-IR	Far IR	Micro-radio
10^{-11}	10^{-7}	10^{-6}	10^{-5}	10^{-4}	10 m
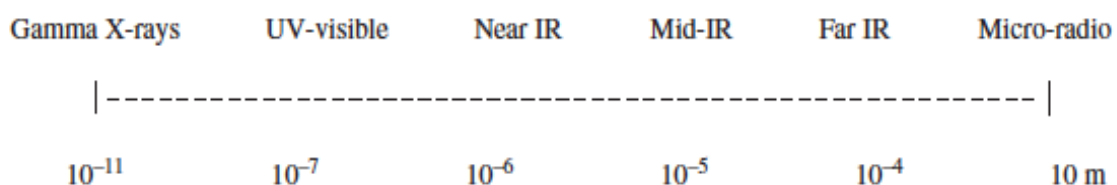
Figure 3-4 Electromagnetic spectrum on the wavelength scale [259].

The way in which radiation is employed in IR and Raman spectroscopies is different. In IR spectroscopy, infrared energy covering a range of frequencies is directed onto the sample. Absorption occurs where the frequency of the indicent radiation matches that of a vibration so that the molecule is promoted to a vibrational excited state. The loss of this frequency of radiation from the beam after it passes through the sample is then detected. In contrast, Raman spectroscopy uses a single frequency of radiation to irradiate unit of energy different from the incident beam, which is detected. Thus, unlike IR, Raman scattering does not require matching of the incident radiation to the energy difference between the ground and excited states. In Raman scattering, the light interacts with the molecule and distorts (polarizes) the cloud of electrons round the nuclei to form a short-lived state called a 'virtual state', which is not stable and the photon is quickly re-radiated.

When light is scattered from a molecule or crystal, most photons are elastically scattered. The scattered photons have the same energy/frequency and wavelength as the incident photons. However, a small fraction of light (1 in 10^6-10^8 photons) is scattered at optical frequencies different from the frequency of the incident photons. The process leading to this inelastic scatter is termed the Raman effect. Raman scattering can occur with a change in vibrational, rotational or electronic energy of a molecule. If the scattering is elastic, the process is called Rayleigh scattering. It it's not elastic, the process is called Raman scattering.
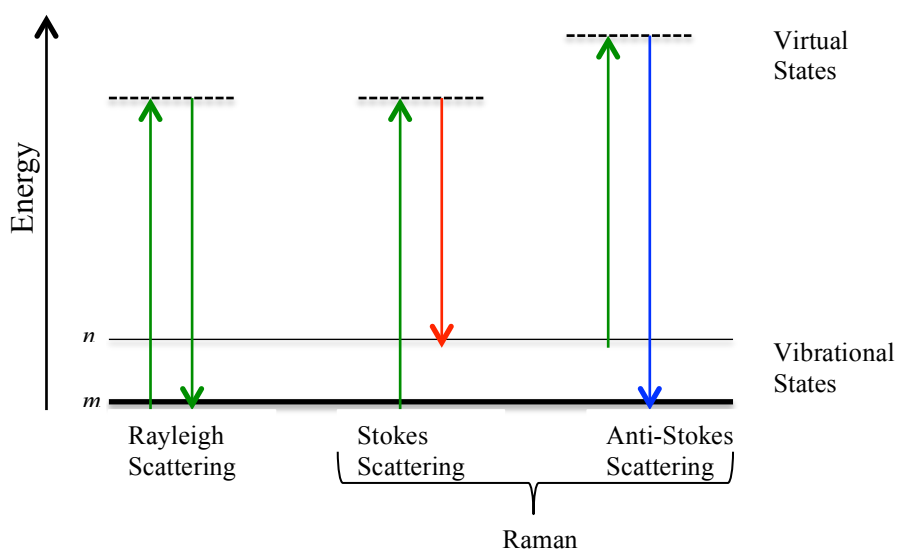
Figure 3-5 Diagram of the Rayleigh and Raman scattering processes. The lowest energy vibrational state m is shown at the foot with states of increasing energy above it. Both the low energy (upward arrows) and the scattered energy (downward arrows) have much larger energies than the energy of a vibration [260]

Figure 3-5 shows the basic processes, which occur for one vibration. At room temperature, most molecules, but not all, are present in the lowest energy vibrational level. Since the virtual states are not real states of the molecule but are created when the laser interacts with the electrons and causes polarization, the energy of these states is determined by the frequency of the light source used. The Rayleigh process will be the most intense process since most photons scatter this way. It does not involve any energy change and consequently the light returns to the same energy state. The Raman scattering process from the ground vibrational state (*m*) leads to absorption of energy by the molecule and its promotion to a higher energy excited vibrational state (*n*). This is called Strokes scattering. Due to thermal energy, some molecules may be present in an excited state such as *n* in Figure 3-5. Scattering from these states to the ground states *m* is called anti-Stokes scattering and involves transfer of energy to the scattered photon. Usually, Raman scattering is recorded only on the low-energy side to give Stokes scattering but occasionally anti-Stokes scattering is preferred.

Figure 3-5 illustrates on key difference between infrared absorption and Raman scattering. As described above, infrared absorption would involve direct excitation of the molecule from state m to state n by a photon of exactly the energy difference between them. In contrast, Raman scattering uses much higher energy radiation and measures the difference in energy between n and m by subtracting the energy of the scattered photon from that of the incident beam (the two vertical arrows in each case). Although different energy ranges are possible, the information of interest to most users is in the $3600 - 400$ cm^{-1} range in infrared spectroscopy and down to 200 cm^{-1} in Raman spectroscopy since this includes most modes which are characteristic of a molecule. Modern Raman equipment can cope with much wider ranges. It is noted that not all vibrations of a molecule need, or in some cases can, be both infrared and Raman active and the two techniques usually give quite different intensity patterns.

Raman spectroscopy is highly sensitive to carbon-carbon bonds and able to provide a wealth of information about their structure. Raman spectroscopy is capable of discerning even slight changes in orientation of C-C bonds making it a very valuable tool in the characterization of carbon nanomaterials [261]. A quantitative analysis of a mixture is typically performed by measuring the relative intensities of bands that are directly proportional to the relative

concentrations of the compounds. Raman spectra in this thesis were used for molecular characterization of carbon materials performed by the Renishaw inVia Raman Spectroscopy used 514.5 nm Ar Laser.

4

SYNTHESIS OF NANOSTRUCTURED CARBONS BY THE MICROWAVE PLASMA CRACKING OF METHANE

4.1   Introduction

Many carbon structures, such as activated carbons, carbon black, carbon membranes, graphene and carbon nanotubes, have been widely used for gas separation, water purification, catalyst supports, electrodes for batteries and fuel cells, and flexible energy storage and conversion devices [25-32]. This is due to their stable physicochemical properties, good conductivity, low cost, and high surface area or porosity [29-33]. Recently, graphitic carbons with highly crystalline structure and large surface area have attracted extensive attention as catalyst supports. Graphitic carbons are usually prepared by two methods: 1) conventional high temperature (>2500 °C) graphitization to form carbons with well-developed graphitic order [262]; and 2) relatively low temperature (<1000 °C) heterogeneous graphitization with the aid of catalysts, e.g. Fe, Co and Ni [27, 263]. Although exhibiting graphitic structure, these materials possess relatively low BET surface areas [264]. In addition, the synthesis procedures employed to produce such materials are rather complicated: it requires a high

processing temperatures between 500 and 1800 °C, and the corresponding aerogels used in the process need to be prepared by the sol−gel method from polymerization of resorcinol with formaldehyde [265].

Recently high energy plasma has become an attractive method for reforming hydrocarbons into hydrogen and carbon. This is a single-stage and non-catalytic reaction, $C_nH_m \rightarrow nC + 0.5mH_2$ [107-110]. It is reported that plasma reforming overcomes many limitations of conventional techniques in terms of cost and deterioration of the catalysts, slow reaction rate, and restrictions on hydrogen production from heavy hydrocarbons [111-113]. In general, plasma is an ionized gas that can be generated by a number of methods, such as combustions, flames, electrically heated furnaces, electric discharges and shocks [114]. The plasma contains reactive radicals, ions and high-energy electrons. Because of the large difference in mass, electrons reach thermodynamic equilibrium much faster amongst themselves than they are in equilibrium with the ions or neutral atoms. Therefore, the temperatures of the electrons, ions and neutrals may be very different. Based on temperature differences, plasma technologies can be generally classified as thermal and non-thermal. Electrons and heavy particles (neutrals, ions) in thermal plasma have the same temperature [120]. For non-thermal plasma, the temperature of heavy particles can be much lower than those of electrons [121]. It can provide an electron temperature of 4000 − 10000 K, and the heavy particle temperatures of 2000 − 6000 K [107]. High-temperature electrons interact with gas molecules to create reactive species, overall gas temperature can remain as low as room temperature [114, 266]. The highly energised electrons fill the system, and collide with other particles (molecules, ions, etc.). The energy transferred from electrons to these particles retains potential energy instead of kinetic energy. Therefore, instead of wasting energy to increase the gas temperature (kinetic movement of the gaseous species), the energy is used more efficiently and specifically in chemical processes, such as ionization and bond dissociation [114]. Microwave plasma is a non-thermal system operating at atmospheric pressure, which holds great potential for large-scale production of hydrogen and high value-added carbon materials by cracking the chemical bonds of hydrocarbons, e.g. methane [108].

In this work, a non-thermal microwave plasma technique was adopted for the synthesis of nanostructured carbon, with the aim to develop a low-energy but flexible technique of

producing high quality carbon structures. The structures of the carbon were characterized by XRD, TEM, SEM and BET surface area analysis. The effects of temperature and power source on BET surface area were clarified. The relationship between carbon collection position and BET surface area was studied for further optimization of the processing technique and tailoring of the carbon structures.

4.2 Experimental methods

The experimental apparatus for the microwave plasma system is schematically shown in Figure 4-1. An electrode-less atmospheric microwave plasma torch system was designed and assembled using a commercially available magnetron (4) with a maximum power of 6 kW produced by the power supply (9). The microwave radiation passed through a three stub tuner (3), and was then fed into a waveguide (5), which was connected laterally to a cavity. The other end of the waveguide was terminated with an adjustable plunger (7) used for impedance matching. A quartz tube (8) with a diameter of 3.4 cm connected with a sample collector (10) at the end was inserted into the nozzle (6) and intersected with the waveguide.
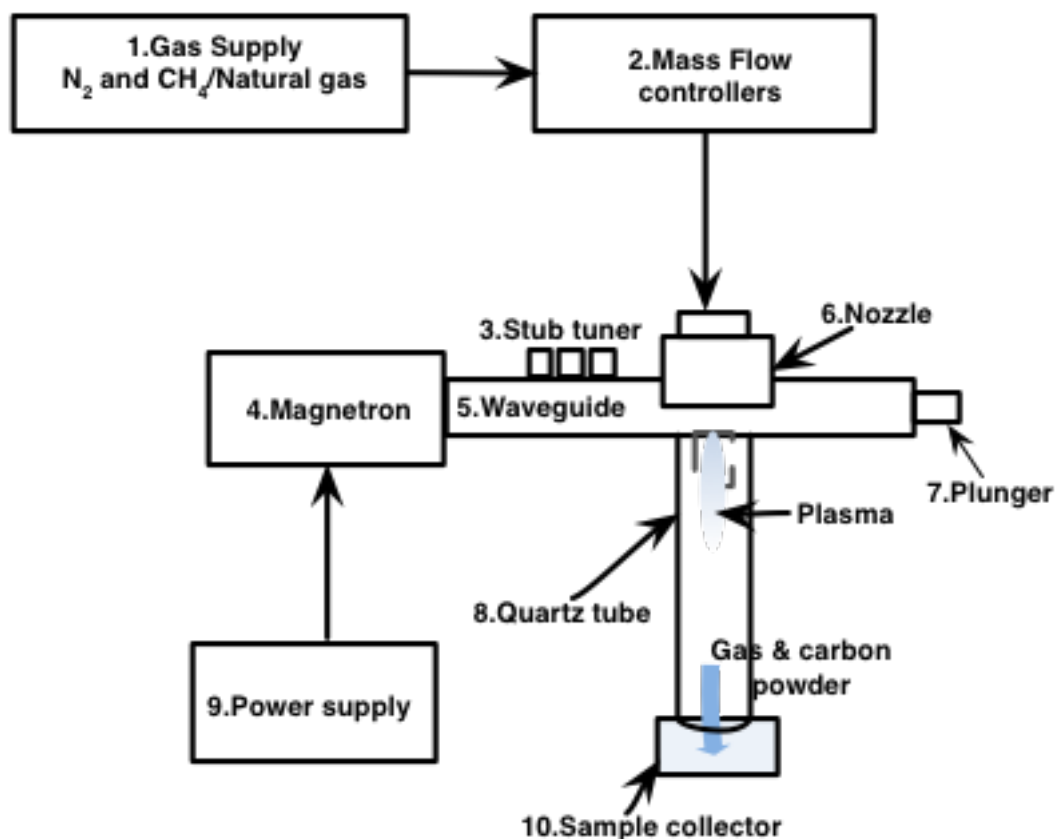
Figure 4-1 Sketch of the plasma reactor

The flow rates of CH_4 and N_2, supplied from compressed gas cylinders (1), were adjusted using a mass flow controller (2). Tangential injection of the working gases enabled good mixing and plasma stabilisation, and helped avoid burning of the quartz tube. A gas mixture of 12 L/min of N_2 and 0.75 L/min of CH_4 was fed into the discharge zone by the nozzle; for pure N_2 gas, the flow rate was set at 12 L/min. The applied microwave power was set up from 1200 to 2000 W. N_2 also acted as a carrier gas, and known as buffer gas when cracking methane in the microwave plasma reactor. Carbon products were collected by a sample collector (10) at the end of the quartz tube of different lengths, from 15, 17, 22, 25, 35, 45 and 55 cm, named as POS-15, POS-17, POS-22, POS-25, POS-35, POS-45, and POS-55, respectively. Temperatures at the sample collection position at the end of the quartz tube were measured before and after the introduction of the methane gas, which are termed as the carrier gas temperature and the reaction temperature, respectively.

The produced carbon powder particles were dispersed in acetone and cleaned with an ultrasonicator to remove possible organic impurities from the carbon particles, which were

subsequently filtered, and then dried in a vacuum oven at 160 °C for 2 h. The morphology of the powder mixtures was characterized by a high resolution transmission electron microscope (TEM), TECNAI, FEI Company. The particle sizes of the powder mixtures were calculated, using the *Image Tool v.3.00 software,* from the TEM images as the equivalent circle diameter, ECD = $(4A/\pi)^{1/2}$, where A represents the projected particle area. X-ray diffraction (XRD) was performed using an XTra diffractometer, manufactured by Thermo ARL (US), with Cu Kα radiation. For comparison, the BET surface area and porosity of each sample were determined from N_2 adsorption at 77 K using two independent surface area/pore size analyzers, a Quantachrome AUTOSORB-1 and a TRISTAR II 3020. The cleaned carbon samples were degassed for 8 h at 573 K to remove any moisture or adsorbed contaminants that may be presented on their surfaces. The BET surface area of the carbons was determined by applying the BET equation imbedded in the manufacture supplied software to the adsorption data. The pore size distribution was evaluated by the density functional theory (DFT) method [251, 252].

4.3   Results and discussion

4.3.1 XRD of plasma carbon
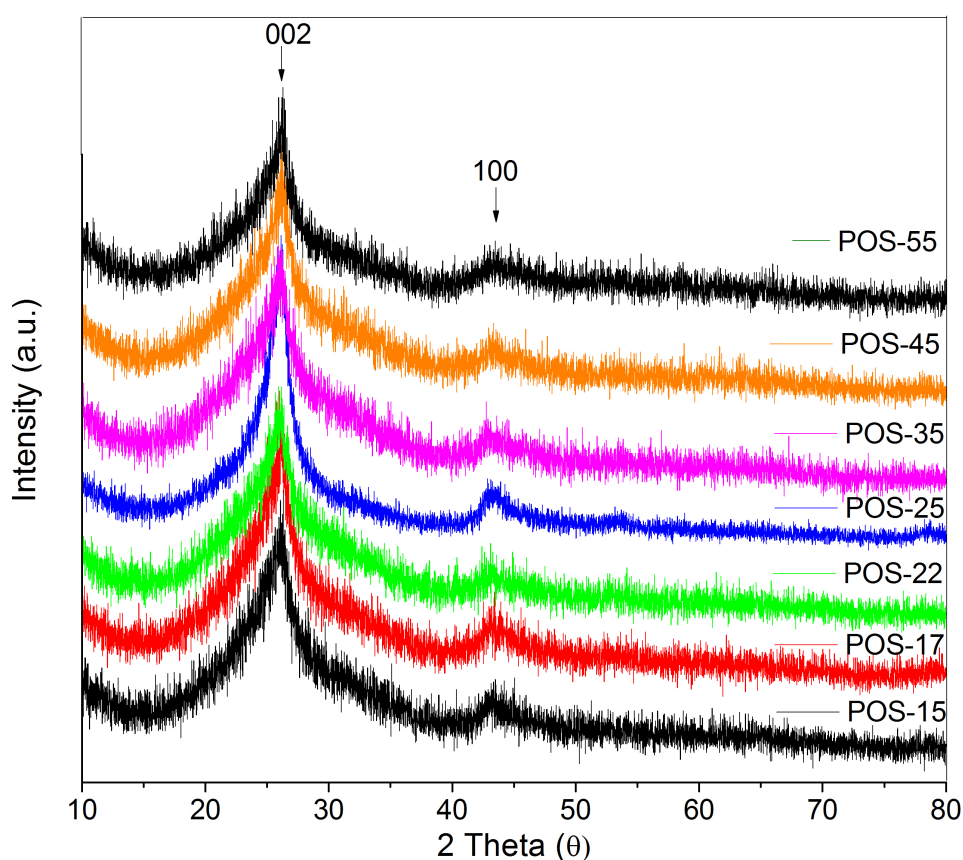
Figure 4-2 XRD patterns of plasma carbon samples

The XRD patterns of these plasma carbon samples at different sample collection positions are shown in Figure 4-2. The XRD peaks at around $2\theta = 26°$ and $43°$ are assigned to the (002) and (100) diffractions of the graphitic framework, respectively [26], indicating the formation of graphitic structures by the plasma system. Moreover, it can be seen that the (002) peaks of all samples have a relatively low intensity and spread over a broad range. This suggests the existence of a certain amount of amorphous carbon or a low level of crystallinity.

4.3.2 TEM of plasma carbon

The TEM micrographs from the plasma carbon samples are shown in Figure 4-3. From Figure 3a, it is noted that the carbon consists of fine spherical particles of about 40.8±8.7 nm in diameter and thin graphitic sheets of "crumpled paper" morphology. Figure 4-3 shows a high magnification image of a spherical particle, which clearly reveals a partial ordered graphitic texture. The Bragg fringes are present: the length of the distorted fringes (L_2) is similar to the length of rectilinear fringes, L_1, 2-3 nm; the average number of fringes within the coherent graphene stacks (N) is 3-4, revealing these graphene stacks lead to the formation of the carbon nanoparticles [121]. Figure 4-3c exhibits a "crumpled-paper" morphology, typical of multilayered graphene, as shown by Zheng et al. [267] and De Fonton et al. [180] to describe polyaromatic carbon fragments making the pore walls in cokes. From Figure 4-3d, the lattice spacing of two adjacent graphite sheets is ~ 0.34 nm, which is consistent with the separation of (002) planes of hexagonal graphitic structures [268]. Both Figure 4-3 b and d indicate that there are a large amount of defects in the carbon structure. Experimental data and molecular dynamic simulations [269, 270] suggest that defects are required for the nucleation and growth of carbon nanostructures. The defects may deteriorate the mechanical properties of the nanostructures, but may also provide specific binding sites for dopants or for gaseous molecules in further functionalization of the carbon nanostructures, e.g. for catalyst loading, gas sensing, hydrogen storage, or CO_2 capture. It has been reported that defect-free nanostructures should form in the temperature range from 1800 to 3200 K[1] [271]. In the current plasma reactor, the temperature is lower for defect-free carbon nanostructures.

---

[1] Kintech Laboratory - Nucleation and Growth of Carbon Nanostructures. Available at: http://www.kintechlab.com/solutions/nanotechnology/nucleation-and-growth-of-carbon-nanostructures/ (Last accessed: 17/07/2012).
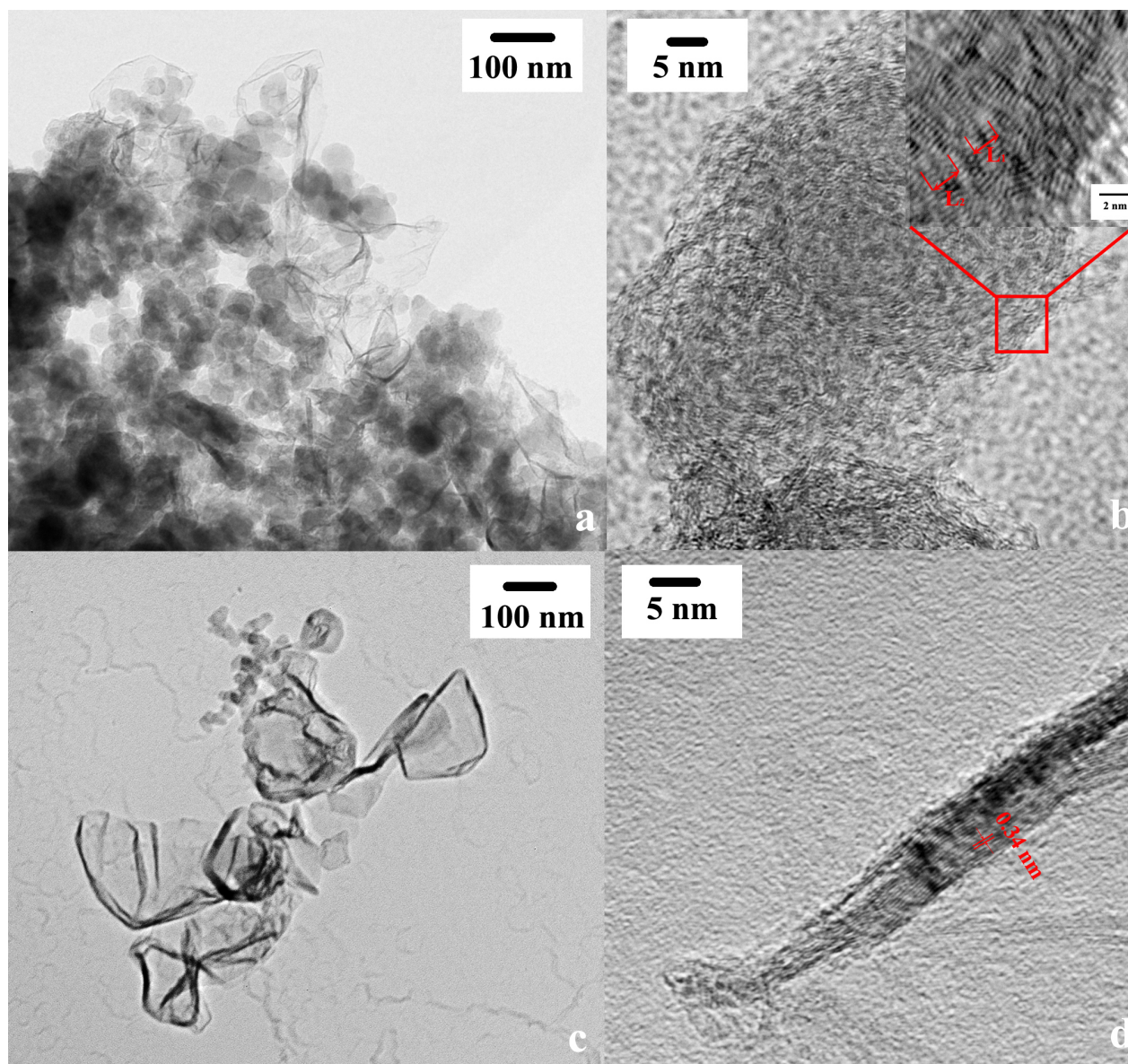
Figure 4-3 a) TEM image of carbon nanostructures synthesised by the non-thermal plasma process; b) HRTEM image of a carbon nanoparticle; c) TEM image of a "crumpled paper sheet" carbon; d) HRTEM image of a graphitic carbon nano-platelet in a relatively amorphous carbon matrix

4.3.3 BET surface area and Porosity

The BET surface area and porosity of the carbon materials synthesized with the power of 1500 W were determined from the nitrogen adsorption/desorption isotherm (Figure 4). The values of the BET surface area, pore volumes and pore sizes are summarized in Table 1. The N_2 isotherms shown in Figure 4 exhibit types III and V characteristics according to the

IUPAC classification of adsorption isotherms, which are characteristic of weak affinities of adsorbents to adsorbates [272], as a result of the co-existence of mesoporous and macroporous surfaces [273]; in the current case, the macropores are mainly due to the packing of the carbon powder particles. The weak adsorbate-adsorbent interactions lead to a low uptake of adsorbate at a low relative pressure. However, the interactions become stronger at a higher relative pressure, resulting in accelerated uptakes [253]. The N_2 isotherms show small adsorption hysteresis at a relatively high pressure, indicating the existence of mesopores in the carbon adsorbents. The pore size distribution of the plasma carbon collected from the quartz tube of different lengths was evaluated by the density functional theory, and the results are shown in Figure 5. The samples show a wide distribution of pore sizes up to 240 nm, but with a distinct bimodal feature, dominated by mesopores at around 17 nm and then large pores from 40-240 nm. Such bimodal distribution may be desirable for many types of practical applications, e.g. mesopores for loading of catalysts and macropores for easy access of reactants in chemical synthesis and/or gas sorption. The characteristic pore-size distribution may be attributed to the dynamic environment in the specific plasma chamber, which results in rapid intermix and growth of disordered and graphitic carbon structures. The mesopores were formed due to the rapid growth of the carbon nanoparticles and the graphene stacks, whereas the macropores were due to impingement and aggregation of such particles, as is evident from Figure 3.
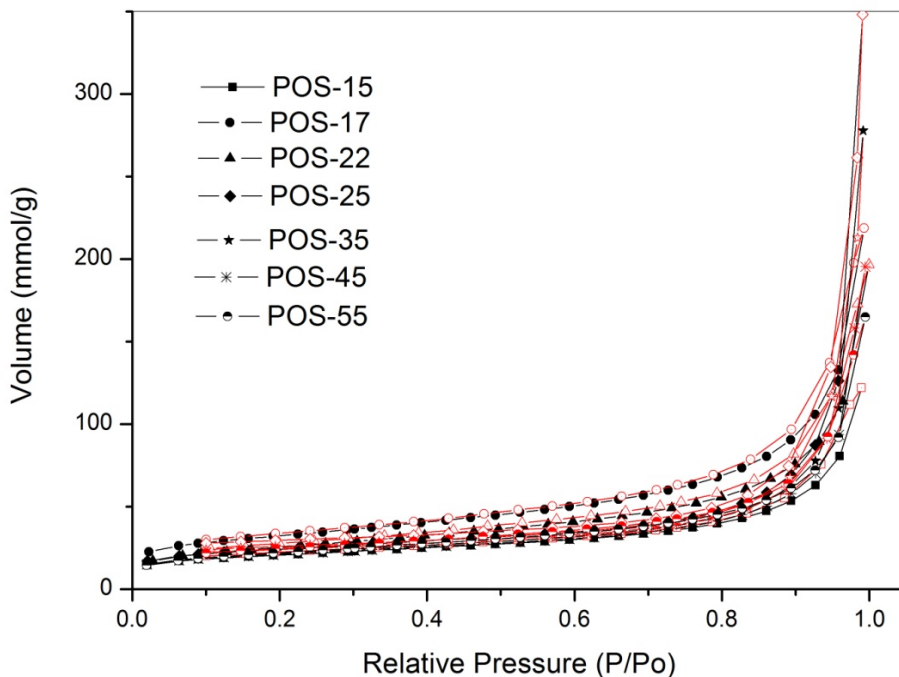
Figure 4-4 N_2 isotherms at 77 K of plasma carbons collected at the end of the quartz tube of different lengths, black for adsorption and red for desorption
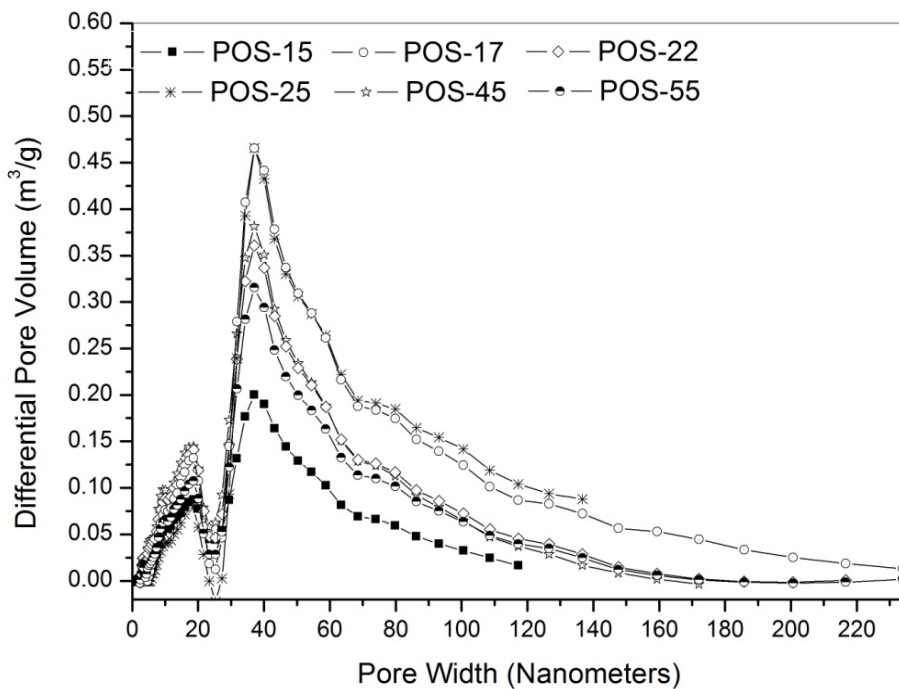
Figure 4-5 Pore-size distributions calculated from N_2 adsorption isotherms given in Figure 4-4, using the DFT model

Table 4-1 Physical properties of plasma carbons

Sample	S_{BET} (m²/g)	V_p (cm³/g)ᵃ	Pore Diameter (nm)
POS-15	74.0	0.1245	17 nm, > 40 nm
POS-17	111.7	0.2055	17 nm, > 40 nm
POS-22	94.7 ± 2.78%	0.1786 ± 4.39%	17 nm, > 40 nm
POS-25	83.9	0.1953	17 nm, > 40 nm
POS-35	74.5	0.1696	17 nm, > 40 nm
POS-45	75.7	0.1448	17 nm, > 40 nm
POS-55	76.8	0.1422	17 nm, > 40 nm

ᵃ V_p is the total pore volume, derived from the amount of vapor adsorbed at p/p^0 =0.96.

The BET surface areas of the samples collected at different distances from the plasma source with a power of 1500 W are shown in Figure 4-6, along with the variations between the carrier gas and reaction temperatures. It is noted that the sample collected at about 17 cm from the plasma source possesses the highest BET surface area of 111 m²/g and total pore volume of 0.2055cm³/g, which is associated with the largest temperature difference of 470 °C. This position may represent the "optimum collecting distance" for rapid carbon growth or CH_4 decomposition, where rapid carbon formation yields the most porosity. The rather large temperature difference is the result of several factors: 1) energy required to warm up the extra CH_4 gas molecules; 2) the net endothermic reaction of CH_4 decomposition into H_2 and carbon (with a reaction enthalpy of 75.6 kJ/mol [274]); and 3) relatively high thermal gradient in this region. It should also be noted that as the gas passes along the quartz tube away from the plasma source, high-energy charged particles/atoms/molecules still exist but rapidly reduce with increasing distance due to lack of excitation energy. There may be some level of exothermic heat provided by the recombination of radicals/ions [275], which could reduce the temperature difference at a position further away from the plasma. For carbon materials collected near the plasma tip, e.g. 15 cm away from the plasma zone (Figure 6), the dynamic turbulence of the plasma may sweep away relatively small nuclei and light graphene, and may also render particle coalescence. Both mechanisms can largely reduce the effective surface area of the resulting carbon structure. For carbon collected further away from the plasma source, i.e. over 20 cm in this case, the temperature drops rapidly and there is

insufficient thermal gradient to drive preferential carbon growth, leading to some level of reduction in the BET surface area. Hence, samples collected at a short distance of 15 cm and a great distance above 35 cm from the plasma source show apparently similar values of the BET surface area, but the dominant mechanism influencing the surface area is different. Further investigation of the processing conditions will be carried out to tailor the morphology, porosity and particle size of the carbon structure.
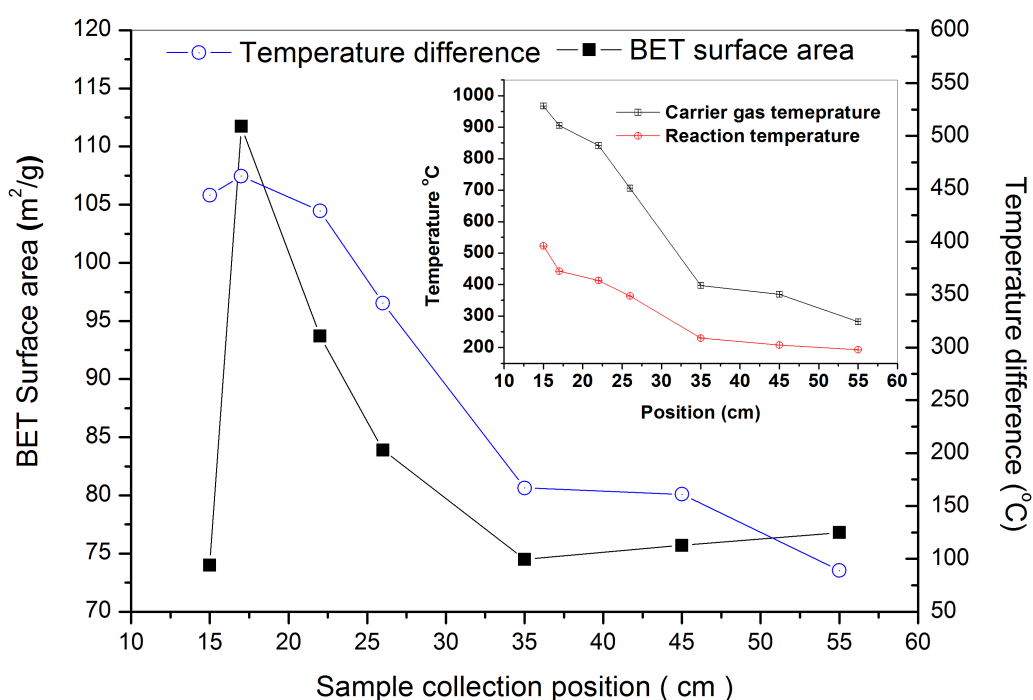
Figure 4-6 BET surface area and temperature difference vs. sample collection position with a power of 1500 W and a gas mixture of 12 L/min N_2 and 0.75 L/min CH_4
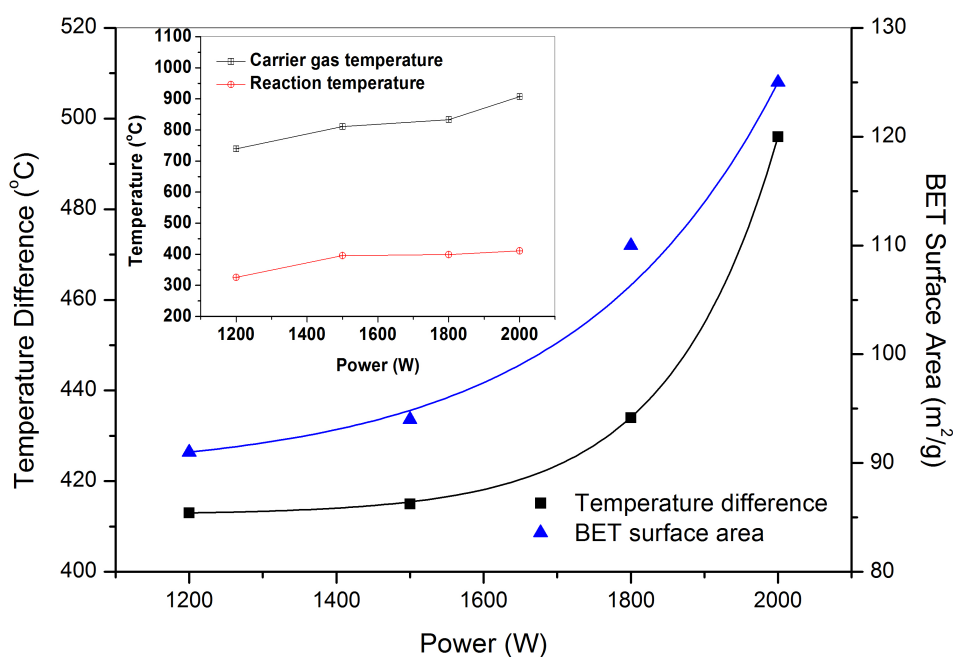
Figure 7 BET surface area and temperature difference vs. power source at a distance of 22 cm from the plasma source with a gas mixture of 12 L/min N_2 and 0.75 L/min CH_4

Figure 7 shows the relationship between power supply, BET surface area and the temperature difference at a collection position of 22 cm from the plasma source. It is shown that the BET surface area increases with increasing power supply, which also leads to an increase in the temperature difference from around 400 to 500 °C, as shown in Figure 7. It is also interesting to note that the highest BET surface area of 125 m^2/g at the power of 2000 W corresponds with the largest temperature difference of 496 °C. The same trend between BET surface area and temperature difference was also observed with the variation of the collection position as in Figure 6. Thus a higher power or feeding rate enhances endothermic CH_4 decomposition, leading to a larger temperature difference (drop), and a greater non-equilibrium driving force for carbon nanostructures to grow, which results in more porosity at the microscopic level in each of the particles and at macroscopic level due to the impingement of such growing particles. Further research is ongoing to understand in detail the formation process of carbon, so that other types of carbon nanostructures may also be generated from this process.

4.4 Summary

A method of obtaining high-purity carbon nanostructures is reported here. The technique uses a low-energy cold plasma process to crack methane and then form carbon nanostructures in-situ. TEM images reveal that the formed carbon structures consist of relatively spherical nanoparticles of 40.8±8.7 nm in diameter and multilayered graphene resembling crumpled paper sheets. Both amorphous and crystalline regions are observed in the carbon nanostructures. A large BET surface area of 125 m^2/g is obtained at 2000 W. For carbon materials collected at different positions at 1500W, the highest BET surface area and pore volume are 111 m^2/g and 0.2055 cm^3/g, respectively. The carbon structure with the highest BET surface area corresponds to the most reactive region for rapid CH_4 decomposition and carbon formation, where the actual temperature gradient or the temperature difference is also the greatest. The process is being optimized for improved control and formation of different types of carbon nanostructures, and potentially offers a cost-effective technique of generating high value-added carbon products, while producing high purity hydrogen.

5

OPTIMIZATION OF THERMAL TREATMENT CONDITIONS FOR CARBON MATERIALS PRODUCED BY THE MICROWAVE PLASMA ROUTE

5.1   Introduction

Activated carbons are widely used as adsorbents in many applications such as water treatment, air pollution control, solvent recovery, catalyst support and CO_2 capture [219, 229]. Their performance in different applications is determined by both their textural and surface properties. There are three main methods to modify carbon: physical, chemical and biological methods. Physical activation involves the carbonization of a carbonaceous precursor followed by the gasification of the resulting char in the presence of suitable oxidizing / gasifying agents such as CO_2 and steam at high temperature (e.g., 1073 -1373 K) [219, 220]. After physical thermal treatment, the physical characteristics such as BET surface area and pore volume can be increased. The chemical thermal treatment may be further

divided into two broad groups, those resulting in acidic and basic surface. The third type of chemical thermal treatment is the surface impregnation of carbon with active metals and their oxides. A modified carbon by a variety of chemical processes containing different functional groups could be used for technological applications such as extracting metallic cations from aqueous and nonaqueous solutions, in catalysis, for treatment of waste and toxic effluents produced, and so on [213-215]. Biological thermal treatment is used to remove the microorganisms in water by giving rise to the formation of bacteria colonies by the adsorption of bacteria/ microorganisms on the activated carbons. The porous structure of activated carbon particles provides bacteria with a protective environment, and the presence of a large variety of surface functional groups on carbon particles enhances the adhesion of the microorganisms of activated carbon [229, 230].

In the previous Chapter, nano-sized carbon powder was successfully produced with a mixture of microstructures by means of a microwave plasma reactor, which was referred as plasma carbon (PC) [276]. The plasma carbon consists of structures of spherical particles and graphene sheets. The goal of this study was to find the optimum treatment conditions for increasing BET surface area and pore volume by simultaneously considering the treatment temperature, time and pressure. To achieve the required physical characteristic enhancements, several important factors including temperature, gases, gas flow rate, sample quantity, and time were considered. Although carbon thermal treatments have been extensively studied in the past, much less studies have been reported on optimizing thermal treatment conditions using response surface methodology.

Response surface methodology (RSM) is a statistical technique for designing experiments, reducing the quantity of actual experiments, building models, evaluating the effects of multiple factors, and searching for optimum conditions for desirable output responses [277]. The Box-Behnken design (BBD) method, a fractional factorial design for three independent variables, was used to plan the experiments [248, 249, 278]. Desirable production output based on BET surface area and yield were considered as responses. The effects of thermal treatment conditions on BET surface area of the plasma carbon were analyzed.

5.2 Experiment Methods

5.2.1 Thermal Treatment Process

The carbon materials to be modified were produced by the microwave plasma reactor in the previous study [276]. The plasma carbon (0.05 g) was loaded in a thermal furnace, heated up to the designed thermal treatment temperatures under the N_2 gas flow of 80 ml/min, and the CO_2 gas flow of 80 ml/min was then introduced to the furnace for the various designed thermal treatment time. After thermal treatment, the samples were cooled to room temperature under the N_2 gas flow. The samples were kept in the glove box for further characterization.

5.2.2 Catalytic Modification in the Plasma Reactor

The catalyst preparation method may be referred to Reference [279]. $Ni(NO_3)_2$ and $Mg(NO_3)_2$ powders were mixed thoroughly, followed by addition of citric acid and de-ionized water to form a solution, and then, the solution was evaporated. The solid obtained was dried at 373 K in air, and subsequently calcined at 600 °C in air. Finally a black powder of catalyst precursor was obtained.

The Ni-MgO catalyst precursor of 10 mg was packed into the plasma reactor chamber at 22cm from the plasma source, followed by heating the sample in a flow of pure N_2 and keeping the pure N_2 gas flow for 10 min, and then, introducing the feedgas, CH_4. After certain reaction time (20 min and 40 min), the black carbon products were obtained. The raw products could be further purified by means of immersion with a low concentration of nitric acid solution so as to dissolve the catalyst particles attached at the extremities of the carbon samples, followed by washing by de-ionized water and drying at 473 K under vacuuming.

5.2.3 Experimental Design Using Response Surface Methodology (RSM)

Response surface methodology (RSM) was used to qualify the relationship between the controllable input parameters and obtained response results, also formed as surfaces [280, 281]. In this work, the thermal treatment process was designed and optimized statistically by applying RSM through three levels Box-Behnken design (BBD). BBD is used to calibrate full quadratic models. A Box-Behnken design has points at the center and the midpoint of each side, as shown in Figure 2-19. There are no corner points and the design is spherical so it is rotatable and, for a small number of factors (four or less), require fewer runs than Central Composite Designs [240, 248, 249, 278].
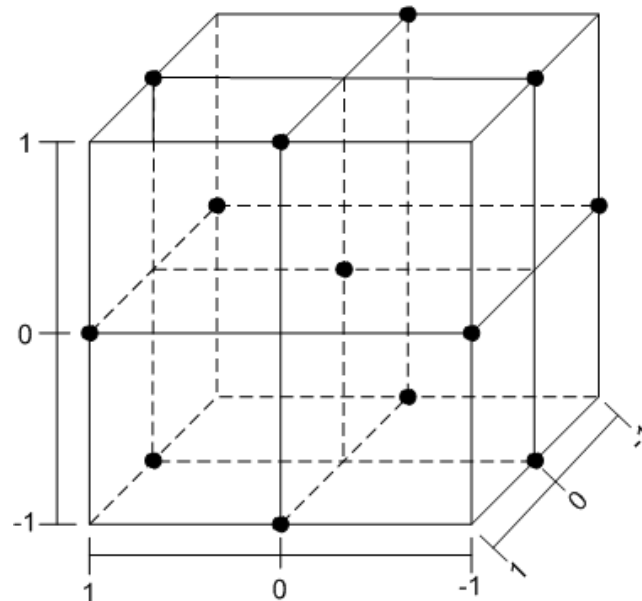
Figure 5-1 The positions of the data points for BBD.

The thermal treatment temperature, time and pressure were chosen as independent variables X_1, X_2 and X_3, respectively. BET surface area (Y_1) and yield rate (Y_2) were considered as response variables. The response variables were correlated to the independent variables by the following polynomial Equation 1:

$$Y_i = a + \sum_{i=1}^{3} b_i X_i + \sum_{i=1}^{3} c_i X_i^2 + \sum_{i=1}^{2} \sum_{j=i+1}^{3} d_{ij} X_i X_j \qquad \text{Equation 24}$$

where, Y is the response and a, b_i, c_i, and d_{ij} are coefficients of the intercept, linear, square and interaction effects, respectively. The regression model was statistically analyzed by means of design expert software (Stat-Ease, Inc., Version 8, Minneaplis, USA). The settings of low and high values for the independent variables were (low and high values): temperature = 800 and 1000 °C; time = 60 and 180 min; pressure = 1 and 1000 kPa. Each variable was coded at three levels: -1, 0 and +1. The ranges and the levels of the variables investigated are given in Table 5-1. The complete design matrixes together with the results of two responses obtained from the experimental work are given in Table 5-2. The standard deviations of response 1, BET surface area and response 2 yield are respectively 20.40 and 6.23 according to the three replicate experiments at the central point (Run 3,5 and 12).

Table 5-1 Independent variables and their levels (actual and coded)

Variables	Code	Unit	Coded variable levels		
			-1	0	1
Temperature	X_1	°C	800	900	1000
Time	X_2	min	60	120	180
Pressure	X_3	100 kPa	1	5.5	10

Table 5-2 Box-Behnken design (BBD) matrix

	Factor 1	Factor 2	Factor 3	Response 1	Response 2
Run	Temperature	Time	Pressure	BET	Yield rate
	°C	min	100 kPa	m^2/g	wt. %
1	1000	60	5.5	560	2
2	1000	180	5.5	779	2
3	900	120	5.5	302	85
4	900	180	10	258	72
5	900	120	5.5	238	75
6	800	120	1	173	91
7	900	180	1	291	78
8	800	60	5.5	171	96
9	800	180	5.5	147	90
10	800	120	10	171	94
11	900	60	1	228	84
12	900	120	5.5	350	90
13	1000	120	1	715	3
14	900	60	10	335	80
15	1000	120	10	756	2

5.2.4 Characterization of plasma carbon

The microstructure of the modified carbon samples were characterized by a transmission electron microscope (TEM), JEOL JEM 2000-EX. BET surface area and porosity of each sample were determined from argon adsorption at 77 K using the surface area/pore size analyzer, Quantachrome AUTOSORB-1. The modified carbon samples were degassed for 8 h at 300 °C to remove any moisture or adsorbed contaminants that may be present in the materials. The BET surface areas of the samples were determined using the BET equation imbedded in the manufacture-supplied. The total pore volume V was estimated by converting the amount of argon gas adsorbed (expressed in cm^3/g STP) to liquid volume of the adsorbate at a relative pressure of 0.99. The Raman Spectroscopy performed by the Renishaw inVia Raman Spectroscopy used 514.5 nm Ar Laser.

5.3   Results and discussion

5.3.1 Statistical approach for optimization of thermal treatment conditions

The quadratic regression models for the BET surface area (Y_1), m^2/g, and yield rate (Y_2), %, referred to the amount of obtained carbon after thermal treatment as a percentage of the total amount carbon sample, based on coded factors are given by Equation 25 and Equation 26, respectively.

$Y_1 = 285.96 + 267.73\ X_1 + 23.52\ X_2 + 14.06\ X_3 + 62.47\ X_1X_2 + 10.87\ X_1X_3 - 35.00\ X_2X_3 + 147.07\ X_1{}^2 - 29.89\ X_2{}^2 + 11.32\ X_3{}^2$ Equation 25

$Y_2 = 83.33 - 45.22\ X_1 - 2.50\ X_2 - 0.97\ X_3 + 1.50\ X_1X_2 - 1.05\ X_1X_3 - 0.50\ X_2X_3 - 33.44\ X_1{}^2 - 2.39\ X_2{}^2 - 2.44\ X_3{}^2$ Equation 26

where X_1, X_2 and X_3 are the coded values of the process variables, thermal treatment temperature (°C), time (min) and pressure (100 kPa), respectively.

Table 5-3 Analysis of variance (ANOVA) for three factors (X_1, X_2, X_3) corresponding to the responses of BET surface area and yield rate.

Coded Variables	Sum of Squares of		Mean Square of		F value of		p-value Prob > F	
	BET surface area	Yield rate	BET surface area	Yield rate	BET surface area	Yield rate	BET surface area	Yield rate
Model	688046.50	20575.77	76449.61	2286.20	28.67	79.84	0.00	< 0.0001
X_1	576738.00	16380.50	576738.00	16380.50	216.29	572.08	< 0.0001	< 0.0001
X_2	4095.13	50.00	4095.13	50.00	1.54	1.75	0.27	0.24
X_3	1596.13	8.00	1596.13	8.00	0.60	0.28	0.47	0.62
X_1X_2	14762.25	9.00	14762.25	9.00	5.54	0.31	0.07	0.60
X_1X_3	462.25	4.00	462.25	4.00	0.17	0.14	0.69	0.72
X_2X_3	4900.00	1.00	4900.00	1.00	1.84	0.03	0.23	0.86
X_1^2	79425.64	4123.10	79425.64	4123.10	29.79	144.00	0.00	< 0.0001
X_2^2	3123.10	21.56	3123.10	21.56	1.17	0.75	0.33	0.43
X_3^2	400.64	21.56	400.64	21.56	0.15	0.75	0.71	0.43
Residual	13332.42	143.17	2666.48	28.63	-	-	-	-

$$Y_1 = 285.96 + 267.73\, X_1 + 23.52\, X_2 + 14.06\, X_3 + 147.07\, X_1^2 \qquad \text{Equation 27}$$

$$Y_2 = 83.33 - 45.22\, X_1 - 2.50\, X_2 - 0.97\, X_3 - 33.44\, X_1^2 \qquad \text{Equation 28}$$

Analysis of variance (ANOVA) was further carried out to justify the adequacy of the models. ANOVA consists of classifying and cross-classifying statistical results and was tested by the means of a specific classification difference, which was carried out by Fisher's statistical test (*F*-test). The F-value is defined as the ratio of the mean square of regression to the error, representing the significance of each controlled variable on the tested model. Prob>F is the probability of seeing the observed F-value if the null hypothesis is true (there is no curvature). The probability equals the proportion of the area under curve of the F-distribution that lies beyond the observed F-value [282]. The F distribution itself is determined by the degree of freedom associated with the variances being compared. It is generally accepted that if the Prob>F value is less than 0.05 then the individual terms in the model have a significant effect on the response [240]. Table 5-3 and Table 5-4 list the significant parameters and statistical test results of the models. From the ANOVA (Table 5-3), the F-value of 27.42 for the model Y_1 implies the model is significant; there is only 0.1 % chance that such large 'F-Value' could occur due to noise. Values of 'Prob> F' less than 0.0500 indicate model terms are significant. In this case, X_1 and X_1^2 are significant. Whereas X_2, X_3, X_1X_3, X_1X_2, X_2X_3, X_2^2 and X_3^2 are insignificant to predict BET surface area; in model Y_2, F-value of 79.40

implies the model is significant. There is only a 0.01% chance that a " F-Value" could occur due to noise. In model Y_2, according to the value of 'Prob>F', X_1 and X_1^2 are significant model terms. The insignificancy of some terms indicates that the models can be simplified to improve the models. The simplified models of Y_1 and Y_2 are listed as Equation 27and Equation.

The model determination coefficient R^2 is a statistical measure of how well a model approximate real data points. An adjusted R^2 statistic is preferred since R^2 always increases as more terms are added to the model. The closer the R^2 is to 1, the better the model fits the experimental data, the less the difference between the predicted and observed values. From Table 5-4, these values were follows: $R^2 = 0.9407$ and Adj-$R^2 = 0.9258$ for Y_1; $R^2 = 0.9905$ and Adj-$R^2 = 0.9867$ for Y_2, indicating that models are well fitted.

Table 5-4 Statistical R^2 and adj-R^2 obtained from the ANOVA for the simplified models.

Variables	Accuracy of Fitting to	
	BET surface area	Yield rate
R^2	0.9407	0.9905
Adj R^2	0.9258	0.9867

5.3.2 Response surface contours

To investigate the effects of thermal treatment conditions on BET surface area and yield rate, 3D-contour plots were drawn according to the models. Figure 5-2 shows the 3D response surface, which was constructed to show the interaction effects of thermal treatment variables (thermal treatment time and temperature) on BET surface area (Y_1). For this response surface, the thermal treatment pressure was fixed at 5500 kPa. Figure 5-3 shows 3D response surface of BET surface area versus thermal treatment pressure and temperature when the thermal treatment time was fixed to 120 min. As seen from Figure 5-2 and Figure 5-3, BET surface area increases significantly with temperature, but just slightly with time or pressure. The highest BET surface area of 779 m^2/g was obtained from the experiment when the thermal treatment temperature was 1000 °C at 5500 kPa for 180 min thermal treatment. Figure 5-4 and Figure 5-5 show the 3D response surface for the yield as a function of thermal treatment temperature, time and pressure, indicating that yield rate decreases dramatically

with an increase of temperature. The extent of burn-off of carbon at 1000 °C was significant. The activation of PC materials with CO_2 must have involved the $C–CO_2$ reaction [283]. This would lead to the removal of carbon atoms and cause the loss of the materials, thereby contributing to the development of micropore structure. The thermal treatment time and pressure show very little effect on yield rate because the mass of PC modified in each experiment was only 0.05g and the thermal treatment reaction finished so quickly that the effects of thermal treatment time and pressure on carbon structure change were not evident. The results obtained in this study are in agreement with the work of Sudaryanto et al.[284], where activation temperature was found to play an important role on the yield of activated carbon whereas activation time did not show much effect on the carbon yield. It is possible that the thermal treatment time and pressure should show some effects on changes of carbon structure and yield rate when the mass of loaded samples reaches a certain amount. The thermal treatment at high temperature gives rise to the combined effects of $C-CO_2$ reaction and volatile material loss. Similar results were obtained by Lua and Guo [87] who prepared activated carbons from oil-palm shells by CO_2 activation; the higher the activation temperature, the greater the surface areas of the resultant activated carbons due to the development and widening of microporosity and mesoporosity.
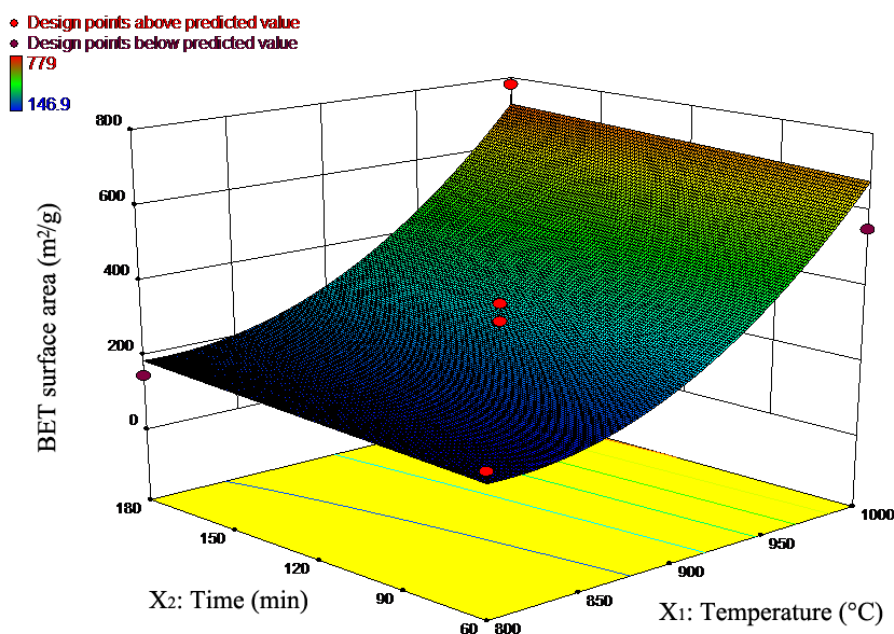
Figure 5-2 3D response surface plot of BET surface area versus thermal treatment time and temperature (at pressure = 5500 kPa)
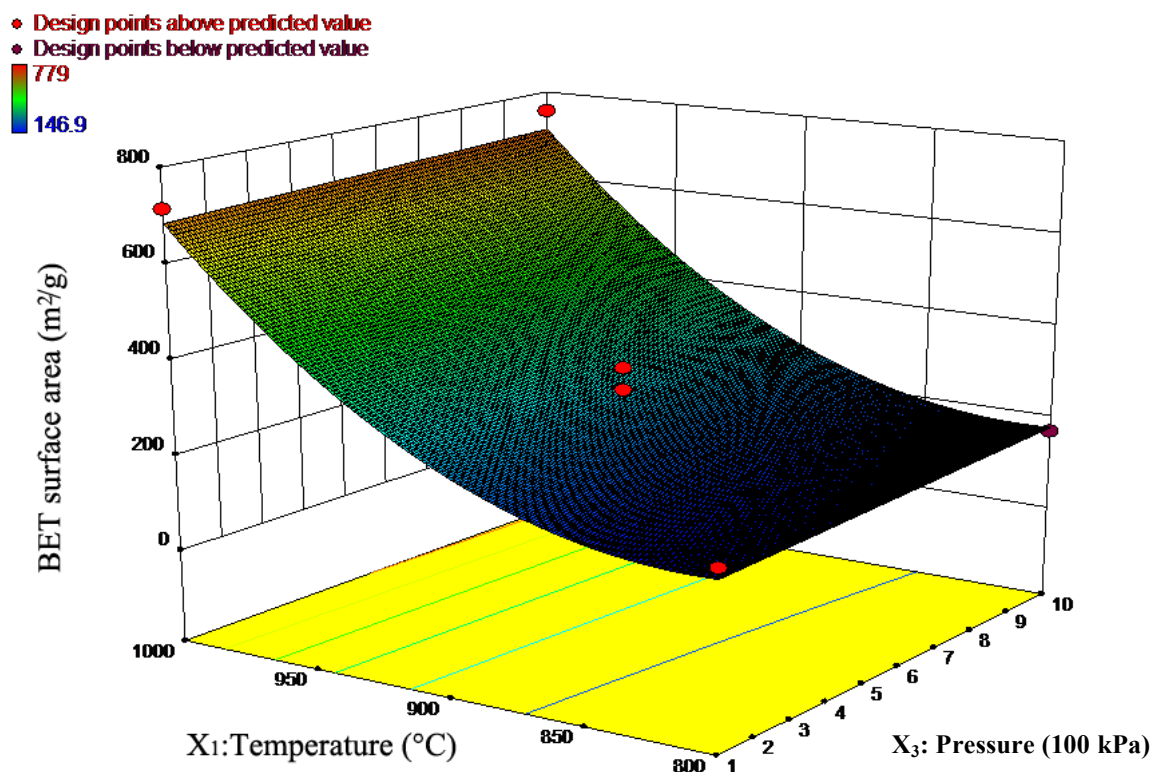
Figure 5-3 3D response surface plot of BET surface area versus thermal treatment pressure and temperature (at time = 120 min)
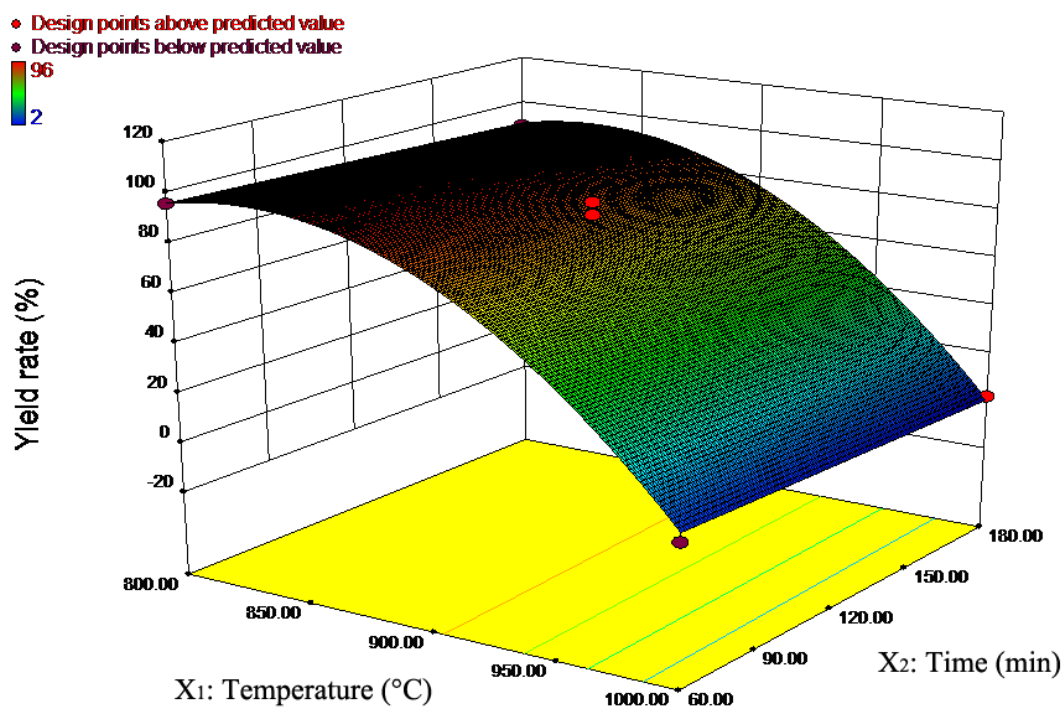
Figure 5-4 3D response surface plot of yield rate versus thermal treatment time and temperature (at pressure = 5500 kPa
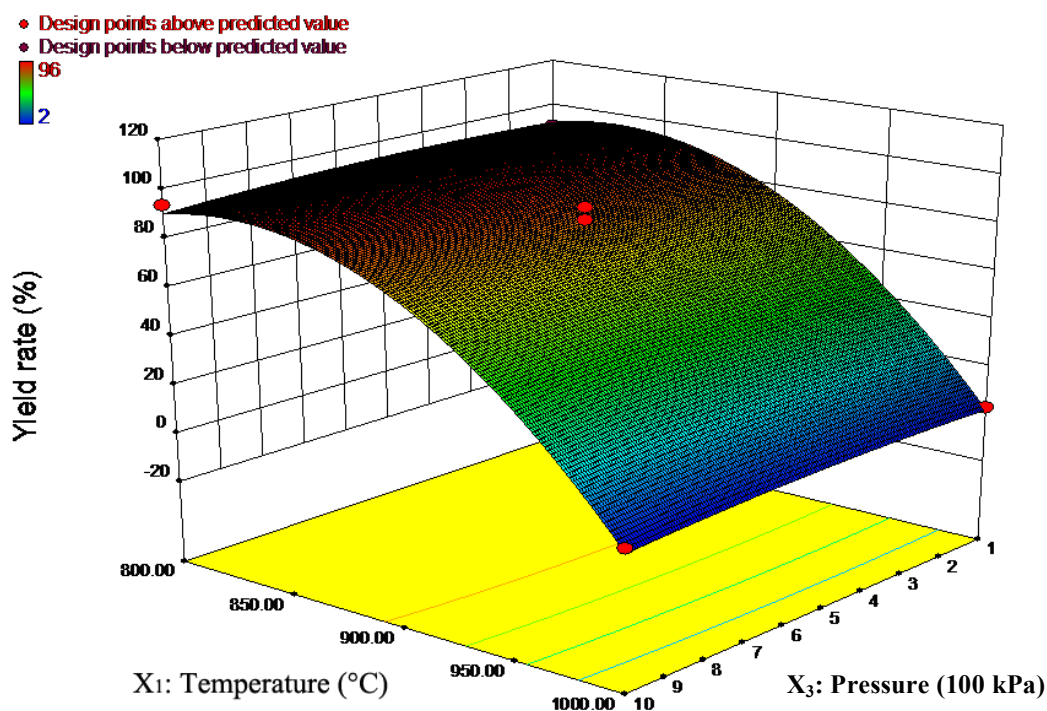
Figure 5-5 3D response surface plot of yield rate versus thermal treatment pressure and temperature (at time = 120 min)

5.3.3 Optimum thermal treatment conditions

The optimum thermal treatment conditions can be determined for modifying the plasma carbon with the thermal furnace. However, it is difficult to optimize both of these responses under the same conditions because the interest regions of these factors are different. Indeed, when Y_1 increases, Y_2 decreases. Thus, it is difficult to find a balance between high BET surface area and high yield rate. Multiple response optimizations could be generated from the contour plots for each response in the experimental ranges of each factor. To identify the optimum conditions, the targeted criteria were set as maximum values for the response Y_1 and in range of 30-60 % for response Y_2, whereas the values of the variables (thermal treatment temperature, time and pressure) were determined in the ranges studied. Optimal thermal treatment conditions were obtained as: 950 °C thermal treatment temperature for 120 min at 100 kPa pressure. This optimal point has been verified by three independent experiments. The errors between the predicted values by the model and the experimental values for BET surface area and yield rate were 3.7 and 2.3%, respectively.

Table 5-5 Comparation of predicted and experimental results in BET surface area and yield rate

Temperature	Time	Pressure	BET Surface area (m^2/g)		Error	Yield rate (%)		Error
°C	min	kPa	Experimental	Predicted	(%)	Experimental	Predicted	(%)
950	120	100	459	442	3.7	55.3	51.5	2.3

5.3.4 Characterization of optimum plasma carbon

The argon isotherm, pore size distribution and Raman spectrum were used to characterize three selected samples: the processed PC, the modified PC with BET surface area of 756 m^2/g (m-PC) and the modified PC using optimum conditions (o-PC) determined in Section 3.3. Figure 5-6 shows the argon isotherms of as-synthesized PC, m-PC and o-PC at 77 K. The presence of a steep increase at very low relative pressure P/P_0 reflects the presence of micropores. The hysteresis loop can be observed at high relative pressure, which can be related to capillary condensation on mesopores. According to IUPAC classification categories, isotherms can be labeled as Type II or Type IV, which corresponds to a mesoporous material. The argon uptake of o-PC and m-PC rapidly increases with the relative pressure, which indicates that the mesoporous structure in the o-PC and m-PC is developed with an increase of thermal treatment time and temperature, due to the break-up of some of micropores (<1 nm) and the opening up of accessible mesopores.
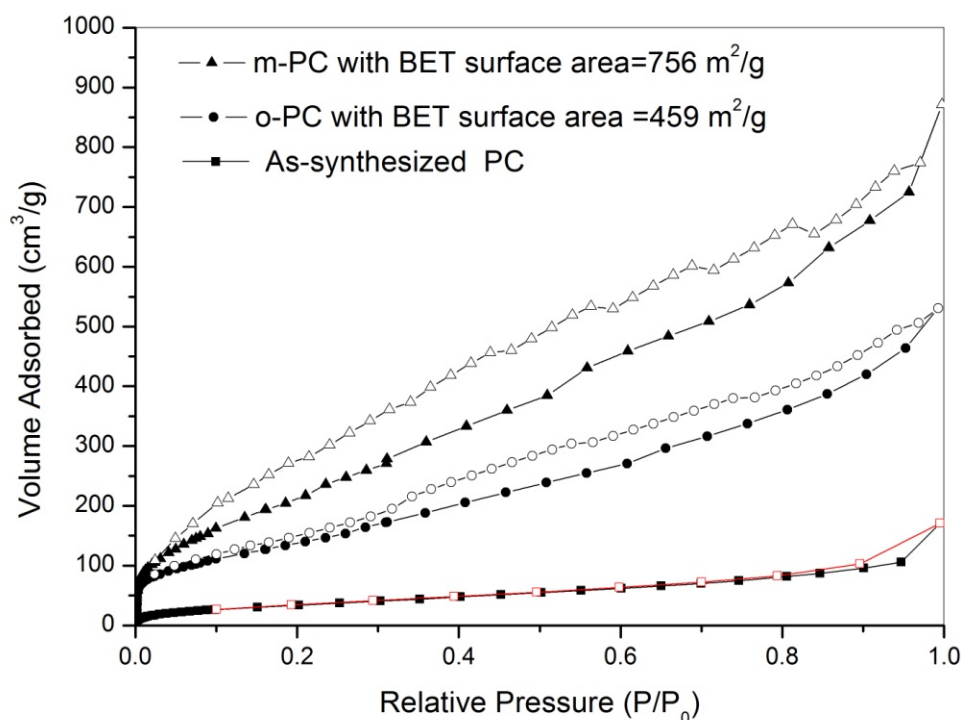
Figure 5-6 Argon isotherms of as-synthesized PC, m-PC and o-PC at 77 K.

Figure 5-7 shows the pore size distributions for as-synthesized PC, m-PC and o-PC by DFT method from argon isotherms. It can be seen that the development of porosity is strongly dependent on the thermal treatment process. For example, as-synthesized PC without thermal treatment has two peaks at 0.26 nm and 0.8 nm. With 120 min thermal treatment at 950 °C, more micropores at 0.3 nm (see the magnified graph in Figure 5-7) and 0.8 nm are generated, and also some micropores break and develop to mesopores at 1.5 nm in half pore width. With same thermal treatment time and higher temperature (1000 °C), the peaks shift to larger half pore width, and both the micropores volumes and the mesopores volumes have increased. This is because that the accessible micropores and mesopores have increased after the heating, there may be some levels of micropores become mesopores. The treatment must be able to 'open up' the blocked micropores in the as-synthesized plasma carbon.
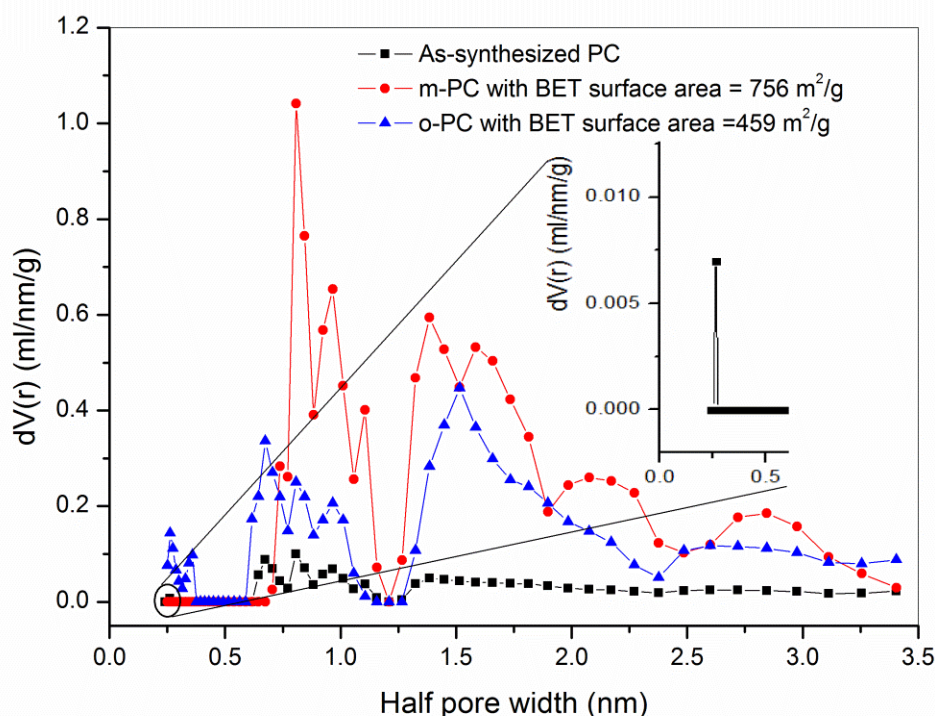
Figure 5-7 Pore-size distributions of as-synthesized PC, m-PC and o-PC, using Ar probe and the DFT model

Raman spectroscopy was also performed to examine the structural properties of the various PC samples. Figure 5-8 shows the Raman spectra for the as-synthesized PC, m-PC (run 15) and o-PC. All the patterns show two peaks located at ~ 1350 and 1580 cm^{-1}. The peak at 1350 cm^{-1} is known as the D-band for disorder carbon, and the peak at 1580 cm^{-1} is called the G-band for graphite [285, 286]. It has been demonstrated that the integral intensity ratio I(D)/I(G) and the full width at half maximum (FWHM) of these bands have a strong correlation to the microstructure of carbonaceous materials [287, 288]. Table 5-6 shows the I(D)/I(G) and the FWHM of the D-band, which were evaluated using the curve fitting of the Raman spectra. A lower ratio of (I(D)/I(G)) indicates a higher degree of crystallinity in the modified PC compared to the as-synthesized PC. The improvement in crystallinity of the PC by the thermal treatment at 950 °C for 120 min might benefit from the reaction of disordered structure in the as-synthesized PC with CO_2 at high temperature. After the treatment, the ~55 wt.% enhanced crystalline carbon was obtained since the ~ 45 wt.% sample including the amorphous structure and the impurities was burnt off. Indeed, the increase in activation temperature quickens the gasification reactions of carbon [289].
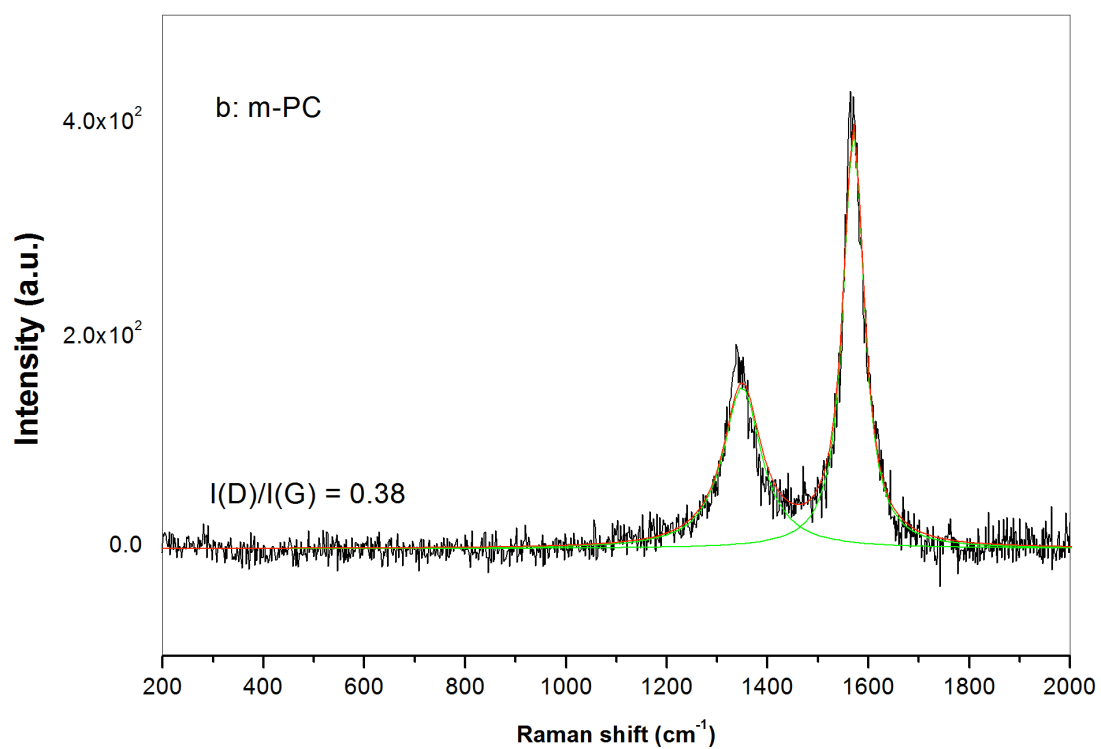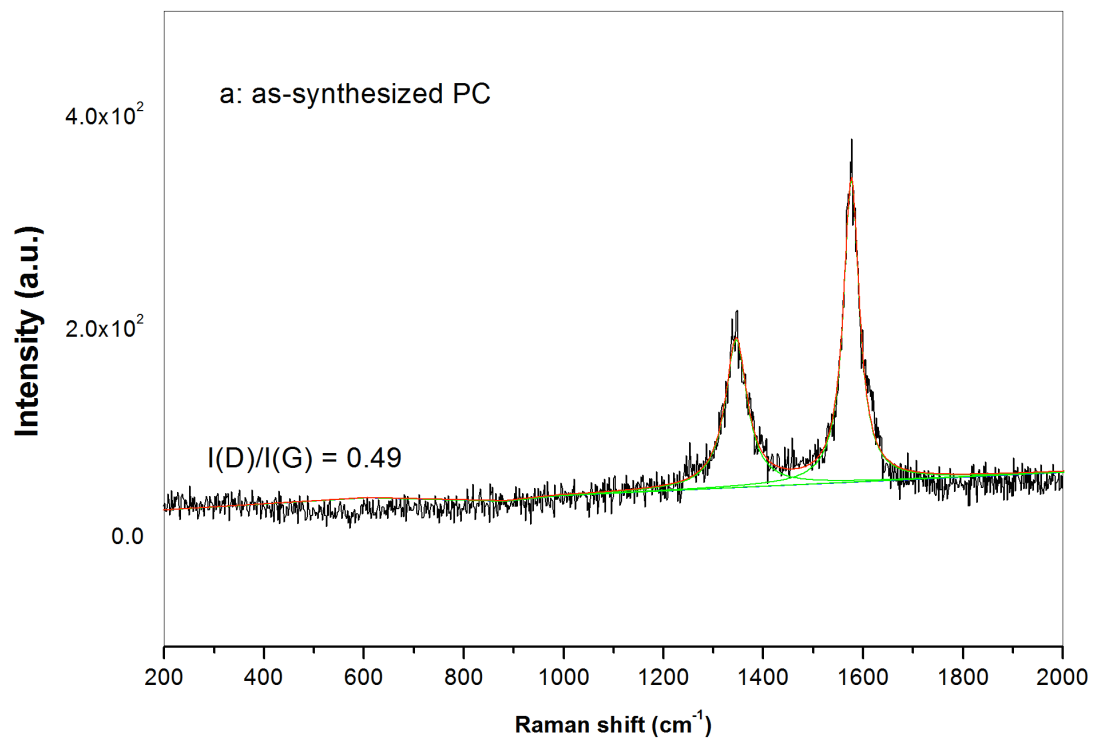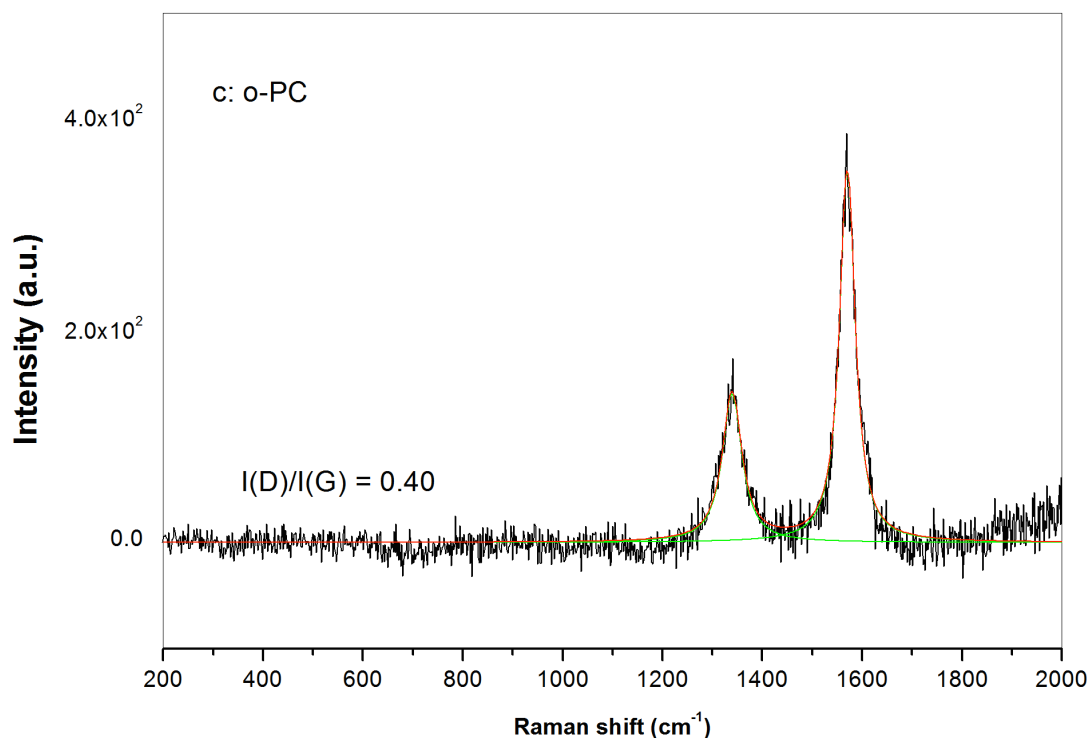
Figure 5-8 Raman spectrum of as-synthesized PC (a), m-PC (b) and o-PC (c).

Table 5-6 the I(D)/I(G) and FWHM of the D-band, evaluated from the Raman spectra

	I(D)/I(G)	FWHM (D) (cm^{-1})
As-synthesized PC	0.49	54
O-PC	0.40	47
m-PC (Run15)	0.38	46

To support the results from Raman spectroscopy, TEM observation was conducted as shown in Figure 5-9. A large amount of amorphous carbon particles can be detected in the as-synthesized PC sample (in Figure 5-9a). After thermal treatment at the optimum conditions (Figure 5-9b), the graphite sheets and graphite particles are more pronounced. The amorphous structure is more difficult to detect from the TEM image.
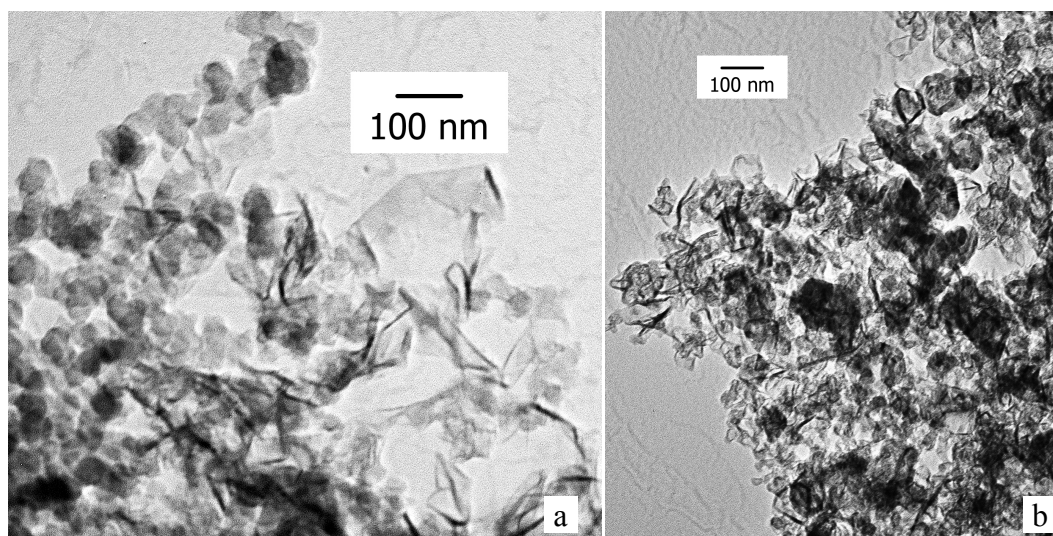
Figure 5-9 TEM images of as-synthesized PC (a) and o-PC (b).

5.3.5 Application of a catalyst in plasma reactor for carbon product

The attempt to produce the novel carbon structure by the plasma reactor has recently generated the attention. From the literature review and the previous experience, a possible method for preparation carbon nanotubes by the catalytic decomposition of hydrocarbons in the plasma reactor is being considered. This process can produce a large amount of carbon nanofibers with good facilities in purification of the products. The set-up of the plasma reactor and the preparation of the catalyst, as well as reaction conditions used, all need to be taken into consideration.

A mechanism of growth of carbon nanofibers was first proposed by Baker [290]. The diffusion of carbon through the catalyst particle is generally considered to be the rate-determining step in the growth of carbon nanofibers, and the driving force which pushed the carbon diffusion from the metal-gas interface to the metal-nanofibers interface was suggested to originate from the concentration gradient of dissolved carbon between the two interfaces described the above. The feed gas molecules adsorb and decompose in the metal-gas interface and subsequently carbon precipitated to form carbon nanofibers in the metal-nanofiber interface. According to the proposed model, many researchers have produced MWNTs using hydrocarbons (CH_4, C_2H_2, C_2H_4, C_3H_6, etc.) or CO as feed gas and Fe, Ni or Co as catalysts. Large-scale synthesis of CNTs has been developed in recent years.

This part of work is to apply MgO-NiO as a catalyst for novel carbon nano structures from methane reforming in the plasma reactor. It has been that carbon nanotubes (CNTs) with small and even diameter could be prepared from catalytic decomposition of CH_4 or CO by using a Ni-MgO catalyst in a fix-bed continuous flow reactor. The obtained CNTs are used to compare with the catalyzed plasma carbon. XRD, SEM, TEM and BET surface area are performed to characterize the catalyzed plasma carbon.

5.3.5.1 *XRD of catalyzed carbon produced by the plasma reactor*

It has been reported that the binary system consisting of NiO and MgO can form a solid solution due to very good mutual solubility between NiO and MgO [279]. This can be brought out by the results of the XRD as shown in Figure 5-10. XRD pattern does not have a significant difference of MgO and NiO since the peaks of MgO and NiO are very close to each other. The dimension of the crystal cell of the formed catalyst is between those of NiO and MgO, which implies the formation of $MgNiO_x$ solid-solution. Also it has been proved the NiO-MgO system is highly dispersed and evenly solubility between NiO and MgO. From XRD pattern of the catalyzed plasma carbon, the peak at around $2\theta=43°$ are assigned to the (100) diffraction of the graphitic framework. No other phase is detected, which means there is no catalyst existing without washing. The possible reason is that the plasma temperature is much higher (>750 °C) than catalyst melting points (600-650 °C).
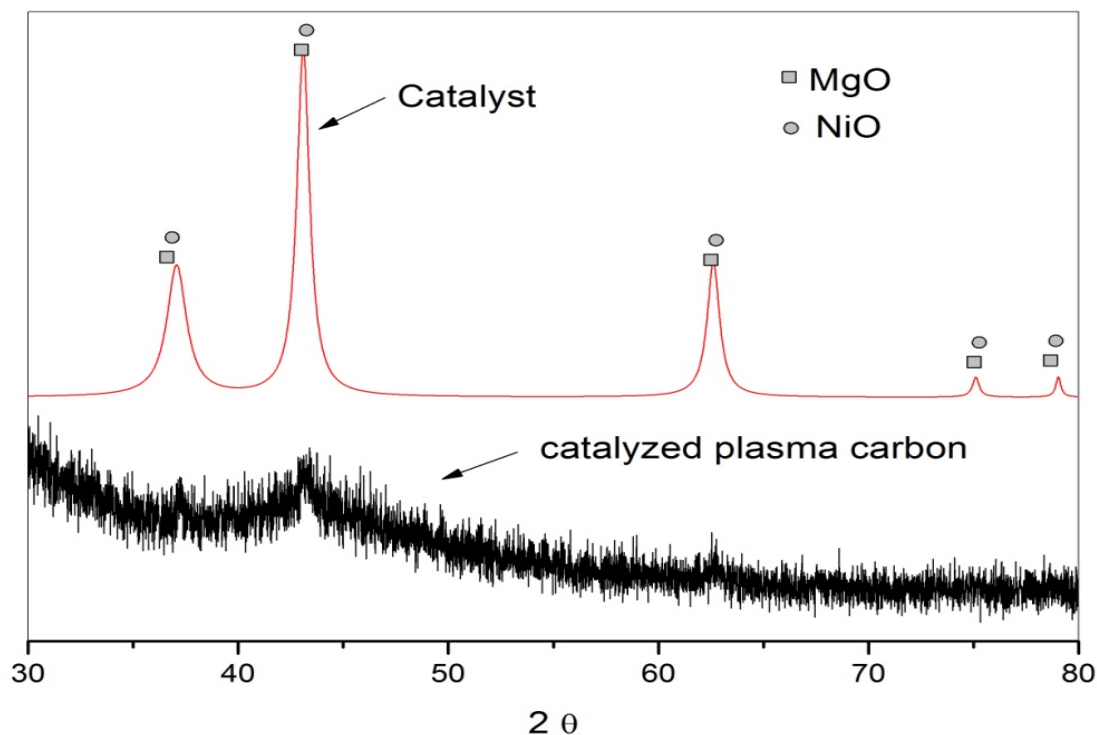
Figure 5-10 XRD patterns of the catalyst $MgNiO_x$ and the catalyzed plasma carbon

5.3.5.2 SEM of Catalyst

Figure 5-11 shows the SEM image of the obtained catalyst $MgNiO_x$. The NiO particles with the diameter of 110 nm are evenly diffused on the host component MgO. Table 5-7 shows the element composition of the obtained catalyst. The main compositions are O, Mg and Ni, corresponding to XRD results. C is from the coating process, Al is from the sample pallet and Cu is impurities.
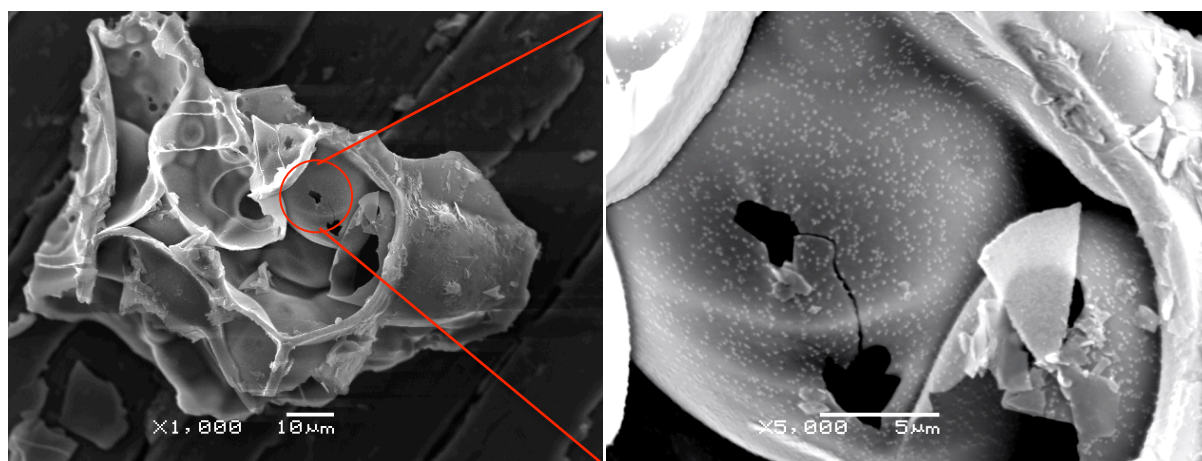
Figure 5-11 SEM images of the catalyst $MgNiO_x$.

Table 5-7 Elements analysis of the catalyst MgNiO$_x$ from EDX spectrum

Element	Weight%	Atomic%
C K	12.69	22.09
O K	40.43	52.85
Mg K	15.61	13.43
Al K	1.22	0.95
Ni K	29.63	10.55
Cu K	0.42	0.14
Totals	100.00	

It has been accepted that the growth of carbon nanotubes by catalytic decomposition of hydrocarbons includes the following steps: at first, the feed hydrocarbon molecules are adsorbed and decomposed on certain surface active sites of the metal particles of the catalyst to form carbon species; and then, some of the surface carbon species dissolve into the bulk and diffuse through the metal particle from the front face (i.e. the metal-gas interface) to the rear face (i.e. the metal-nanotube interface), where carbon is deposited in the form of the nanotube. The evenly diffused nanoparticles on the surface of the bulk MgNiO$_x$ are very good active sites to form carbon nanotube and the diameters of carbon nanotubes are depending on the particle size of the active sites. From Figure 5-12 and, the 20 min formed carbon particles can be seen to grow from the host MgNiO$_x$ surface. Table 5-8 indicates the elemental composition, comparing with the Table 5-7, the carbon component obviously increases. Figure 5-13 shows the SEM of catalyzed plasma carbon for longer production of 40 min, it can be seen the longer nanofibers are formed during the longer reaction time. And also the amorphous carbon structure can be seen in the area without the catalysts.
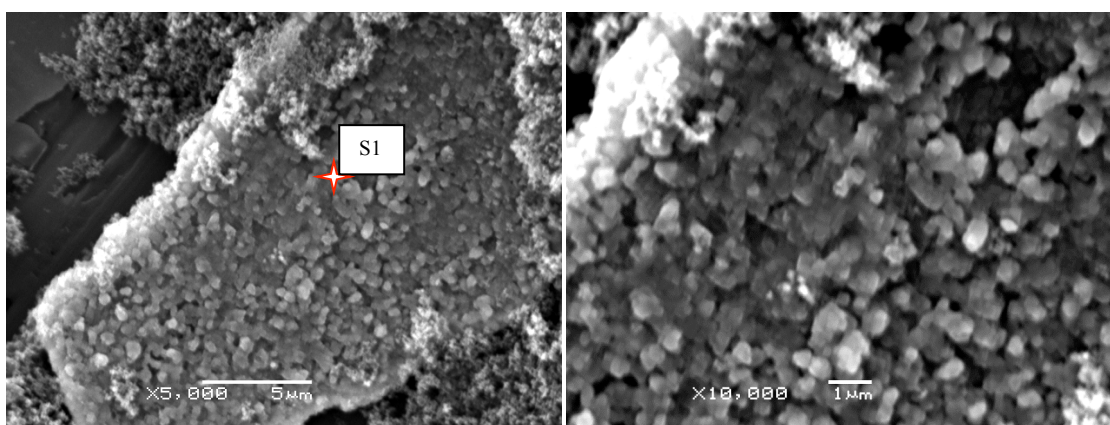
Figure 5-12 SEM images of catalyzed carbon produced by the plasma reactor for 20 min.

Table 5-8 Elements analysis of the catalyzed carbon produced by the plasma reactor from EDX spectrum

Element	Weight%	Atomic%
C K	75.96	88.11
O K	2.93	2.70
Mg K	3.09	1.87
Al K	8.20	4.48
Ni K	9.73	2.44
Cu K	0.46	0.11
Totals	100.00	
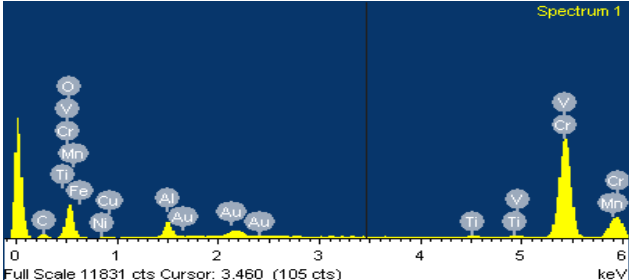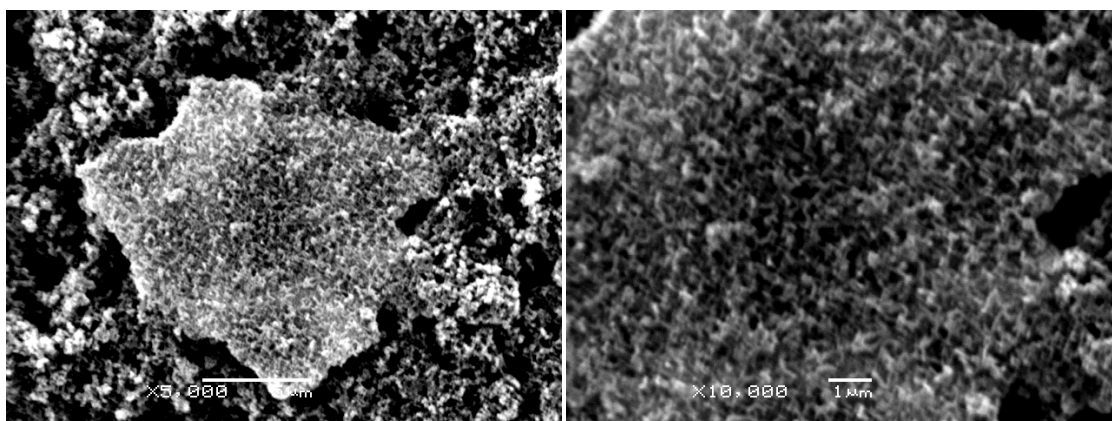
Figure 5-13 SEM images of catalyzed carbon produced by the plasma reactor for 40 min.

5.3.5.3 *TEM of the catalyzed carbon produced by the plasma reactor*

To compare with the carbon structures, the catalyzed plasma carbon, uncatalyzed plasma carbon and the CNTs produced by a thermal reactor using the same catalyst are performed the TEM observation. Figure 5-14 gives the TEM observations on the catalyzed plasma carbon, uncatalyzed plasma carbon and CNTs produced by a thermal reactor. From Figure 5-14b, it can be seen that the obtained carbon samples are mixed structures of the onion-like graphite and the carbon fibers with the outer diameter of 11-25 nm and the tube length up to 430 nm. Figure 5-14c shows the twisted carbon nanotube with the diameter of 15-25 nm and the tube length up to 10 μm produced by the thermal reactor using the same catalyst [279]. Figure 5-14d shows the TEM image of uncatalyzed plasma carbon, which consists of onion-like graphite and graphite sheets. According to the microscopy of the catalyzed plasma carbon, the uncatalyzed plasma carbon and the carbon nanotube, the catalyzed plasma carbon didn't grow up to the CNTs due to the burn-off of the catalyst and afterwards the plasma reactor still continued to produce the normal plasma carbon, thus the catalyzed plasma carbon structure consists of the short carbon nanotubes and the graphite. To improve the catalyzed

plasma carbon to pure CNTs, a lower temperature less than 650 °C is needed through adjustable reactor parameters, such as the power and the cooling system.
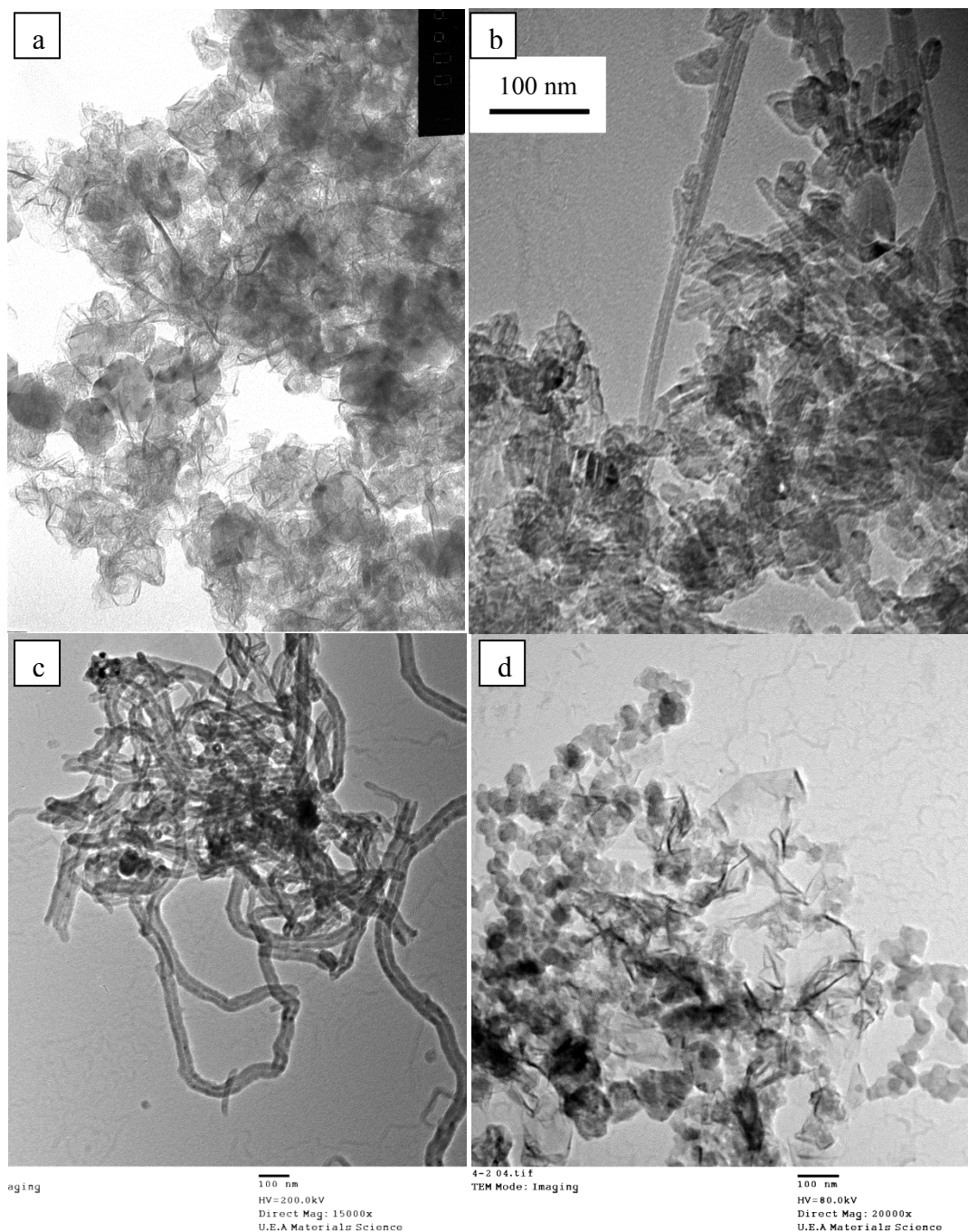
Figure 5-14 TEM images of (a) and (b) the catalyzed carbon produced by the plasma reactor, (c) CNTs produced by a thermal reactor; (d) uncatalyzed plasma carbon

5.3.5.4 BET surface area and Porosity

The BET surface area and porosity of CNTs, the catalyzed plasma carbon and uncatalyzed plasma carbon collecting at the same position were determined from the argon adsorption/desorption isotherm (Figure 5-15). The values of the BET surface area, pore volumes and pore sizes are summarized in the Table 5-9. The argon isotherms shown in Figure 5-15 exhibit types III and V characteristics according to the IUPAC classification of adsorption isotherms, which are characteristic of weak affinities of adsorbents to adsorbates, as a result of the co-existence of mesoporous and macroporous surfaces; in the current case, the macropores are mainly due to the packing of the carbon powder particles or stacked carbon nanofibres. The isotherms show small adsorption hysteresis at a relatively high pressure, indicating the existence of mesopores in the carbon adsorbents. The BET surface area of uncatalyzed plasma carbon, catalyzed plasma carbon and CNTs are 96.7, 456 and 204.7 m^2/g, respectively. The pore size distribution was evaluated by the density functional theory, and the results are shown in Figure 5-16. The catalyzed plasma carbon possesses a distinct bimodal pore size distribution feature, dominated at around 1.0 nm and 1.5 nm. The pore volume of catalyzed plasma carbon is much larger than uncatalyzed sample and CNTs.
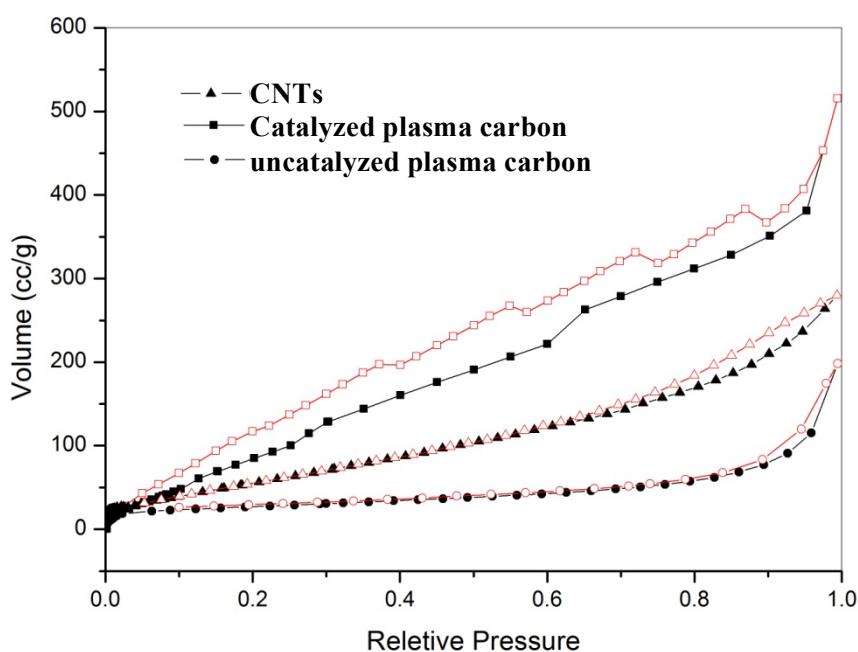
Figure 5-15 Argon isotherm at 77k of catalyzed plasma carbon, raw plasma carbon and CNTs.
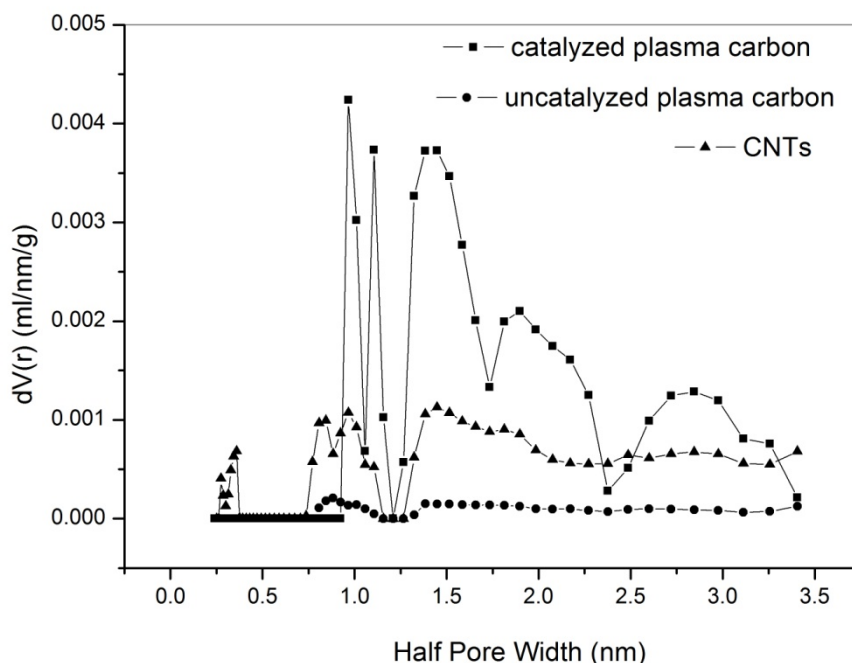
Figure 5-16 Pore-size distributions of catalyzed plasma carbon, uncatalyzed plasma carbon and CNTs, calculated from argon adsorption isotherms given in Figure 5-15, using the DFT model

Table 5-9 Physical properties of catalyzed plasma carbon, uncatalyzed plasma carbon and CNTs

Sample	S_{BET} (m^2/g)	V_p (cm^3/g)^a	Pore Size (nm)
Catalyzed plasma carbon	456	0.6334	1.0 nm, >1.5 nm
Uncatalyzed plasma carbon	94.7	0.1786	0.9 nm, >1.5 nm
CNTs	204.7	0.3442	0.36 nm, 0.9 nm, >1.5 nm

^{a} V_p is the total pore volume, derived from the amount of vapor adsorbed at P/P_0 =0.96.

5.3.5.5 Summary and future work

By using the MgNiO$_x$ catalyst in the plasma reactor for methane reforming, the catalyzed plasma carbon with short carbon nanofibers were produced from catalytic decomposition of methane. The results of XRD measurements indicated that NiO and MgO components in this catalyst formed a MgNiO$_x$ solid solution, in which only a quite small proportion of Ni^{2+} could be reduced to Ni^0. This would be in favor of inhibiting the formation of large metal particles at the surface of the catalyst, making the carbon nanofibers grown on this catalyst. But the

$MgNiO_x$ cannot be detected in catalyzed plasma carbon sample because the temperature of plasma reactor increased quickly to > 800 °C that was higher than the melting point of $MgNiO_x$. Thus the carbon nanofibers cannot grow up to longer size after the catalyst burn-off and subsequently normal plasma carbon structure was produced in the plasma reactor as reported previously in Chapter 4. TEM observation could confirm the above point. The catalyzed plasma carbon showed a better porosity of BET surface area of 456 m^2/g and a total pore volume of 0.6334 cm^3/g, comparing with the uncatalyzed plasma carbon and pure CNTs produced in a thermal reactor using the same catalyst.

The catalyst $MgNiO_x$ as a catalyst can be used to get the novel carbon structures in the plasma reactor. To produce the longer nanotubes, the plasma reactor needs to be re-designed to reduce the reaction temperature lower than the catalyst melting point.

5.4   Conclusions

The response surface methodology was applied to optimize the thermal treatment conditions of the plasma carbon to enhance BET surface area. The thermal treatment temperature, time and pressure were evaluated as variables and their effects of the BET surface area and yield of carbon were investigated. The analysis of variance showed that the statistical model can accurately evaluated the relationship between the responses and the studied factors, and the temperature was the significant parameter in the thermal treatment process. An increase in thermal treatment temperature resulted in an increase in BET surface area. However, at the same time, the increase of temperature reduced the modified carbon yield. The optimal surface area of the modified plasma carbon was achieved at 950 °C within 100 kPa pressure for 120 min thermal treatment. From comparison of predicted and experimental values, the error is as small as 3.7 and 2.3% for BET surface area and yield rate, respectively.

BET isotherm and pore size distribution indicate that the increases of BET surface area and pore volume are due to the generation of micropores, the break-up of some level of micropores to mesopores and the opening up of accessible porosities in the graphitic carbon

regions as the amorphous carbon was removed from the surface. From the Raman and TEM results, it can be concluded that a higher degree of crystallinity carbon structure was obtained at high thermal treatment temperatures, the amorphous material was burnt off during thermal treatment process.

The catalyst $MgNiO_x$ as a catalyst can be used to obtain the novel carbon structures in the plasma reactor. However, the current cooling system of the plasma reactor need to be further improved to ensure a suitable temperature for the catalytic process.

6

EFFECTS OF CARBON STRUCTURES ON HYDROGEN STORAGE PROPERTIES OF MgH$_2$

6.1   Introduction

Hydrogen storage in solid materials for the development of hydrogen-powered vehicles has emerged as a promising and practical option because it stores hydrogen in a safe and compact way. Magnesium hydride, MgH$_2$, has been considered as one of promising hydrogen storage materials due to its high hydrogen capacity of 7.6 wt %, high abundance, low cost and light weight [291, 292]. However, the practical application of magnesium has been greatly hindered by its slow kinetics and high operation temperature. According to recent studies, the desorption kinetics and temperatures of MgH$_2$ have been dramatically improved by ball milling with some transition metals, oxides and carbides [293-297]. Titanium compounds have been successfully used to improve the sorption kinetics in several typical hydrogen storage systems, exhibiting a high affinity toward hydrogen even at moderate temperatures. Recently, it has been found that the temperature for hydrogen release from MgH$_2$ can be greatly reduced by doping it with TiC [293, 294, 298].

Mg-C composite system has also drawn considerable interests following the observation that the hydrogen storage performance of Mg could be improved by adding graphite, carbon

nanotubes and fullerene [299-301]. Wu et al.[300] prepared various Mg/carbon composites by mechanical milling and investigated their hydrogen storage behaviors. It was found that all the carbon additives exhibited prominent effect over the noncarbon additives in improving the hydrogen capacity and dehydriding/hydriding kinetics of Mg. And among the various carbon additives, the purified single-walled carbon nanotubes (SWNTs) exhibited the most prominent 'catalytic' effect on the hydrogen storage properties of Mg. Wang et al.[299] investigated the hydrogen storage properties of various carbon additives mechanically milled with LiBH$_4$/MgH$_2$ composite. Again they found that SWNTs presented the most prominent effect on the kinetic improvement and cyclic stability of Li-Mg-B-H system. In addition, it was reported that graphite facilitates the hydrogen sorption kinetics of ball-milled Mg and Mg$_2$Ni metal hydrides [302-304]. Furthermore, graphite as a codopant of titanium-based catalyst enhanced significantly both the hydrogenation and the dehydrogenation kinetics of catalyzed MgH$_2$ and NaAlH$_4$ [305]. Lototskyy et al. [306] studied the kinetics and mechanism of Mg-hydrogen interactions during milling in presence of various types of carbon, including graphite, activated carbon, multi-wall carbon nanotubes and expandable graphite. They found introduction of carbon significantly changes the hydrogenation behavior of Mg and the carbon acts as a carrier of the 'activated' hydrogen by a mechanism of spill-over. The use of various carbon species (graphite, activated carbon, carbon black, carbon nanotubes, fullerenes, nanodiamonds and other forms of nanoscale carbon) ball milled with Mg or MgH$_2$ reduces hydrogen sorption temperature, improves kinetics and also prevents MgH$_2$ particle growth during the dehydrogenation/hydrogenation cycling [299-301].

In Chapter 4 and 5, I successfully produced nano-sized carbon powders with a mixture of microstructures by a microwave plasma reactor. The thermal treatment were applied to improve the surface area of the produced carbon and a optimum treatment conditions were obtained by RSM, which was referred as plasma carbon (PC) [307]. In this chapter, the PC is employed to enhance hydrogen storage properties of Mg-based system. Response surface methodology (RSM) is a useful optimization tool, and is also used to study the interactions of two or more variables. RSM has been used to optimized activated carbon (ACs) for hydrogen storage [237] to achieve outstanding absolute hydrogen storage capacities, as high as 6.6 wt. %, onto ACs, but rarely seen applied to optimize catalysts or additives in Mg-based hydrogen storage systems to improve hydrogen storage properties. The preparation conditions, PC

content and milling time, are optimized for better hydrogen storage properties. RSM based on central composite design (CCD) was used to design experiments, build models and determine the optimum preparation conditions for dehydrogenation onset desorption temperature and rehydrogenation rate. The effects of preparation conditions (plasma carbon content and co-milling time) on de-/rehydrogenation properties of 20h-milled MgH$_2$/TiC are also analyzed. Finally, other carbon structures: activated carbon (AC) and carbon nanotubes (CNTs) are milled with 20h-milled MgH$_2$/TiC based on the optimum experimental conditions to compare the effects of different structures on hydrogen storage properties of the Mg-based system.

6.2   Experimental Methods

6.2.1 Preparation of the Plasma Carbon and Mg/TiC by milling

Nano-structured plasma carbon is produced by methane cracking to form carbon and hydrogen in the relatively low-energy microwave plasma reactor and then modified by using a thermal treatment process, which has been described in Chapter 4 [307] and Chapter 5, respectively. Carbon nanotubes (CNTs) are provided by Xiamen University [308]. Activated carbon nanopowder (<50 nm particle size by TEM, ≥ 99 %) is purchased from Sigma Aldrich. The MgH$_2$/TiC sample is prepared by mechanically milling MgH$_2$ (from Th. Goldschmidt AG, Degussa, ~95 % MgH$_2$, 5 % Mg, 50μm) with 2 mol. % TiC (from Sigma-Aldrich, ~95%, < 200 nm) for 20 h within the glove box under argon protection.

The modified plasma carbon (PC) powders at the optimal modification conditions were washed by acetone and deionized water subsequently for three times and then dried in the vacuum oven at 180 °C for 6 h. The cleaned carbon powder was milled with 20 h-milled mixture of (MgH$_2$ + 2 mol % TiC), which is referred to (MgH$_2$/TiC + PC). For various milling time with various weight percentage of PC to MgH$_2$/TiC, the mixtures were used for dehydrogenation and rehydrogenation.

6.2.2 Optimization of sample preparation conditions of (MgH$_2$/TiC + PC)

Response surface methodology (RSM) is used to qualify the relationship between the controllable input parameters and obtained response results, also formed as surfaces [280, 281]. A Central Composite Design (CCD) is one of the most popular experimental designs to apply RSM and used to obtain optimum preparation variables for minimizing desorption onset temperature and maximizing absorption rate during dehydrogenation and rehydrogenation process. CCD has been widely used for fitting a second-order model and to come out with a minimum number of experiments for a complex experimental process [102, 242, 243]. The CCD consists of a two-level (±1) factorial design with center points and axial points, which are a distance of -alpha & +alpha from the centre of the design (Figure 2-18a). The regular CCD can be modified by choosing alpha = 1.0, which is named as a face centered CCD (Figure 2-18b).
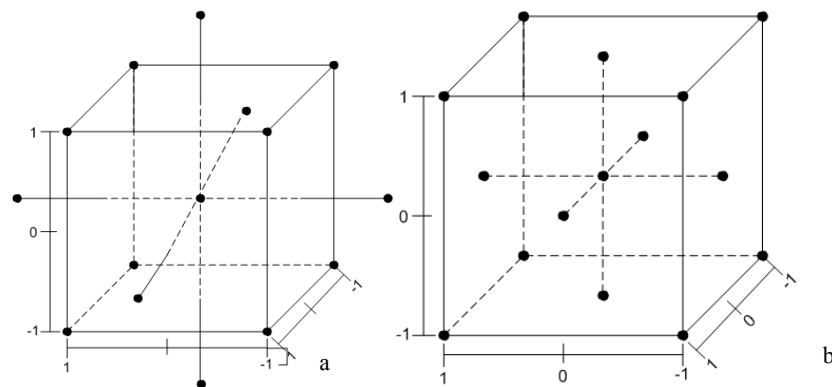
Figure 6-1 Orientation of points at design space (a) CCD and (b) face centered CCD.

Table 6-1 Independent variables and their levels (actual and coded)

Variables	Code	Unit	Coded variable levels		
			-1	0	1
Content of PC	X_1	wt%	0	5	10
Milling time	X_2	min	0	30	60

Here, the independent variables were X_1 and X_2 representing the content of plasma carbon and co-milling time. The settings of low and high values for the independent variables were as follows (low and high values): the PC content of 0 and 10 wt. %; the milling time of 0 and

60 min. Each variable was coded at three levels: -1, 0 and +1. Three replicates at the centre (0,0) of the design were performed to allow the estimation of the error. The CCD is shown in Table 6-1. All experiments were carried out in a randomized order to minimize the effect of unexpected factors. The scheme and complete design matrix of the experiments were shown in Table 6-2.

Concerning the optimization for onset desorption temperature (Y_1) and absorption rate (Y_2), the responses Y_1 and Y_2 were analyzed using Design Expert software (Stat-Ease, Inc., Version 8, Minneaplis, USA). A quadratic polynomial regression model was assumed for predicting responses. The model proposed for each response Y was

$$Y = A_0 + A_1X_1 + A_2X_2 + A_{12}X_1X_2 + A_{11}X_1^2 + A_{22}X_2^2 \qquad \text{Equation 29}$$

Where Y is measured response, X_1 and X_2 are the content of PC and milling time for each run, respectively, A_0 is a constant; A_1 and A_2 are linear coefficients; A_{12} is cross-product coefficients; and A_{11} and A_{22} are quadratic coefficients. The goodness of fit of the model was evaluated by the coefficient of determination R^2 and the analysis of variance (ANOVA).

Table 6-2 Central Composite Design (CCD) matrix

Run	Coded X_1 Content of PC wt. %	Coded X_2 Milling time min	Actual X_1 Content of PC wt. %	Actual X_2 Milling time min
1	1	1	10	60
2	0	-1	5	0
3	-1	0	0	30
4	0	0	5	30
5	0	0	5	30
6	-1	1	0	60
7	0	1	5	60
8	1	0	10	30
9	-1	-1	0	0
10	0	0	5	30
11	1	-1	10	0

6.2.3 Materials characterization

The morphology of the powder mixtures was characterized by a transmission electron microscope (TEM), TECNAI, FEI Company. X-ray diffraction (XRD) was performed using an XTra manufactured by Thermo ARL (US) diffractometer with Cu Kα radiation.

The BET surface area and porosity of each sample were determined from argon isotherm at 77 K using the surface area/pore size analyzers, Quantachrome AUTOSORB-1. The cleaned carbon samples were degassed for 8 h at 300 °C to remove any moisture or adsorbed contaminants that may be presented on their surfaces. The manufacturer's software can provide BET surface area of the carbons by applying the BET equation to the adsorption data. The pore size distribution was evaluated by density functional theory (DFT) method [251, 252].

6.2.4 Measurement of hydrogen storage

The hydrogen sorption behavior of the mixtures was studied by Intelligent Gravimetric Analyzer (IGA-003, Hidden Isochem Ltd.). The desorption was performed from room temperature to 500°C under 100 kPa Helium pressure at a heating rate of 10°C/min and He flow rate of 150 ml/min. Hydrogen absorption was measured at hydrogen pressure of 1000 kPa with the flow rate of 150 ml/min and isothermal temperature of 300 °C for 240 min after the sample was thoroughly dehydrogenated. The heating rate was set at 10°C/min. The rehydrogenation rate was determined from the instantaneous rate at the point of 50% conversion. Desorption kinetics were measured at 300 °C with an initial helium pressure of 10 kPa.

6.3   Results and Discussions

6.3.1 Statistical analysis for optimization of PC content and milling time in 20 h-milled MgH$_2$/TiC

Figure 6-2 presents thermogravimetry (TG) curves of all experimental runs based on CCD. The overall weight loss during dehydrogenation process is in the range of 5.2 ~ 6.5 wt.% that is very close to the theoretic hydrogen capacities. Thus the dehydrogenations of the (MgH$_2$/TiC + PC) mixtures are thoroughly completed. Figure 6-3 shows derivative thermogravimetric (DTG) curves calculated from Figure 6-2, which are used to identify the onset and peak desorption temperatures. It is reported that the onset and peak temperatures obtained from DTG are in good agreement with that measured by Differential Thermal Analysis (DTA) [309, 310]. This means that the maximum rate of weight loss occurs at the greatest temperature differential recorded by DTA [309, 310]. The lowest desorption onset temperature is about 180 °C from Run 5, which is dehydrogenation of 20h-milled MgH$_2$/TiC milled with 5 wt.% PC for 30 min. After dehydrogenation, the samples are situ re-hydrogenated, and the rehydrogenation results are showed in Figure 6-4. It is found that the rehydrogenation kinetics are influenced by both carbon additives and co-milling time. The results will be further analyzed by RSM in the following section. The desorption onset temperature and absorption rate of (MgH$_2$/TiC + PC) mixtures, calculated from Figure 6-3 and Figure 6-4, are listed in Table 6-3. The standard deviations of response 1, Onset Desorption Temperature, and response 2, absorption rate, are respectively 8.48 and 0.048 according to the three replicate experiments at the central point (Run 4,5 and 10).
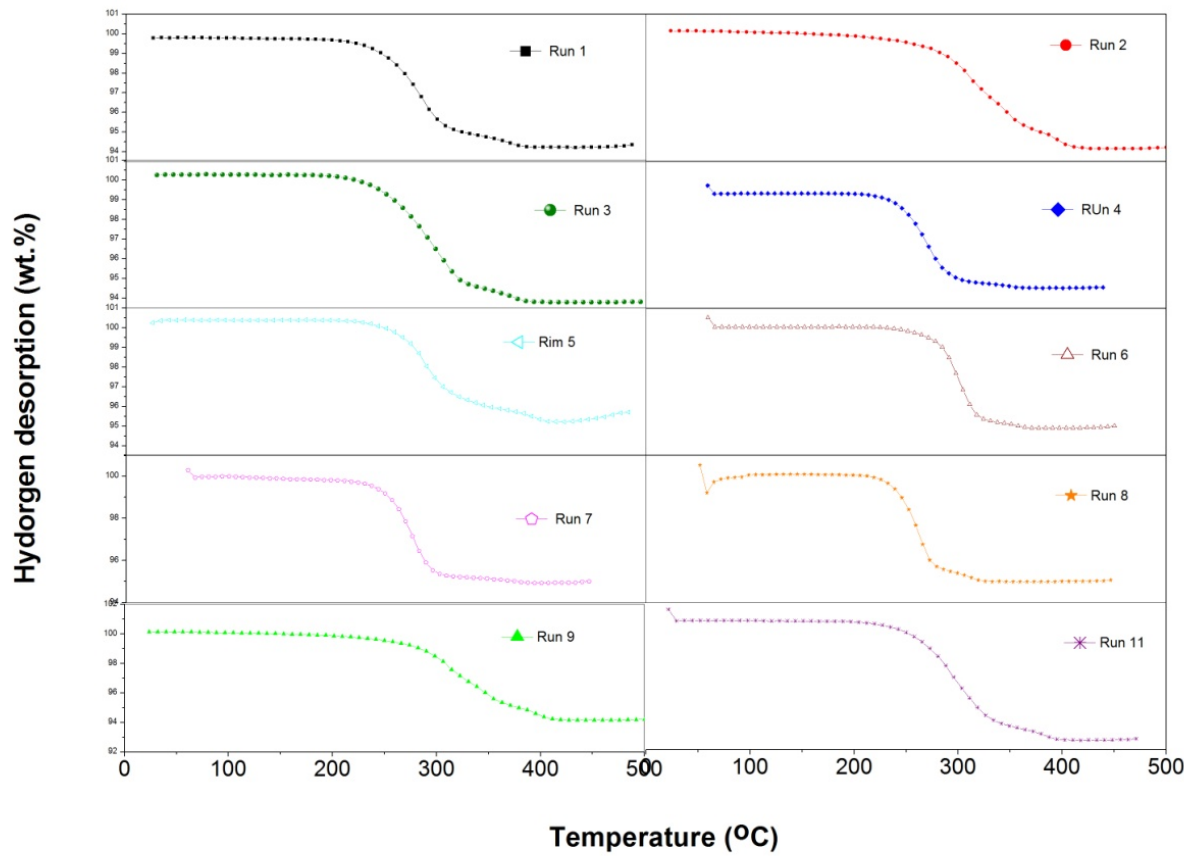
Figure 6-2 TG curves of all (MgH$_2$/TiC + PC) mixtures based on CCD.
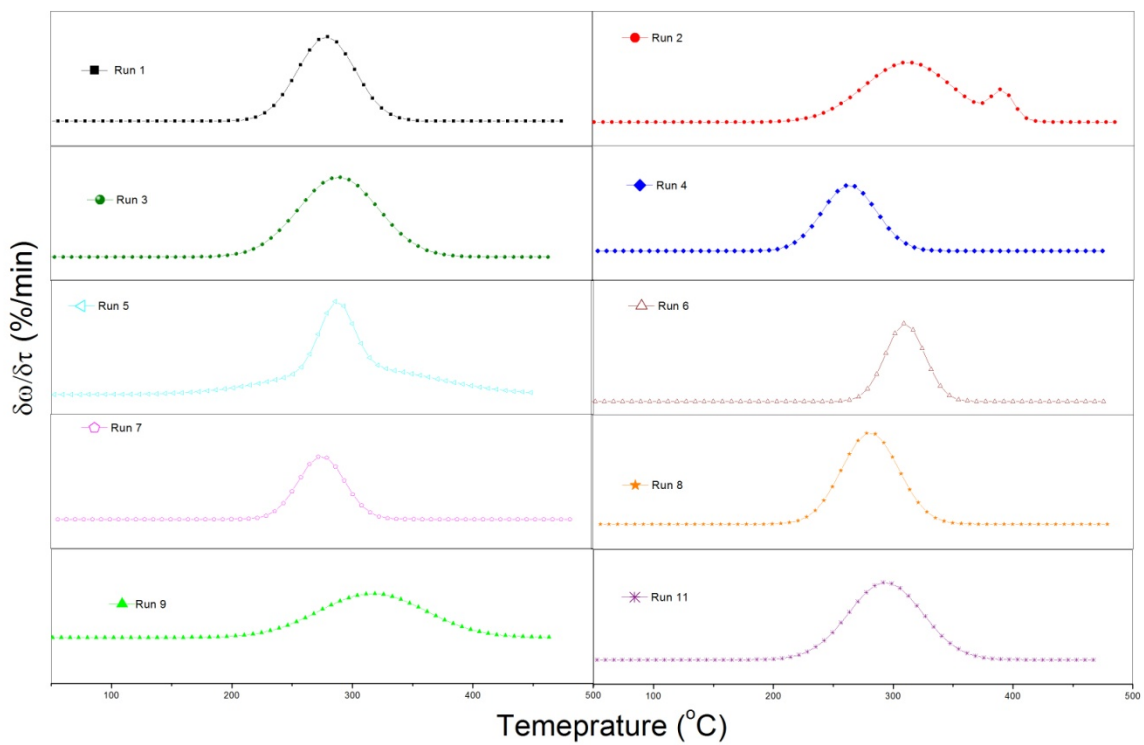
Figure 6-3 DTG of all samples based on CCD, derived from Figure 6-2

113
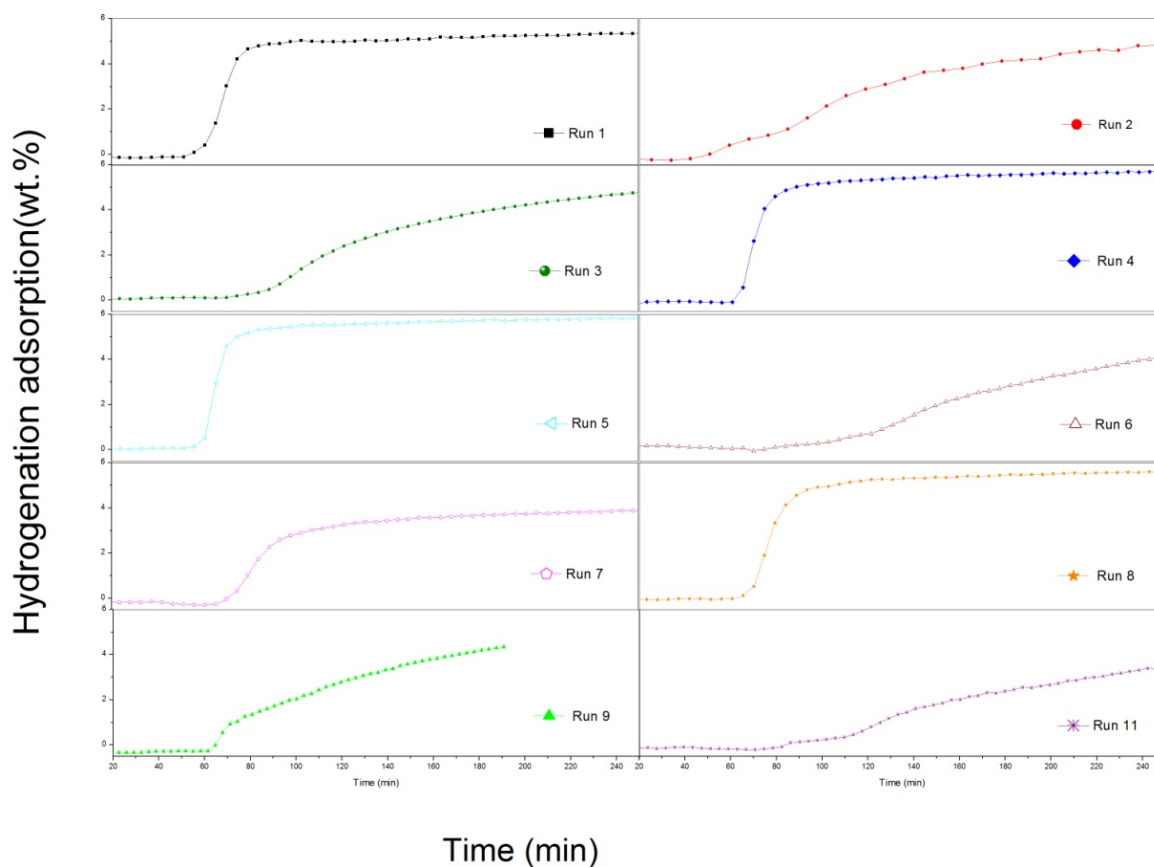
Figure 6-4 Rehydrogenation of all samples at 300 °C and 1000 kPa H$_2$ pressure.

Table 6-3 Onset desorption temperature and absorption rate of the (MgH$_2$/TiC + PC) mixtures

Run	Responses	
	Onset Desorption Temperature	Absorption Rate
	°C	wt. %/min
1	185	0.6800
2	197	0.03625
3	213	0.04018
4	162	0.5487
5	180	0.5052
6	234	0.04054
7	198	0.3335
8	201	0.4500
9	230	0.03534
10	180	0.4330
11	192	0.03187

CCD is used to develop a correlation between content of PC and milling time on onset desorption temperature and rehydrogenation rate based on RSM. The quadratic regression

model for onset desorption temperature (Y_1) and absorption rate (Y_2) in terms of coded factors are given by Equation 2 and Equation 3, respectively.

$$Y_1 = 177.89 - 17.33\ X_1 - 1.17\ X_2 - 1.25\ X_1\ X_2 + 23.26\ X_1^2 + 13.76\ X_2^2 \qquad \text{Equation 30}$$

$$Y_2 = 0.44 + 0.17\ X_1 + 0.16\ X_2 + 0.16\ X_1 X_2 - 0.11\ X_1^2 - 0.17\ X_2^2 \qquad \text{Equation 31}$$

Table 6-4 Analysis of variance (ANOVA) for two factors A and B for onset desorption temperature and absorption rate.

| Term | Onset desorption temperature (Y_1) | | | | Absorption rate (Y_2) | | | |
| | original model | | simplified model | | original model | | simplified model | |
	F Value	p-value Prob > F	F Value	p-value Prob > F	F Value	p-value Prob > F	F Value	p-value Prob > F
Model	5.1743	0.0477	11.5400	0.0042	10.84478	0.01025	9.6207	0.0088
X_1-Content	10.9143	0.0214	14.9300	0.0062	17.04109	0.00910	12.7995	0.0117
X_2-Time	0.0494	0.8328	-	-	14.07891	0.01326	10.5746	0.0174
X_1X_2	0.0242	0.8824	-	-	9.66074	0.02661	7.2562	0.0359
X_1^2	8.3006	0.0345	11.0100	0.0128	2.98830	0.14444	-	-
X_2^2	2.9054	0.1490	3.8200	0.0914	7.05081	0.04514	7.8526	0.0311
Lack of Fit	1.8822	0.3654	1.2000	0.5139	4.5535	0.1853	5.7550	0.1535
R^2	0.8301		0.8318		0.8651		0.9156	

Table 6-4 presents the analysis of variance (ANOVA) applied to the quadratic model developed to the fit the dehydrogenation onset temperature and absorption rate data. The model Y_1, F-value of 5.17 implies the model is significant; there is only 4.77% chance that a 'F-value' this large could occur due to noise. Value of 'Prob > F' less than 0.05 indicate the model terms are significant. In this case, X_2, X_1X_2 and X_2^2 are not significant to predict onset desorption temperature; in model Y_2, X_1^2 are insignificant model terms to predict absorption rate. The insignificance of some terms indicates the models can be simplified to improve the accuracy. The simplified models from Equation 30 and Equation 31 to fit the responses lead to Equation 32 and Equation 33. And the simplified ANOVA has been listed in Table 4.

The test of lack-of-fit is used to determine whether discrepancies between measured and expected values can be attributed to random or systematic error. The lack-of-fit test compares the residual error to pure error from replicated performance. F-values of 1.88 for Y_1 and 4.55 for Y_2, implied the lack of fit of Y_1 is not significant, whereas the lack of fit of Y_2 is significant to pure error. How well the estimated model fits the data can be measured by the value of R^2. The closer the R^2 is to 1, the better the model fits the experimental data, the less difference between the predicted and observed values. The R^2 of Y_1 and Y_2 is respectively

0.8318 and 0.9156 by the simplified models, which means the onset desorption temperature and rehydrogenation rate can be predicted adequately by Y$_1$ Equation 32 and Y$_2$ Equation 33.

$$Y_1 = 177.95 - 17.50 \times X_1 + 23.13 \times X_1^2 + 13.63 \times X_2^2 \qquad \text{Equation 32}$$

$$Y_2 = 0.40 + 0.17 X_1 + 0.16 X_2 + 0.16 X_1 X_2 - 0.20 X_2^2 \qquad \text{Equation 33}$$
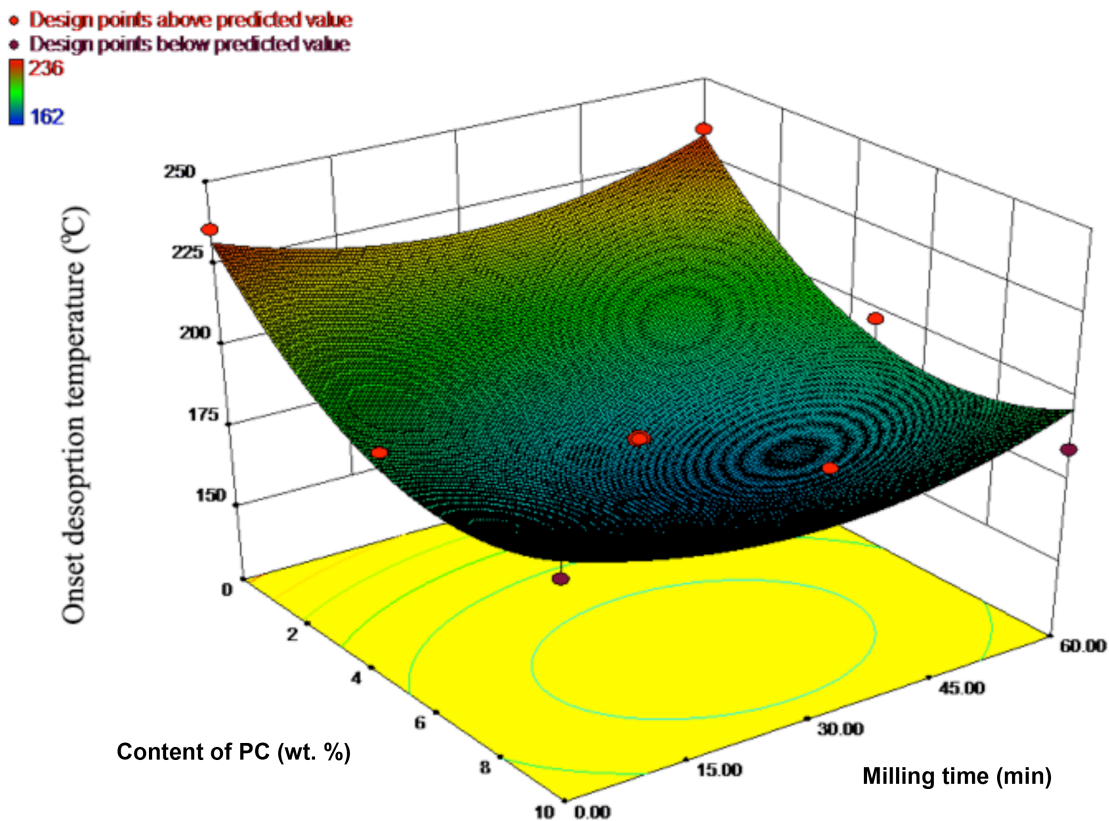
Figure 6-5 3D response surface of dehydrogenation onset desorption temperature according to Equation 32

Figure 6-5 shows the 3D response surface of onset desorption temperature as a function of the two factors (content of PC and milling time) according to Equation 32. Red points and pink points in Figure 6-5 are the designed points that are experimental data, above and below the response surface, respectively, indicating the modeled response surface can match the data. From Figure 6-5, as the PC content in the composites increases from 0 to ~7 wt%, hydrogen desorption onset temperature decreases from 236 °C to ~180 °C. And with increasing PC content from ~7 to 10 wt%, the onset desorption temperature has a slight increase. With an increase in milling time from 0 to about 30 min, the dehydrogenation onset desorption temperature attends the lowest down to ~180 °C. But the onset desorption

116

temperature increases with the longer milling time from 30 min to 60 min. This is due to the fact less agglomeration and homogeneous dispersion of the MgH$_2$/TiC particles supported by PC (as shown in Figure 6-9) comparing with the morphology of MgH$_2$/TiC without PC. Also the porous carbon nanoparticles could transfer hydrogen atoms or molecules from/to Mg, which may also provide additional diffusion channels for diffusion of hydrogen atoms and improve the hydrogen sorption kinetics [11, 311]. It need to be noticed there is a threshold of different content of PC in the (MgH$_2$/TiC + PC) mixture, the PC plays a negative role on hydrogen sorption of Mg if the threshold point has been surpassed. The reason could be the large amount of extra carbon material, especially amorphous carbon, would cover the MgH$_2$ surface and hinder the hydrogen transport. It has been found the plasma carbon contains not only graphene layers and porous carbon particles but also amorphous carbon particles [307]. It has been reported that SWNTs is the best additive, followed by amorphous carbon, fullerene and graphite, for the hydrogen storage performance of different Mg/C composites at relative low temperature [11, 300]. Also, too long time milling will destroy and break the carbon structures, which has been reported by other researchers [312, 313]. From response surface Figure 6-5, the threshold point of PC content in terms of onset desorption temperature can be detected easily, which is 6.89 wt. % of PC with the onset desorption temperature of 175 °C.
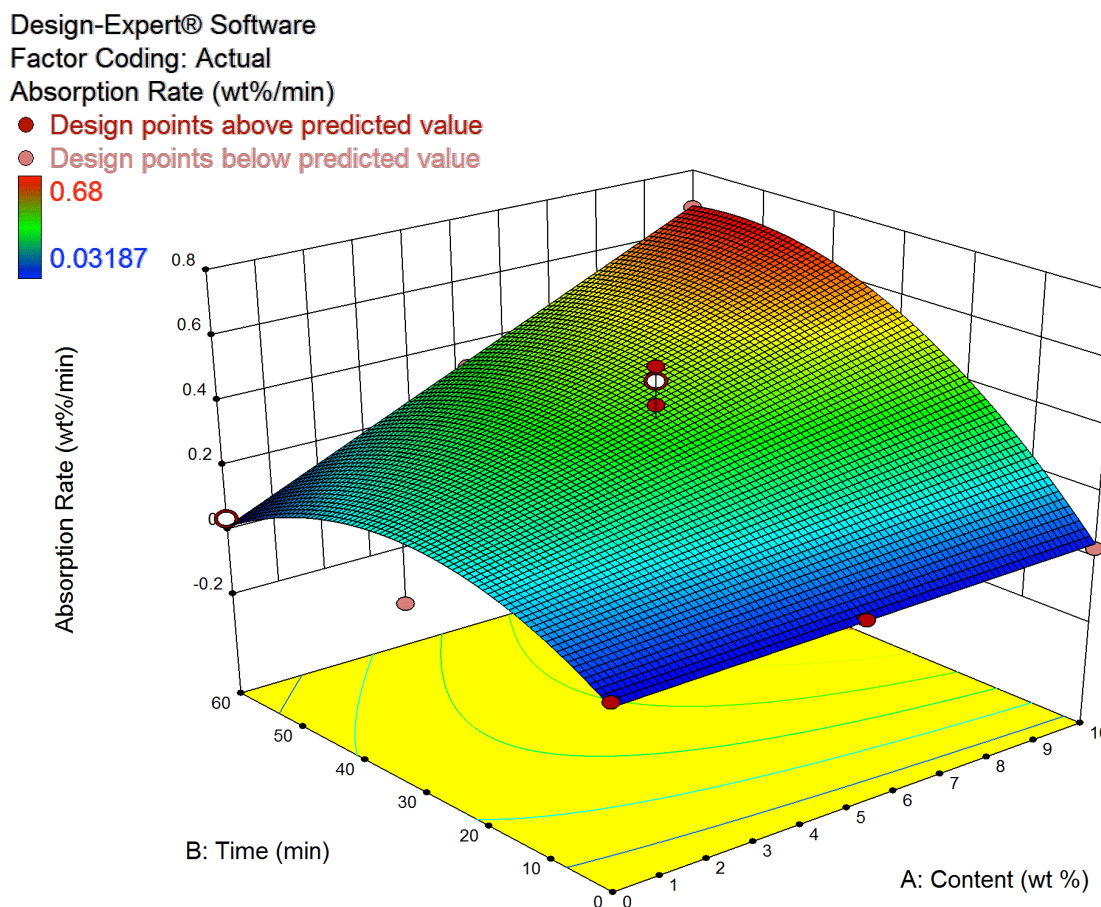
Figure 6-6 3D response surface of hydrogen absorption rate, according to Equation 33

Figure 6-6 shows the hydrogen absorption rate as a function of PC content in the (MgH$_2$/TiC + PC) mixture and milling time, fitted from Equation 33. During the co-milling time range from 15 min to 60 min, the absorption rate increases with the increase of PC content in the (MgH$_2$/TiC + PC) mixture. With the increase of milling time, the rehydrogenation rate starts increasing due to the attribution of milling to mix the MgH$_2$/TiC and PC till a certain milling time depending on the content of PC, such as 30 min milling time for about below 6 % PC in the (MgH$_2$/TiC + PC) mixture. Afterwards the structure of PC is broken and destroyed by high energy milling, resulting in the decrease in rehydrogenation rate. The maximum rehydrogenation rate is ~0.68wt. %/min at a milling time of 60 min with an additive of 10 wt. % PC.

When simply adding PC in the 20h- milled MgH$_2$/TiC without milling, as shown in Figure 6-6, rehydrogenation rate doesn't change with the increase of PC content since the PC cannot mix with MgH$_2$/TiC properly to generate active interface between the 20h- milled MgH$_2$/TiC

and carbon materials. After milling, the rehydrogenation rate is increasing with the increase of PC content from 0 to 10 wt. %. The hydrogenation process of Mg can be well understood in the following steps: dissociation of hydrogen molecules into atoms, diffusion of hydrogen atoms, nucleation of the MgH$_2$ phase, and further hydrogen diffusion into bulk magnesium through the formed MgH$_2$ layer [300, 314]. It has been well established that metallic catalysts may facilitate the dissociation of hydrogen molecules. Apart from the catalysis, the other reason facilitates rehydrogenation rate of Mg, may be due to "spillover" effect on the carbon [315, 316]. The widely accepted mechanism of the hydrogen spillover effect is that hydrogen molecules are first dissociated by the doped metal clusters on the carbon surface, and the resulting hydrogen atoms can then diffuse away from the metal clusters and bind to the surface of the porous carbon materials [305, 308, 315-318]. Here, hydrogen absorption was measured at hydrogen pressure of 1000 kPa and the temperature of 300 °C for 240 min. Taking Run 5 as an example, the total hydrogen weight loss of Run 5 from TG (Figure 6-2) is 5.14 wt. % under 100 kPa He gas flow from room temperature to 500 °C; but the hydrogen weight gain is 5.82 wt. % during absorption process at 1000 kPa hydrogen gas flow and 300 °C (Figure 6-4). About 0.68 wt. % weight difference between hydrogen desorption and adsorption could be caused by hydrogen spillover effect on carbon. A very recent report [315] has claimed that a Pt-decorated SWNT could take a 1.2 % of hydrogen by forming C-H bonds. Earlier works also reported hydrogen "spillover" effect on porous materials can happen at room temperature or even above 300 °C [317-319]. Also Wang et al. [320] investigated the effects of different carbon materials were used as a co-catalyst with Ti on the dehydrogenation and hydrogenation kinetics of NaAlH$_4$, and concluded that carbon most likely was imparting an electronic contribution through the interaction of its facile π-electrons with Ti through a hydrogen spillover mechanism. A part of TiC nano-particles in 20h-milled MgH$_2$/TiC composite is inserted into the MgH$_2$ grain boundary, and the rest of it is evenly dispersed on the surface of or among the MgH$_2$ particles [297, 307], which may form an interface with the plasma carbon material. Hereby, in our work, the hydrogen spillover effect on carbon surface might result in greater rehydrogenation capacity and faster rehydrogenation kinetics of Mg/TiC. However, the effect of hydrogen pressure and reaction temperature on the spillover effect yet is still not clear and will be further studied in the future.

The main objective of the optimization is to determine the optimal PC content and milling time for the preparation of the (MgH_2/TiC + PC) mixture for the promising hydrogen storage properties. However, it is difficult to optimize both responses because the interest regions of factors are different. Indeed, when Y_1 decrease, Y_2 response increase at a certain range of the factors. Thus it is difficult to find a balance for achieving both low onset desorption temperature and high absorption rate. To solve this problem, the function of desirability was applied. The optimal experimental conditions with the highest desirability were obtained as: 7 wt% PC milling with 20h-milled MgH_2/TiC for 30 min milling to achieve results of 175 °C onset desorption temperature and 0.4651 wt. %/min absorption rate. The experiments according to the optimized condition were repeated by three independent experiments to compare with the predicted values. Table 6-5 shows the modeling values and the average experimental results obtained in the aforementioned conditions. The differences between the predicted values and the experimental values of the onset desorption temperature and absorption rate were 8.5 % and 5.2 %, respectively, which is under acceptable range.

Table 6-5 Comparison of predicted and experimetnal results on onset desorption temperature and absorption rate

PC content (wt. %)	Milling Time (min)	Onset desorption temperature (°C)		Difference (%)	Absorption rate (wt. %/min)		Difference (%)
		Experimental	Predicted		Experimental	Predicted	
7	30	191	175	8.5	0.4905	0.4651	5.2

6.3.2 Microstructure analysis of MgH_2/TiC milled with PC, AC and CNTs

In our effort to further understand the effects of carbon structures on hydrogen storage properties of Mg-based materials, 7 wt % activated carbon (AC) and 7 wt % carbon nanotubes (CNTs) are used to mill with 20h-milled MgH_2/TiC composite for 30 min, respectively, to compare the results with the (MgH_2/TiC + 7 wt. % PC).

The BET surface area and porosity of carbon materials and co-milled MgH_2/TiC with carbon materials were determined from the argon adsorption/desorption isotherm (Figure 6-7). The

values of the BET surface area, pore volumes and pore sizes are summarized in Table 6-6. BET surface areas of original PC, AC and CNTs are 459, 264 and 228 m^2/g, respectively. After milling, the BET surface areas of (MgH$_2$/TiC + 7PC), (MgH$_2$/TiC + 7AC) and (MgH$_2$/TiC + 7 CNTs) mixtures are 43, 53 and 121 m^2/g, respectively. From the pore size distribution, shown in Figure 6-8, it can be seen that the PC possesses a quite small amount of supermicropores with the size of 0.26 nm and an amount of micropores at 0.8 and 1.5 nm; the pore size distribution of AC focuses on supermicropore at 0.24 and 0.68 nm; the pore size of CNTs only distribute at 0.96 and 1.5 nm. After milling with MgH$_2$/TiC, the micropores with size less than 1 nm in the (MgH$_2$/TiC + 7PC) and (MgH$_2$/TiC + 7AC) disappear and their pore size distributions concentrate on mesopores with two peaks at 1.1 and 1.4 nm in half pore width. The pore volume and pore size distribution of (MgH$_2$/TiC + 7CNTs) does not change obviously.
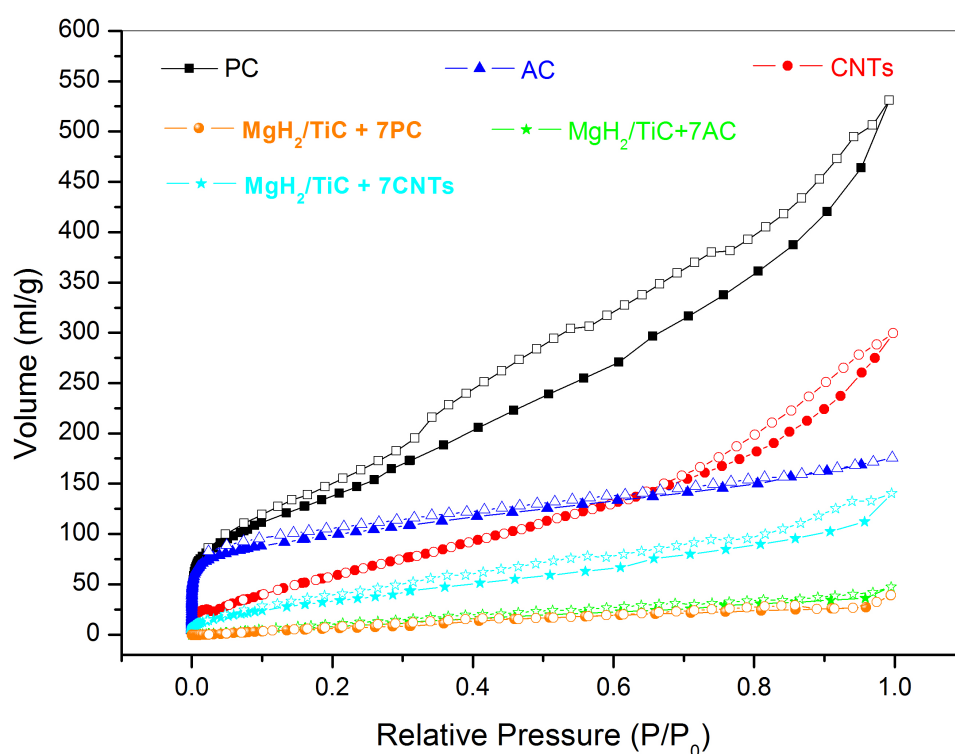
Figure 6-7 Argon isotherms at 77 K of PC (black), CNTs (red) and AC (blue), filled symbols for adsorption and unfilled symbols for desorption
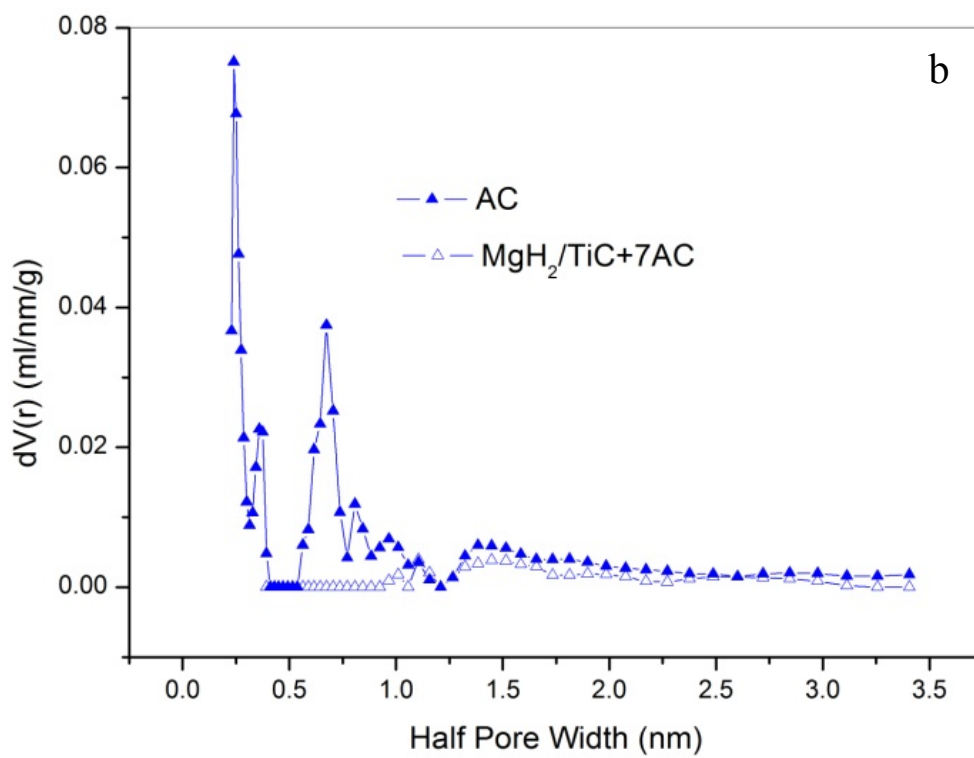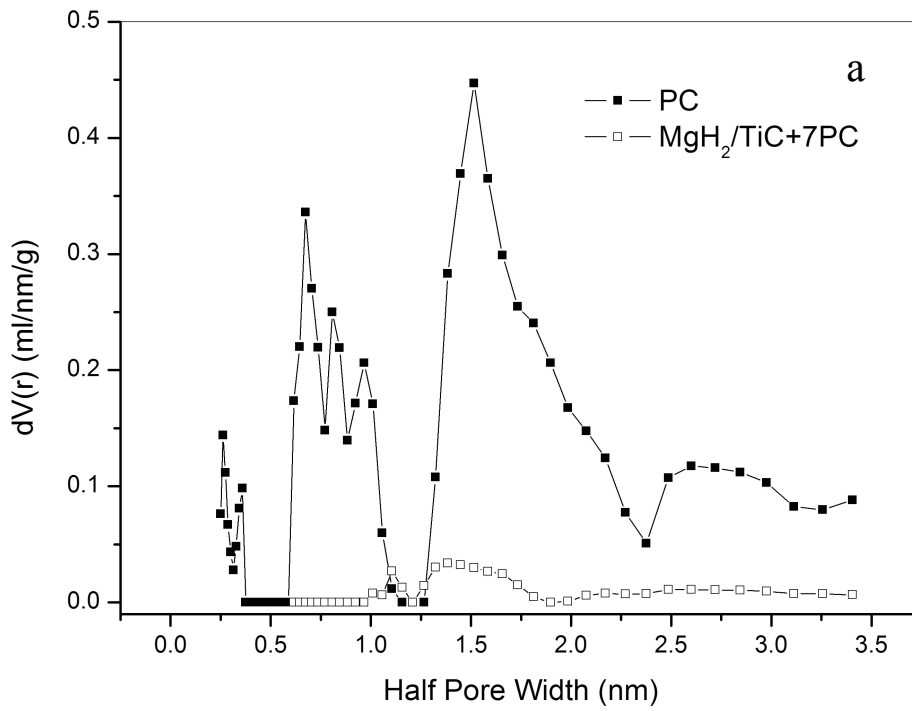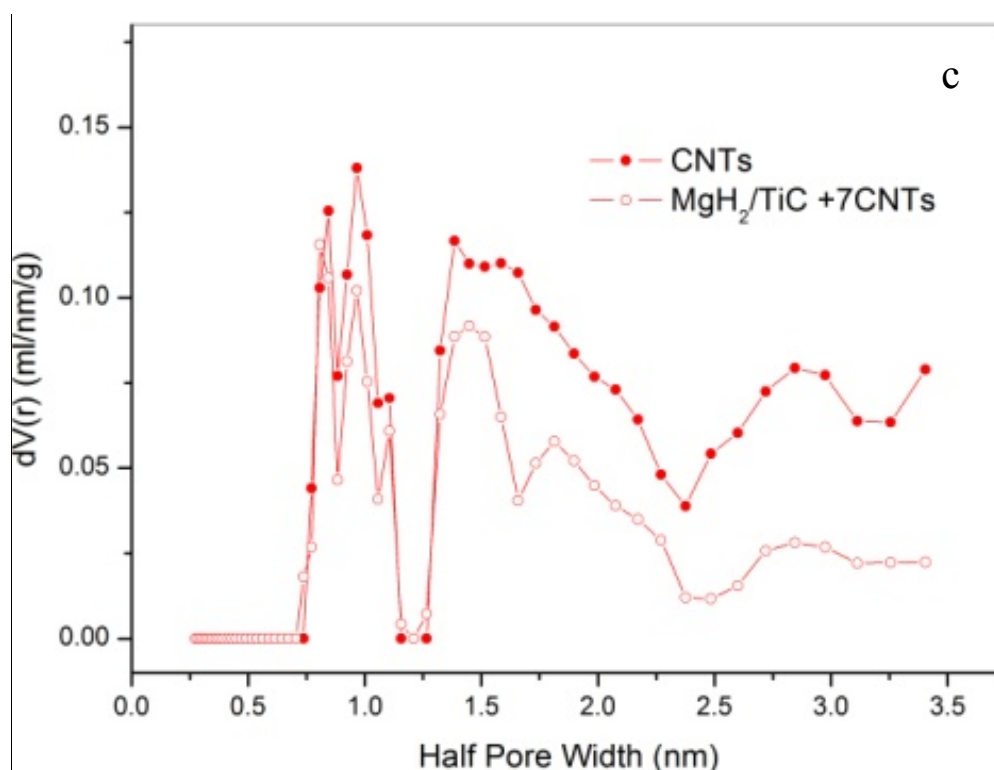
Figure 6-8 Pore-size distributions calculated from argon adsorption isotherms given in Figure 6-7, using the DFT model. (a) PC and MgH$_2$/TiC+PC; (b) AC and MgH$_2$/TiC+AC; (c) CNTs and MgH$_2$/TiC+CNTs.

Table 6-6 Surface characterizations of the carbon materials and MgH$_2$/TiC + carbon materials obtained by Ar measurement at 77K

Surface properties	PC	MgH$_2$/TiC+7PC	AC	MgH$_2$/TiC+7AC	CNTs	MgH$_2$/TiC+7CNTs
BET surface area (m^2/g)	459	43	264	53	228	121
Total pore volume (cm^3/g)	0.43	0.034	0.22	0.058	0.37	0.17

Figure 6-9a shows the TEM images of the MgH$_2$ mechanically milled with TiC for 20 h, where the average size of the large aggregated particles is estimated to be about 35 nm in diameter. Many much darker small particles decorating the large particles are proved to be TiC nanoparticles. The nanostructure of Plasma carbon has been presented in our previous publication [307], which mainly compose of amorphous structure, graphite and graphene layers, shown in Figure 6-9b. In Figure 6-9c which is the TEM image of MgH$_2$/TiC +7PC, it is clearly seen that the MgH$_2$/TiC nanoparticles are uniformly dispersed on graphene. Figure 6-9d shows the TEM images of the original AC, revealing that AC contains a disordered

porous structure. Figure 6-9e for the composite of MgH$_2$/TiC+7AC, shows the MgH$_2$/TiC particles are incorporated into graphitic turbostratic stacking. Figure 6-9f shows the TEM of CNTs used in this work. The multi-walled CNTs are very uniform in diameter along the tube-length with the outer diameters in range of 10–50 nm and the inner diameters in range of 3–7 nm. In addition, agglomeration is lower for the samples with carbon materials than in the samples without them, which is because of the lubricant effect of the carbon as reported in the literature [19] and [321].
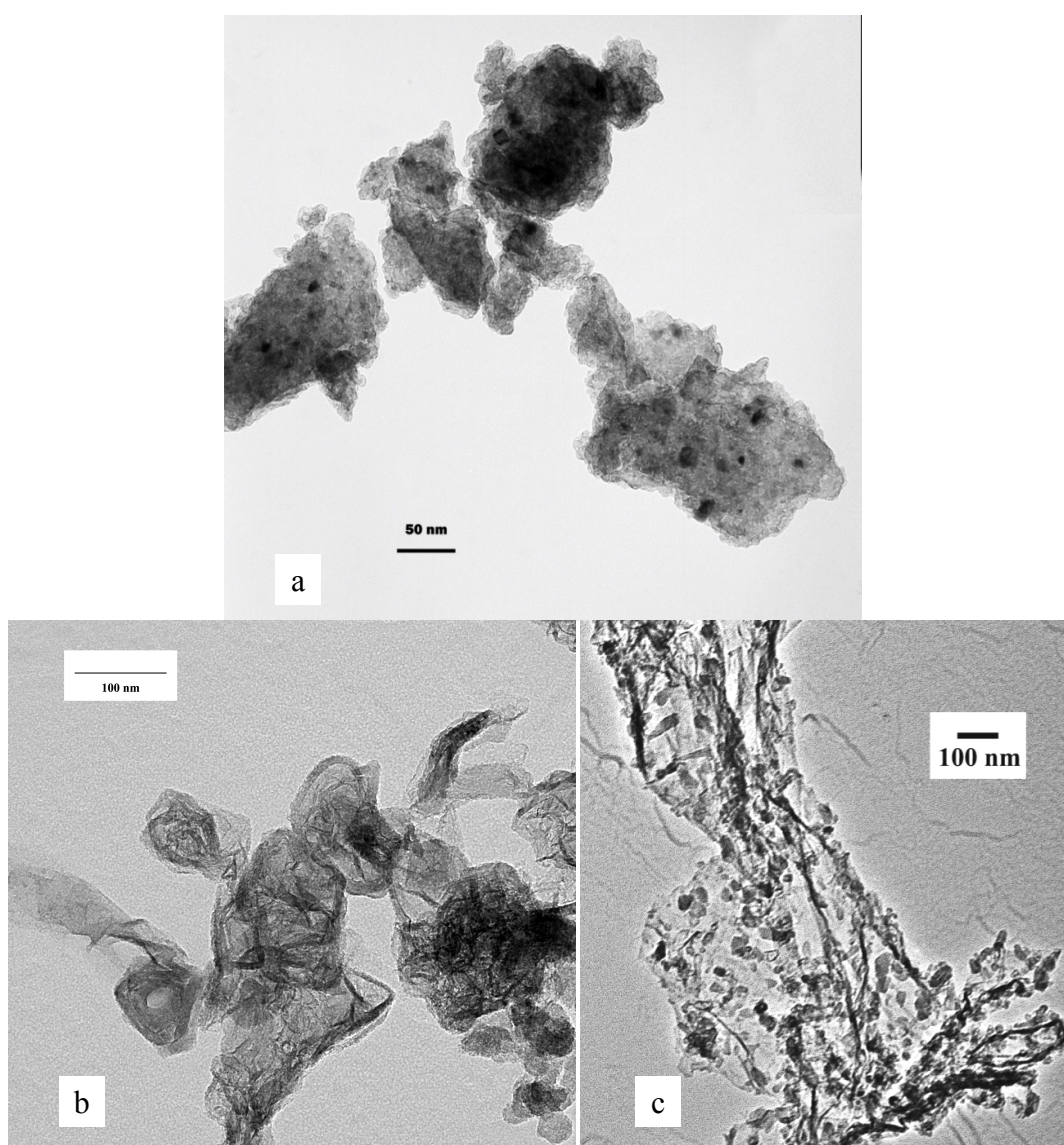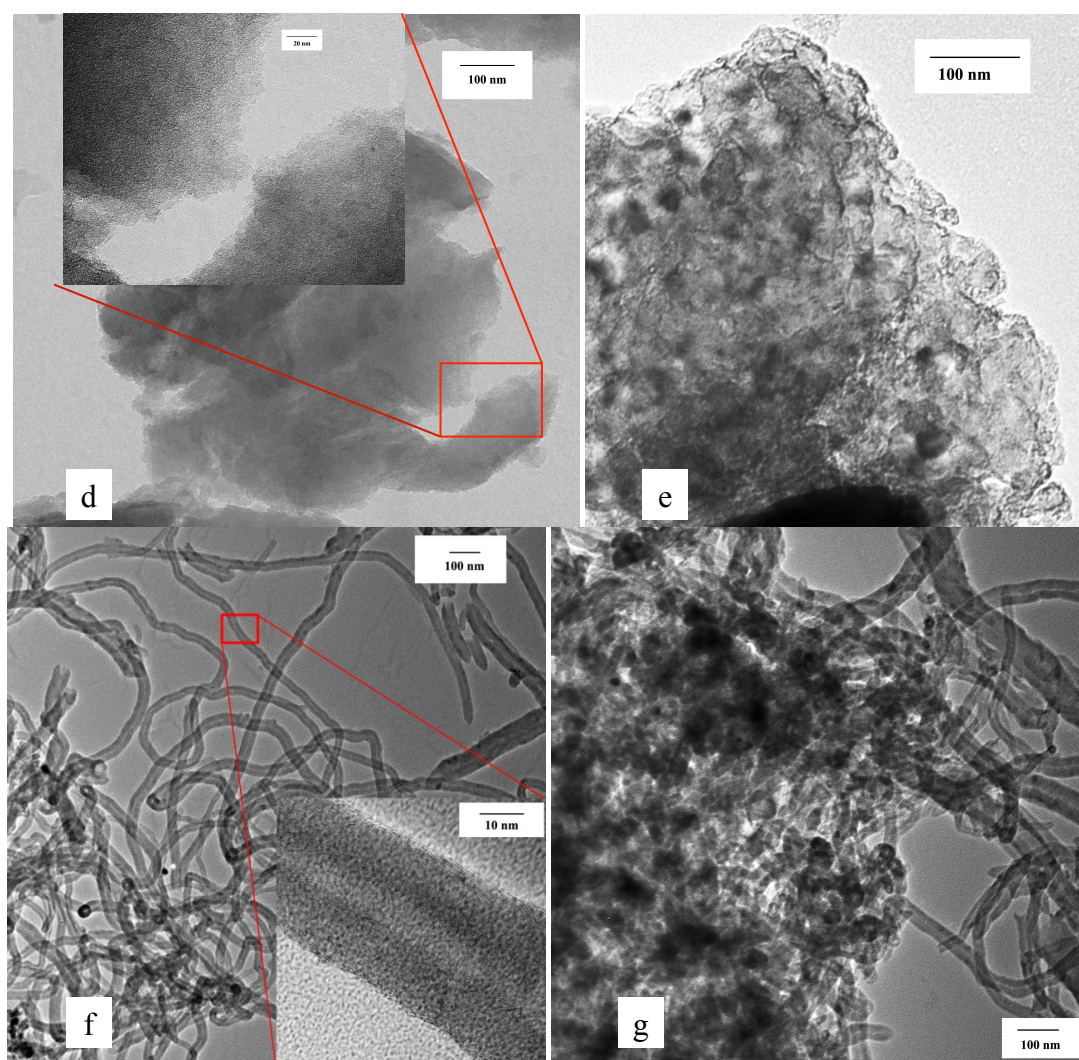
Figure 6-9 TEM images of (a) 20h-milled MgH$_2$/TiC; (b) cleaned plasma carbon; (c) MgH$_2$/TiC +7PC; (d) activated carbon; (e) MgH$_2$/TiC + 7AC; (f) purified CNTs; (g) MgH$_2$/TiC +7CNTs

6.3.3 Effects of PC, AC and CNTs on dehydrogenation of 20h-milled MgH$_2$/TiC

The dehydrogenation kinetics of MgH$_2$/TiC can be considerably improved with the addition of different carbon materials. Figure 6-10 shows the hydrogen desorption thermogravimetry and derivative thermogravimetry of the various (MgH$_2$/TiC + 7PC, 7AC and 7CNTs) composites and the original 20h-milled MgH$_2$/TiC, and Figure 6-11 lists the onset desorption temperature and peak temperature of hydrogen desorption from Figure 6-10. To distinguish TiC and PC effects on dehydrogenation of MgH$_2$, the two samples of 20h milled MgH$_2$ and

20h milled MgH$_2$ milled with 7 wt. % PC for 30 min were also measured for TG and dehydrogenation kinetics.

The 20h milled MgH$_2$ dehydrogenated from 300 °C and the 20h milled MgH$_2$ + 7PC started to desorb hydrogen at 235 °C, indicating the PC additive has a positive effect on reducing dehydrogenation temperature of MgH$_2$. As discussed earlier, carbon additives play the double roles in influencing hydrogen desorption of MgH$_2$: (1) the lubricating effect of carbon reduces the agglomeration of the MgH$_2$ particles; (2) the PC provide an interface for the diffusion of the atomic hydrogen to reach Mg/MgH$_2$. TiC is a very positive catalyst for hydrogen storage of MgH$_2$, which we have already reported in the previous publication [294, 297]. In Figure 6-10, it can be seen that after 20h milling with TiC, the onset desorption temperature was reduced to 213 °C. The onset dehydrogenation temperature of (MgH$_2$/TiC + 7PC) was observed to shift to 191 °C, which was about 160 °C lower than that of the original 20h-milled MgH$_2$/TiC and 20h milled MgH$_2$ + 7PC. The onset desorption temperatures of (MgH$_2$/TiC + 7CNTs) and (MgH$_2$/TiC + 7AC) was reduced to 209 and 205 °C, respectively. Thus both TiC and the carbon additives have a positive effect on reducing dehydrogenation onset temperature of MgH$_2$.
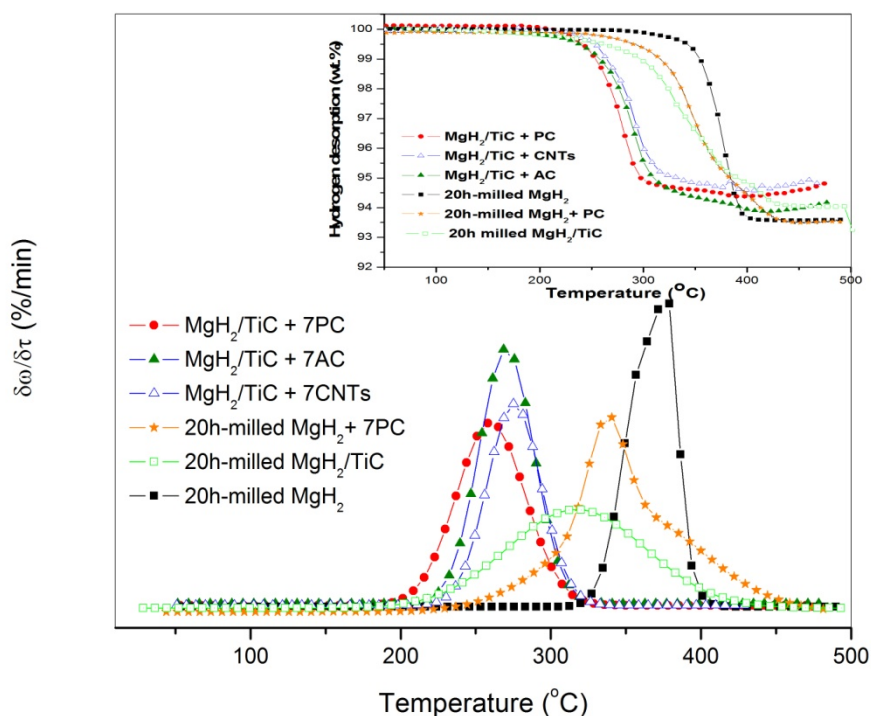
Figure 6-10 TG-DTG curves of MgH$_2$/TiC + 7PC, MgH$_2$/TiC + 7CNTs, MgH$_2$/TiC + 7AC, and 20h milled MgH$_2$+7PC
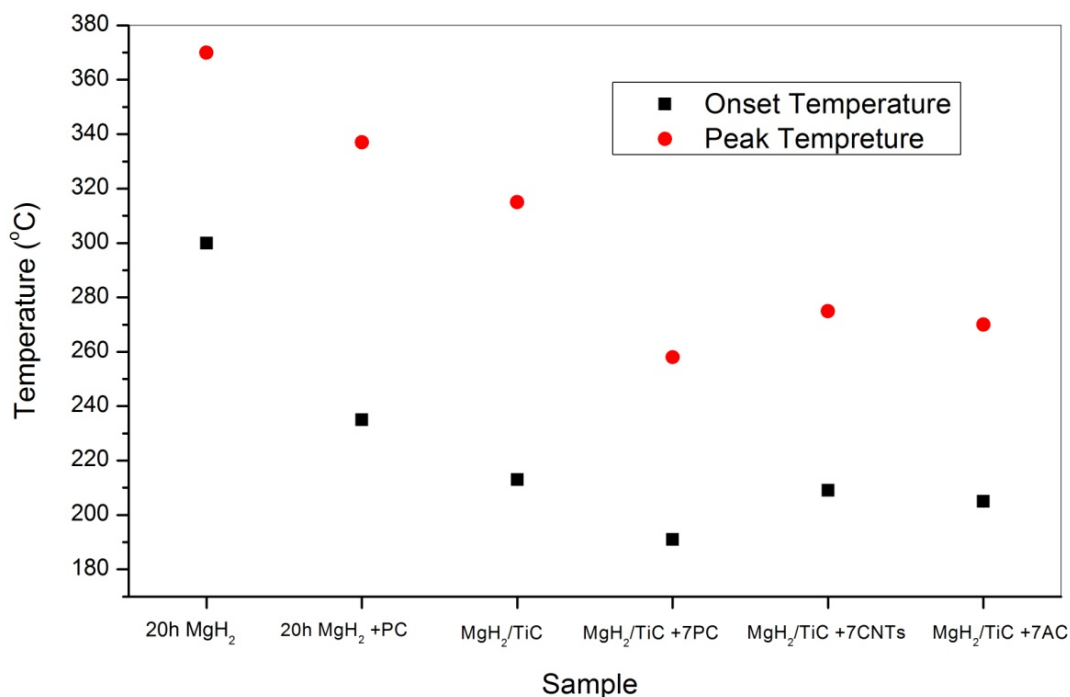
Figure 6-11 Dehydrogenation of onset and peak temperature of MgH_2/TiC + 7PC, MgH_2/TiC + 7CNTs, MgH_2/TiC + 7AC, and 20h milled MgH_2+7PC.
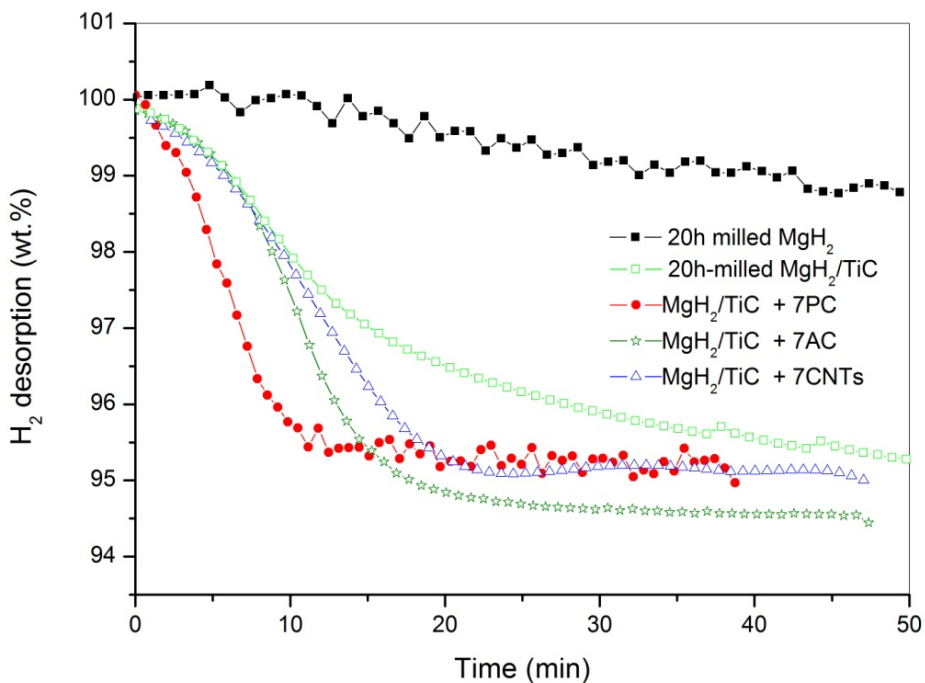
Figure 6-12 Hydrogen desorption kinetics of 20h-milled MgH_2/TiC + 7 PC, MgH_2/TiC + 7CNTs and MgH_2/TiC + 7AC at 250 °C within 10 kPa helium.

Hydrogen desorption kinetics also demonstrates this improvements. Figure 6-12 shows the hydrogen desorption kinetics of the composites at 250 °C. It was observed that the 20h-milled MgH$_2$/TiC needs 22 min to release about 3.7 wt.% H$_2$, whereas by adding PC, AC and CNTs additives, the hydrogen desorption can reach to 4.6 wt.% H$_2$ in 11 min, 15 min and 18 min, respectively. Therefore, three various carbon materials demonstrated prominent advantage in reducing the dehydrogenation temperature of 20h-milled MgH$_2$/TiC, and the PC shows the most promising effect on improving the dehydrogenation kinetics.

The grain size and particle size are not the key factors that are responsible for the improved dehydrogenation kinetics of 20 h-milled MgH$_2$/TiC because either grain size or particle size has not been changed during milling with varied carbon structures for 30 min, from TEM images Figure 6-9. Here, the possible reason is that the effects of three different carbon structures on the dehydrogenation of MgH$_2$/TiC system. First of all, the influence of carbon additives on the hydrogen desorption benefits from the dispersion effect of carbon and the facilitation of hydrogen diffusion. The TEM images show that the MgH$_2$/TiC particles are dispersed most evenly on graphite sheets of PC compared to AC and CNTs. PC shows the most promising effect on MgH$_2$ dehydrogenation. Thus all the carbon additives, including PC, AC and CNTs, show the positive effect on hydrogen desorption of MgH$_2$. Secondly, because the porous carbon nanoparticles could transfer hydrogen atoms or molecules from/to Mg, which may also provide additional diffusion channels for diffusion of hydrogen atoms and improve the hydrogen sorption kinetics [11, 311].

Apart from the dispersion effect and the additional hydrogen diffusion channels of carbon additives, the effect of plasma carbon materials on improving the reversible hydrogen desorption and absorption of 20 h milled MgH$_2$/TiC has been explained by the 'spillover' effect in the section 3.1. It is found that the doping on the ACs can enhance the hydrogen 'spillover' but is less effective than that on the graphene [322]. More transparent graphene structure of PC can be seen from the TEM images Figure 6-9b and c than AC and CNTs. An important feature of the stacked graphene layers in PC is in the presence of a 2D electron system (formed by π electrons) on their 'surface'[323]. Presence of the 2D negative electron charges creates favorable conditions for the spill-over of monatomic hydrogen carrying an effective positive charge [306]. A possibility for the improvements of hydrogen sorption

performances of the Mg-C materials via a H spill-over mechanism was also pointed out by Wu and Cheng [323]. Thus, PC as an additive has a pronounced effect on improving hydrogen storage properties of MgH$_2$ with and without TiC

Many researchers have reported that the combination of carbon with transition metals leads to synergetic effects on improving the hydrogen storage properties of magnesium hydride [18, 20, 323-325]. Our previous work [294, 297] indicated that TiC is a very effective catalyst on de-/rehydrogenation of MgH$_2$. It is found that TiC is a very catalyst upon dehydrogenation reactions. PC also shows a promising effect on improving dehydrogenation temperature of MgH$_2$ without TiC. 20 h milled MgH$_2$/TiC milling with PC has the lowest desorption onset and peak temperature (Figure 6-11). Thus there is an interaction between TiC and carbon additives, especially PC. The co-catalytic effect for dehydrogenation may be understood as a spillover mechanism through the interaction of facile π-electrons of carbon with the catalyst TiC. Similarly, the metallic catalysts promote recombination of H atoms during dehydrogenation: the improved rates of decomposition of MgH$_2$ ball milled with CNFs and MWCNTs with metallic impurities (Fe, Ni) were observed by Lillo-Rodenas et al.[326].

6.4 Conclusions

The effects of milling time and content of PC on the hydrogen storage properties of (MgH$_2$/TiC + PC) composite were investigated using a central composite design. The regression coefficients of polynomial of the responses showed that models can well evaluate the onset desorption temperature and rehydrogenation rate of (MgH$_2$/TiC + PC) composite. The optimal experimental conditions were obtained as: 7 wt% PC milling with 20h-milled MgH$_2$/TiC for 30 min co-milling, the predicted and experimental values of onset desorption temperature are 191 and 174.68 °C, and the predicted and experimental values of rehydrogenation rate is 0.1328 and 0.1261 °C/min.

To compare the effects of different carbon structures, other carbon materials, activated carbon (AC) and carbon nanotubes (CNTs) were employed to the MgH$_2$/TiC + 7 C system with the

optimal conditions of 7 wt. % carbon additive co-milling with the 20 h milled MgH$_2$/TiC for 30 min. Our results suggest that all carbon additives, including PC, AC and CNTs have positive effects on dehydrogenation properties of MgH$_2$/TiC due to dispersion effect of carbon and facilitating the hydrogen atoms diffusion.

PC has the most promising effects on reducing dehydrogenation temperature down to 184 °C and improving the dehydrogenation kinetics of MgH$_2$/TiC. The TEM images show that the MgH$_2$/TiC particles are dispersed most evenly on graphite sheets of PC compared to AC and CNTs. Another possible reason can be explained by H spill-over mechanism of Mg-C materials due to the stacked graphene layers existing in PC. Finally, TiC is still a good catalyst for enhancing the de-/rehydrogenation kinetics even when carbon material is added. The synergetic role of the metallic catalyst and carbon additives achieves better hydrogen storage performance.

7

MgO AND MgO/PLASMA CARBON FOR CO$_2$ CAPTURE AND CO$_2$/H$_2$ SEPARATION

7.1   Introduction

Climate change resulting from the emission of greenhouse gases, especially CO_2, has become a widespread concern in recent years, thus there exists an urgent need to develop methods for CO_2 capture and storage from large point sources such as power plants. Depending on different plant configurations, CO_2 emissions from thermal power plant flue gas can be reduced by three methods: pre-combustion capture, post-combustion capture and oxyfuel combustion [327]. Among the three methods, pre-combustion capture, i.e., fuel gasification followed by the shifted-syngas reaction to yield hydrogen, could become the technology of choice for new-build power plants. A mixture mainly consisting of CO_2 and H_2 is obtained as the gas stream to be processed, with minor quantities of H_2O and N_2 and some other impurities such as CO and H_2S [328]. Large-scale high-purity H_2 is generally produced by pressure-swing adsorption of the shifted syngas. The target of the separation process is to remove CO_2 from the gas mixture and transport it to a storage location. The high

concentrations (~20-40%) of CO_2 in the feed stream as well as its pressure of ~1000 – 1500 kPa is beneficial for an adsorption-based separation process where adsorbent regeneration is performed by a pressure swing.

Consequently, much effort has been made over the last decade to develop various chemical and physical methods for CO_2 capture and separation [327, 329, 330]. Among these approaches, porous or nanosized solid adsorbents have been widely investigated as a medium for CO_2 capture and separation, as researchers attempt to exploit their large accessible surface areas and large pore volumes. Various amines compounds [331-333], metal oxides [91, 334], amine containing polymers [335], zeolites [336] and porous carbons [86, 337] are identified as efficient CO_2 capture sorbents.

Porous carbon materials have been actively considered as CO_2 sorbent, due to their highly developed porosity, extended surface area, surface chemistry, and thermal stability [338]. Previous studies have been carried out on the use of activated carbons, carbon fibers, carbon molecular sieves, carbon nanotubes, and graphite nanofibers as adsorbents for CO_2 capture [86, 89, 337, 339]. Porous carbons also have high selectivity for CO_2, which is strongly retained while H_2 is retained less or not at all on these materials.

In addition to the physical adsorption of porous carbon, a chemisorption involving a chemical activation between a substrate and CO_2 may play an important role. Metal oxides (such as CaO and MgO) are promising capture materials given their ability to retain high adsorption capacities at temperatures above 300°C. Sorbents consisting of MgO loaded on Al_2O_3 can be prepared by impregnation, and their CO_2 adsorption capacities reach 42 and 60 mg/g in the absence and presence of water vapor, respectively [81]. Other MgO-based sorbents are prepared by modification of dolomite for CO_2 removal in syngas at high temperature (300-450 °C) and high pressure (20 atm). Their capacity achieves 102-117 mg/g [93]. An adsorption capacity of 80 mg/g CO_2 is reported over mesoporous MgO synthesized from rice husk ash [92]. Although MgO shows high CO_2 adsorption capacity, it requires regeneration temperature greater than 450 °C.

Carbon sorbents loaded with chemicals are typically produced through impregnation of activated carbon with suitable organic or inorganic compounds, carefully selected for specific

applications, such as CO_2 capture or CO_2/H_2 gas mixture selection. For example, highly efficient removal of acid gases such as SO_2 and CO_2 is exhibited by porous carbons loaded with bases like NaOH, KOH, or K_2CO_3 [340]. Alternatively to impregnation, carbon adsorbents loaded with additives can be prepared by blending methods, consisting of thermal treatment of a carbon precursor with a precursor of the additives. Bhagiyalakshmi et al. [35] synthesized an ordered mesoporous carbon supported MgO (MgO-OMC) material that has a CO_2 adsorption capacity of 92 mg/g at 25 °C and is regenerable at 200 °C.

The evaluation of suitable adsorbents for selective removal of CO_2 from CO_2/H_2 gas mixture requires reliable and extensive adsorption equilibrium data for the pure components. The results that can be obtained from adsorption process simulators are strongly dependent on the model used for predicting the mixed-gas adsorption equilibria [341]. Recently, adsorption isotherms of CO_2, N_2, and H_2 on an activated carbon have been applied to a pre-combustion CO_2 capture process, and experimental adsorption data of binary mixtures of CO_2/H_2 and CO_2/N_2 have been reported for model validation purposes [328, 342, 343].

One of the objectives of the present work was to develop a new reversible solid sorbent for use in CO_2 adsorption and separation at low temperature. Magnesium oxide nanoparticles were synthesized by two different methods: by high energy ball milling and by a chemical method. The modified plasma carbon (PC) was mixed with MgO by the ball milling and chemical coprecipitation methods, respectively, to form porous-carbon-supported MgO adsorbent. All samples were characterized by XRD, SEM and a porosity test. The CO_2 adsorption capacity of the synthesized MgO materials was examined using thermogravimetric analysis at 50 °C and 100 kPa CO_2 flow and regeneration was measured at 200 °C and 100 kPa He flow. The pure gas isotherms of CO_2 and H_2 on the MgO samples and MgO/PC samples were measured gravimetrically up to 1500 kPa at 25 °C. The dual-site Langmuir (DSL) isotherm model was used to fit the experimental data; the adsorption equilibria of a binary CO_2/H_2 mixture were estimated from the DSL model, based on the fitting parameters derived from the single gas adsorption isotherms.

7.2   Experimental methods

7.2.1 Synthesis of MgO samples

7.2.1.1   Mechanical Mill Method

The as-received MgO was mechanically milled for 60 h to refine the particle size. The product is referred to here as 60h-MgO. The 60h-MgO was further milled with the modified plasma carbon (Run 12 condition in Chapter 5) for another 60 min, and the product is here identified as 60h-MgO/PC. The weight ratio of 60h-MgO to the modified plasma carbon was 1:10.

7.2.1.2   Chemical Methods

(1) Magnesium oxide: 10 wt% aqueous NaOH solution was slowly added to 10 wt% Mg(NO$_3$)$_2$ solution with vigorous stirring at 25 °C. The precipitate was aged for 3 h, then filtered and washed thoroughly with distilled water until the pH of the filtrate solution was neutral. The filter cake was dried in an oven at 120 °C for 12 h and subsequently calcined either at 600 °C or 800 °C, for 5h in flowing N$_2$ at 80 ml/min, the calcined products being referred to as MgO-600 and MgO-800, respectively.

(2) MgO-Plasma carbon: Modified plasma carbon was added to 10 wt% Mg(NO$_3$)$_2$ solution with stirring and 10 wt% aqueous NaOH solution was slowly added to the mixed solution with stirring at 25 °C. The product was aged for 3h. The weight ratio of modified plasma carbon to MgO was 1:10. This was filtered and washed thoroughly with distilled water until the pH of the filtrate solution was neutral. The filter cake was dried in an oven at 120 °C for 12 h and subsequently calcined at 800 °C for 5h in flowing N$_2$. This product is here identified as MgO/PC-800.

7.2.2 Materials characterization

The BET surface area and porosity of each sample were determined from N$_2$ isotherm at 77 K using a Quantachrome AUTOSORB-1surface area/pore size analyzer, which have been explained in Section 3.3 of Chapter 3. The cleaned carbon samples were degassed for 8 h at 300 °C to remove any moisture or adsorbed contaminants presented on their surfaces. The manufacturer's software calculates the BET surface area of the sample by applying the BET equation to the adsorption data. The pore size distribution was evaluated by a density functional theory (DFT) method [251, 252].

The morphology of the powder mixtures was characterized by a JEOL 6300 scanning electron microscope (SEM). X-ray diffraction (XRD) was performed using a Thermo ARL (US) XTra diffractometer with Cu Kα radiation.

7.2.3 Gas adsorption measurements

Thermogravimetric analyses were carried out using an Intelligent Gravimetric Analyzer (IGA-003, Hidden Isochem Ltd.). The CO$_2$ adsorption/desorption and CO$_2$/H$_2$ mixture gases selective measurements were also performed using the thermogravimetric analyses. The initial activation of the samples was carried out from room temperature to 500°C under 100 kPa He pressure at a heating rate of 10°C/min and He flow rate of 100 ml/min. The adsorption and desorption runs were conducted using high purity CO$_2$ (99.999%) gas and He flow, respectively. The adsorption runs were conducted at 50 °C under atmospheric pressure, and desorption at 200 °C. Buoyancy correction (details as seen in Chapter 3) has been performed from the measured data to obtain the accurate adsorbate mass.

7.2.4 Gas adsorption equilibrium model

7.2.4.1 Pure gas adsorption

The experimental data of adsorption isotherms of the pure gases CO$_2$ and H$_2$ were correlated with the dual-site Langmuir (DSL) isotherm models, Equation 34 [328]. The single gas DSL model based on the Langmuir equation has four parameters (q_{s1}, q_{s2}, b_1, and b_2) describing

the adsorption of a pure component on a heterogeneous adsorbent that is composed of two homogeneous but energetically different sites [342-345].

$$q = \frac{q_{s1}b_1P}{1 + b_1P} + \frac{q_{s2}b_2P}{1 + b_2P}$$

Equation 34

where q is the absorbed amount, P is pressure, q_{s1} and q_{s2} are the saturation capacities at site 1 and 2, respectively, so the total saturation capacity is the sum of those on each site ($q_s = q_{s1} + q_{s2}$); b_1 and b_2 are the affinity parameters or free energy for site 1 and 2, respectively, which are considered to be temperature-dependent as expressed in Equation 35, where the subscript j represents the free energy level of site 1 or 2, at which $b_{o,j}$ are the pre-exponential factors or adsorption entropies, and E_j is their corresponding adsorption energies. In this formulation, $j = 1$ always denotes the higher adsorbate-adsorbent free energy and $j = 2$ always denotes the lower adsorbate-adsorbent free energy. For single-gas adsorption, this always makes the free energy of site 1 higher than that of site 2. However, for mixed-gas adsorption these two free energies are free to be assigned to either site 1 or site 2, as explained below.

$$b_j = b_{0,j} \, exp\left(\frac{E_j}{RT}\right) \quad j = 1,2$$

Equation 35

Fitting of the models to the experimental data was done with the OriginLab 8.0, and the values of the different fitting parameters were found by minimizing the sum of the standard deviations. How well the model approximates real data points was determined statistically by the adjusted R^2. The closer the $Adj\text{-}R^2$ is to 1, the better the model fits the experimental data, and the less the difference between the predicted and observed values.

7.2.4.2   Binary gases CO_2/H_2 adsorption

Successful prediction of the adsorption equilibria of binary gases relies on an accurate measurement of pure gas adsorption data and on a reliable correlation of these data with an isotherm model. Using the pure gas isotherm parameters, adsorption equilibrium of binary gases can be predicted by extending the corresponding pure gas equations to the case of binary gases.

The extension of Equation 34 to a binary system is straightforward, as shown by Myers [99]. Because there are two sites that each component adsorbs on, it is obvious that four different adsorbate-adsorbent free energies exist: two free energies for component A and two free energies for component B. The energetic site matching concepts have been discussed by other researchers [328, 342, 343, 346].

When components A and B obey the perfect positive (PP) correlation for energetic site matching, the corresponding extended DSL equations are given by

Equation 36

$$q_A = \frac{q_{s1,A}b_{1,A}y_A P}{1 + b_{1,A}y_A P + b_{1,B}y_B P} + \frac{q_{s2,A}b_{2,A}y_A P}{1 + b_{2,A}y_A P + b_{2,B}y_B P}$$

Equation 37

$$q_B = \frac{q_{s1,B}b_{1,B}y_B P}{1 + b_{1,A}y_A P + b_{1,B}y_B P} + \frac{q_{s2,A}b_{2,B}y_B P}{1 + b_{2,A}y_A P + b_{2,B}y_B P}$$

In contrast, when components A and B obey the perfect negative (PN) correlation for energetic site matching, the corresponding amount adsorbed for each component is given by

Equation 38

$$q_A = \frac{q_{s1,A}b_{1,A}y_A P}{1 + b_{1,A}y_A P + b_{2,B}y_B P} + \frac{q_{s2,A}b_{2,A}y_A P}{1 + b_{2,A}y_A P + b_{1,B}y_B P}$$

Equation 39

$$q_B = \frac{q_{s1,B}b_{1,B}y_B P}{1 + b_{2,A}y_A P + b_{1,B}y_B P} + \frac{q_{s2,B}b_{2,B}y_B P}{1 + b_{1,A}y_A P + b_{2,B}y_B P}$$

where y_A and y_B are the gas-phase mole fractions of components A and B and q_A and q_B are the adsorbed amounts of components A and B from a binary gas mixture.

7.3   Results

7.3.1 Characterization of MgO samples

Figure 7-1 and Figure 7-2 show the XRD patterns of the as-received MgO, milled MgO and chemically synthesized MgO samples. All the diffraction peaks at around 37°, 43°, 62°, 75° and 79° can be indexed to a face-centered cubic phase of MgO. The phase Fe in Figure 7-1 is an impurity from the milling vessel or milling balls during extended milling process. The peak at around 26° is assigned to the (002) diffraction of the graphitic structures.

The morphology and size of the samples are analyzed by SEM observation, shown in Figure 7-3. From Figure 7-3a, it can be seen that the as-received MgO particles with irregular morphology exhibit a wide distribution in the size range of microns. The size of most particles is less than 5 μm. However, the size of a small amount of the particles is larger than 10 μm. This suggests that particle aggregation is taking place. In order to further refine the powders, ball milling experiments were conducted. Figure 7-3b shows the SEM images of the MgO powder milled for 60 hours. The particle size of the 60h-MgO has clearly decreased, the average particle size is 100±60 nm. More homogeneous spherical particles of 60h-MgO can be observed. The kind of agglomeration is relatively loose and can be dispersed after milling. The SEM/EDX results of 60h-MgO/PC (Table 7-1 S1 and S2) show that the MgO particles clustering with carbon is homogeneous and comprised uniform, worm-like carbon particles with a particle size of approximately 1 μm. From Figure 7-3d and e, it can be seen that the chemically synthesized MgO at 600 and 800 °C have similar morphology, showing regular spherical particles with an average particle size of 310±70 nm for MgO-600 and 360±80 nm for MgO-800, respectively. When introducing PC by the coprecipitation method, the MgO nanoparticles are interconnected with PC, as shown in Figure 7-3f. Table 7-1 summarizes the EDX analysis results of S3 and S4, showing that the Mg/C molar ratios detected from the random areas are similar. This result suggests a homogeneous distribution of MgO in the composites.
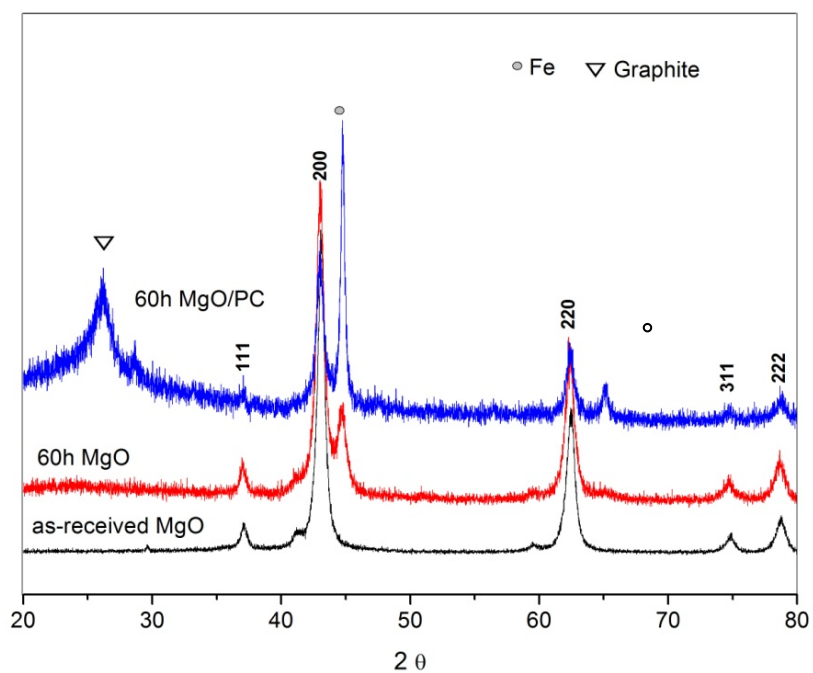
Figure 7-1 XRD patterns of as-received MgO, 60h-MgO and 60h-MgO/PC.
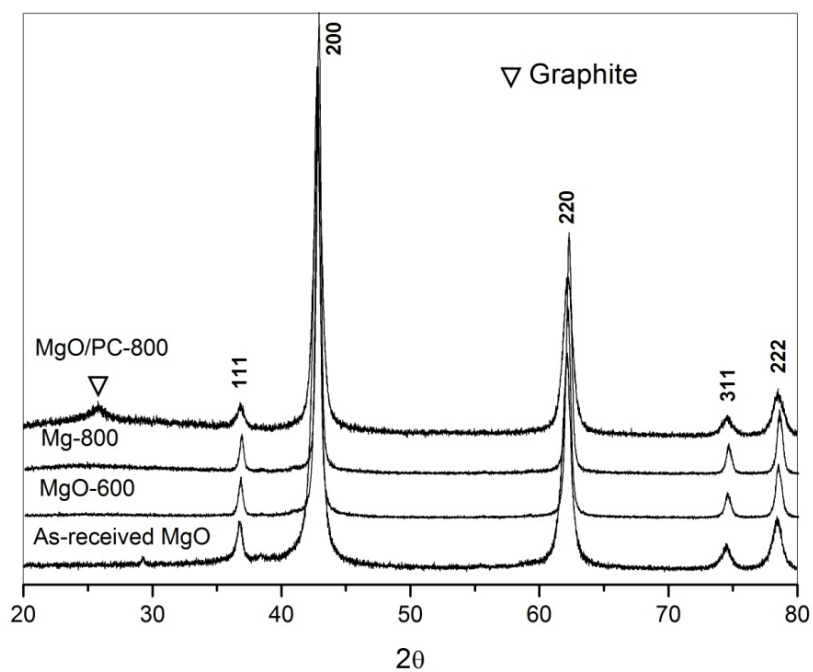
Figure 7-2 XRD patterns of as-received MgO, MgO-600, MgO-800 and MgO/PC-800
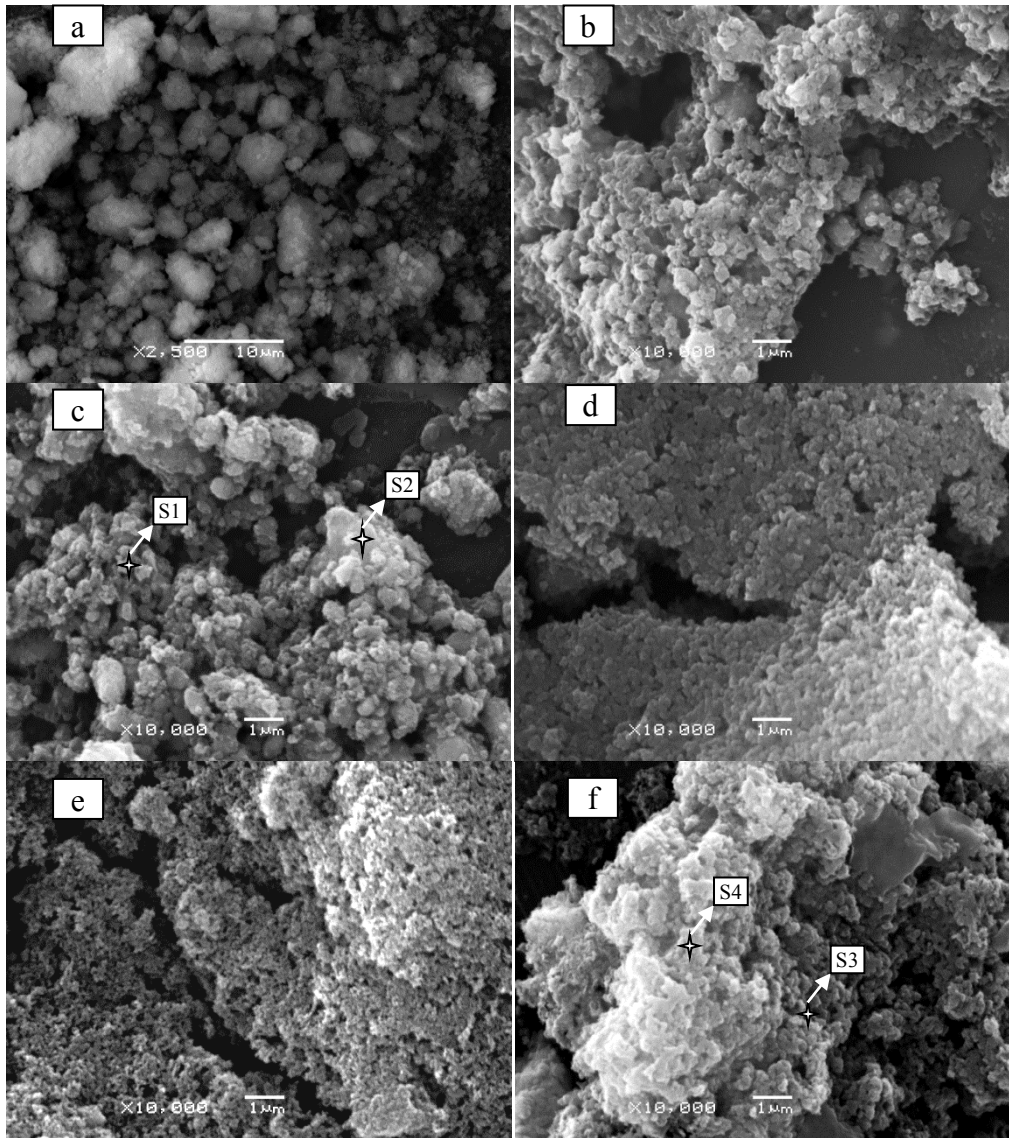
Figure 7-3 SEM images of (a) as-received MgO, (b) 60h-MgO, (c) 60h-MgO/PC, (d) MgO-600, (e) MgO-800, (f) MgO/PC-800.

Table 7-1 Element SEM/EDX analysis of S1 and S2 in Figure 7-4c, S3 and S4 in Figure 7-5f

	S1		S2		S3		S4	
	Wt. %	At. %	Wt. %	At. %	Wt.%	At. %	Wt.%	At. %
C	3.89	7.09	-	-	8.30	12.76	7.46	11.48
O	24.52	33.53	45.79	56.32	45.05	51.96	45.28	52.26
Mg	15.26	13.73	51.70	41.85	39.71	30.53	43.61	33.56
Al	56.32	45.65	2.51	1.83	6.94	4.74	3.95	2.70
Total	100	-	100	-	100	-	100	-

7.3.2 Surface area and pore size distribution

The N_2 isotherm curves for the adsorption and desorption on the surface of the as-received sample and all other synthesized samples are shown in Figure 7-6, Figure 7-7, and Figure 7-8. The values of the BET surface area, pore volumes and pore sizes are summarized in Table 7-2. According to *International Union of Pure and Applied Chemistry* (IUPAC) classification [272], N_2 isotherms for all synthesized MgO are of similar shape to be type IV isotherm, referring to Chapter 3 section 3.3, that indicates capillary condensation in slit-shaped mesopores. From Figure 7-6 and Table 7-2, the BET surface area decreases from 133 to 100 m^2/g on extended milling due to the destruction of the porous structure by high energy milling. With mixing of 60 h milled MgO and PC for further 60 min, the BET surface area of the obtained MgO/PC increases to 190 m^2/g due to incorporation of high BET surface area PC. The pure PC (Figure 7-8) is used as a reference in the following study of adsorption capacity; its isotherms also show representative type IV curves and its BET surface area is 350 m^2/g. For chemically synthesized MgO samples, the BET surface area increase to 151 and 142 m^2/g at heat treatment temperature of 600 and 800 °C, respectively.

The synthesis mechanism has been reported by Ling et al. and Przepiórski et al.[347, 348]. The following chemical reactions take place:

$$Mg^{2+} + 2OH^- \rightarrow Mg(OH)_2.$$ Reaction 1

$$Mg(OH)_2 \rightarrow MgO + H_2O$$ Reaction 2

When Mg ion and hydroxyl ion disperse equally in the solvent, each Mg^{2+} ion is octahedrally surrounded by six hydroxyl ions, forming octahedral $Mg(OH)_2$ (Reaction 1). The selected reaction temperature and the selected reaction time are crucial factors that lead to the nano scale morphology. When $Mg(OH)_2$ is heat-treated in air or a protection gas (Here, N_2 is used as the protection gas), Reaction 2 takes place: during the thermal decomposition process, the hydrogen bonds associated with two hydroxyl ions are partially broken, releasing some water molecules. Molecule-sized pores are generated when the H_2O molecules are released during heat treatment and the closed pores can be opened up by the gas flow. Meanwhile, small

MgO units are generated during this process. As a result, nanoparticles and mesopores coexist. The mesopores could provide abundant surface area, which results in the large BET surface area of MgO. A slight decrease in BET surface area with an increase of calcination temperature has been reported by other researchers to be due to an increase in crystallinity [34, 347].

Figure 7-9 and Figure 7-10 show the DFT pore size distribution from adsorption data for the samples. The pore size distribution reveals that as-received MgO contains mesopores with major half pore diameter at about 1.6 nm. After 60 h milling, the MgO shows a bimodal feature at around 0.9 nm and 1.5 nm, because extensive high energy milling reduces particle sizes, destroys the porous structures and causes agglomeration of nanoparticles. On blending 60h-MgO with PC for 60 min, the bimodal pore size distribution feature of 60h-MgO and PC was dispersed and the pore size was distributed at 1.20 nm due to homogeneous mixing.

The as-received MgO and synthesized MgO at 600 °C and 800 °C have a similar porosity (Figure 7-10). The average pore size of as-received MgO, MgO-600 and MgO-800 are 3.6, 2.6 and 7.3 nm, respectively. From Figure 7-10, it can be seen that more mesopores are generated at the calcination temperature of 800 °C comparing with the one at 600 °C due to the larger volume of pores at the half pore diameter of ~ 1.5 nm. Both BET surface area and the pore volume of MgO-800 can be improved by adding PC in the synthesis process, thus PC contributes to improving the porosity of the synthesized MgO.
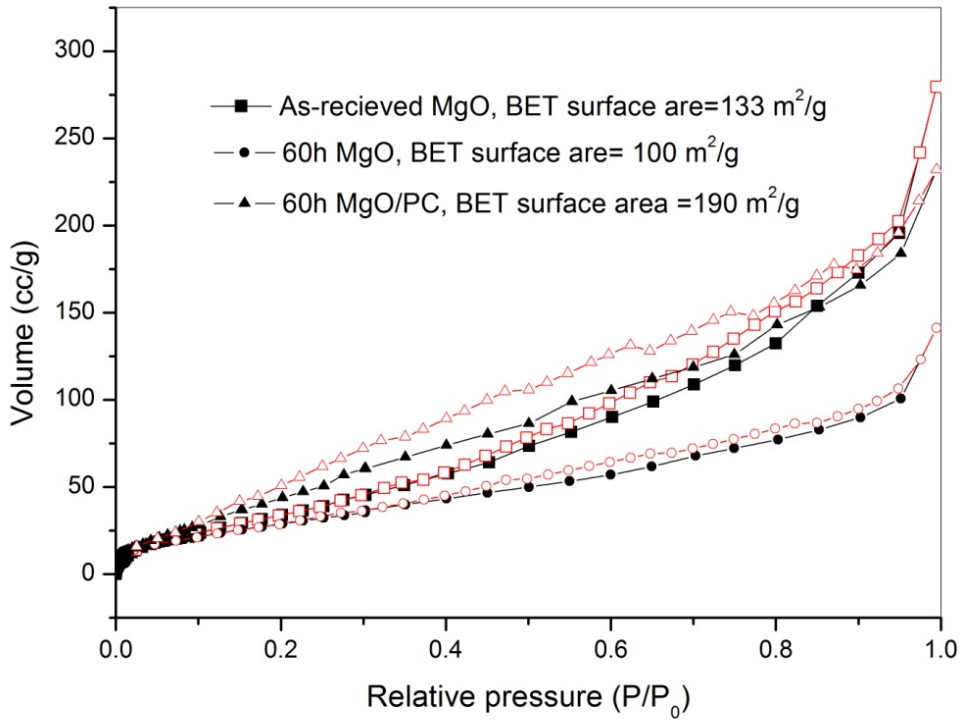
Figure 7-6 N$_2$ isotherms of as-received MgO, 60h-MgO and 60h-MgO/PC.
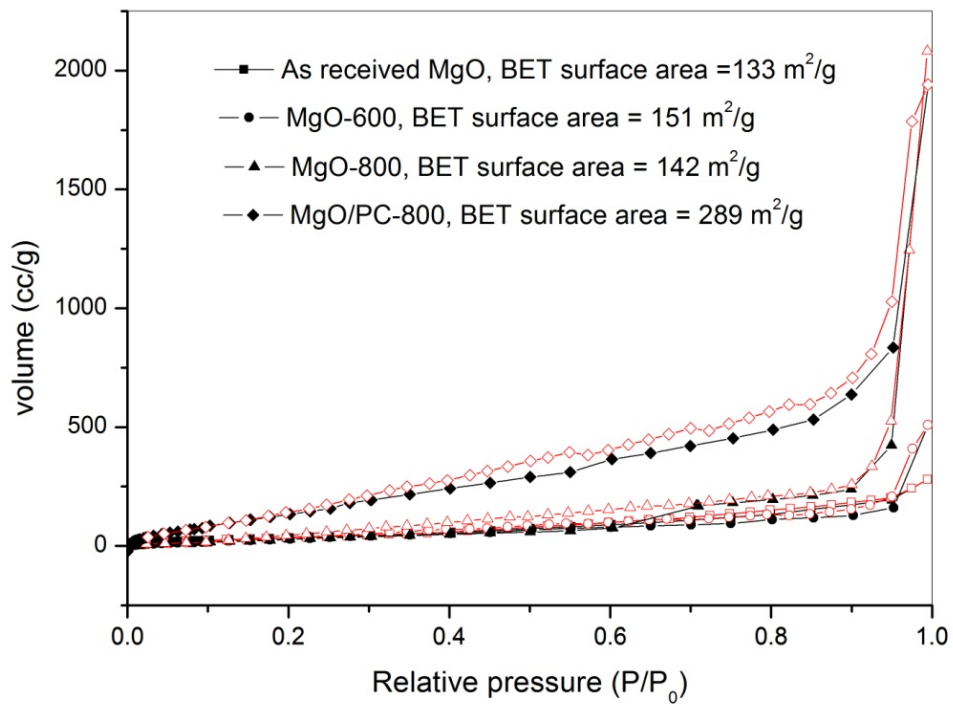
Figure 7-7 N$_2$ isotherms of as-received MgO, MgO-600 and MgO-800 at 77K.
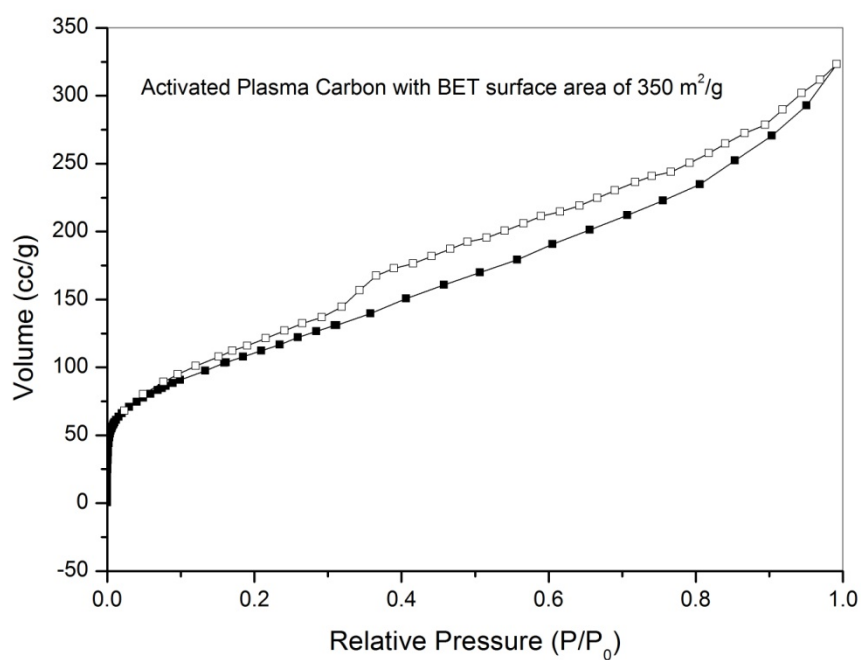
Figure 7-8 N$_2$ isotherm of the modified PC at 77K.
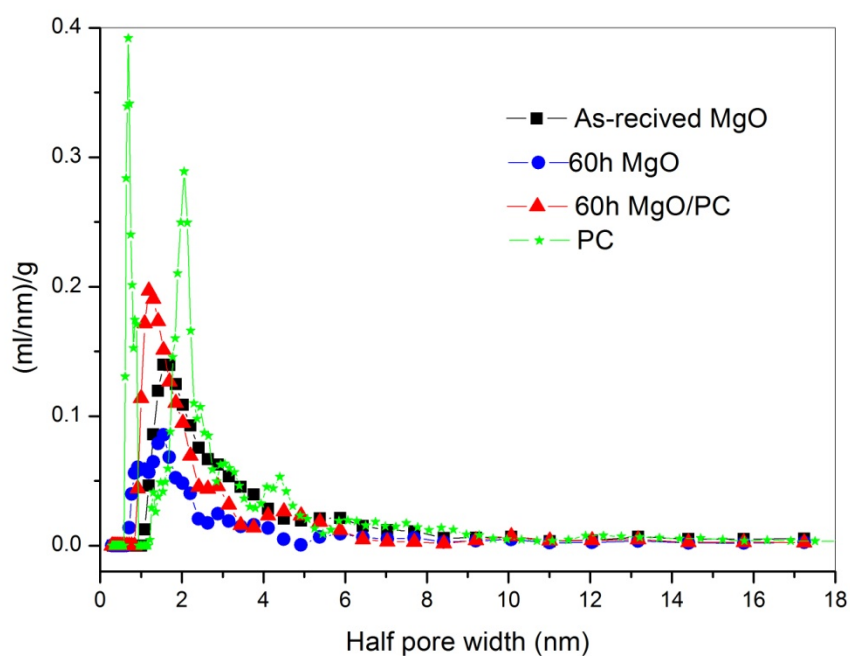
Figure 7-9 pore size distribution of as-received MgO, 60h-MgO, 60h-MgO/PC and PC by DFT method.
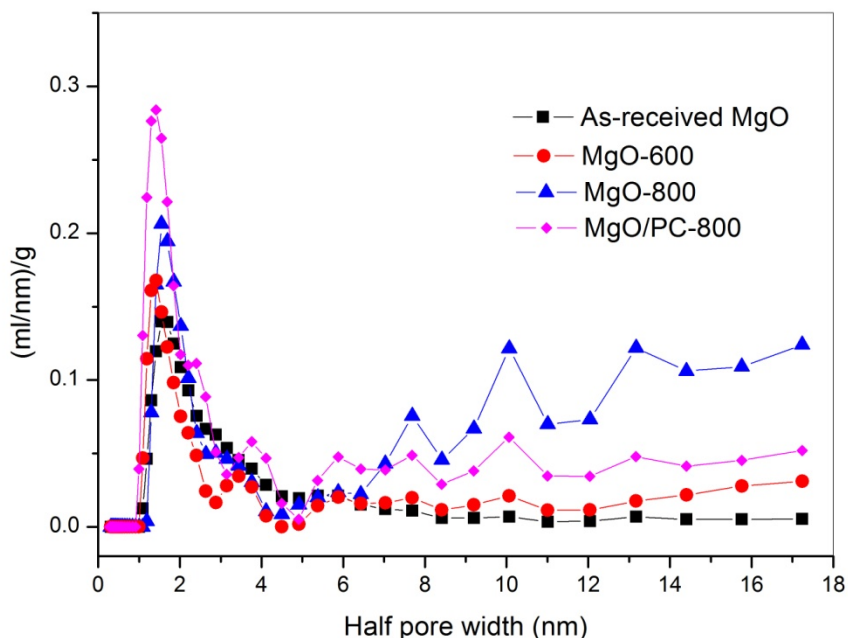
Figure 7-10 Pore sized distribution of as-received MgO, MgO-600, MgO-800 and MgO/PC-800 by DFT.

Table 7-2 BET surface area and pore size of all samples.

Sample	BET surface area (m^2/g)	Half pore width (nm)	Weight loss (wt.%)
As-received MgO	133	1.6	5.40
60h-MgO	100	0.9 and 1.5	3.84
60h-MgO/PC	190	1.2	7.04
MgO-600	151	1.5	2.54
MgO-800	142	1.5	3.24
MgO/PC-800	289	1.5	6.61
The modified PC	349	0.7 and 2.1	---

7.3.3 Thermogravimetric analysis

Due to the porous structure of the material, several impurities, such as moisture, SO_x, NO_x and CO_x, are efficiently physisorbed in the samples. Heat treatment is used to remove these impurities. Figure 7-11 shows the heat treatment up to 500°C under 100 kPa He flow, recorded by the thermogravimetry analysis. The weight loss of as-received MgO, 60h-MgO, 60h-MgO/PC, MgO-600, MgO-800 and MgO/PC-800 are 5.4 %, 3.84 %, 7.04 %, 2.54%, 3.24 % and 6.61%, respectively, which are obviously correlated to BET surface area, as shown in Table 7-2.
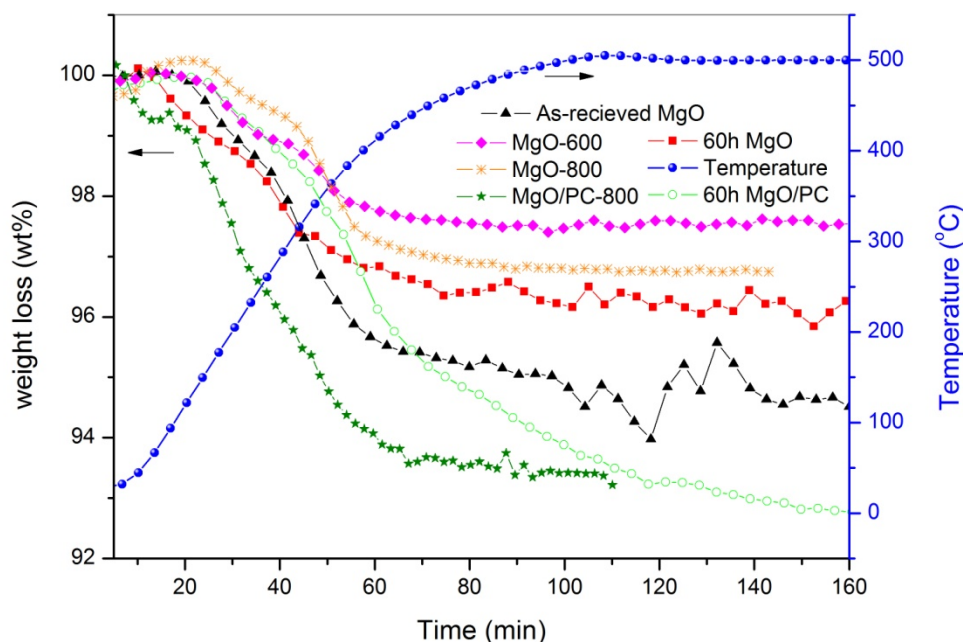
Figure 7-11 Activation of all materials from room temperature to 500 °C at 100 kPa He flow.

Thermogravimetric analysis is also employed to examine the capacity and stability of the MgO samples in capturing CO_2 gas from room temperature up to 500 °C at 100 kPa CO_2 gas flow. The result (Figure 7-12) shows that the as-received MgO, 60h-MgO, 60h-MgO/PC, MgO-600 and MgO-800 can absorb ~ 1.8, 1.6, 1.6, 1.8 and 4 wt% CO_2 at the adsorption temperature of 140 °C. It can be seen that higher calcination temperature has a positive effect on improving CO_2 adsorption capacity because high temperature (>800 °C) facilitates mesopores generation.

The CO_2 adsorption of the MgO samples reached a maximum at about 140 °C, after which desorption process started. At temperature higher than 300 °C, 60h-MgO and 60h-MgO/PC again absorbed CO_2 due to chemical absorption, as reported by Park et al. [349]. High energy ball milling facilitates nucleation by creating many defects on the surface and/or in the interior of the materials, or by the additive providing active sites for nucleation. It also shortens diffusion distances by reducing the effective particle size [350-353]. Thus the nano-scaled 60h-MgO and 60h-MgO/PC can chemically react with CO_2 at a relatively low temperature of about 300 °C, comparing with the normal reaction temperature of MgO and CO_2 of about 450 °C [78].

To determine whether CO_2 absorption between the room temperature and 140 °C is due to physical or chemical sorption, the MgO-600 and MgO-800 samples were kept at 50 °C and 100 kPa CO_2 flow for 120 min and then analyzed by XRD. The XRD results (Figure 7-13) show no new phase is formed after CO_2 adsorption, suggesting that the CO_2 adsorption at low temperature 50 °C is purely physical.
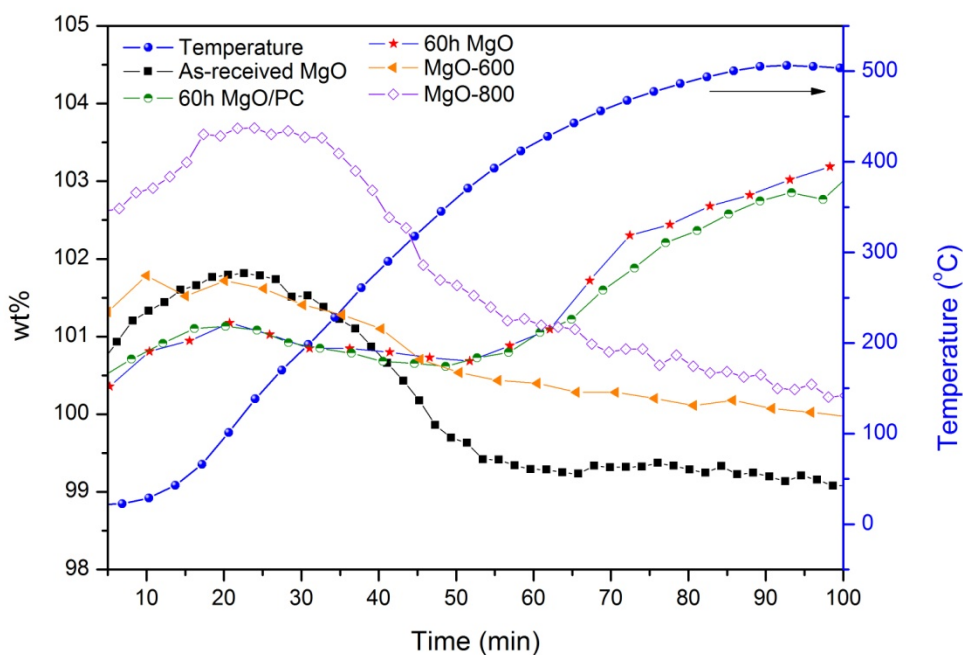
Figure 7-12 Thermogravimetry curves of as-received MgO, MgO-600 and MgO-800 from room temperature to 500 °C at 100 kPa CO_2 gas flow.
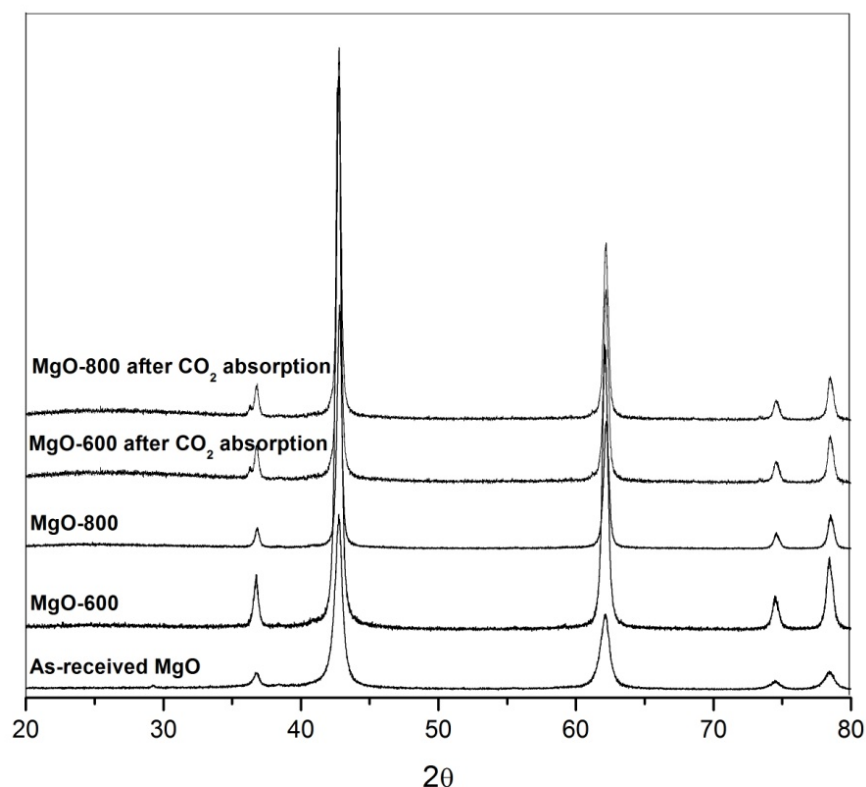
Figure 7-13 XRD patterns of the MgO samples before and after CO_2 absorption at 50 °C.

7.3.4 CO_2 storage

The CO_2 adsorption capacity of the synthesized MgO materials was examined using IGA (Figure 7-14). A temperature of 50 °C was chosen to model temperatures used in precombustion capture from fuel gas processes [88, 330]. Samples (15 mg) were kept at a constant temperature of 50 °C under 100 kPa CO_2 with a flow rate of 100 ml/min for absorption till reaching equilibrium, after which the gas was switched to pure He at a flow rate of 100 ml/min, while increasing the temperature to 200 °C for regeneration. This gave CO_2 absorption capacity at 50 °C, on as-received MgO, MgO-800 and MgO/PC-800 of 101.01, 101.42 and 102.04 wt%, respectively. At 200 °C complete regeneration occurred. It can be seen that the CO_2 absorption capacity correlates with the BET surface area: MgO/PC-800 with the largest surface area had the largest CO_2 absorption capacity. The BET surface area of MgO-800 is 142 m^2/g; slightly larger than that of the as-received MgO (133 m^2/g). This corresponds to the CO_2 capacity of MgO-800 and as-received MgO - 101.42 and 101.01 wt%, respectively. This response to CO_2 also correlated with BET surface area: MgO/PC-800

with the largest surface area of 289 m^2/g has the largest weight gain with CO_2. Gas adsorption was reversible and repeatable. It is reported that CO_2 adsorbed on the pure MgO can be regenerated at high temperature of > 450 °C, whereas CO_2 absorbed on our synthesized MgO samples was regenerated at 200 °C, this suggests that the CO_2 absorption of MgO-800 is weaker than the chemisorptions of CO_2 by the pure MgO reported in the reference [94].
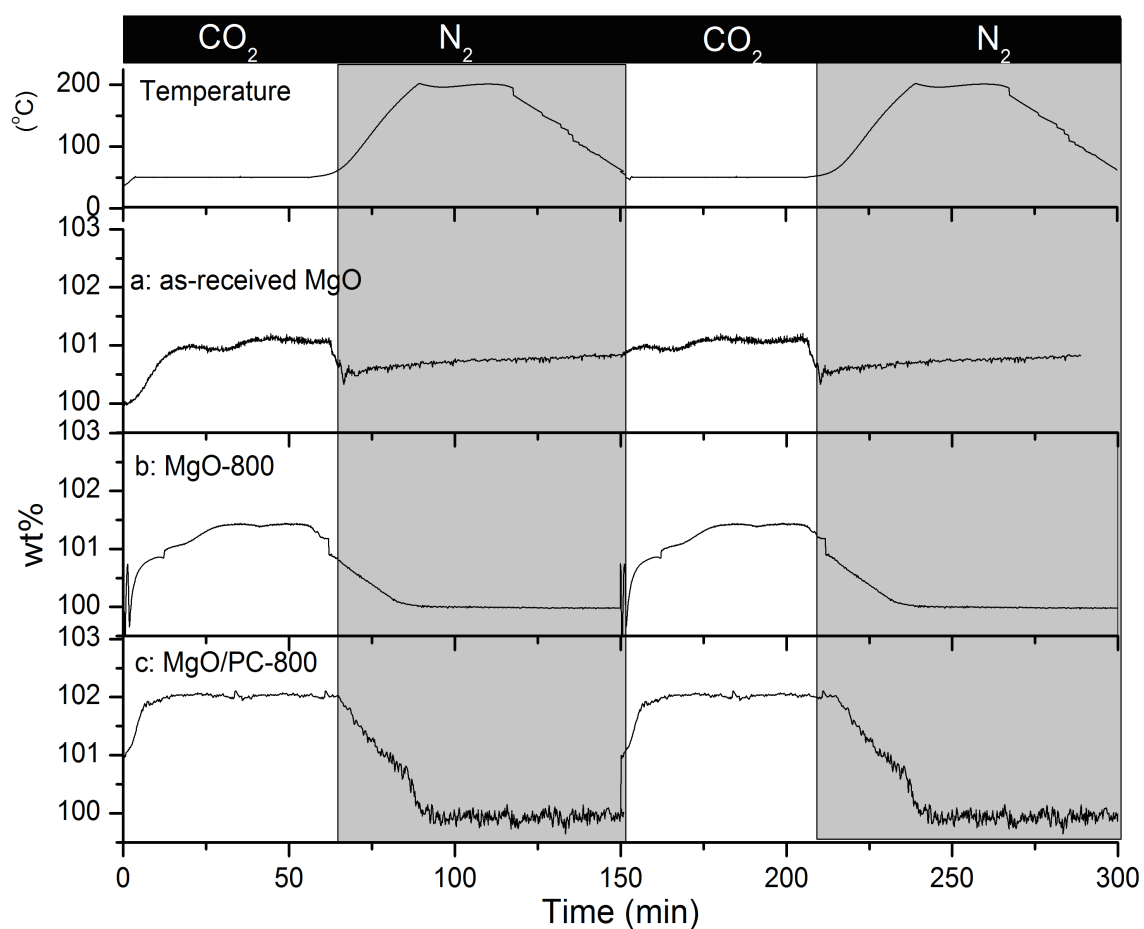
Figure 7-14 CO_2 absorption at 50 °C at 100 kPa CO_2 flow and desorption at 200 °C at 100 kPa N_2 flow: (a) as-received MgO, (b) MgO-800, and (c) MgO/PC-800

7.3.5 CO_2 and binary mixture CO_2/H_2 adsorption equilibria on synthesized MgO materials for CO_2 capture

7.3.5.1 Pure gas adsorption isotherm

The experimental absolute adsorption isotherms of pure CO_2 on the MgO samples and PC at 25 °C are shown in Figure 7-15 and Figure 7-16, which have been corrected by the buoyancy correction (section 3.4 in Chapter 37.2.4.1). The density of 1.28 g/cm^3 determined by helium isotherm at 77 K was used to calculate the CO_2 isotherm of MgO/PC-800. The theoretical density of MgO (3.58 g/cm^3) was used in buoyancy correction for the CO_2 isotherms of the as-received MgO, 60h-MgO and MgO-800. Figure 7-15 shows that the CO_2 storage capacity of MgO/PC-800 is up to 6.16 mmol/g at 25 °C and 1500 kPa CO_2 pressure. As-received MgO and MgO-800 both have the same CO_2 adsorption capacity of 2.1 mmol/g at 25 °C and 1500 kPa CO_2 pressure, because of their similar particle size and porosity, and similar crystalline structure. The 60h-MgO and 60h-MgO/PC have the much lower CO_2 adsorption capacities of 0.48 and 0.98 mmol/g, respectively, since the porous structure has been destroyed by high energy milling. Thus, it can be concluded that the high energy ball milling has a negative effect on the CO_2 storage capacity of MgO.

The high CO_2 capacity of MgO/PC-800 benefits from the addition of PC that can absorb about 13.7 mmol/g CO_2 at 25 °C and 1500 kPa CO_2 pressure (Figure 7-16). Bhagiyalakshmi et al. [35] found the mesoporous carbon supported MgO materials adsorbed CO_2 up to 92 mg/g at 25 °C at 100 kPa CO_2 and the mesoporous carbon improved the CO_2 storage capacity of MgO at room temperature. Also, Ma et al. [354] reported the combination of MgO nanoparticles and high surface area carbon materials ensures that the MgO/nanoporous carbon composites have high methanol adsorption capacity for vapor phase separation at 298 K. Therefore, it can be concluded that the introduction of PC improves the CO_2 adsorption capacity of the chemically synthesized MgO at 800 °C. Figure 7-17 shows the experimental H_2 isotherms of as-received MgO, MgO-800 and MgO/PC-800 at 25 °C. It can be seen that CO_2 always adsorbs more strongly than H_2 on all samples at 25 °C. Here, experimental results for the milled MgO samples are omitted due to their very low CO_2 absorption.
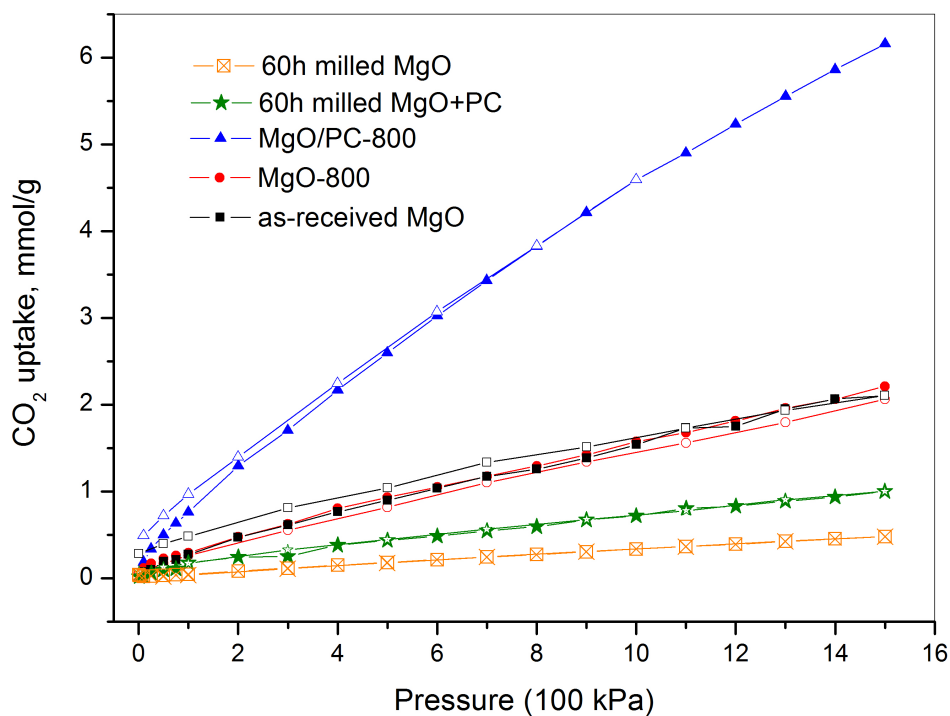
Figure 7-15 CO$_2$ isotherm of the synthesized MgO at 25 °C, the solid symbols are adsorption and the hollow symbols are desorption processes.
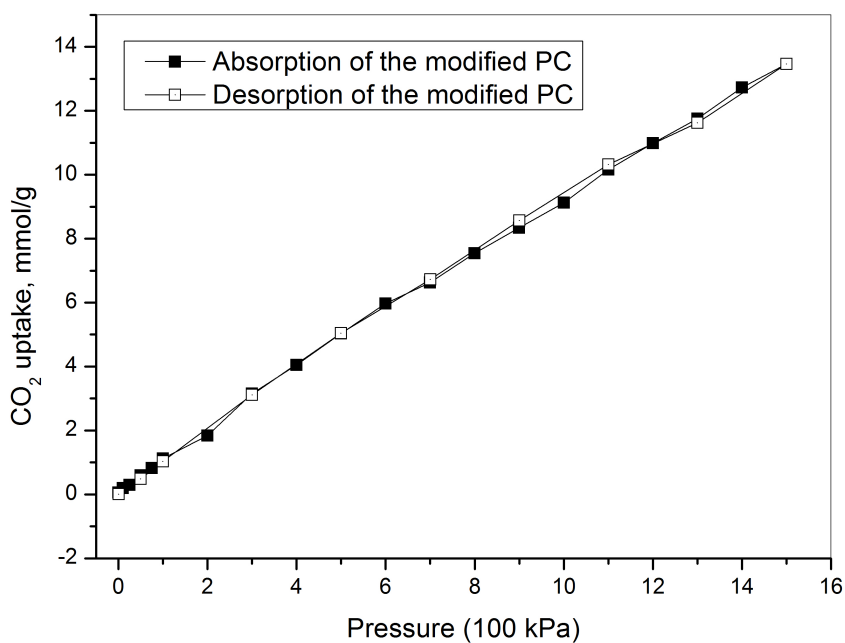
Figure 7-16 CO$_2$ isotherm of the modified PC at 25 °C, the solid symbols are adsorption and the hollow symbols are desorption processes.
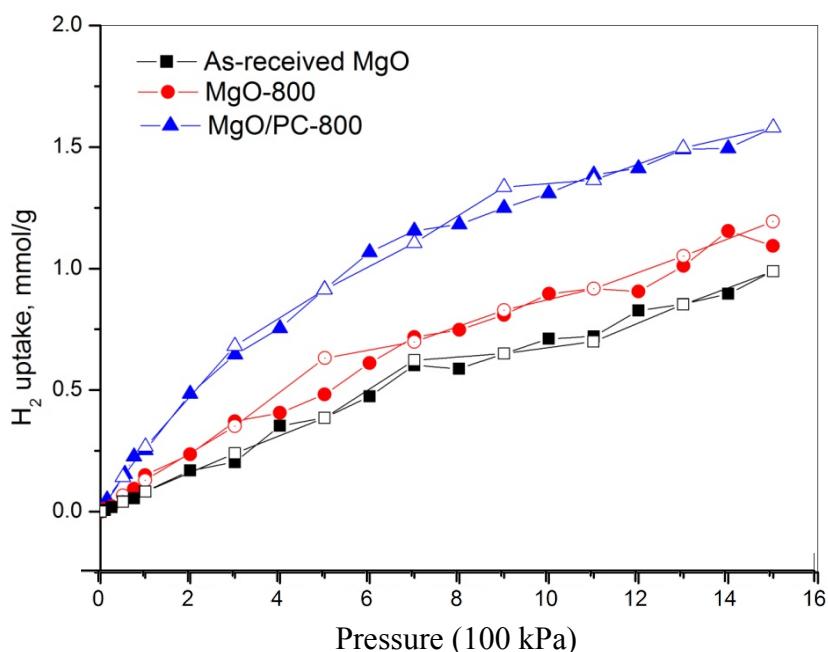
Figure 7-17 H_2 isotherms at 25 °C up to 1500 kPa, the solid symbols are adsorption and the hollow symbols are desorption processes.

7.3.5.2 *Pure gas adsorption equilibrium fitting*

Figure 7-18a shows the very good agreement between DSL fitting curves and the experimental data in predicting pure CO_2 adsorption on as-received MgO, MgO-800 and MgO/PC-800. The predictions from the DSL model are nearly identical with data over the entire adsorbed-phase loading range. Figure 7-18b also shows good agreement between the DSL model and experimental data in predicting pure H_2 adsorption. It is noted that H_2 is not only a light gas but also that it barely adsorbs on the MgO samples. This actually yields bad quality experimental data and gives a poor fit. The closer the Adj-R^2 is to 1, the better the model fits the experimental data and the less is the difference between the predicted and observed values. From Table 7-3, the values of Adj-R^2 are 0.9980, 0.9990, 0.9999, 0.9941, 0.9929 and 0.9979, indicating that the models are well fitted.
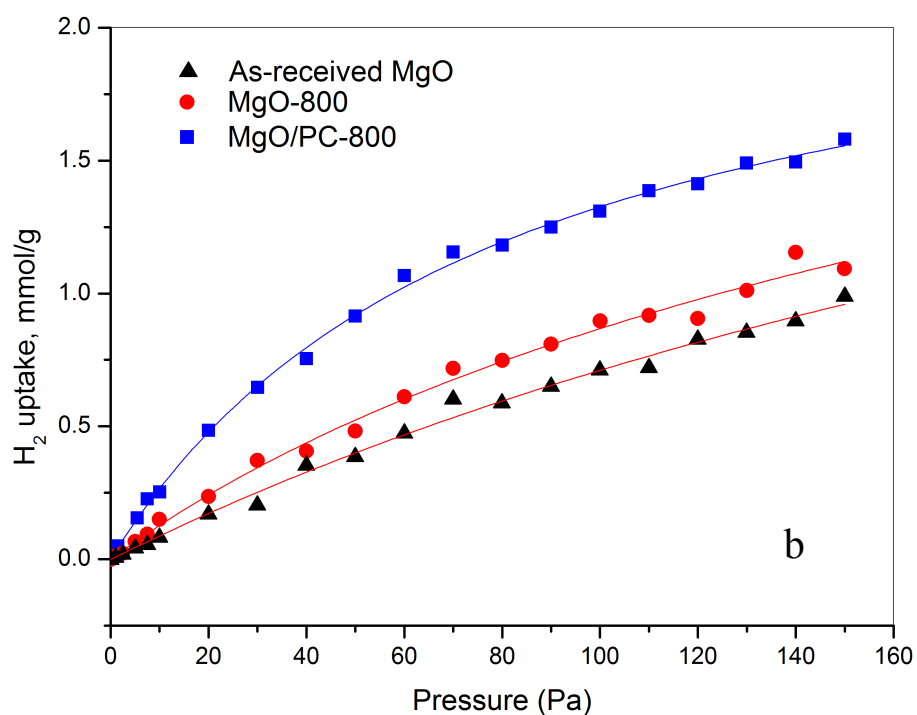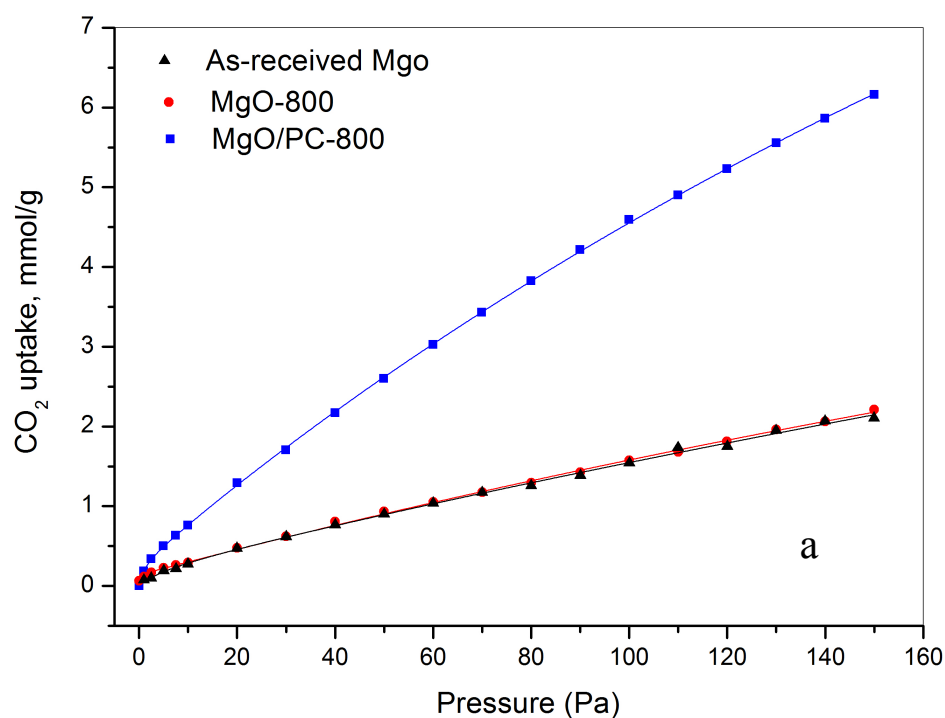
Figure 7-18 Fitting of pure CO$_2$ (a) and H$_2$ (b) adsorption isotherm on as-received MgO, MgO-800 and MgO/PC-800 with the dual-site Langmuir (DSL) equation at 25 °C. Symbols are absolute experimental data; lines: fitted DSL equation. Parameters values are given in Table 7-3.

Table 7-3 Isotherm fit parameters by DSL

Sample		Adj. R^2	q_{s1}	b_1	q_{s2}	b_2
CO_2 adsorption isotherm	As-received MgO	0.9980	17.91	8.05E-6	0.22	0.0018
	MgO-800	0.9990	12.30	1.32E-5	0.14	0.52
	MgO/PC-800	0.9999	24.12	2.16E-5	0.28	0.011
H_2 adsorption isotherm	As-received MgO	0.9941	3.19	2.87E-5	0	2.0E-4
	MgO-800	0.9929	2.57	3.40E-5	0.38	1.31E-4
	MgO/PC-800	0.9979	2.38	1.26E-4	0	1.9E-4

7.3.5.3 *Prediction of binary CO_2/H_2 adsorption equilibria*

The optimal parameters from the pure gas adsorption DSL models will be used for the dual gases adsorption prediction. The adsorption equilibria of binary CO_2/H_2 system are predicted from both the PP (Equation 36 and Equation 37) and PN (Equation 38 and Equation 39) forms of the extended DSL model using only the pure gas fitting parameters in Table 7-3. Figure 7-19 compares the binary CO_2/H_2 gases mixture's adsorption on the as-received MgO, MgO-800 and MgO/PC-800 predicted from the DSL model. From the Figure 7-19 PP (left) correlation results, the H_2 capacities of the as-received MgO, MgO-800 and MgO/PC-800 are about 1.3, 1 and 4.2 mmol/g at 1500 kPa pressure, which is much higher than the experimental pure H_2 capacities. Also the CO_2 adsorption amount is close to the H_2 adsorption amount under the PP model for the binary CO_2/H_2 system, and this is not correct because the CO_2 adsorption is much stronger than H_2 adsorption for all the MgO samples. The Figure 7-19 PN (right) correlation predictions are more reasonable compared with the pure gas experimental data than the PP correlation. Garcia et al. [328] also reported that the extended DSL model with the binary pairs CO_2-N_2 and CO_2-H_2 correlating with the PN prediction and the correlation for the binary pair N_2-H_2 being of PP form is the one that most accurately predicts the gas-mixture behavior. In the present work the PN form is employed for the CO_2/H_2 gas mixture isotherm prediction. Figure 7-20 shows the binary CO_2/H_2 adsorption equilibria at different proportions of CO_2 from the DSL model, PN form predictions at 1500 kPa and 25 °C. Here, the volume proportion of CO_2 in the CO_2/H_2 gas mixture is referred to as yCO_2. The CO_2 uptake and total uptake increase with an increasing proportion of CO_2 in the binary CO_2/H_2 gas mixture. When the ratio of CO_2 to H_2 reaches

80:20 vol.%, the MgO/PC-800 can absorb or separate 3.5 mmol/g CO_2 from the CO_2/H_2 mixture.
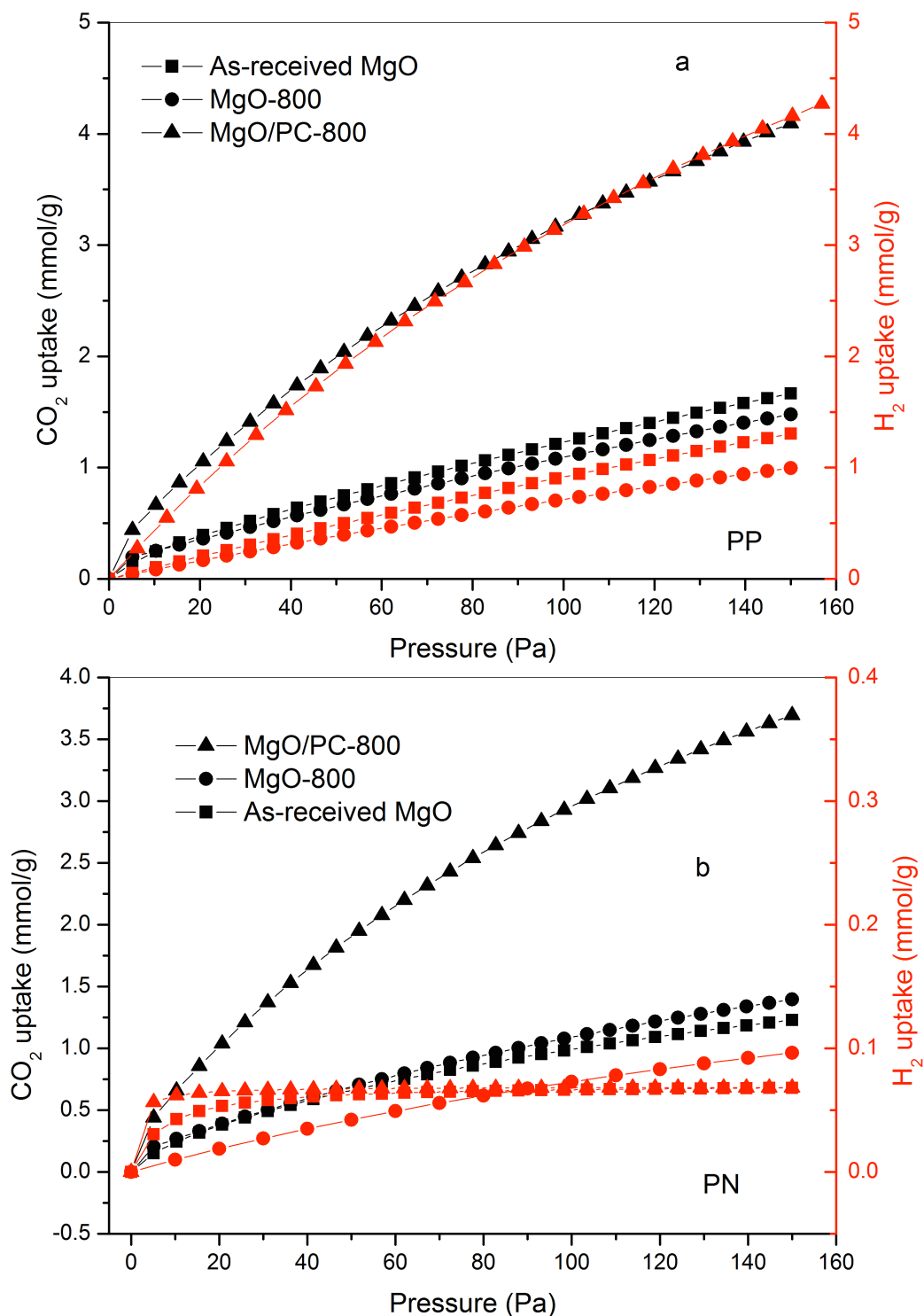
Figure 7-19 Component adsorbed amounts of a CO_2/H_2 gases mixture (80/20 vol. %) on as-received MgO, MgO-800 and MgO/PC-800 at 25 °C predicted from DSL model based on PP (a) and PN (b). Black patterns are CO_2 uptake, Blue patterns are H_2 uptake.
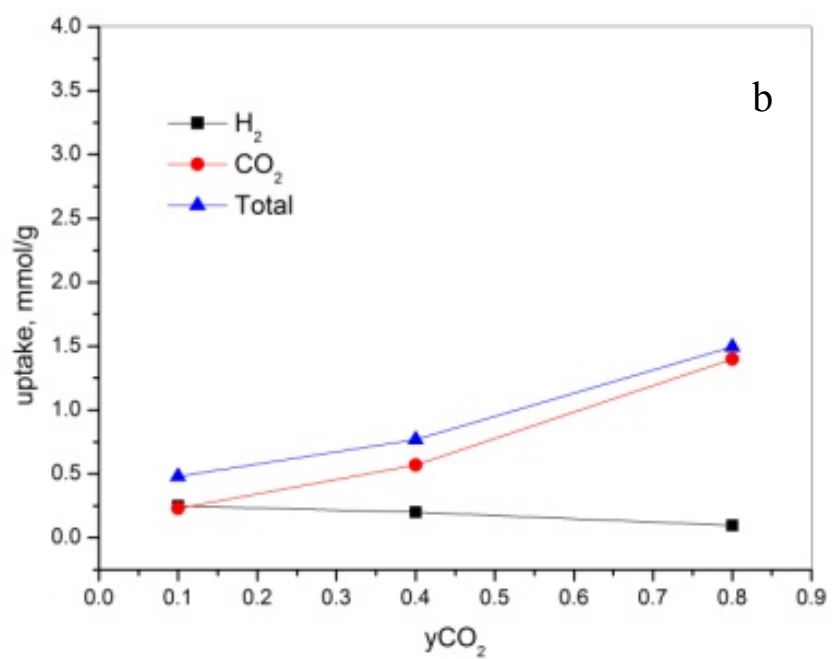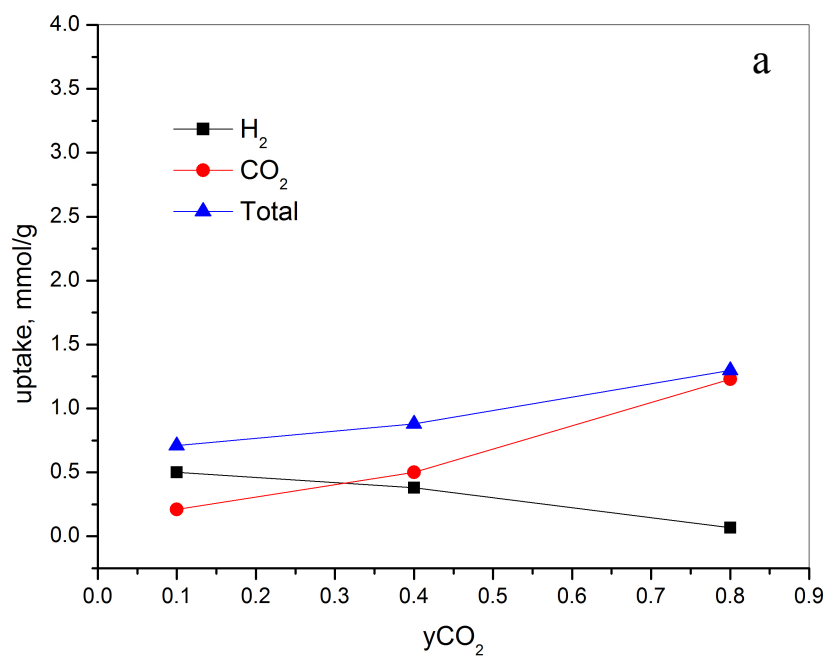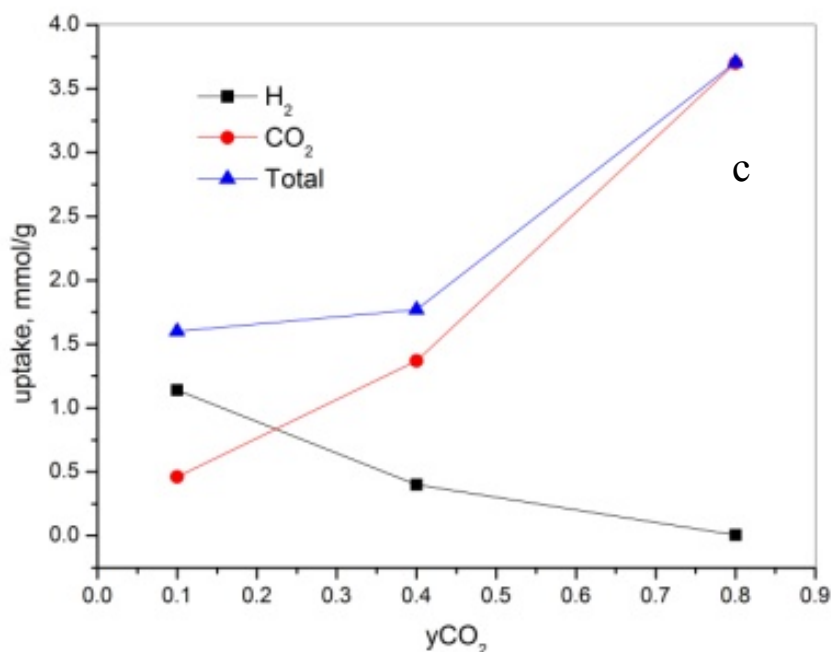
Figure 7-20 Binary CO_2-H_2 adsorption equilibria on the as-received MgO (a), MgO-800 (b) and MgO/PC-800 (c) from DSL model PN form predictions at 1500 kPa and 25 °C

7.4   Discussion

High-energy ball milling was employed to uniformly reduce the particle size of the as-received MgO and mix the milled MgO with the modified PC. The particle size was reduced from ~ 5 μm to 100±60 nm after 60 h ball milling. The BET surface area was also decreased from 133 to 100 m²/g with extended milling due to the destruction of porous structure by high energy milling. The chemically synthesized MgO samples treated at 600 and 800 °C have smaller particle sizes of 310±70 and 360±80 nm and larger BET surface area of 151 and 142 m²/g than the as-received MgO, because the molecule-sized pores were generated when H_2O molecules were released during heat treatment and the closed pores could be opened up by the gas flow. The as-received MgO and MgO-800 have the same CO_2 adsorption capacity at 25 °C and 1500 kPa CO_2 pressure of 2.1 mmol/g because of their similar crystalline structure, particle size and porosity of them. The 60h-MgO and 60h-MgO/PC show much lower CO_2 adsorption capacities of 0.48 and 0.98 mmol/g, respectively. Notably, the XRD results proved

that the CO_2 adsorptions on all obtained MgO samples at 25 °C were physical in nature. Therefore, it can be concluded that the CO_2 adsorption performance was positively correlated with BET surface area and the porosities. This result is in good agreement with those of Liu et al. [355] and Ruminski et al.[94].

It is reported that the typical CO_2 adsorption capacity of pure MgO is 0.13 to 0.64mmol/g (5.74 to 28mg/g) [100, 356], which is less than the CO_2 adsorption capacity of MgO/PC-800 (0.98 mmol/g). The high CO_2 adsorption capacity of MgO/PC-800 is due to the presence of MgO in the modified PC, which can hold the CO_2 molecules with a weaker affinity and traps them into the pores in MgO. However, Bhagiyalakshmi et al. [35] reported the chemisorption of CO_2 over ordered mesoporous carbon-supported MgO (Mg-OMC) at the low temperatures of 25, 75 and 100 °C. The maximum CO_2 adsorption capacity of Mg-OMC was found to be 92 mg/g at 25 °C, and the desorption of adsorbed CO_2 completed at 200 °C. The differences between the MgO/PC-800 and the reference MgO-OMC are found in their BET surface area and crystalline structure. The BET surface area of MgO-OMC is up to 714 m^2/g - much larger than MgO/PC-800- and the crystalline structure of MgO-OMC derives from Mg distributed over the uniformly ordered mesoporous carbon. The above two points show that the CO_2 adsorption reactions on MgO/PC-800 and MgO-OMC are different. But it still cannot clearly be explained why the CO_2 storage capacity is higher than theoretical capacity and what the effect is of carbon structures on the CO_2 adsorption process. On the basis of our work and the literature it is suspected that the mechanism of CO_2 adsorption is neither simple physisorption nor simple chemisorption. Further studies need to be performed to clarify the CO_2 adsorption mechanism on porous carbon supported MgO at low temperature.

7.5   Summary and conclusions

Magnesium oxide (MgO) nanoparticles were synthesized by two different methods: high energy ball milling and the chemical method. Modified plasma carbon (PC) was mixed with MgO, both by the ball milling and chemical coprecipitation methods, respectively, to form porous carbon supported MgO. The results indicate that high energy ball milling has a

negative effect on improving BET surface area of the as-received MgO. The CO_2 storage capacity of MgO/PC-800 ranges up to 6.16 mmol/g at 25 °C and 1500 kPa CO_2 pressure. The introduction of PC improves the CO_2 adsorption capacity of the chemical synthesized MgO by improving surface area.

The dual-site Langmuir (DSL) model was employed for predicting adsorption equilibria of CO_2/H_2 gas mixtures. DSL model simulates pure CO_2 adsorption and H_2 adsorption very well and can be used to predict the binary CO_2/H_2 gas mixture separation. According to the prediction, when the ratio of CO_2 to H_2 in the CO_2/H_2 gas mixture reached 80:20 vol. %, the MgO/PC-800 could adsorb or separate 3.5 mmol/g CO_2 in the CO_2/H_2 mixture.

8

GENERAL DISCUSSION

The use of hydrogen as an alternative energy carrier and the capture of CO_2 at concentrated power generation sites are two effective means of combating climate change. The key challenges are to develop an effective storage media in the former, and an effective sorbent in the latter. Here, carbon-based storage or sorbent nanostructures were obtained from a non-thermal plasma technology via. methane cracking into hydrogen and carbon. Such technique has many advantages over others, including high energy efficiencies, high energy density and relative low temperatures, and fast reaction time and non/less CO_2 emission. More importantly for this project, it offers the possibility of achieving a wide range of carbon structures from the fundamental building block – carbon atoms, while the generated hydrogen can be collected for further use.

Porous carbon materials have drawn intensive attention as sorbents for hydrogen and CO_2, due to their high stabilities and low costs. Such materials are usually obtained from carbonaceous sources, such as nutshells, coconut husk, peat, wood, or polymetric precursors and a subsequent modification/activation process is frequently used to enhance porosity. Xia et al. has demonstrated nitrogen-doped carbon materials are prepared using zeolite EMC-2 as a hard template and acetonitrile as the carbon source via chemical vapour deposition (CVD). The synthesized carbon products exhibiting high surface area up to 3360 m^2/g and high pore volumes up to 1.71 cm^3/g have total hydrogen storage capacities up to 6 wt.% at 77K and 2000 kPa and a high CO_2 uptake capacity of up to 6.9 mmol/g at 273 K and ambient pressure

[357, 358]. Zhu et al has developed a synthesis method of porous carbon spheres with a high specific surface area of 2032 m^2/g, which derived from a poly-precursor and used KOH as the activation agent. However, such methods usually lead to a very low yield. Here, the non-thermal microwave plasma technique offers an alternative route for the synthesis of controlled nanostructures of carbon, with high quality and yield. As the facility was still under development, the main product generated by methane cracking is carbon with the highest BET surface area of 125 m^2/g. After thermal treatment, with CO_2 as the activation agent, the porosity was increased up to 779 m^2/g. BET analysis indicates that this increase is mainly due to an increase in micropores and mesopores, Figure 5-6 and Figure 5-7. This is due to the oxidative effect of CO_2 at temperature that removed pore-blocking amorphous carbon atoms and opened up microporosities. The treated carbon products were then used for improving H_2 storage properties of Mg-based materials and for CO_2 absorption.

The obtained plasma carbon consists of fine spherical particles of about 40.8±8.7 nm in diameter and multilayer graphene sheets. It is also noted that there are a large number of defects in the plasma carbon structure. Experimental data and molecular dynamic simulations [269, 270] suggest that defects are required for the nucleation and growth of carbon nanostructures. The defects may deteriorate the mechanical properties of the nanostructures, but may also provide specific binding sites for dopants or for gaseous molecules in further functionalization of the carbon nanostructures, e.g. for catalyst loading, gas sensing, hydrogen storage, or CO_2 capture. The surfaces of the plasma carbon contain the co-existence of mesoporous and macroporous surfaces. The plasma carbon shows a bimodal distribution of pore sizes at 17 nm and 40-240 nm. Such bimodal distribution may be desirable for many types of practical applications, e.g. mesopores for loading of catalysts and macropores for easy access of reactants in chemical synthesis and/or gas sorption. The characteristic pore-size distribution may be attributed to the dynamic environment in the specific plasma chamber, which results in rapid intermix and growth of disordered and graphitic carbon structures. The mesopores were formed due to the rapid growth of the carbon nanoparticles and the graphene stacks, whereas the macropores were due to impingement and aggregation of such particles. In comparison with other porous carbons, such as activated carbon, template carbon, carbide derived carbon, polymer derived carbon and recent graphene oxide derived carbon, the multi-structures of the plasma carbon combine amorphous and crystalline

structures with a wide pore range from mesopores to macropores. After applied the thermal treatment on the synthesized plasma carbon, BET surface area was markedly enhanced and the accessible micropores and mesopores were also increased since the blocked micropores in the as-synthesized plasma carbon were 'opened up' during the treatment and new pores could be generated by heating with gas flow. It is envisaged that chemical activation by KOH may further modify the as-produced carbon structures, as it did for the synthetic carbon. However, this was not carried out due to safety regulations in our laboratory.

The specific structures of the plasma carbon also show promising effects in reducing dehydrogenation temperature and improving the dehydrogenation kinetics of MgH_2/TiC, compared to the activated carbon and the lab synthesized CNTs. Apart from acting as a dispersion aid to Mg-based particles and providing additional hydrogen diffusion channels, the stacked graphenic / graphitic layers in the PC offer enriched sp^2 electron bonding (formed by π electrons) with "electron-rich surfaces" [323], which creates favorable conditions for the spill-over of monatomic hydrogen carrying an effective positive charge [306]. A possibility for the improvements of hydrogen sorption performances of the Mg-C materials via an H spill-over mechanism was also pointed out by Wu and Cheng [323]. Many researchers have reported that the combination of carbon with transition metals leads to synergetic effects on improving the hydrogen storage properties of magnesium hydride [18, 20, 323-325]. Our previous work [294, 297] indicates that TiC exhibits effective catalysis on de-/rehydrogenation of MgH_2. The PC also shows a promising effect on improving dehydrogenation temperature of MgH_2 without TiC. The 20h-milled MgH_2/TiC mixed with PC shows the lowest desorption onset and peak temperatures (Figure 6-11). Thus there exists a synergetic effect between TiC and the carbon additives, especially PC. The synergetic co-catalytic effect for dehydrogenation may be understood as due to a spillover mechanism through the interaction of facile π-electrons of carbon with the catalyst TiC. This mechanism is similar to the effect of metallic catalysts in promoting the recombination of H atoms during dehydrogenation, e.g. the improved rates of decomposition of MgH_2 ball milled with CNFs and MWCNTs with metallic impurities (Fe, Ni) were observed by Lillo-Rodenas et al.[326].

The modified PC was also used as additives in the chemically synthesized MgO for CO_2 adsorption. The CO_2 storage capacity of MgO/PC-800 is up to 6.16 mmol/g, which is much

higher than the CO_2 adsorption capacity of 2.1 mmol/g of as-received MgO and MgO-800 at 25 °C and 1500 kPa CO_2 pressure. The high CO_2 capacity of MgO/PC-800 benefits from the improvement of surface area and porosity by the addition of PC. The MgO/PC-800 and PC can absorb respectively 6.16 and 13.7 mmol/g CO_2 at 25 °C and 1500 kPa of CO_2 pressure. Bhagiyalakshmi et al. [35, 92] report the mesoporous carbon supported MgO materials show a maximum CO_2 chemical adsorption of 100 mg/g at 100 °C and nearly 80 mg/g at 25 °C. The high CO_2 adsorption capacity of this mesoporous carbon supported MgO is due to the presence of MgO in the non-framework of ordered mesoporous carbon that holds the CO_2 molecules with a relatively weak affinity and traps them into the pores by chemical reaction to form $MgCO_3$. It has been confirmed in Chapter 7 that the CO_2 adsorptions of MgO/PC-800 and other obtained MgO composites are physisorption. Thus, the CO_2 adsorption property of them depends on the porosity characteristics of the sample. Compared with the existence of MgO, individual PC with a relatively high BET surface area of 350 m^2/g shows an exceptional CO_2 adsorption capacity of 13.7 mmol/g (60 wt.%). The reason of the negative effect of MgO on CO_2 adsorption could be that the synthesized MgO is not of a mesoporous structure with a poor porosity level, which is not able to chemically absorb CO_2 at relative low temperature. Recently, Srinivas et al [359] synthesized a new type of hierarchically porous carbon sturecture of simultaneously high surface area up to 2734 m^2/g from controlled carbonization of the MOFs. This hierarchically porous carbon exhibits a significant amount of CO_2 adsorption, over 27 mmol/g (119 wt.%) at 3000 kPa and 27 °C. It has been reported that MgO powder can be employed as a template for synthesis of nanoporous carbons with a high specific surface area by carbonization over the temperature range, 500 – 1000 °C [360]. The MgO-templated nanoporous carbons exhibited CO_2 adsorption of 4.41 mmol /g at 100 kPa.

Porous carbon materials have been used in gas storage due to their highly developed porosity, extended surface area, surface chemistry, and thermal stability. Previous studies have been carried out toward the use of activated carbons, activated carbon fibers, carbon molecular sieves, carbon nanotubes and graphite nanofibers as adsorbents for CO_2 capture. Among those, activated carbon is considered as the efficient and convenient material for CO_2 adsorption. The effects on CO_2 adsorption differ in micropores, mesopores and macropores [361]. For instance, in micropores adsorption is governed by CO_2-surface interactions with

wall-wall interactions also playing a significant role. Within mesopores, the fluid-fluid interactions become more important leading to capillary condensation in the pores. Condensation in mesopores is represented by the formation of a liquid-like phase at a pressure lower than the saturation pressure of the bulk fluid. It is noted that the conditions of the bulk phase transition to condensed phase are shifted, taking place at lower pressures or/and higher temperature due to the fluid-wall interactions. In macropores, the fluid-wall interactions play a less important role and the density of the fluid in macropores can be equated to the bulk density of the fluid at a given temperature and pressure. Mesopore and macropore play also an essential role in the transport of adsorbate molecules inside the micropore volume. All activated carbons contain micropores, mesopores and macropores within their structures but the relative proportions and pore size vary considerably according to the raw material and the synthesis methods. Earlier literatures [362] have stated that CO_2 can tightly fit inside ultra-micropores (less than 0.7 nm) as a single layer [360]. For pores larger than 0.85 nm, CO_2 molecules can form a monolayer along the pore wall and then the additional layers next to the monolayer. The monolayer and pore filling mechanism can be observed for the larger pore widths of 2 to 2.7 nm, as one can see the slope of isotherms increases gradually due to the formation of monolayer and then it shows a small jump in adsorption isotherm at high pressures due to the pore filling behavior (as shown in Figure 5-6). The capillary condensation is observed in the case of adsorption in the larger mesopores. The optimum plasma carbon consisting of micropores 0.7 nm and mesopores 2.1 nm in half-pore width shows a very promising CO_2 absorption capacity of up to 13.7 mmol/g at 25 °C and 1500 kPa, as shown in Figure 7-8 and Figure 7-16. From Figure 7-9 and Figure 7-10, the trend in CO_2 adsorption capacity is related to the larger microporosity, the improved CO_2 adsorption capacity is a result of the improved microporosity of samples.

Overall, the foregoing discussion has demonstrated a successful use of the low-energy plasma technique for the synthesis of porous carbon materials. A thermal treatment process improves the surface area and porosity of the synthesized plasma carbon. The multi-structures of the obtained plasma carbon, in comparison with the activated carbon and the CNTs, are beneficial to enhance hydrogen storage properties of Mg-based materials. In the end, the mechanism of micro-, meso- and macro-pore on gas sorption, especially CO_2 adsorption, has also been discussed.

<div align="right">

9

</div>

CONCLUSIONS AND FUTURE WORK

9.1 Conclusions

One of the attractive methods of producing hydrogen and high value-added carbon is plasma-reforming of hydrocarbons. Here, nanostructured carbons have been produced by methane cracking in a relatively low-energy cold plasma reactor, designed in-house specifically for such purpose. Carbon samples collected at different positions in the reactor show similar structural morphologies, indicating extensive structural uniformity of the carbon during processing. The effects of flow rate, temperature and power were evaluated for the formation of the carbon structures.

- The obtained carbon structures consist of amorphous carbon, spherical nanoparticles of 40.8±8.7 nm in diameter and multilayered graphene sheets.
- BET surface area and pore volume of the carbon materials vary from 74-125 m^2/g and from 0.12-0.20 cm^3/g, respectively. Such variations are closely associated with the magnitude of temperature drop at the sample collection position in the cold-plasma chamber before and after methane loading.
- For carbon materials collected at different positions at 1500 W, the highest BET surface area and pore volume are 111 m^2/g and 0.2055 cm^3/g, respectively.
- The highest BET surface area of 125 m^2/g is obtained at a power of 2000 W. The carbon structure with the highest BET surface area corresponds to the most reactive

region for rapid CH_4 decomposition and carbon formation, where the actual temperature gradient or the temperature difference is also the greatest.

The obtained carbon materials were used to improve hydrogen storage of MgH_2/TiC and CO_2 storage of MgO. For these objectives, a thermal treatment method was used to enhance BET surface area and pore volume. Response surface methodology (RSM) was adopted here to evaluate the effects of the thermal treatment temperature, time and pressure on BET surface area and yield of carbon. The optimum thermal treatment conditions were also obtained by RSM.

- The treatment temperature was identified as a significant factor in the thermal treatment process; an increase in thermal treatment temperature resulted in an increase in BET surface area and a decrease of yield.
- The increases of BET surface area and pore volume are due to the generation of micropores, the break-up of some micropores to form mesopores and the opening up of accessible porosities in the graphitic carbon regions as the amorphous carbon is removed from the surface.
- The optimal surface area of the modified plasma carbon was achieved at 950 °C within 100 kPa pressure for 120 min thermal treatment.

The Mg-C composite system has drawn considerable interest following the observation that the hydrogen storage performance of Mg could be improved by adding graphite, carbon nanotubes and fullerene. MgH_2/TiC was milled with the optimum plasma carbon (PC), activated carbon (AC) and carbon nanotubes (CNTs), respectively, for the investigation of effects of the different carbon structures on hydrogen storage of Mg-based materials.

- All carbon additives, including PC, AC and CNTs have positive effects on dehydrogenation properties of MgH_2/TiC due to dispersion effect of carbon and facilitating the hydrogen atoms diffusion.
- PC shows the most effective in reducing dehydrogenation temperature, down to 184 °C, and improving the dehydrogenation kinetics of the MgH_2/TiC.
- MgH_2/TiC particles can be dispersed most evenly on graphite sheets of PC, compared to AC and CNTs.

- TiC is still effective for enhancing the de-/re- hydrogenation kinetics even when carbon is added. The synergetic role of the metallic catalyst and carbon additives further improves hydrogen storage performance.

Modified plasma carbon (PC) was mixed with MgO, by ball milling and chemical co-precipitation methods, respectively, to form porous-carbon supported MgO for CO_2 capture and separation. The dual-site Langmuir (DSL) model was employed for predicting adsorption equilibria of CO_2/H_2 gas mixtures based on the experimental data of pure CO_2 adsorption and pure H_2 adsorption.

- High-energy ball milling shows a negative effect on improving BET surface area of the as-received MgO due to the destruction of porous structure by the high-energy milling.
- The introduction of PC improves the CO_2 adsorption capacity of the chemical synthesized MgO by improving surface area. The CO_2 storage capacity of MgO/PC-800 ranges up to 6.16 mmol/g at 25 °C and 1500 kPa CO_2 pressure.
- The DSL model simulates pure CO_2 adsorption and H_2 adsorption very well and can be used to predict the separation of binary CO_2/H_2 gas mixtures.
- According to the prediction, when the ratio of $CO_2:H_2$ in the CO_2/H_2 gas mixture reached 80:20 vol%, MgO/PC-800 could adsorb or separate 3.5 mmol/g CO_2 in the CO_2/H_2 mixture.

9.2   Recommendation for future work

- **To separate graphene from the carbon materials produced by the plasma reactor**

The carbon products by the low-energy plasma reactor consist of amorphous structures, spherical nanoparticles and multilayered graphene sheets. Different carbon structures have great different properties and applications. Thus the mixed carbon structures of the plasma carbon products should be separated and the fractionations with similar properties should be collected individually. Density gradient ultracentrifugation and electrophoresis techniques are recently used to achieve high-resolution sorting of carbon materials, such as graphene and

carbon nanotubes. Graphene flakes with superior performance in transparent conductors, selective optical properties could be obtained after separation.

- **To produce carbon nanotubes in an improved plasma reactor**

In Chapter 5, the catalyst MgNiOx was used for novel carbon nano structures from methane reforming in the plasma reactor. The short carbon nanofibers were produced from catalytic decomposition of methane because the carbon nanofibers cannot continually grow up to longer size after the catalyst burn-off in the plasma reactor. Thus, the current cooling system of the plasma reactor needs to be further improved to achieve the suitable temperature for the catalytic process. The catalyst is considered to be sputtered on a silica substrate as a nano-film, which makes carbon nanofiber/tube effectively grow on the substrate.

- **To further study carbon 'catalytic' mechanism on improving hydrogen storage properties of MgH$_2$/TiC**

The mechanism of carbon nanostructures improving hydrogen storage properties of MgH$_2$/TiC is not clarified according to the current techniques and analysis results. The more measurement and analysis need to be performed, such as FTIR, XPS etc.

- **To perform the CO$_2$/H$_2$ mixture gases separation experiment: Column Breakthrough Experiments**

The CO$_2$/H$_2$ mixture gases separation data can be obtained in a single-bed adsorption unit that could be merged in the IGA system. The schematic and detailed description of the system has been reported previously [363]. The predicted CO$_2$/H$_2$ separation results can be evaluated by the breakthrough experiments.

- **To explore the synthesis of mesoporous MgO with higher surface area and investigation its CO$_2$ storage properties.**

The formation of mesoporous structure and high surface area are beneficial for CO$_2$ adsorption. Thus the improvement of surface area and further formation of mesoporous Mg can be considered as a research direction for CO$_2$ adsorption. Moreover, the addition of novel catalysts can be another option to improve CO$_2$ storage properties of porous MgO.

To further study the effect of meso-porous structure on CO_2 capture of other metal oxides, e.g. mesoporous CaO and Al_2O_3.

REFERENCES

[1]   J. D. Figueroa, T. Fout, S. Plasynski, H. McIlvried, and R. D. Srivastava, "Advances in CO_2 capture technology—The U.S. Department of Energy's Carbon Sequestration Program," *International Journal of Greenhouse Gas Control,* vol. 2, pp. 9-20, 1// 2008.

[2]   U. S. D. o. Energy. (2009). *Targets for onboard hydrogen storage systems for light-duty vehicles.* Available: http://www.sciencedirect.com/science?_ob=RedirectURL&_method=externObjLink&_locator=url&_cdi=271472&_issn=03603199&_origin=article&_zone=art_page&_plusSign=%2B&_targetURL=http%3A%2F%2Fwww1.eere.energy.gov%2Fhydrogenandfuelcells%2Fstorage%2Fpdfs%2Ftargets_onboard_hydro_storage.pdf

[3]   L. Zhou, "Progress and problems in hydrogen storage methods," *Renewable and Sustainable Energy Reviews,* vol. 9, pp. 395-408, // 2005.

[4]   A. Züttel, "Materials for hydrogen storage," *Materials Today,* vol. 6, pp. 24-33, // 2003.

[5]   L. Zhou, Y. Zhou, and Y. Sun, "Studies on the mechanism and capacity of hydrogen uptake by physisorption-based materials," *International Journal of Hydrogen Energy,* vol. 31, pp. 259-264, // 2006.

[6]   W. Grochala and P. P. Edwards, "Thermal decomposition of the non-interstitial hydrides for the storage and production of hydrogen," *Chemical Reviews,* vol. 104, pp. 1283-1315, // 2004.

[7]   U. Eberle, G. Arnold, and R. Von Helmolt, "Hydrogen storage in metal-hydrogen systems and their derivatives," *Journal of Power Sources,* vol. 154, pp. 456-460, // 2006.

[8]   L. Schlapbach and A. Züttel, "Hydrogen-storage materials for mobile applications," *Nature,* vol. 414, pp. 353-358, // 2001.

[9]   B. Sakintuna, F. Lamari-Darkrim, and M. Hirscher, "Metal hydride materials for solid hydrogen storage: a review," *International Journal of Hydrogen Energy,* vol. 32, pp. 1121-1140, 2007.

[10]   M. Tian and C. Shang, "Nano-structured MgH_2 catalyzed by TiC nanoparticles for hydrogen storage," *Journal of Chemical Technology & Biotechnology,* vol. 86, pp. 69-74.

[11]   C. Z. Wu, P. Wang, X. Yao, C. Liu, D. M. Chen, G. Q. Lu*, et al.*, "Effect of carbon/noncarbon addition on hydrogen storage behaviors of magnesium hydride," *Journal of Alloys and Compounds,* vol. 414, pp. 259-264, 2006.

[12]   K. Yamamoto, S. Tanioka, Y. Tsushio, T. Shimizu, T. Morishita, S. Orimo*, et al.*, "Influence of elemental diffusion on low temperature formation of MgH_2 in $TiMn_{1.3}T_{0.2}$-Mg (T = 3d-transition elements)," *Journal of Alloys and Compounds,* vol. 243, pp. 144-150, 10/15/ 1996.

[13]   G. Liang, E. Wang, and S. Fang, *J. Alloys Compd.,* vol. 223, // 1995.

[14]   M. Terzieva, M. Khrussanova, P. Peshev, and D. Radev, "Hydriding and dehydriding characteristics of mixtures with a high magnesium content obtained by sintering and mechanical alloying," *International Journal of Hydrogen Energy,* vol. 20, pp. 53-58, 1// 1995.

[15]   M. Y. Song, "Improvement in hydrogen storage characteristics of magnesium by mechanical alloying with nickel," *Journal of Materials Science,* vol. 30, pp. 1343-1351, // 1995.

[16]   C. X. Shang, M. Bououdina, Y. Song, and Z. X. Guo, "Mechanical alloying and electronic simulations of (MgH$_2$+M) systems (M=Al, Ti, Fe, Ni, Cu and Nb) for hydrogen storage," *International Journal of Hydrogen Energy,* vol. 29, pp. 73-80, // 2004.

[17]   N. Hanada, T. Ichikawa, and H. Fujii, "Catalytic effect of nanoparticle 3d-transition metals on hydrogen storage properties in magnesium hydride MgH$_2$ prepared by mechanical milling," *Journal of Physical Chemistry B,* vol. 109, pp. 7188-7194, // 2005.

[18]   H. Imamura, I. Kitazawa, Y. Tanabe, and Y. Sakata, "Hydrogen storage in carbon/Mg nanocomposites synthesized by ball milling," *International Journal of Hydrogen Energy,* vol. 32, pp. 2408-2411, 2007.

[19]   H. Imamura, N. Sakasai, and T. Fujinaga, "Characterization and hydriding properties of Mg-graphite composites prepared by mechanical grinding as new hydrogen storage materials," *Journal of Alloys and Compounds,* vol. 253-254, pp. 34-37, 1997.

[20]   H. Imamura, Y. Takesue, T. Akimoto, and S. Tabata, "Hydrogen-absorbing magnesium composites prepared by mechanical grinding with graphite: effects of additives on composite structures and hydriding properties," *Journal of Alloys and Compounds,* vol. 293-295, pp. 564-568, 1999.

[21]   C. X. Shang and Z. X. Guo, "Effect of carbon on hydrogen desorption and absorption of mechanically milled MgH$_2$," *Journal of Power Sources,* vol. 129, pp. 73-80, 4/15/ 2004.

[22]   A. Reyhani, S. Z. Mortazavi, S. Mirershadi, A. N. Golikand, and A. Z. Moshfegh, "H2 adsorption mechanism in Mg modified multi-walled carbon nanotubes for hydrogen storage," *International Journal of Hydrogen Energy,* vol. 37, pp. 1919-1926, 2012.

[23]   A. Ranjbar, M. Ismail, Z. P. Guo, X. B. Yu, and H. K. Liu, "Effects of CNTs on the hydrogen storage properties of MgH$_2$ and MgH$_2$-BCC composite," *International Journal of Hydrogen Energy,* vol. 35, pp. 7821-7826, 2010.

[24]   M. T. R. Mohammad Songolzadeh , Mansooreh Soleimani, "Carbon Dioxide Capture and Storage: A General Review on Adsorbents," *World Academy of Science, Engineering and Technology,* vol. 70, pp. 225-232, 2012.

[25]   Z. Chen, W. Ren, L. Gao, B. Liu, S. Pei, and H.-M. Cheng, "Three-dimensional flexible and conductive interconnected graphene networks grown by chemical vapour deposition," *Nat Mater,* vol. 10, pp. 424-428, 2011.

[26]   D. Zhai, H. Du, B. Li, Y. Zhu, and F. Kang, "Porous graphitic carbons prepared by combining chemical activation with catalytic graphitization," *Carbon,* vol. 49, pp. 725-729, 2010.

[27]   M. Sevilla and A. B. Fuertes, "Catalytic graphitization of templated mesoporous carbons," *Carbon,* vol. 44, pp. 468-474, 2006.

[28]   J. Wu, K. Gerstandt, H. Zhang, J. Liu, and B. J. Hinds, "Electrophoretically induced aqueous flow through single-walled carbon nanotube membranes," *Nat Nano,* vol. 7, pp. 133-139, 2012.

[29]   S. M. Saufi and A. F. Ismail, "Fabrication of carbon membranes for gas separation-a review," *Carbon,* vol. 42, pp. 241-259, 2004.

[30]   S. Li, Y. Luo, W. Lv, W. Yu, S. Wu, P. Hou*, et al.,* "Vertically Aligned Carbon Nanotubes Grown on Graphene Paper as Electrodes in Lithium-Ion Batteries and Dye-Sensitized Solar Cells," *Advanced Energy Materials,* vol. 1, pp. 486-490, 2011.

[31] G. Wang, X. Shen, J. Yao, and J. Park, "Graphene nanosheets for enhanced lithium storage in lithium ion batteries," *Carbon,* vol. 47, pp. 2049-2053, 2009.

[32] J. Wang, G. Yin, Y. Shao, S. Zhang, Z. Wang, and Y. Gao, "Effect of carbon black support corrosion on the durability of Pt/C catalyst," *Journal of Power Sources,* vol. 171, pp. 331-339, 2007.

[33] S.-Y. Yang, K.-H. Chang, H.-W. Tien, Y.-F. Lee, S.-M. Li, Y.-S. Wang*, et al.*, "Design and tailoring of a hierarchical graphene-carbon nanotube architecture for supercapacitors," *Journal of Materials Chemistry,* vol. 21, pp. 2374-2380, 2011.

[34] S. Veldurthi, C.-H. Shin, O.-S. Joo, and K.-D. Jung, "Synthesis of mesoporous MgO single crystals without templates," *Microporous and Mesoporous Materials,* vol. 152, pp. 31-36, 4/1/ 2012.

[35] M. Bhagiyalakshmi, P. Hemalatha, M. Ganesh, P. M. Mei, and H. T. Jang, "A direct synthesis of mesoporous carbon supported MgO sorbent for CO_2 capture," *Fuel,* vol. 90, pp. 1662-1667, 4// 2011.

[36] S. Yang, X. Lin, A. J. Blake, G. S. Walker, P. Hubberstey, N. R. Champness*, et al.*, "Cation-induced kinetic trapping and enhanced hydrogen adsorption in a modulated anionic metal–organic framework," *Nat Chem,* vol. 1, pp. 487-493, 09//print 2009.

[37] Y. Fukai, *The Metal-Hydrogen System-Basic Bulk Properties* vol. 21: Springer 2005.

[38] L. Schlapbach, D. Shaltiel, and P. Oelhafen, "Catalytic effect in the hydrogenation of Mg and Mg compounds: Surface analysis of $MgMg_2Ni$ and Mg_2Ni," *Materials Research Bulletin,* vol. 14, pp. 1235-1246, // 1979.

[39] I. P. Jain, C. Lal, and A. Jain, "Hydrogen storage in Mg: A most promising material," *International Journal of Hydrogen Energy,* vol. 35, pp. 5133-5144, 5// 2010.

[40] H. Reule, M. Hirscher, A. Weißhardt, and H. Kronmüller, "Hydrogen desorption properties of mechanically alloyed MgH_2 composite materials," *Journal of Alloys and Compounds,* vol. 305, pp. 246-252, // 2000.

[41] G. Friedlmeier and M. Groll, "Experimental analysis and modelling of the hydriding kinetics of Ni-doped and pure Mg," *Journal of Alloys and Compounds,* vol. 253-254, pp. 550-555, // 1997.

[42] L. Guoxian, W. Erde, and F. Shoushi, "Hydrogen absorption and desorption characteristics of mechanically milled $Mg35wt.\%FeTi_{1.2}$ powders," *Journal of Alloys and Compounds,* vol. 223, pp. 111-114, // 1995.

[43] A. Zaluska, L. Zaluski, and J. O. Ström-Olsen, "Nanocrystalline magnesium for hydrogen storage," *Journal of Alloys and Compounds,* vol. 288, pp. 217-225, // 1999.

[44] R. W. P. Wagemans, J. H. Van Lenthe, P. E. De Jongh, A. J. Van Dillen, and K. P. De Jong, "Hydrogen storage in magnesium clusters: Quantum chemical study," *Journal of the American Chemical Society,* vol. 127, pp. 16675-16680, // 2005.

[45] V. M. Skripnyuk, E. Rabkin, Y. Estrin, and R. Lapovok, "Improving hydrogen storage properties of magnesium based alloys by equal channel angular pressing," *International Journal of Hydrogen Energy,* vol. 34, pp. 6320-6324, // 2009.

[46] M. Zhu, H. Wang, L. Z. Ouyang, and M. Q. Zeng, "Composite structure and hydrogen storage properties in Mg-base alloys," *International Journal of Hydrogen Energy,* vol. 31, pp. 251-257, // 2006.

[47] S. S. Han, N. H. Goo, and K. S. Lee, "Effects of sintering on composite metal hydride alloy of Mg_2Ni and TiNi synthesized by mechanical alloying," *Journal of Alloys and Compounds,* vol. 360, pp. 243-249, // 2003.

[48] L. Zaluski, A. Zaluska, P. Tessier, J. O. Ström-Olsen, and R. Schulz, "Catalytic effect of Pd on hydrogen absorption in mechanically alloyed Mg_2Ni, $LaNi_5$ and FeTi," *Journal of Alloys and Compounds,* vol. 217, pp. 295-300, // 1995.

[49] S. G. Porutsky, E. A. Zhurakovsky, S. A. Mogilevsky, V. N. Verbetsky, O. S. Bakuma, and K. N. Semenenko, "Electronic structure of Mg_2FeH_6 and Mg_2CoH_5 hydrides and binding role of hydrogen in them," *Solid State Communications,* vol. 74, pp. 551-553, // 1990.

[50] S. Bouaricha, J. P. Dodelet, D. Guay, J. Huot, S. Boily, and R. Schulz, "Hydriding behavior of Mg-Al and leached Mg-Al compounds prepared by high-energy ball-milling," *Journal of Alloys and Compounds,* vol. 297, pp. 282-293, // 2000.

[51] G. Liang, J. Huot, S. Boily, A. Van Neste, and R. Schulz, "Hydrogen storage properties of nanocrystalline $Mg_{1.9}Ti_{0.1}Ni$ made by mechanical alloying," *Journal of Alloys and Compounds,* vol. 282, pp. 286-290, // 1999.

[52] A. Y. Yermakov, N. V. Mushnikov, M. A. Uimin, V. S. Gaviko, A. P. Tankeev, A. V. Skripov*, et al.*, "Hydrogen reaction kinetics of Mg-based alloys synthesized by mechanical milling," *Journal of Alloys and Compounds,* vol. 425, pp. 367-372, // 2006.

[53] J. Dufour and J. Huot, "J. Alloy. Compd," vol. 439, // 2007.

[54] G. Barkhordarian, T. Klassen, and R. Bormann, "Fast hydrogen sorption kinetics of nanocrystalline Mg using Nb_2O_5 as catalyst," *Scripta Materialia,* vol. 49, pp. 213-217, // 2003.

[55] O. Friedrichs, F. Aguey-Zinsou, J. R. A. Fernández, J. C. Sánchez-López, A. Justo, T. Klassen*, et al.*, "MgH_2 with Nb_2O_5 as additive, for hydrogen storage: Chemical, structural and kinetic behavior with heating," *Acta Materialia,* vol. 54, pp. 105-110, // 2006.

[56] K. F. Aguey-Zinsou, J. R. Ares Fernandez, T. Klassen, and R. Bormann, "Effect of Nb_2O_5 on MgH_2 properties during mechanical milling," *International Journal of Hydrogen Energy,* vol. 32, pp. 2400-2407, // 2007.

[57] M. R. Reda, "The effect of organic additive in Mg/graphite composite as hydrogen storage materials," *Journal of Alloys and Compounds,* vol. 480, pp. 238-240, // 2009.

[58] J. Bloch and M. H. Mintz, "Kinetics and mechanisms of metal hydrides formation - A review," *Journal of Alloys and Compounds,* vol. 253-254, pp. 529-541, // 1997.

[59] R. L. Holtz and M. A. Imam, "Hydrogen storage characteristics of ball-milled magnesium-nickel and magnesium-iron alloys," *Journal of Materials Science,* vol. 34, pp. 2655-2663, 1999/06/01 1999.

[60] C. Iwakura, S. Nohara, S. G. Zhang, and H. Inoue, "Hydriding and dehydriding characteristics of an amorphous Mg_2Ni-Ni composite," *Journal of Alloys and Compounds,* vol. 285, pp. 246-249, // 1999.

[61] G. S. Walker, M. Abbas, D. M. Grant, and C. Udeh, "Destabilisation of magnesium hydride by germanium as a new potential multicomponent hydrogen storage system," *Chemical Communications,* vol. 47, pp. 8001-8003, 2011.

[62] W. Oelerich, T. Klassen, and R. Bormann, "Comparison of the catalytic effects of V, V_2O_5, VN, and VC on the hydrogen sorption of nanocrystalline Mg," *Journal of Alloys and Compounds,* vol. 322, pp. L5-L9, 6/28/ 2001.

[63] M. Polanski, J. Bystrzycki, R. A. Varin, T. Plocinski, and M. Pisarek, "The effect of chromium (III) oxide (Cr_2O_3) nanopowder on the microstructure and cyclic hydrogen storage behavior of magnesium hydride (MgH_2)," *Journal of Alloys and Compounds,* vol. 509, pp. 2386-2391, 2/3/ 2011.

[64] W. Oelerich, T. Klassen, and R. Bormann, "Metal oxides as catalysts for improved hydrogen sorption in nanocrystalline Mg-based materials," *Journal of Alloys and Compounds,* vol. 315, pp. 237-242, // 2001.

[65] D. L. Croston, D. M. Grant, and G. S. Walker, "The catalytic effect of titanium oxide based additives on the dehydrogenation and hydrogenation of milled MgH2," *Journal of Alloys and Compounds,* vol. 492, pp. 251-258, 3/4/ 2010.

[66] C. M. P. Fry, D. M. Grant, and G. S. Walker, "Catalysis and evolution on cycling of nano-structured magnesium multilayer thin films," *International Journal of Hydrogen Energy,* vol. 39, pp. 1173-1184, 1/13/ 2014.

[67] C. M. P. Fry, D. M. Grant, and G. S. Walker, "Improved hydrogen cycling kinetics of nano-structured magnesium/transition metal multilayer thin films," *International Journal of Hydrogen Energy,* vol. 38, pp. 982-990, 1/24/ 2013.

[68] G. Liang, "Synthesis and hydrogen storage properties of Mg-based alloys," *Journal of Alloys and Compounds,* vol. 370, pp. 123-128, // 2004.

[69] S. Zhou, Q. Zhang, W. Ran, Z. Han, H. Niu, S. Han*, et al.*, "Evolution of magnesium during reactive milling under hydrogen atmosphere with crystallitic carbon as milling aid," *Journal of Alloys and Compounds,* vol. 581, pp. 472-478, 12/25/ 2013.

[70] J. G. Lu, M. D. Chen, Y. Ji, and H. Zhang, "Membrane-based CO_2 absorption into blended amine solutions," *Ranliao Huaxue Xuebao/Journal of Fuel Chemistry and Technology,* vol. 37, pp. 740-746, // 2009.

[71] M. K. Mondal, H. K. Balsora, and P. Varshney, "Progress and trends in CO_2 capture/separation technologies: A review," *Energy,* vol. 46, pp. 431-441, 10// 2012.

[72] W. J. Choi, J. B. Seo, S. Y. Jang, J. H. Jung, and K. J. Oh, "Removal characteristics of CO_2 using aqueous MEA/AMP solutions in the absorption and regeneration process," *Journal of Environmental Sciences,* vol. 21, pp. 907-913, // 2009.

[73] A. B. a. R. Rao, E. S. , "A technical, economic, and environmental assessment of amine-based CO_2 capture technology for power plant greenhouse gas control: Environmental Science and Technology," *Fuel and Energy Abstracts,* vol. 36, pp. 4467-4475, 9// 2002.

[74] S. Ma'mun, V. Y. Dindore, and H. F. Svendsen, "Kinetics of the reaction of carbon dioxide with aqueous solutions of 2-((2-aminoethyl)amino)ethanol," *Industrial and Engineering Chemistry Research,* vol. 46, pp. 385-394, // 2007.

[75] Y. Zhao, Y. Han, T. Ma, and T. Guo, "Simultaneous desulfurization and denitrification from flue gas by ferrate(VI)," *Environmental Science and Technology,* vol. 45, pp. 4060-4065, // 2011.

[76] X. S. Yin, S. P. Li, Q. H. Zhang, and J. G. Yu, "Synthesis and CO_2 adsorption characteristics of lithium zirconates with high lithia content," *Journal of the American Ceramic Society,* vol. 93, pp. 2837-2842, // 2010.

[77] P. C. Lin, C. W. Huang, C. T. Hsiao, and H. Teng, "Magnesium hydroxide extracted from a magnesium-rich mineral for CO_2 sequestration in a gas-solid system," *Environmental Science and Technology,* vol. 42, pp. 2748-2752, // 2008.

[78] K. K. Han, Y. Zhou, Y. Chun, and J. H. Zhu, "Efficient MgO-based mesoporous CO_2 trapper and its performance at high temperature," *Journal of Hazardous Materials,* vol. 203–204, pp. 341-347, 2/15/ 2012.

[79] K. Wang, X. Guo, P. Zhao, F. Wang, and C. Zheng, "High temperature capture of CO_2 on lithium-based sorbents from rice husk ash," *Journal of Hazardous Materials,* vol. 189, pp. 301-307, // 2011.

[80] B. B. Sakadjian, M. V. Iyer, H. Gupta, and L. S. Fan, "Kinetics and structural characterization of calcium-based sorbents calcined under subatmospheric conditions for the high-temperature CO_2 capture process," *Industrial and Engineering Chemistry Research,* vol. 46, pp. 35-42, // 2007.

[81] L. Li, X. Wen, X. Fu, F. Wang, N. Zhao, F. Xiao*, et al.*, "MgO/Al_2O_3 Sorbent for CO_2 Capture," *Energy & Fuels,* vol. 24, pp. 5773-5780, 2010/10/21 2010.

[82] A. Meisen and X. Shuai, "Research and development issues in CO_2 capture," *Energy Conversion and Management,* vol. 38, Supplement, pp. S37-S42, // 1997.

[83] C. Chen, D.-W. Park, and W.-S. Ahn, "CO_2 capture using zeolite 13X prepared from bentonite," *Applied Surface Science,* 2013.

[84] R. Krishna and J. M. van Baten, "A comparison of the CO_2 capture characteristics of zeolites and metal–organic frameworks," *Separation and Purification Technology,* vol. 87, pp. 120-126, 3/5/ 2012.

[85] X. Li, J. E. Remias, J. K. Neathery, and K. Liu, "NF/RO faujasite zeolite membrane-ammonia absorption solvent hybrid system for potential post-combustion CO_2 capture application," *Journal of Membrane Science,* vol. 366, pp. 220-228, 1/1/ 2011.

[86] I. D. MacKie and G. A. Dilabio, "CO_2 adsorption by nitrogen-doped carbon nanotubes predicted by density-functional theory with dispersion-correcting potentials," *Physical Chemistry Chemical Physics,* vol. 13, pp. 2780-2787, // 2011.

[87] A. C. Lua and J. Guo, "Microporous Oil-Palm-Shell Activated Carbon Prepared by Physical Activation for Gas-Phase Adsorption," *Langmuir,* vol. 17, pp. 7112-7117, 2012/10/19 2001.

[88] A. A. Olajire, "CO_2 capture and separation technologies for end-of-pipe applications – A review," *Energy,* vol. 35, pp. 2610-2628, 6// 2010.

[89] M. S. Shafeeyan, W. M. A. W. Daud, A. Houshmand, and A. Shamiri, "A review on surface modification of activated carbon for carbon dioxide adsorption," *Journal of Analytical and Applied Pyrolysis,* vol. 89, pp. 143-151, 11// 2010.

[90] R. T. Symonds, D. Y. Lu, R. W. Hughes, E. J. Anthony, and A. Macchi, "CO_2 capture from simulated syngas via cyclic Carbonation/Calcination for a naturally occurring limestone: Pilot-plant testing," *Industrial and Engineering Chemistry Research,* vol. 48, pp. 8431-8440, // 2009.

[91] S. C. Lee, H. J. Chae, S. J. Lee, B. Y. Choi, C. K. Yi, J. B. Lee*, et al.*, "Development of Regenerable MgO-Based Sorbent Promoted with K_2CO_3 for CO_2 Capture at Low Temperatures," *Environmental Science & Technology,* vol. 42, pp. 2736-2741, 2008/04/01 2008.

[92] M. Bhagiyalakshmi, J. Y. Lee, and H. T. Jang, "Synthesis of mesoporous magnesium oxide: Its application to CO_2 chemisorption," *International Journal of Greenhouse Gas Control,* vol. 4, pp. 51-56, 1// 2010.

[93] A. Hassanzadeh and J. Abbasian, "Regenerable MgO-based sorbents for high-temperature CO2 removal from syngas: 1. Sorbent development, evaluation, and reaction modeling," *Fuel,* vol. 89, pp. 1287-1297, 6// 2010.

[94] A. M. Ruminski, K.-J. Jeon, and J. J. Urban, "Size-dependent CO_2 capture in chemically synthesized magnesium oxide nanocrystals," *Journal of Materials Chemistry,* vol. 21, pp. 11486-11491, 2011.

[95] G. Xiao, R. Singh, A. Chaffee, and P. Webley, "Advanced adsorbents based on MgO and K_2CO_3 for capture of CO_2 at elevated temperatures," *International Journal of Greenhouse Gas Control,* vol. 5, pp. 634-639, 7// 2011.

[96] F. Y. Chang, K. J. Chao, H. H. Cheng, and C. S. Tan, "Adsorption of CO_2 onto amine-grafted mesoporous silicas," *Separation and Purification Technology,* vol. 70, pp. 87-95, // 2009.

[97] M. L. Gray, K. J. Champagne, D. Fauth, J. P. Baltrus, and H. Pennline, "Performance of immobilized tertiary amine solid sorbents for the capture of carbon dioxide," *International Journal of Greenhouse Gas Control,* vol. 2, pp. 3-8, // 2008.

[98] A. Brunetti, F. Scura, G. Barbieri, and E. Drioli, "Membrane technologies for CO_2 separation," *Journal of Membrane Science,* vol. 359, pp. 115-125, 9/1/ 2010.

[99]   A. L. Myers, "Activity coefficients of mixtures adsorbed on heterogeneous surfaces," *AIChE Journal,* vol. 29, pp. 691-693, 1983.

[100]   R. Philipp and K. Fujimoto, "FTIR spectroscopic study of CO_2 adsorption/desorption on MgO/CaO catalysts," *Journal of Physical Chemistry,* vol. 96, pp. 9035-9038, // 1992.

[101]   M. A. Bezerra, R. E. Santelli, E. P. Oliveira, L. S. Villar, and L. A. Escaleira, "Response surface methodology (RSM) as a tool for optimization in analytical chemistry," *Talanta,* vol. 76, pp. 965-977, 9/15/ 2008.

[102]   H. Mazaheri, K. T. Lee, S. Bhatia, and A. R. Mohamed, "Subcritical water liquefaction of oil palm fruit press fiber in the presence of sodium hydroxide: An optimisation study using response surface methodology," *Bioresource Technology,* vol. 101, pp. 9335-9341, 2010.

[103]   X.-F. Guo and G.-J. Kim, "Ultrafine carbon black produced by pyrolysis of polyethylene using a novel DC-thermal plasma process," *Journal of Physics and Chemistry of Solids,* vol. 69, pp. 1224-1227, 2008/6//.

[104]   E. Sivertsen, F. Bjerke, T. Almøy, V. Segtnan, and T. Næs, "Multivariate optimization by visual inspection," *Chemometrics and Intelligent Laboratory Systems,* vol. 85, pp. 110-118, // 2007.

[105]   M. Bououdina, D. Grant, and G. Walker, "Effect of processing conditions on unsupported Ni-based catalysts for graphitic-nanofibre formation," *Carbon,* vol. 43, pp. 1286-1292, 5// 2005.

[106]   Y. Tian, Y. Zhang, B. Wang, W. Ji, and K. Xie, "Coal-derived carbon nanotubes by thermal plasma jet," *Carbon,* vol. 42, pp. 2597-2601, 2004.

[107]   M. Jasinski, J. Mizeraczyk, Z. Zakrzewski, T. Ohkubo, and J. S. Chang, "CFC-11 destruction by microwave torch generated atmospheric-pressure nitrogen discharge," *Journal of Physics D: Applied Physics,* vol. 35, pp. 2274-2280, 2002.

[108]   M. Jasinski, M. Dors, and J. Mizeraczyk, "Production of hydrogen via methane reforming using atmospheric pressure microwave plasma," *Journal of Power Sources,* vol. 181, pp. 41-45, 2008.

[109]   M. Moisan, Z. Zakrzewski, and J. C. Rostaing, "Waveguide-based single and multiple nozzle plasma torches: the TIAGO concept," *Plasma Sources Science and Technology,* vol. 10, p. 387, 2001.

[110]   H. S. Uhm, Y. C. Hong, and D. H. Shin, "A microwave plasma torch and its applications," *Plasma Sources Science and Technology,* vol. 15, p. S26, 2006.

[111]   J. D. Holladay, J. Hu, D. L. King, and Y. Wang, "An overview of hydrogen production technologies," *Catalysis Today,* vol. 139, pp. 244-260, 2009.

[112]   R. B. Biniwale, A. Mizuno, and M. Ichikawa, "Hydrogen production by reforming of iso-octane using spray-pulsed injection and effect of non-thermal plasma," *Applied Catalysis A: General,* vol. 276, pp. 169-177, 2004.

[113]   L. Bromberg, D. R. Cohn, A. Rabinovich, and N. Alexeev, "Plasma catalytic reforming of methane," *International Journal of Hydrogen Energy,* vol. 24, pp. 1131-1137, 1999.

[114]   C.-j. Liu, G.-h. Xu, and T. Wang, "Non-thermal plasma approaches in CO_2 utilization," *Fuel Processing Technology,* vol. 58, pp. 119-134, 1999.

[115]   P. K. Chu, J. Y. Chen, L. P. Wang, and N. Huang, "Plasma-surface modification of biomaterials," *Materials Science and Engineering: R: Reports,* vol. 36, pp. 143-206, 2002.

[116]   J. Yang, F. Z. Cui, I. S. Lee, and X. Wang, "Plasma surface modification of magnesium alloy for biomedical application," *Surface and Coatings Technology,* vol. 205, pp. S182-S187, 2010.

[117] M. Chernyshova, L. Karpinski, M. Scholz, B. Ulejczyk, J. K. Lee, and K. Jung, "PROCESS OF THIN FILM DEPOSITION USING DENSE PLASMA FOCUS," presented at the 34th EPS Conference on Plasma Phys. , Warsaw, 2007.

[118] H.-H. Kim, "Nonthermal Plasma Processing for Air-Pollution Control: A Historical Review, Current Issues, and Future Prospects," *Plasma Processes and Polymers,* vol. 1, pp. 91-110, 2004.

[119] G. Petitpas, J. D. Rollier, A. Darmon, J. Gonzalez-Aguilar, R. Metkemeijer, and L. Fulcheri, "A comparative study of non-thermal plasma assisted reforming technologies," *International Journal of Hydrogen Energy,* vol. 32, pp. 2848-2867, 2007.

[120] O. P. Solonenko, *Thermal Plasma Torches and Technologies: Plasma Torches: Basic Studies and Design* vol. 1-19, 281: Cambridge International Science, 2000.

[121] M. Moreno-Couranjou, M. Monthioux, J. Gonzalez-Aguilar, and L. Fulcheri, "A non-thermal plasma process for the gas phase synthesis of carbon nanoparticles," *Carbon,* vol. 47, pp. 2310-2321, 2009.

[122] E. Pfender, "Thermal plasma technology: Where do we stand and where are we going?," *Plasma Chemistry and Plasma Processing,* vol. 19, pp. 1-31, 1999.

[123] A. W. Weimer, *Carbide, nitride, and boride materials synthesis and processing*: Springer, 1997.

[124] F. Fabry, G. Flamant, and L. Fulcheri, "Carbon black processing by thermal plasma. Analysis of the particle formation mechanism," *Chemical Engineering Science,* vol. 56, pp. 2123-2132, 2001.

[125] L. Dever, R. Durand, J. C. Fontes, and P. Vachier, "Etude pedogenetique et isotopique des neoformations de calcite dans un sol sur craie Caracteristiques et origines," *Geochimica et Cosmochimica Acta,* vol. 47, pp. 2079-2090, 1983.

[126] R. Pristavita, N. Y. Mendoza-Gonzalez, J. L. Meunier, and D. Berk, "Carbon blacks produced by thermal plasma: the influence of the reactor geometry on the product morphology," *Plasma Chemistry and Plasma Processing,* vol. 30, pp. 267-279, 2010.

[127] H. Okuno, E. Grivei, F. Fabry, T. M. Gruenberger, J. Gonzalez-Aguilar, A. Palnichenko*, et al.*, "Synthesis of carbon nanotubes and nano-necklaces by thermal plasma process," *Carbon,* vol. 42, pp. 2543-2549, 2004.

[128] D. Harbec, J. L. Meunier, L. Guo, and J. Jureidini, "A parametric study of carbon nanotubes production from tetrachloroethylene using a supersonic thermal plasma jet," *Carbon,* vol. 45, pp. 2054-2064, 2007.

[129] S. I. Choi, J. S. Nam, C. M. Lee, S. S. Choi, J. I. Kim, J. M. Park*, et al.*, "High purity synthesis of carbon nanotubes by methane decomposition using an arc-jet plasma," *Current Applied Physics,* vol. 6, pp. 224-229, 2006.

[130] S. I. Choi, J. S. Nam, J. I. Kim, T. H. Hwang, J. H. Seo, and S. H. Hong, "Continuous process of carbon nanotubes synthesis by decomposition of methane using an arc-jet plasma," *Thin Solid Films,* vol. 506-507, pp. 244-249, 2006.

[131] J. Hahn, S. B. Heo, and J. S. Suh, "Catalyst free synthesis of high-purity carbon nanotubes by thermal plasma jet," *Carbon,* vol. 43, pp. 2638-2641, 2005.

[132] T. Ohishi, Y. Yoshihara, and O. Fukumasa, "Continuous synthesis of carbon nanoclusters using well-controlled thermal plasmas," *Surface and Coatings Technology,* vol. 202, pp. 5329-5332, 2008.

[133] X.-F. Guo and G.-J. Kim, "Ultrafine carbon black produced by pyrolysis of polyethylene using a novel DC-thermal plasma process," *Journal of Physics and Chemistry of Solids,* vol. 69, pp. 1224-1227, 2008/6// 2008.

[134] J.-c. Wang, Z.-p. Zhu, L.-p. Chang, and W.-r. Bao, "Synthesis of single-wall and cup-stacked carbon nanotubes by methane decomposition using constrained thermal plasma jet," *Carbon,* vol. 49, p. 353, 2010.

[135] J. Hahn, J. H. Han, J.-E. Yoo, H. Y. Jung, and J. S. Suh, "New continuous gas-phase synthesis of high purity carbon nanotubes by a thermal plasma jet," *Carbon,* vol. 42, pp. 877-883, 2004.

[136] D. Harbec, J. L. Meunier, L. Guo, R. Gauvin, and N. El Mallah, "Carbon nanotubes from the dissociation of C_2Cl_4 using a dc thermal plasma torch," *Journal of Physics D: Applied Physics,* vol. 37, pp. 2121-2126, 2004.

[137] C. D. Bromberg L, Rabinovich A, Alexeev N. , "Hydrogen manufacturing using low current, non-thermal plasma boosted fuel converters.," *Energy for the 21st century: Hydrogen Energy Symposium,* 2001.

[138] R. Castell, E. J. Iglesias, and J. Ruiz-Camacho, "Glow discharge plasma properties of gases of environmental interest," *Brazilian Journal of Physics,* vol. 34, pp. 1734-1737, 2004.

[139] http://en.wikipedia.org/wiki/Corona_discharge.

[140] C. Liu, N. Cui, N. M. D. Brown, and B. J. Meenan, "Effects of DBD plasma operating parameters on the polymer surface modification," *Surface and Coatings Technology,* vol. 185, pp. 311-320, 2004.

[141] C.-J. Liu, B. Xue, B. Eliasson, F. He, Y. Li, and G.-H. Xu, "Methane Conversion to Higher Hydrocarbons in the Presence of Carbon Dioxide Using Dielectric-Barrier Discharge Plasmas," *Plasma Chemistry and Plasma Processing,* vol. 21, pp. 301-310, 2001.

[142] V. Goujard, J.-M. Tatibouet, and C. Batiot-Dupeyrat, "Use of a non-thermal plasma for the production of synthesis gas from biogas," *Applied Catalysis A: General,* vol. 353, pp. 228-235, 2009.

[143] W. Cho, S. H. Lee, W. S. Ju, and Y. Baek, "Conversion of natural gas to hydrogen and carbon black by plasma and application of plasma black," 2004, pp. 181-183.

[144] J. H. Kim, Y. C. Hong, D. H. Shin, H. S. Uhm, and H. K. Shin, "Characterization of Carbon Powder Produced by a Microwave-Plasma Torch at Atmospheric Pressure," *Plasma Science, IEEE Transactions on,* vol. 34, pp. 2600-2605, 2006.

[145] T. Zieliński, T. Opalińska, and J. Kijeński, "Acetylene and Ethylene Carbon Blacks Production in Plasma Process," in *Plasma Processes and Polymers,* ed: Wiley-VCH Verlag GmbH & Co. KGaA, 2005, pp. 443-453.

[146] L. Fulcheri, N. Probst, G. Flamant, F. Fabry, E. Grivei, and X. Bourrat, "Plasma processing: a step towards the production of new grades of carbon black," *Carbon,* vol. 40, pp. 169-176, 2002.

[147] M. Meyyappan, "A review of plasma enhanced chemical vapour deposition of carbon nanotubes," *Journal of Physics D: Applied Physics,* vol. 42, p. 213001, 2009.

[148] S. Sufian, S. Yusup, G. S. Walker, and A. M. Shariff, "Synthesis of graphitic nanofibres using iron (III) oxide catalyst for hydrogen storage application," *Materials Research Innovations,* vol. 13, pp. 221-224, 2009.

[149] O. Smiljanic, B. L. Stansfield, J. P. Dodelet, A. Serventi, and S. Desilets, "Gas-phase synthesis of SWNT by an atmospheric pressure plasma jet," *Chemical Physics Letters,* vol. 356, pp. 189-193, 2002.

[150] H. Takikawa, M. Ikeda, K. Hirahara, Y. Hibi, Y. Tao, P. A. Ruiz Jr*, et al.*, "Fabrication of single-walled carbon nanotubes and nanohorns by means of a torch arc in open air," *Physica B: Condensed Matter,* vol. 323, pp. 277-279, 2002.

[151] O. Smiljanic, B. L. Stansfield, J. P. Dodelet, and A. Serventi, "Gas-phase synthesis of SWNT by an atmospheric pressure plasma jet," *Chemical Physics Letters,* vol. 356, pp. 189-193, 2002.

[152] J. Ondrej, P. Synek, L. Zajickova, and V. Kudrle, "Carbon nanotubes synthesis in microwave plasma torch at atmospheric pressure," *Materials Science and Engineering: C,* vol. 26, pp. 1189-1193, 2006.

[153] L. ZaJICKOVA, M. Ellas, L. Zajickova, and O. Jasek, "Atmospheric pressure microwave torch for synthesis of carbon nanotubes," *Plasma Physics and Controlled Fusion,* vol. 47, p. B655, 2005.

[154] A. Dato, V. Radmilovic, Z. Lee, J. Phillips, and M. Frenklach, "Substrate-Free Gas-Phase Synthesis of Graphene Sheets," *Nano Letters,* vol. 8, pp. 2012-2016, 2012/04/11 2008.

[155] Y.-F. Wang, C.-H. Tsai, W.-Y. Chang, and Y.-M. Kuo, "Methane steam reforming for producing hydrogen in an atmospheric-pressure microwave plasma reactor," *International Journal of Hydrogen Energy,* vol. 35, pp. 135-140, 2010.

[156] D. R. L. Vander Wal, M. T. a. Prof. Thomas, and V. E. Curtis, "Directed synthesis of metal-catalyzed carbon nanofibers and graphite encapsulated metal nanoparticles," *The Journal of Physical Chemistry B,* vol. 104, pp. 11606-11611, 2000.

[157] R. Ritikos, S. A. Rahman, S. M. A. Gani, M. R. Muhamad, and Y. K. Yap, "Catalyst-free formation of vertically-aligned carbon nanorods as induced by nitrogen incorporation," *Carbon,* vol. 49, pp. 1842-1848, 2011.

[158] A. Kocbach, Y. Li, K. Yttri, F. Cassee, P. Schwarze, and E. Namork, "Physicochemical characterisation of combustion particles from vehicle exhaust and residential wood smoke," *Particle and Fibre Toxicology,* vol. 3, p. 1, 2006.

[159] C. Journet, W. K. Maser, P. Bernier, A. Loiseau, M. Lamy de la Chapelle, S. Lefrant*, et al.*, "Large-scale production of single-walled carbon nanotubes by the electric-arc technique," *Nature,* vol. 388, pp. 756-758, // 1997.

[160] Y. Yabe, Y. Ohtake, T. Ishitobi, Y. Show, T. Izumi, and H. Yamauchi, "Synthesis of well-aligned carbon nanotubes by radio frequency plasma enhanced CVD method," *Diamond and Related Materials,* vol. 13, pp. 1292-1295, // 2004.

[161] K. I. Yoshie, S. Kasuya, K. Eguchi, and T. Yoshida, "Novel method for C_{60} synthesis: A thermal plasma at atmospheric pressure," *Applied Physics Letters,* vol. 61, pp. 2782-2783, // 1992.

[162] C. S. Lee, "A climatological model for forecasting typhoon rainfall in Taiwan," *26th Conference on Hurricanes and Tropical Meteorology,* pp. 132-133, // 2004.

[163] J. Hahn, J. H. Han, J. E. Yoo, H. Y. Jung, and J. S. Suh, "New continuous gas-phase synthesis of high purity carbon nanotubes by a thermal plasma jet," *Carbon,* vol. 42, pp. 877-883, 2004.

[164] O. Smiljanic, B. L. Stansfield, J. P. Dodelet, A. Serventi, and S. Désilets, "Gas-phase synthesis of SWNT by an atmospheric pressure plasma jet," *Chemical Physics Letters,* vol. 356, pp. 189-193, // 2002.

[165] Y. Tian, Y. Zhang, B. Wang, W. Ji, Y. Zhang, and K. Xie, "Coal-derived carbon nanotubes by thermal plasma jet," *Carbon,* vol. 42, pp. 2597-2601, // 2004.

[166] T. Watanabe, T. Notoya, T. Ishigaki, H. Kuwano, H. Tanaka, and Y. Moriyoshi, "Growth mechanism for carbon nanotubes in a plasma evaporation process," *Thin Solid Films,* vol. 506-507, pp. 263-267, 2006.

[167] H. Shi, L. Lai, I. K. Snook, and A. S. Barnard, "Relative Stability of Graphene Nanoflakes Under Environmentally Relevant Conditions," *The Journal of Physical Chemistry C,* vol. 117, pp. 15375-15382, 2013/07/25 2013.

[168] R. S. Edwards and K. S. Coleman, "Graphene Film Growth on Polycrystalline Metals," *Accounts of Chemical Research,* vol. 46, pp. 23-30, 2013/01/15 2012.

[169] M. G. Panthani, C. M. Hessel, D. Reid, G. Casillas, M. José-Yacamán, and B. A. Korgel, "Graphene-Supported High-Resolution TEM and STEM Imaging of Silicon Nanocrystals and their Capping Ligands," *The Journal of Physical Chemistry C,* vol. 116, pp. 22463-22468, 2012/10/25 2012.

[170] L. Tang, R. Ji, X. Cao, J. Lin, H. Jiang, X. Li*, et al.*, "Deep Ultraviolet Photoluminescence of Water-Soluble Self-Passivated Graphene Quantum Dots," *ACS Nano,* vol. 6, pp. 5102-5110, 2012/06/26 2012.

[171] Z. Tang, H. Kang, Z. Shen, B. Guo, L. Zhang, and D. Jia, "Grafting of Polyester onto Graphene for Electrically and Thermally Conductive Composites," *Macromolecules,* vol. 45, pp. 3444-3451, 2012/04/24 2012.

[172] S. W. Lee, C. Mattevi, M. Chhowalla, and R. M. Sankaran, "Plasma-Assisted Reduction of Graphene Oxide at Low Temperature and Atmospheric Pressure for Flexible Conductor Applications," *The Journal of Physical Chemistry Letters,* vol. 3, pp. 772-777, 2012/03/15 2012.

[173] V. Strong, S. Dubin, M. F. El-Kady, A. Lech, Y. Wang, B. H. Weiller*, et al.*, "Patterning and Electronic Tuning of Laser Scribed Graphene for Flexible All-Carbon Devices," *ACS Nano,* vol. 6, pp. 1395-1403, 2012/02/28 2012.

[174] I. Kaminska, M. R. Das, Y. Coffinier, J. Niedziolka-Jonsson, J. Sobczak, P. Woisel*, et al.*, "Reduction and Functionalization of Graphene Oxide Sheets Using Biomimetic Dopamine Derivatives in One Step," *ACS Applied Materials & Interfaces,* vol. 4, pp. 1016-1020, 2012/02/22 2012.

[175] F. Schäffel, M. Wilson, and J. H. Warner, "Motion of Light Adatoms and Molecules on the Surface of Few-Layer Graphene," *ACS Nano,* vol. 5, pp. 9428-9441, 2011/12/27 2011.

[176] X.-F. Li, L.-L. Wang, K.-Q. Chen, and Y. Luo, "Tuning the Electronic Transport Properties of Zigzag Graphene Nanoribbons via Hydrogenation Separators," *The Journal of Physical Chemistry C,* vol. 115, pp. 24366-24372, 2011/12/15 2011.

[177] Z. Sun, D. K. James, and J. M. Tour, "Graphene Chemistry: Synthesis and Manipulation," *The Journal of Physical Chemistry Letters,* vol. 2, pp. 2425-2432, 2011/10/06 2011.

[178] J. Pu, S. Wan, W. Zhao, Y. Mo, X. Zhang, L. Wang*, et al.*, "Preparation and Tribological Study of Functionalized Graphene–IL Nanocomposite Ultrathin Lubrication Films on Si Substrates," *The Journal of Physical Chemistry C,* vol. 115, pp. 13275-13284, 2011/07/14 2011.

[179] O. Akhavan, E. Ghaderi, and A. Esfandiar, "Wrapping Bacteria by Graphene Nanosheets for Isolation from Environment, Reactivation by Sonication, and Inactivation by Near-Infrared Irradiation," *The Journal of Physical Chemistry B,* vol. 115, pp. 6279-6288, 2011/05/19 2011.

[180] S. De Fonton, A. Oberlin, and M. Inagaki, "Characterization by electron microscopy of carbon phases (intermediate turbostratic phase and graphite) in hard carbons when heat-treated under pressure," *Journal of Materials Science,* vol. 15, pp. 909-917, 1980.

[181] L. K. Kim KS, Ju W, Hong SH, "Synthesis of nanostructured carbonaceous materials by thermal decomposition of methane using DC thermal plasmas," presented at the 17th international symposium on plasma chemistry, Toronto, Ontario, Canada, 2005.

[182] T. Zielinski and J. Kijenski, "Plasma carbon black-the new active additive for plastics," *Composites Part A: Applied Science and Manufacturing,* vol. 36, pp. 467-471, 2005.

[183] H. Conrads and M. Schmidt, "Plasma generation and plasma sources," *Plasma Sources Science and Technology,* vol. 9, p. 441, 2000.

[184] C. Liu, A. Marafee, R. Mallinson, and L. Lobban, "Methane conversion to higher hydrocarbons in a corona discharge over metal oxide catalysts with OH groups," *Applied Catalysis A: General,* vol. 164, pp. 21-33, 1997.

[185] M. W. Li, G. H. Xu, Y. L. Tian, L. Chen, and H. F. Fu, "Carbon Dioxide Reforming of Methane Using DC Corona Discharge Plasma Reaction," *Journal of Physical Chemistry A,* vol. 108, pp. 1687-1693, 2004.

[186] S. Chavadej, K. Supat, L. L. Lobban, and R. G. Mallinson, "Partial oxidation of methane and carbon dioxide reforming with methane in corona discharge with/without Pt/KL catalyst," *Journal of Chemical Engineering of Japan,* vol. 38, pp. 163-170, 2005.

[187] S. L. Yao, E. Suzuki, N. Meng, and A. Nakayama, "A High-Efficiency Reactor for the Pulsed Plasma Conversion of Methane," *Plasma Chemistry and Plasma Processing,* vol. 22, pp. 225-237, 2002.

[188] S. Kado, Y. Sekine, T. Nozaki, and K. Okazaki, "Diagnosis of atmospheric pressure low temperature plasma and application to high efficient methane conversion," *Catalysis Today,* vol. 89, pp. 47-55, 2004.

[189] S. Kado, K. Urasaki, Y. Sekine, K. Fujimoto, T. Nozaki, and K. Okazaki, "Reaction mechanism of methane activation using non-equilibrium pulsed discharge at room temperature," *Fuel,* vol. 82, pp. 2291-2297, 2003.

[190] S. Kado, K. Urasaki, Y. Sekine, and K. Fujimoto, "Direct conversion of methane to acetylene or syngas at room temperature using non-equilibrium pulsed discharge," *Fuel,* vol. 82, pp. 1377-1385, 2003.

[191] Istadi and N. A. S. Amin, "Co-generation of synthesis gas and C_{2+} hydrocarbons from methane and carbon dioxide in a hybrid catalytic-plasma reactor: A review," *Fuel,* vol. 85, pp. 577-592, 2006/4// 2006.

[192] B. Eliasson, C. J. Liu, and U. Kogelschatz, "Direct conversion of methane and carbon dioxide to higher hydrocarbons using catalytic dielectric-barrier discharges with zeolites," *Industrial and Engineering Chemistry Research,* vol. 39, pp. 1221-1227, 2000.

[193] Q. Z. Liu, J. v. Paradijs, and E. P. J. v. d. Heuvel, "A catalogue of low-mass X-ray binaries," *A&A,* vol. 368, pp. 1021-1054, 2001.

[194] M. Heintze and B. Pietruszka, "Plasma catalytic conversion of methane into syngas: the combined effect of discharge activation and catalysis," *Catalysis Today,* vol. 89, pp. 21-25, 2004.

[195] H. K. Song, H. Lee, J. W. Choi, and B. K. Na, "Effect of electrical pulse forms on the CO_2 reforming of methane using atmospheric dielectric barrier discharge," *Plasma Chemistry and Plasma Processing,* vol. 24, pp. 57-72, 2004.

[196] X. Zhang, B. Dai, A. Zhu, W. Gong, and C. Liu, "The simultaneous activation of methane and carbon dioxide to C_2 hydrocarbons under pulse corona plasma over La_2O_3/Al_2O_3 catalyst," *Catalysis Today,* vol. 72, pp. 223-227, 2002.

[197] D. W. Larkin, L. Zhou, L. L. Lobban, and R. G. Mallinson, "Product selectivity control and organic oxygenate pathways from partial oxidation of methane in a silent electric discharge reactor," *Industrial and Engineering Chemistry Research,* vol. 40, pp. 5496-5506, 2001.

[198] B. Eliasson and U. Kogelschatz, "Nonequilibrium volume plasma chemical processing," *Plasma Science, IEEE Transactions on,* vol. 19, pp. 1063-1077, 1991.

[199] F. Alexander, *Plasma Chemistry.* New York: Cambridge University Press, 2008.

[200] J. Hahn, H. Y. Jung, D. W. Kang, J. E. Yoo, and J. S. Suh, "Selective synthesis of high-purity carbon nanotubes by thermal plasma jet," *Carbon,* vol. 42, pp. 3024-3027, 2004.

[201] V. K. Liau, M. T. C. Fang, J. D. Yan, and A. I. Al-Shamma'a, "A two-temperature model for a microwave generated argon plasma jet at atmospheric pressure," *Journal of Physics D: Applied Physics,* vol. 36, p. 2774, 2003.

[202] A. Bernard, P. Cloth, H. Conrads, A. Coudeville, G. Gourlan, A. Jolas*, et al.*, "The dense plasma focus A high intensity neutron source," *Nuclear Instruments and Methods,* vol. 145, pp. 191-218, 1977.

[203] B. Deepak, T. R. Govindan, and M. Meyyappan, "Modelling of magnetic field profile effects in a helicon source," *Plasma Sources Science and Technology,* vol. 13, p. 553, 2004.

[204] "Modeling of a helicon plasma source," *IEEE Transactions on Plasma Science,* vol. 31, p. 464, 2003.

[205] "Optimization of plasma density and radial uniformity of a point-cusp magnetic field applied capacitive plasma," *Journal of Vacuum Science & Technology A Vacuum Surfaces and Films,* vol. 18, p. 823, 2000.

[206] C. Carter and J. Khachan, "Downstream plasma characteristics from a single loop antenna in a helicon processing reactor," *Plasma Sources Science and Technology,* vol. 8, p. 432, 1999.

[207] M. A. Lieberman and S. Ashida, "Global models of pulse-power-modulated high-density, low-pressure discharges," *Plasma Sources Science and Technology,* vol. 5, p. 145, 1996.

[208] C. Charles, W. Cox, R. W. Boswell, R. Laine, and M. Perren, "Experimental investigation of a conical helicon double layer thruster arrangement," *Plasma Sources Science and Technology,* vol. 19, p. 045003, 2010.

[209] F. C. M and M. M, "Microwave Discharges, Fundamentals and Applications," presented at the NATO ASI Series, Series B: Physics vol 302, New York: Plenum, 1993.

[210] S. A. Gower, "Development of a high power microwave plasma beam applicator," *Review of Scientific Instruments,* vol. 72, p. 4273, 2001.

[211] P. Chingombe, B. Saha, and R. J. Wakeman, "Surface modification and characterisation of a coal-based activated carbon," *Carbon,* vol. 43, pp. 3132-3143, // 2005.

[212] C. Y. Yin, M. K. Aroua, and W. M. A. W. Daud, "Review of modifications of activated carbon for enhancing contaminant uptakes from aqueous solutions," *Separation and Purification Technology,* vol. 52, pp. 403-415, 1// 2007.

[213] J. M. Encinar, F. J. Beltran, A. Ramiro, and J. F. Gonzalez, "Pyrolysis/gasification of agricultural residues by carbon dioxide in the presence of different additives: influence of variables," *Fuel Processing Technology,* vol. 55, pp. 219-233, 1998.

[214] Z. Merzougui and F. Addoun, "Effect of oxidant treatment of date pit activated carbons application to the treatment of waters," *Desalination,* vol. 222, pp. 394-403, 2008.

[215] Shen, "Surface Chemical Functional Groups Modification of Porous Carbon," *Recent Patent on Chemical Engineering,* vol. 1, pp. 27-40, 2008.

[216] B. R. Puri, "PHYSICOCHEMICAL ASPECTS OF CARBON AFFECTING ADSORPTION FROM THE AQUEOUS PHASE," 1983, pp. 77-93.

[217] Y. Otake and R. G. Jenkins, "Characterization of oxygen-containing surface complexes created on a microporous carbon by air and nitric acid treatment," *Carbon,* vol. 31, pp. 109-121, // 1993.

[218] A. Miyazaki, K. Shibazaki, Y. Nakano, M. Ogawa, and I. Balint, "Efficient catalytic reduction of concentrated nitric acid on the adsorption sites of activated carbon," *Chemistry Letters,* vol. 33, pp. 418-419, // 2004.

[219] J. W. Patrick, *Porosity in Carbons: Characterization and applications*. London: Halsted Press, 1995.

[220] H. Marsh and F. Rodríguez-Reinoso, *Activated Carbon*: Elsevier Science Limited., 2006.

[221] M. Ahmedna, W. E. Marshall, and R. M. Rao, "Surface properties of granular activated carbons from agricultural by-products and their effects on raw sugar decolorization," *Bioresource Technology,* vol. 71, pp. 103-112, // 2000.

[222] A. Ould-Idriss, M. Stitou, E. M. Cuerda-Correa, C. Fernández-González, A. Macías-García, M. F. Alexandre-Franco*, et al.*, "Preparation of activated carbons from olive-tree wood revisited. II. Physical activation with air," *Fuel Processing Technology,* vol. 92, pp. 266-270, // 2011.

[223] A. A. Attia, W. E. Rashwan, and S. A. Khedr, "Capacity of activated carbon in the removal of acid dyes subsequent to its thermal treatment," *Dyes and Pigments,* vol. 69, pp. 128-136, // 2006.

[224] H. L. Chiang, P. C. Chiang, and C. P. Huang, "Ozonation of activated carbon and its effects on the adsorption of VOCs exemplified by methylethylketone and benzene," *Chemosphere,* vol. 47, pp. 267-275, // 2002.

[225] J. R. Rangel-Mendez and F. S. Cannon, "Improved activated carbon by thermal treatment in methane and steam: Physicochemical influences on MIB sorption capacity," *Carbon,* vol. 43, pp. 467-479, // 2005.

[226] J. W. Yoo, T. Y. Kim, S. Y. Cho, S. G. Rho, and S. J. Kim, "Adsorption and desorption characteristics of maltooligosaccharide for the surface treated activated carbons," *Adsorption,* vol. 11, pp. 719-723, // 2005.

[227] Ö. Şahin and C. Saka, "Preparation and characterization of activated carbon from acorn shell by physical activation with H_2O–CO_2 in two-step pretreatment," *Bioresource Technology,* vol. 136, pp. 163-168, 5// 2013.

[228] M. L. Sekirifa, M. Hadj-Mahammed, S. Pallier, L. Baameur, D. Richard, and A. H. Al-Dujaili, "Preparation and characterization of an activated carbon from a date stones variety by physical activation with carbon dioxide," *Journal of Analytical and Applied Pyrolysis,* vol. 99, pp. 155-160, 1// 2013.

[229] M. Belhachemi, R. V. R. A. Rios, F. Addoun, J. Silvestre-Albero, A. Sepilveda-Escribano, and F. Rodriguez-Reinoso, "Preparation of activated carbon from date pits: Effect of the activation agent and liquid phase oxidation," *Journal of Analytical and Applied Pyrolysis,* vol. 86, pp. 168-172, 2009.

[230] J. Rivera-Utrilla, I. Bautista-Toledo, M. A. Ferro-García, and C. Moreno-Castilla, "Activated carbon surface modifications by adsorption of bacteria and their effect on aqueous lead adsorption," *Journal of Chemical Technology & Biotechnology,* vol. 76, pp. 1209-1215, 2001.

[231] R. H. Myers and D. C. Montgomery, *Response Surface Methodology: Process and Product Optimization Using Designed Experiments*: Wiley, 2002.

[232] G. E. P. Box and N. R. Draper, *Empirical model-building and response surfaces*: Wiley, 1987.

[233] R. H. Myers, D. C. Montgomery, and C. M. Anderson-Cook, *Response Surface Methodology: Process and Product Optimization Using Designed Experiments*: Wiley, 2011.

[234] D. C. Montgomery, *Design and Analysis of Experiments, Minitab Manual*: John Wiley & Sons, 2010.

[235] A. J. G. Schoofs, *Experimental Design and Structural Optimization*: Technische Universiteit Eindhoven, 1987.

[236] A. M. M. Vargas, C. A. Garcia, E. M. Reis, E. Lenzi, W. F. Costa, and V. C. Almeida, "NaOH-activated carbon from flamboyant (Delonix regia) pods: Optimization of preparation conditions using central composite rotatable design," *Chemical Engineering Journal,* vol. 162, pp. 43-50, // 2010.

[237] W. Zhao, V. Fierro, C. Zlotea, E. Aylon, M. T. Izquierdo, M. Latroche*, et al.*, "Optimization of activated carbons for hydrogen storage," *International Journal of Hydrogen Energy,* vol. 36, pp. 11746-11751, 2011.

[238] M. Arulkumar, P. Sathishkumar, and T. Palvannan, "Optimization of Orange G dye adsorption by activated carbon of Thespesia populnea pods using response surface methodology," *Journal of Hazardous Materials,* vol. 186, pp. 827-834, // 2011.

[239] T. Lundstedt, E. Seifert, L. Abramo, B. Thelin, A. Nyström, J. Pettersen*, et al.*, "Experimental design and optimization," *Chemometrics and Intelligent Laboratory Systems,* vol. 42, pp. 3-40, // 1998.

[240] D. C. Montgomery, *Design and analysis of experiments*, 7th ed.: Wiley, 2009.

[241] M. D. Morris, "Class of three-level experimental designs for response surface modeling," *Technometrics,* vol. 42, pp. 111-121, // 2000.

[242] K. Mahalik, J. N. Sahu, A. V. Patwardhan, and B. C. Meikap, "Statistical modelling and optimization of hydrolysis of urea to generate ammonia for flue gas conditioning," *Journal of Hazardous Materials,* vol. 182, pp. 603-610, 2010.

[243] J. N. Sahu, B. C. Meikap, and A. V. Patwardhan, "Optimization for the Production of Ammonia from Urea in a Semi-batch Reactor for Safe Feedstock in Power Plants: Experimental and Statistical Studies," *CLEAN – Soil, Air, Water,* vol. 38, pp. 533-542, 2010.

[244] M. K. B. Gratuito, T. Panyathanmaporn, R. A. Chumnanklang, N. Sirinuntawittaya, and A. Dutta, "Production of activated carbon from coconut shell: Optimization using response surface methodology," *Bioresource Technology,* vol. 99, pp. 4887-4895, // 2008.

[245] B. H. Hameed, I. A. W. Tan, and A. L. Ahmad, "Optimization of basic dye removal by oil palm fibre-based activated carbon using response surface methodology," *Journal of Hazardous Materials,* vol. 158, pp. 324-332, // 2008.

[246] V. Torné-Fernández, J. M. Mateo-Sanz, D. Montané, and V. Fierro, "Statistical optimization of the synthesis of highly microporous carbons by chemical activation of kraft lignin with NaOH," *Journal of Chemical and Engineering Data,* vol. 54, pp. 2216-2221, // 2009.

[247] M. T. Izquierdo, A. Martínez de Yuso, B. Rubio, and M. R. Pino, "Conversion of almond shell to activated carbons: Methodical study of the chemical activation based on an experimental design and relationship with their characteristics," *Biomass and Bioenergy,* vol. 35, pp. 1235-1244, // 2011.

[248] G. E. P. Box and N. R. Draper, "A basis for the selection of a response surface design," *Journal of the American Statistical Association,* vol. 54, pp. 622-654, 1959.

[249] G. E. P. Box and D. W. Behnken, "Some new three level designs for the study of quantitative variables," *Technometrics,* vol. 2, pp. 455-475, 1960.

[250] W. L. Bragg, "The diffraction of Short Electromagnetic Waves by a crystal," *Proceeding of the Cambridge Philosophical Society,* vol. 17, pp. 43-57, 1913.

[251] R. Evans, U. M. B. Marconi, and P. Tarazona, "Capillary condensation and adsorption in cylindrical and slit-like pores," *Journal of the Chemical Society, Faraday Transactions 2: Molecular and Chemical Physics,* vol. 82, pp. 1763-1787, 1986.

[252] M. Thommes, "Physical Adsorption Characterization of Nanoporous Materials," *Chemie Ingenieur Technik,* vol. 82, pp. 1059-1073, 2010.

[253] S. J. Gregg and K. S. W. Sing., "Adsorption, surface area, and porosity 2nd ed.," pp. p.3-5, 1982.

[254] J. H. d. Boer, *The Structure and Properties of Porous Materials.* Lonon: Butterworths, 1958.

[255] S. Lowell, J. Shields, G. Charalambous, and J. Manzione, *J.Colloid. Interface Sci.,* vol. 86, p. 191, 1982.

[256] J. H. CHAN and S. T.BALKE, "The thermal degradation kinetics of polypropylene : Part III. Thermogravimetric analyses," *Polymer degradation and stability,* vol. 57, pp. 135-149, 1997.

[257] Z. Li, M. Jinghong, Z. Xinyuan, and L. Borun, "Kinetics of thermal degradation of thermotropic poly(p-oxybenzoate-coethylene terephthalate) by single heating rate methods," *Journal of Applied Polymer Science,* vol. 91, pp. 3915-3920, 2004.

[258] Y. Wang, D. C. Alsmeyer, and R. L. McCreery, "Raman spectroscopy of carbon materials: structural basis of observed spectra," *Chemistry of Materials,* vol. 2, pp. 557-563, 1990/09/01 1990.

[259] M. J. Pelletier, *Analytical Applications of Raman Spectroscopy*: Wiley, 1999.

[260] E. Smith and G. Dent, *Modern Raman Spectroscopy: A Practical Approach*: Wiley, 2013.

[261] A. Jorio, M. A. Pimenta, A. G. S. Filho, R. Saito, G. Dresselhaus, and M. S. Dresselhaus, "Characterizing carbon nanotube samples with resonance raman scattering," *J. New. Phys.,* vol. 5, p. 139, // 2003.

[262] A. B. Fuertes and S. Alvarez, "Graphitic mesoporous carbons synthesised through mesostructured silica templates," *Carbon,* vol. 42, pp. 3049-3055, 2004.

[263] N. Kasahara, S. Shiraishi, and A. Oya, "Heterogeneous graphitization of thin carbon fiber derived from phenol-formaldehyde resin," *Carbon,* vol. 41, pp. 1654-1656, 2003.

[264] T. Hyeon, S. Han, Y.-E. Sung, K.-W. Park, and Y.-W. Kim, "High-Performance Direct Methanol Fuel Cell Electrodes using Solid-Phase-Synthesized Carbon Nanocoils," *Angewandte Chemie International Edition,* vol. 42, pp. 4352-4356, 2003.

[265] F. J. Maldonado-Hódar, C. Moreno-Castilla, J. Rivera-Utrilla, Y. Hanzawa, and Y. Yamada, "Catalytic Graphitization of Carbon Aerogels by Transition Metals," *Langmuir,* vol. 16, pp. 4367-4373, 2000.

[266] Krishna PA, Gary F, Alexander F, and A. MC, "Non-thermal dielectric barrier discharge plasma induces angiogenesis through reactive oxygen species," *J. R. Soc. Interface,* vol. 9, pp. 147-157, January 7, 2012.

[267] J. Zheng, R. Yang, L. Xie, J. Qu, Y. Liu, and X. Li, "Plasma-Assisted Approaches in Inorganic Nanostructure Fabrication," *Advanced Materials,* vol. 22, pp. 1451–1473, 2010.

[268] Gallona HJ , Tu X , Twiggb MV , and Whiteheada JC "Plasma-assisted methane reduction of a NiO catalyst-Low temperature activation of methane and formation of carbon nanofibres," *Applied Catalysis B Environmental,* vol. 106, pp. 616-620, 2011.

[269] F. Ding and K. Bolton, "The importance of supersaturated carbon concentration and its distribution in catalytic particles for single-walled carbon nanotube nucleation," *Nanotechnology,* vol. 17, pp. 543-8, 2006.

[270] A. Hashimoto, K. Suenaga, A. Gloter, K. Urita, and S. Iijima, "Direct evidence for atomic defects in graphene layers," *Nature,* vol. 430, pp. 870-873, 2004.

[271] J. P. Gore and A. Sane, *Flame Synthesis of Carbon Nanotubes. In: Siva Yellampalli, Editor. Carbon Nanotubes - Synthesis, Characterization, Applications.*: InTech, , 2011, p.122-32.

[272] F. Bernardoni, M. Kouba, and A. Y. Fadeev, "Effect of Curvature on the Packing and Ordering of Organosilane Monolayers Supported on Solids," *Chemistry of Materials,* vol. 20, pp. 382-387, 2007.

[273] G. Xu, G. Zeng, Z. Yin, and J. Zhang, "Recent Advances on the Treatment Technologics of Ammonia-Nitrogen Wastewater," *Hunan Nonferrous Metals,* vol. 2, pp. 33-45, 2002.

[274] H. F. Abbas and W. M. A. Wan Daud, "Hydrogen production by methane decomposition: A review," *International Journal of Hydrogen Energy,* vol. 35, pp. 1160-1190, 2009.

[275] C. Chou, "Detailed model of the afterglow region of a microwave generated oxygen plasma," *J. Appl. Phys.,* vol. 72, pp. 870-8, 1992.

[276] M. Tian, S. Batty, and C. Shang, "Synthesis of nanostructured carbons by the microwave plasma cracking of methane," *Carbon,* vol. 51, pp. 243-8, 2012.

[277] A. Vohra and T. Satyanarayana, "Statistical optimization of the medium components by response surface methodology to enhance phytase production by Pichia anomala," *Process Biochemistry,* vol. 37, pp. 999-1004, 2002.

[278] G. E. P. Box, "Multi-factor designs of first order," *Biometrika,* vol. 39, pp. 49-57, 1952.

[279] P. Chen, H. B. Zhang, G. D. Lin, Q. Hong, and K. R. Tsai, "Growth of carbon nanotubes by catalytic decomposition of CH_4 or CO on a NiO-MgO catalyst," *Carbon,* vol. 35, pp. 1495-1501, 1997.

[280] J. N. Sahu, J. Acharya, and B. C. Meikap, "Response surface modeling and optimization of chromium(VI) removal from aqueous solution using Tamarind wood activated carbon in batch process," *Journal of Hazardous Materials,* vol. 172, pp. 818-825, 2009.

[281] J. N. Sahu, J. Acharya, and B. C. Meikap, "Optimization of production conditions for activated carbons from Tamarind wood by zinc chloride using response surface methodology," *Bioresource Technology,* vol. 101, pp. 1974-1982, 2009.

[282] W. Zhi, J. Song, F. Ouyang, and J. Bi, "Application of response surface methodology to the modeling of a-amylase purification by aqueous two-phase systems," *Journal of Biotechnology,* vol. 118, pp. 157-165, 2005.

[283] F. Rodriguez-Reinoso and M. Molina-Sabio, "Activated carbons from lignocellulosic materials by chemical and/or physical activation: an overview," *Carbon,* vol. 30, pp. 1111-1118, 1992.

[284] Y. Sudaryanto, S. B. Hartono, W. Irawaty, H. Hindarso, and S. Ismadji, "High surface area activated carbon prepared from cassava peel by chemical activation," *Bioresource Technology,* vol. 97, pp. 734-739, 2006.

[285] W. Li, H. Zhang, C. Wang, Y. Zhang, L. Xu, K. Zhu*, et al.*, "Raman characterization of aligned carbon nanotubes produced by thermal decomposition of hydrocarbon vapor," *Applied Physics Letters,* vol. 70, pp. 2684-2686, 1997.

[286] A. C. Ferrari and J. Robertson, "Resonant Raman spectroscopy of disordered, amorphous, and diamond like carbon," *Phys Rev B,* vol. 61, pp. 14095-14100, 2000.

[287] K. Al-Qurashi and A. L. Boehman, "Impact of exhaust gas recirculation (EGR) on the oxidative reactivity of diesel engine soot," *Combustion and Flame,* vol. 155, pp. 675-695, 2008.

[288] N. P. Ivleva, A. Messerer, X. Yang, and R. Niessner, "Raman microspectroscopic analysis of changes in the chemical structure and reactivity of soot in a diesel exhaust

aftertreatment model system," *Environmental Science and Technology,* vol. 41, pp. 3702-3707, 2007.

[289] A. Bacaoui, A. Yaacoubi, A. Dahbi, C. Bennouna, R. Phan Tan Luu, F. J. Maldonado-Hodar*, et al.*, "Optimization of conditions for the preparation of activated carbons from olive-waste cakes," *Carbon,* vol. 39, pp. 425-432, 2001.

[290] Baker R.T.K., Barber M.A., Harris P.S., F. F.S., and W. R.J., "Nucleation and growth of carbon deposits from the nickel catalyzed decomposition of zcetylene," *Journal of Catalysis,* vol. 26, pp. 51-62, 1972.

[291] M. S. Dresselhaus and I. L. Thomas, "Alternative energy technologies," *Nature,* vol. 414, pp. 332-337, 2001.

[292] M. U. Niemann, S. S. Srinivasan, A. R. Phani, A. Kumar, D. Y. Goswami, and E. K. Stefanakos, "Nanomaterials for hydrogen storage applications: a review," *Journal of Nanomaterials,* vol. 2008, 2008.

[293] L. P. Ma, P. Wang, and H. M. Cheng, "Hydrogen sorption kinetics of MgH_2 catalyzed with titanium compounds," *International Journal of Hydrogen Energy,* vol. 35, pp. 3046-3050, 2010.

[294] M. Tian and C. Shang, "Nano-structured MgH_2 catalyzed by TiC nanoparticles for hydrogen storage," *Journal of Chemical Technology & Biotechnology,* vol. 86, pp. 69-74, 2011.

[295] C. X. Shang, M. Bououdina, Y. Song, and Z. X. Guo, "Mechanical alloying and electronic simulations of (MgH_2+ M) systems (M= Al, Ti, Fe, Ni, Cu and Nb) for hydrogen storage," *International Journal of Hydrogen Energy,* vol. 29, pp. 73-80, 2004.

[296] J. H. Shin, G. J. Lee, Y. W. Cho, and K. S. Lee, "Improvement of hydrogen sorption properties of MgH_2 with various sizes and stoichiometric compositions of TiC," *Catalysis Today,* vol. 146, pp. 209-215, 2009.

[297] M. Tian and C. Shang, "Effect of TiC and Mo_2C on Hydrogen Desorption of Mechanically Milled MgH_2," *Journal of Chemical Science and Technology,* vol. 1, pp. 54-59, 2012.

[298] J. H. Shin, G.-J. Lee, Y. W. Cho, and K. S. Lee, "Improvement of hydrogen sorption properties of MgH_2 with various sizes and stoichiometric compositions of TiC," *Catalysis Today,* vol. 146, pp. 209-215, 2009.

[299] P.-J. Wang, Z.-Z. Fang, L.-P. Ma, X.-D. Kang, and P. Wang, "Effect of carbon addition on hydrogen storage behaviors of Li-Mg-B-H system," *International Journal of Hydrogen Energy,* vol. 35, pp. 3072-3075, 2010.

[300] C. Wu, P. Wang, X. Yao, C. Liu, D. Chen, G. Q. Lu*, et al.*, "Effects of SWNT and metallic catalyst on hydrogen absorption/desorption performance of MgH2," *Journal of Physical Chemistry B,* vol. 109, pp. 22217-22221, 2005.

[301] Z. Z. Fang, X. D. Kang, H. B. Dai, M. J. Zhang, P. Wang, and H. M. Cheng, "Reversible dehydrogenation of $LiBH_4$ catalyzed by as-prepared single-walled carbon nanotubes," *Scripta Materialia,* vol. 58, pp. 922-925, 2008.

[302] S. Ruggeri, L. Roue, G. Liang, J. Huot, and R. Schulz, "Influence of carbon on the electrode characteristics of MgNi prepared by mechanical alloying," *Journal of Alloys and Compounds,* vol. 343, pp. 170-178, 2002.

[303] C. Iwakura, H. Inoue, S. G. Zhang, and S. Nohara, "A new electrode material for nickel-metal hydride batteries: MgNi-graphite composites prepared by ball-milling," *Journal of Alloys and Compounds,* vol. 293-295, pp. 653-657, 1999.

[304] T. Yildirim and S. Ciraci, "Titanium-Decorated Carbon Nanotubes as a Potential High-Capacity Hydrogen Storage Medium," *Physical Review Letters,* vol. 94, p. 175501, 2005.

[305] J. Wang, A. D. Ebner, T. Prozorov, R. Zidan, and J. A. Ritter, "Effect of graphite as a co-dopant on the dehydrogenation and hydrogenation kinetics of Ti-doped sodium aluminum hydride," *Journal of Alloys and Compounds,* vol. 395, pp. 252-262, 2005.

[306] M. Lototskyy, J. M. Sibanyoni, R. V. Denys, M. Williams, B. G. Pollet, and V. A. Yartys, "Magnesium-carbon hydrogen storage hybrid materials produced by reactive ball milling in hydrogen," *Carbon,* vol. 57, pp. 146-160, 2013.

[307] M. Tian, S. Batty, and C. Shang, "Synthesis of nanostructured carbons by the microwave plasma cracking of methane," *Carbon,* 2012.

[308] H.-B. Zhang, X.-L. Liang, X. Dong, H.-Y. Li, and G.-D. Lin, "Multi-Walled Carbon Nanotubes as a Novel Promoter of Catalysts for CO/CO_2 Hydrogenation to Alcohols," *Catalysis Surveys from Asia,* vol. 13, pp. 41-58, 2009.

[309] J. H. Chan and S. T. Balke, "The thermal degradation kinetics of polypropylene: Part III. Thermogravimetric analyses," *Polymer Degradation and Stability,* vol. 57, pp. 135-149, 1997.

[310] X.-G. Li, M.-R. Huang, G.-H. Guan, and T. Sun, "Kinetics of thermal degradation of thermotropic poly(p-oxybenzoate-co-ethylene terephthalate) by single heating rate methods," *Polymer International,* vol. 46, pp. 289-297, 1998.

[311] P.-J. Wang, Z.-Z. Fang, L.-P. Ma, X.-D. Kang, and P. Wang, "Effect of carbon addition on hydrogen storage behaviors of Li-Mg-B-H system," *International Journal of Hydrogen Energy,* vol. 35, pp. 3072-3075, 2008.

[312] N. Pierard, A. Fonseca, J. F. Colomer, C. Bossuot, J. M. Benoit, G. Van Tendeloo, *et al.*, "Ball milling effect on the structure of single-wall carbon nanotubes," *Carbon,* vol. 42, pp. 1691-1697, 2004.

[313] X. H. Chen, H. S. Yang, G. T. Wu, M. Wang, F. M. Deng, X. B. Zhang, *et al.*, "Generation of curved or closed-shell carbon nanostructures by ball-milling of graphite," *Journal of Crystal Growth,* vol. 218, pp. 57-61, 2000.

[314] X. Xu and C. Song, "Improving hydrogen storage/release properties of magnesium with nano-sized metal catalysts as measured by tapered element oscillating microbalance," *Applied Catalysis A: General,* vol. 300, pp. 130-138, 2006.

[315] J. A. Menéndez , L. R. Radovic, B. Xia, and J. Phillips, "Low-Temperature Generation of Basic Carbon Surfaces by Hydrogen Spillover," *The Journal of Physical Chemistry,* vol. 100, pp. 17243-17248, 2012/09/19 1996.

[316] C.-S. Tsao, Y. Liu, H.-Y. Chuang, H.-H. Tseng, T.-Y. Chen, C.-H. Chen, *et al.*, "Hydrogen Spillover Effect of Pt-Doped Activated Carbon Studied by Inelastic Neutron Scattering," *The Journal of Physical Chemistry Letters,* vol. 2, pp. 2322-2325, 2012/09/19 2011.

[317] G. M. Pajonk, S. J. Teichner, and J. E. Germain, Eds. , "Spillover of Adsorbed Species," presented at the Elsevier, Amsterdam, 1983.

[318] N. M. Rodriguez and R. T. K. Baker, "Interaction of Hydrogen with Metal Sulfide Catalysts - Direct Observation of Spillover," *Journal of Catalysis,* vol. 140, pp. 287-301, 1993.

[319] M. Boudart, A. W. Aldag, and M. A. Vannice, "On the slow uptake of hydrogen by platinized carbon," *Journal of Catalysis,* vol. 18, pp. 46-51, 1970.

[320] J. Wang, A. D. Ebner, and J. A. Ritter, "Kinetic behavior of Ti-doped $NaAlH_4$ when cocatalyzed with carbon nanostructures," *The journal of physical chemistry. B,* vol. 110, pp. 17353-17358, 2006.

[321] S. Aminorroaya, H. K. Liu, Y. Cho, and A. Dahle, "Microstructure and activation characteristics of Mg-Ni alloy modified by multi-walled carbon nanotubes," *International Journal of Hydrogen Energy,* vol. 35, pp. 4144-4153, 2010.

[322] Y. Wang, K. Wang, C. Guan, Z. He, Z. Lu, T. Chen, *et al.*, "Surface functionalization-enhanced spillover effect on hydrogen storage of Ni-B nanoalloy-doped activated carbon," *International Journal of Hydrogen Energy,* vol. 36, pp. 13663-13668, 2010.

[323] C. Wu and H.-M. Cheng, "Effects of carbon on hydrogen storage performances of hydrides," *Journal of Materials Chemistry,* vol. 20, pp. 5390-5400, 2010.

[324] X. Yao, C. Wu, A. Du, J. Zou, Z. Zhu, P. Wang, *et al.*, "Metallic and Carbon Nanotube-Catalyzed Coupling of Hydrogenation in Magnesium," *Journal of the American Chemical Society,* vol. 129, pp. 15650-15654, 2012/09/26 2007.

[325] M. A. Lillo-Rodenas, K. F. Aguey-Zinsou, D. Cazorla-Amoros, A. Linares-Solano, and Z. X. Guo, "Effects of Carbon-Supported Nickel Catalysts on MgH_2 Decomposition," *The Journal of Physical Chemistry C,* vol. 112, pp. 5984-5992, 2012/09/26 2008.

[326] M. A. Lillo-Rodenas, Z. X. Guo, K. F. Aguey-Zinsou, D. Cazorla-Amoros, and A. Linares-Solano, "Effects of different carbon materials on MgH_2 decomposition," *Carbon,* vol. 46, pp. 126-137, 2008.

[327] M. K. Mondal, H. K. Balsora, and P. Varshney, "Progress and trends in CO_2 capture/separation technologies: A review," *Energy,* 2012.

[328] S. García, J. J. Pis, F. Rubiera, and C. Pevida, "Predicting Mixed-Gas Adsorption Equilibria on Activated Carbon for Precombustion CO2 Capture," *Langmuir,* vol. 29, pp. 6042-6052, 2013/05/21 2013.

[329] Cheng-Hsiu Yu, Chih-Hung Huang, and C.-S. Tan, "A Review of CO_2 Capture by Absorption and Adsorption " *Aerosol and Air Quality Research,* vol. 12, pp. 745-769, 2012.

[330] D. M. D'Alessandro, B. Smit, and J. R. Long, "Carbon Dioxide Capture: Prospects for New Materials," *Angewandte Chemie International Edition,* vol. 49, pp. 6058-6082, 2010.

[331] M. B. Yue, L. B. Sun, Y. Cao, Z. J. Wang, Y. Wang, Q. Yu, *et al.*, "Promoting the CO_2 adsorption in the amine-containing SBA-15 by hydroxyl group," *Microporous and Mesoporous Materials,* vol. 114, pp. 74-81, 9/1/ 2008.

[332] R. S. Franchi, P. J. E. Harlick, and A. Sayari, "Applications of pore-expanded mesoporous silica. 2. Development of a high-capacity, water-tolerant adsorbent for CO_2," *Industrial and Engineering Chemistry Research,* vol. 44, pp. 8007-8013, // 2005.

[333] S. Kim, J. Ida, V. V. Guliants, and J. Y. S. Lin, "Tailoring pore properties of MCM-48 silica for selective adsorption of CO_2," *Journal of Physical Chemistry B,* vol. 109, pp. 6287-6293, // 2005.

[334] B. Feng, H. An, and E. Tan, "Screening of CO_2 adsorbing materials for zero emission power generation systems," *Energy and Fuels,* vol. 21, pp. 426-434, // 2007.

[335] X. Xu, C. Song, J. M. Andresen, B. G. Miller, and A. W. Scaroni, "Novel polyethylenimine-modified mesoporous molecular sieve of MCM-41 type as high-capacity adsorbent for CO_2 capture," *Energy and Fuels,* vol. 16, pp. 1463-1469, // 2002.

[336] R. V. Siriwardane, M. S. Shen, E. P. Fisher, and J. Losch, "Adsorption of CO_2 on zeolites at moderate temperatures," *Energy and Fuels,* vol. 19, pp. 1153-1159, // 2005.

[337] C. F. Martín, M. G. Plaza, J. J. Pis, F. Rubiera, C. Pevida, and T. A. Centeno, "On the limits of CO_2 capture capacity of carbons," *Separation and Purification Technology,* vol. 74, pp. 225-229, // 2010.

[338] L.-Y. Meng and S.-J. Park, "MgO-templated porous carbons-based CO_2 adsorbents produced by KOH activation," *Materials Chemistry and Physics,* vol. 137, pp. 91-96, 11/15/ 2012.

[339] A. A. Olajire, "CO$_2$ capture and separation technologies for end-of-pipe applications: A review," *Energy,* vol. 35, pp. 2610-2628, 2011.

[340] J. Przepiórski, "Chapter 9 Activated carbon filters and their industrial applications," in *Interface Science and Technology*. vol. Volume 7, J. B. Teresa, Ed., ed: Elsevier, 2006, pp. 421-474.

[341] Z. Pan and L. D. Connell, "Comparison of adsorption models in reservoir simulation of enhanced coalbed methane recovery and CO2 sequestration in coal," *International Journal of Greenhouse Gas Control,* vol. 3, pp. 77-89, 1// 2009.

[342] S. J. Bhadra, A. D. Ebner, and J. A. Ritter, "On the Use of the Dual Process Langmuir Model for Predicting Unary and Binary Isosteric Heats of Adsorption," *Langmuir,* vol. 28, pp. 6935-6941, 2012/05/01 2012.

[343] J. A. Ritter, S. J. Bhadra, and A. D. Ebner, "On the Use of the Dual-Process Langmuir Model for Correlating Unary Equilibria and Predicting Mixed-Gas Adsorption Equilibria," *Langmuir,* vol. 27, pp. 4700-4712, 2011/04/19 2011.

[344] D. M. Ruthven, *Principles of Adsorption and Adsorption Processes*. New York: John Wiley & Sons, 1984.

[345] D. D. Do, *Adsorption Analysis: Equilibria and Kinetics* vol. 2. London: Imperial College Press, 1998.

[346] H. Moon and C. Tien, "Adsorption of gas mixtures on adsorbents with heterogeneous surfaces," *Chemical Engineering Science,* vol. 43, pp. 2967-2980, // 1988.

[347] Z. Ling, M. Zheng, Q. Du, Y. Wang, J. Song, W. Dai*, et al.*, "Synthesis of mesoporous MgO nanoplate by an easy solvothermal–annealing method," *Solid State Sciences,* vol. 13, pp. 2073-2079, 12// 2011.

[348] J. Przepiórski, A. Czyżewski, J. Kapica, and M. de la Casa-Lillo, "Preparation and properties of porous carbon material containing magnesium oxide," in *Polish Journal of Chemical Technology* vol. 13, ed, 2011, p. 42.

[349] J. Park and K. B. Yi, "Effects of preparation method on cyclic stability and CO$_2$ absorption capacity of synthetic CaO–MgO absorbent for sorption-enhanced hydrogen production," *International Journal of Hydrogen Energy,* vol. 37, pp. 95-102, 1// 2012.

[350] M. Y. Song, E. I. Ivanov, B. Darriet, M. Pezat, and P. Hagenmuller, "Hydriding properties of a mechanically alloyed mixture with a composition Mg$_2$Ni," *International Journal of Hydrogen Energy,* vol. 10, pp. 169-178, 1985.

[351] M. Y. Song, E. Ivanov, B. Darriet, M. Pezat, and P. Hagenmuller, "Hydriding and dehydriding characteristics of mechanically alloyed mixtures Mg-xwt.%Ni (x = 5, 10, 25 and 55)," *Journal of the Less Common Metals,* vol. 131, pp. 71-79, 1987.

[352] M. Y. Song, "Effects of mechanical alloying on the hydrogen storage characteristics of Mg-xwt% Ni (x = 0, 5, 10, 25 and 55) mixtures," *International Journal of Hydrogen Energy,* vol. 20, pp. 221-227, 1995.

[353] C. X. Shang, M. Bououdina, Y. Song, and Z. X. Guo, "Mechanical alloying and electronic simulations of (MgH$_2$+M) systems (M=Al, Ti, Fe, Ni, Cu and Nb) for hydrogen storage," *International Journal of Hydrogen Energy,* vol. 29, pp. 73-80, 2004.

[354] X. Ma, M. Cao, and C. Hu, "MgO modified nanoporous carbon composites for methanol separation," *RSC Advances,* vol. 3, pp. 10396-10402, 2013.

[355] Z. U. W. a. H.-C. Z. Yangyang Liu, "Recent advances in carbon dioxide capture with metal-organic frameworks," *Greenhouse Gases Science and Technology,* vol. 2, pp. 239-259, 2012.

[356] S. J. Gregg and J. D. Ramsay, "Adsorption of carbon dioxide by magnesia studied by use of infrared and isotherm measurements," *Journal of the Chemical Society A: Inorganic, Physical, and Theoretical Chemistry,* pp. 2784-2787, // 1970.

[357] Y. Xia, R. Mokaya, G. S. Walker, and Y. Zhu, "Superior CO_2 Adsorption Capacity on N-doped, High-Surface-Area, Microporous Carbons Templated from Zeolite," *Advanced Energy Materials,* vol. 1, pp. 678-683, 2011.

[358] Y. Xia, R. Mokaya, D. M. Grant, and G. S. Walker, "A simplified synthesis of N-doped zeolite-templated carbons, the control of the level of zeolite-like ordering and its effect on hydrogen storage properties," *Carbon,* vol. 49, pp. 844-853, 3// 2011.

[359] G. Srinivas, V. Krungleviciute, Z.-X. Guo, and T. Yildirim, "Exceptional CO_2 capture in a hierarchically porous carbon with simultaneous high surface area and pore volume," *Energy & Environmental Science,* vol. 7, pp. 335-342, 2014.

[360] L.-Y. Meng and S.-J. Park, "Investigation of Narrow Pore Size Distribution on Carbon Dioxide Capture of Nanoporous Carbons," *BULLETIN OF THE KOREAN CHEMICAL SOCIETY,* vol. 33, pp. 3749-3754, 2012.

[361] J. Wilcox, *Carbon Capture*: Springer, 2012.

[362] A. Wongkoblap, W. Intomya, W. Somrup, S. Charoensuk, S. Junpirom, and C. Tangsathitkulchai, *Pore Size Distribution of Carbon with Different Probe Molecules* vol. 14, 2010.

[363] B. Yuan, X. Wu, Y. Chen, J. Huang, H. Luo, and S. Deng, "Adsorption of CO_2, CH_4, and N_2 on Ordered Mesoporous Carbon: Approach for Greenhouse Gases Capture and Biogas Upgrading," *Environmental Science & Technology,* vol. 47, pp. 5474-5480, 2013/05/21 2013.

Research Article

Nano-structured MgH₂ catalyzed by TiC nanoparticles for hydrogen storage†

Mi Tian and Congxiao Shang*

Abstract

BACKGROUND: Magnesium hydride is considered to be a promising hydrogen storage material because of its high gravimetric and volumetric storage capacities. However, its slow kinetics and high desorption temperature of $>300\,^\circ C$ limit practical applications. In this work, TiC nanoparticles were selected to modify the hydrogen storage properties of MgH_2. Composite mixtures (MgH_2+TiC) were prepared using both cryogenic milling and high-energy ball milling.

RESULTS: The resulting morphology and crystallite structure of the composites were identified by scanning electron microscopy (SEM), transmission electron microscopy (TEM) and X-ray diffraction (XRD). The milled samples show good mixing of the hydride and carbide particles, with MgH_2 particles around $0.09-1\ \mu m$ and TiC particles $10-20$ nm. The (MgH_2+TiC) composites consist of γ-MgH_2, β-MgH_2 and TiC. MgH_2 nano-crystallites of 25 nm were formed after cryomilling. Thermogravimetry reveals that the composites release ~6.5 mass % hydrogen from $190-400\,^\circ C$ at a heating rate of $10\,^\circ C\ min^{-1}$ under He flow, with the onset and peak temperatures at 190 and $280\,^\circ C$, respectively, for the (MgH_2+TiC) after 8 h cryomilling and 60 h ball milling.

CONCLUSION: Results indicate that TiC is an effective catalyst for hydrogen desorption of MgH_2.
© 2010 Society of Chemical Industry

Keywords: hydrogen storage; MgH_2; TiC; nanoparticles; mechanical milling; microstructure; absorption/desorption kinetics

INTRODUCTION

Magnesium hydride is considered a promising hydrogen storage material due to its high capacity of 7.6 wt%, relatively low cost and light weight.[1,2] However, its slow kinetics and high desorption temperature of $>300\,^\circ C$ limits practical applications.[3–6] Many methods such as doping with catalyst, reducing crystallite and particle size have been developed to improve hydrogen sorption properties. It is reported that the sorption kinetics of MgH_2 can be dramatically increased by ball milling with some transition metals, oxides and fluorides,[3,6–8] some metal oxides[9] and metal halide additives.[10] In particular, transition-metal compounds have attracted considerable interest as effective catalysts, due to the high affinity of the transition-metal cation toward hydrogen.[2,11] For example, small additions of Nb_2O_5 significantly improve both the absorption and desorption kinetics of MgH_2.[12,13] Comparative studies based on various transition-metal oxides emphasize that appropriate chemical interaction between catalyst and host hydride is essential to realize high catalytic activity, suggesting the functionality of the contact anion in tailoring the activity of transition-metal cation.[14] Titanium-based compounds have been successfully used to improve sorption kinetics in several hydrogen storage systems, exhibiting high affinity of the Ti cation toward hydrogen even at moderate temperatures. For example, titanium halides are exceptionally effective in reducing the kinetic barrier of dehydrogenation of alkaline alanates.[14–16] In addition, TiN is found to be very active in accelerating the amide/imide conversion as a promising catalyst for the Li–N–H system.[16] It has also been found that the temperature for hydrogen release from MgH_2 can be greatly reduced by doping it with Ti-containing agents (e.g. TiF_3 and TiC).[6,17] The interactions between

the hydrides and the Ti-containing agents weaken the Mg-H bonds and thus facilitate the recombination of hydrogen atoms producing hydrogen molecules.

However, the effect of transition metal carbides on hydrogen sorption of MgH_2 has not yet been well studied. Here, a systematic investigation is carried out on the hydrogen desorption and absorption properties of MgH_2 catalyzed with a small amount of TiC by both cryogenic milling and high-energy ball milling to improve the sorption kinetics and to reduce the desorption temperature of MgH_2.

EXPERIMENTAL METHODS

As-received MgH_2 powder (Th. Goldschmidt AG, Degussa, $\sim95\%$ MgH_2, 5% Mg, 50 μm) was mixed with 2 mol% of titanium carbide nanopowder (Sigma-Aldrich, $\sim95\%$, <200 nm). The powder mixtures were cryogenically milled for 8 h using liquid nitrogen to freeze the sealed milling vial in a SPEX SamplePrep 6750 Freezer/Mill, and then mechanically milled for 16 h and 60 h at ambient temperature using a high energy ball mill (SPEX 8000D), under an argon atmosphere. The initial ball-to-powder weight

* Correspondence to: Congxiao Shang, School of Environmental Sciences, University of East Anglia, Norwich, UK. E-mail: c.shang@uea.ac.uk

School of Environmental Sciences, University of East Anglia, Norwich, UK

69

Effect of TiC and Mo₂C on Hydrogen Desorption of Mechanically Milled MgH₂

Mi Tian[1], Congxiao Shang[2]*

School of Environmental Sciences, University of East Anglia,

Norwich, NR4 7TJ, UK

[1]m.tian@uea.ac.uk, [2]*c.shang@uea.ac.uk

Abstract- **Titanium carbide (TiC) and molybdenum carbide (Mo₂C) particles were selected to modify the hydrogen storage properties of magnesium hydride (MgH₂). (MgH₂+ 2 mol% TiC) and (MgH₂+2 mol% Mo₂C) mixtures were prepared using both cryogenic milling and high-energy ball milling. The morphology and crystallite structure of the mixtures were examined by X-ray diffraction (XRD), scanning electron microscopy (SEM) and transmission electron microscopy (TEM). The milled (MgH₂+TiC) and (MgH₂+Mo₂C) composites consisted of γ-MgH₂ and β-MgH₂. TiC nanoparticles with the size of 10~20 nm after milling were deposited onto the surface or into the grain boundary of MgH₂. Mo₂C were uniformly distributed on the surface of MgH₂ particles. Thermogravimetry and derivative thermogravimetric analyses showed that ~6.5 wt. % hydrogen was desorbed from (MgH₂+TiC) mixture in the temperature range from 190 to 400 °C at a heating rate of 10 °C/min under He flow. The on-set and peak temperatures were 190 and 280 °C, respectively, for (MgH₂+TiC) ball-milled up to 60 hrs after 8 hrs cryomilling. However, (MgH₂+Mo₂C) shows much higher desorption temperature of 300 °C (on-set) and 358 °C (peak), respectively, compared with those recorded for (MgH₂+TiC). The hydrogen desorption activation energy of the milled (MgH₂+TiC) mixture, 104 kJ/mol, was also substantially reduced, compared with that of the (MgH₂+ Mo₂C) mixture, 167 kJ/mol. The addition of TiC nanoparticles has greater effect on reduction of hydrogen desorption temperatures and acceleration of desorption kinetics.**

Keywords- Hydrogen Storage; MgH₂; TiC; Mo₂C; Nanoparticles; Mechanical Milling; Cryogenic Milling

I. INTRODUCTION

Magnesium hydride has been considered one of promising hydrogen storage materials due to its high hydrogen capacity of 7.6 wt %, high abundance, low cost and light weight [1, 2]. However its slow kinetics and high desorption temperature (>300 °C) limit its practical applications. Many methods, such as doping with catalysts, reducing crystallinity and particle size, have been developed to improve the hydrogen desorption properties. According to recent studies, the desorption kinetics and temperatures of MgH₂ have been dramatically improved by ball milling with some transition metals, oxides and carbides [3-6]. Transition-metal compounds attracted considerable interest as effective catalysts, due to the high affinity of transition-metal cation toward hydrogen [2]. Titanium compounds have been successfully used to improve the sorption kinetics in several typical hydrogen storage systems, exhibiting a high affinity toward hydrogen even at moderate temperatures. For example, titanium halides are exceptionally effective in lowering the kinetic barrier of dehydrogenation reactions for alkaline alanates [7-9]. Recently, it has been found that the temperature for hydrogen release from MgH₂ can be greatly reduced by doping it with Ti-containing agents [10, 11]. In addition, it was reported that graphite as a codopant

of titanium-based catalyst enhanced significantly both the hydrogenation and the dehydrogenation kinetics of catalyzed MgH₂ and NaAlH₄ [11, 12]. Comparative studies based on various transition-metal oxides emphasize that an appropriate chemical interaction between catalyst and host hydride is essential for realizing high catalytic activity [13]. The interactions between the hydrides and the transition metal agents weaken the Mg-H bonds and thus facilitate the recombination of hydrogen atoms to the hydrogen molecules.

TiC has been found to be an effective and stable catalyst for hydrogen desorption of MgH₂ in our recent work [4]. However, the effect of other transition metal carbides on the hydrogen sorption of MgH₂ has not been well studied previously. Here, a systematic investigation was carried out on the hydrogen desorption properties of MgH₂ catalyzed by a small amount of TiC or Mo₂C. The effects of TiC and Mo₂C were compared. Both cryogenic milling and high-energy ball milling were used to reduce the hydrogen desorption temperatures and kinetics of MgH₂.

II. EXPERIMENTAL METHODS

As-received MgH₂ powder (from Th. Goldschmidt AG, Degussa, ~95 % MgH₂, 5 % Mg, 50 μm) was mixed with 2 mol. % of TiC powder (from Sigma-Aldrich, ~95 wt. %, < 200 nm) or 2 mol. % of Mo₂C powder (from Sigma-Aldrich, 99.5%, < 44 μm). The mixtures were cryogenically milled for 8 hrs using liquid nitrogen to freeze the sealed milling vial in a SPEX SamplePrep 6750 Freezer/Mill, then mechanically milled for 16 hrs and 60 hrs at ambient temperature using a high energy ball mill, SPEX 8000D, under Argon atmosphere. The initial ball-to-powder weight ratio is 10:1. All the powder handling was performed in a dry glove box under high purity argon.

The morphology of the powder mixtures was characterized by a Jeol 6300 scanning electron microscopy (SEM). The powder particle sizes were calculated from the SEM pictures as the equivalent circle diameter, ECD = $(4A/\pi)^{1/2}$, where A represents the projected particle area, using the _Image Tool v.3.00_ software. A Jeol 1010 transmission electron microscopy (TEM) was used for further examination of the nano-structures of the mixtures. X-ray diffraction (XRD) was performed using an XTra diffractometer, manufactured by Thermo ARL (US), with Cu Kα radiation. The crystallite/gain sizes were calculated from XRD data using Scherrer equation [14].

The hydrogen sorption behavior of the mixtures was studied by Intelligent Gravimetric Analysis (IGA, Hidden Isochem Ltd.). The desorption was performed from 20 to 500 °C under 1 bar helium pressure with a heating rate of 10 °C/min and He flow rate of 150 ml/min.

Synthesis of nanostructured carbons by the microwave plasma cracking of methane

*Mi Tian [a], Simon Batty [b], Congxiao Shang [a],**

[a] *School of Environmental Sciences, University of East Anglia, Norwich NR4 7TJ, UK*
[b] *EnPlas Ltd., Dev Farm, University of East Anglia, Norwich NR4 7TJ, UK*

ARTICLE INFO

ABSTRACT

One of the attractive methods of producing hydrogen and high value-added carbon is plasma-reforming of hydrocarbons. Here, nanostructured carbon was produced by methane cracking in a relatively low-energy cold plasma reactor designed in-house specifically for such purpose. Carbon samples collected at different positions in the reactor show similar structural morphologies, indicating extensive structural uniformity of the carbon during processing. Surface area and microstructure of the materials were characterized by BET surface area analysis, X-ray diffraction and transmission electron microscopy (TEM). The effects of flow rate, temperature and power were evaluated for the formation of the carbon structures. The results show that the BET surface area and pore volume of the carbon materials vary from 74 to 125 m^2/g and from 0.12 to 0.20 cm^3/g, respectively. Such variations are closely associated with the magnitude of temperature drop at the sample collection position in the cold-plasma chamber before and after methane loading. The highest BET surface area of 125 m^2/g is obtained at a power of 2000 W. TEM shows that the carbon consists of spherical particles of 40.8 ± 8.7 nm in diameter and graphene sheets.

© 2012 Elsevier Ltd. All rights reserved.

1. Introduction

Many carbon structures, such as activated carbons, carbon black, carbon membranes, graphene and carbon nanotubes, have been widely used for gas separation, water purification, catalyst supports, electrodes for batteries and fuel cells, and flexible energy storage and conversion devices [1–6]. This is due to their stable physicochemical properties, good conductivity, low cost, and high surface area or porosity [5–9]. Recently, graphitic carbons with highly crystalline structure and large surface area have attracted extensive attention as catalyst supports. Graphitic carbons are usually prepared by two methods: (1) conventional high temperature (>2500 °C) graphitization to form carbons with well-developed graphitic order [10]; and (2) relatively low temperature (<1000 °C) heterogeneous graphitization with the aid of catalysts, e.g. Fe, Co

and Ni [3,11]. Although exhibiting graphitic structure, these materials possess relatively low BET surface areas [12]. In addition, the synthesis procedures employed to produce such materials are rather complicated: it requires a high processing temperatures between 500 and 1800 °C, and the corresponding aerogels used in the process need to be prepared by the sol–gel method from polymerization of resorcinol with formaldehyde [13].

Recently high energy plasma has become an attractive method for reforming hydrocarbons into hydrogen and carbon. This is a single-stage and non-catalytic reaction, $C_nH_m \rightarrow nC + 0.5mH_2$ [14–17]. It is reported that plasma reforming overcomes many limitations of conventional techniques in terms of cost and deterioration of the catalysts, slow reaction rate, and restrictions on hydrogen production from heavy hydrocarbons [18–20]. In general, plasma is an

Corresponding Author: Ms. Mi Tian,

Corresponding Author's Institution:

First Author: Mi Tian

Order of Authors: Mi Tian; Congxiao Shang, PhD

Abstract: Carbon materials were produced by a microwave plasma reactor. Further modifications of the carbon structure to enhance the surface area were carried out in a thermal furnace. The modification conditions were optimized through response surface methodology (RSM). The effects of the modification temperature, time and pressure on BET surface area and yield were studied. From the analysis of variance (ANOVA), the most influential factor for each experimental design response was identified. The predicted BET surface area and yield by RSM were found to agree with the experimental values. The optimum modification conditions for the plasma carbon (PC) were found to be: temperature = 950°C and time = 120 min, pressure = 1 bar CO_2 gas flow. The original PC and modified PC using optimum modification conditions were characterized by BET surface area/pore size analyzer, Raman spectra and transmission electron microscopy (TEM). The maximum BET surface area of 779 m2/g was achieved from the experiment. The main reasons for such the high increase in the BET surface area were due to the opening up of accessible micro/meso pores in the graphitic structure, by the removal of amorphous carbons around the graphite surface.

The 18th Joint Annual Conference of CSCST-SCI

Hydrogen Storage of MgH2 and nano-structured Carbon Produced by Plasma Cracking of Methane

Mi Tian[a], Congxiao Shang[a]*, Kaipei Qiu[a], Simon Batty[b]

a School of Environmental Sciences, University of East Anglia, Norwich, NR4 7TJ, UK; b EnPlas Ltd, Dev Farm, University of East Anglia, Norwich, NR4 7TJ, UK
(* Corresponding author: Tel: +44-1603-593123; E-mail: c.shang@uea.ac.uk)

CARBON PRODUCED BY MICROWAVE COLD PLASMA

A synthetic method for successfully obtaining carbon materials is illustrated. The methodology employed to obtain these carbon powders is based on the cold plasma reactor. TEM images reveal that the formed carbon structures involve various degrees of amorphous phase, crystallinity and graphite sheets. The plasma carbon has maximum surface area of 111 m^2/g. After thermal treatment, the surface area of plasma carbon can be improved to 408 m^2/g. The treated plasma carbon is suitable for gas sorption, gas separation and other applications.

EXPERIMENTAL METHODS

Figure 1 Sketch of the plasma reactor

RESULTS

Figure 2 XRD pattern of plasma carbon

Figure 3 N_2 isotherms and DFT curves at 77K of plasma carbon

The XRD peak at around $2\theta = 26°$ and $43°$ are assigned to the (002) and (100) diffractions of the graphitic framework, respectively[1]. The peaks with a very low intensity suggest the certain amount of amorphous carbon or low level of crystallinity.

Figure 4b represents carbon nanocoils consisting of graphite sheets. It reveals that the lattice spacing of two adjacent graphite sheets is ~ 0.34 nm[2]. Figure 4C shows a certain level of crystallinity from nearly amorphous carbon structure to being very crystalline, in agreement with the XRD results.

N_2 isotherm and DFT curves indicate the porosity of plasma carbon is consist of meso- and macro- pores.

Figure 4 a) TEM image of a plasma carbon sample, b) HRTEM image of area B from Figure 4a, c) HRTEM image of area C from Figure 4a

MODIFICATION FOR H2 STORAGE

Figure 5 Tube furnace for plasma carbon modification

Figure 6 N_2 isotherms at 77K of modified plasma carbon.

Figure 7 TEM image of the modified plasma carbon.
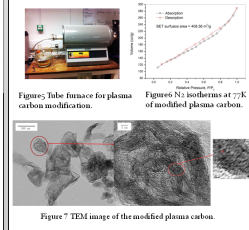
CONCLUSIONS

❖ A synthetic method is developed for successfully obtaining carbon materials using self-designed plasma reactor.

❖ The formed carbon structures involve both amorphous and various crystallinity of graphite sheets.

❖ The highest BET surface area of plasma carbon is 111.74 m^2/g, collected at 17 cm quartz. After treatment, surface area can be up to 408 m^2/g.

MIXING OF MgH2 WITH PLASMA CARBON

MgH_2 prepared by cryomilling and mechanically milling with TiC nanoparticles, and then mixed with plasma carbon with different ratios in distilled tetrahydrofuran (THF). The mixture of MgH_2/TiC and plasma carbon was dried in vacuum oven and then milled for 10 mins in SPEX ball mill. The surface area and microstructure of the materials are characterized by BET method (Brunauer, Emmett and Teller, 1938), X-ray diffraction (XRD), scanning electron microscope (SEM) and transmission electron microscopy (TEM). Hydrogen release and uptake of the composites of MgH_2 and plasma carbon have been investigated by Thermogravimetry-Mass Spectroscopy (TG-MS). The results showed the starting desorption temperature of MgH_2 can be reduced by adding plasma carbon.

EXPERIMENTAL METHODS

Figure 8 Experimental Process

RESULTS AND DISCUSSIONS

Figure 9 XRD patterns of Mg-based materials milled with plasma carbon

XRD patterns show there is no new phase formed except Fe which is from the milling balls or jar. From the SEM image, Figure 10, the samples are inhomogeneous mixture of MgH_2 and plasma carbon. In some area, the plasma carbon covers the surface of MgH_2, and in the other area, MgH_2 is distributed on the plasma carbon.

Figure 10 SEM images of 95 % MgH_2/TiC + 5 % plasma carbon, A and B are spectrum points.

Figure 11 Thermogravimetry (TG) and differential thermogravimetry (DTG) of MgH_2/TiC milled with plasma carbon

Figure 12 Rehydrogenation of dehydrogenated MgH_2/TiC with plasma carbon.

From TG-DTG, Figure 11, 50 % 20h-milled MgH2/TiC + 50% plasma carbon shows the lowest onset and peak temperature, which are 180 and 285 °C, respectively. Figure 12 shows hydrogen uptake at lower temperature for 50 % 20h-milled MgH_2/TiC + 50% plasma carbon. The results indicate that plasma carbon as an additive shows a good effect on hydrogen sorption properties of the composite, MgH_2+TiC +C.

Table 1 Hydrogen sorption parameters of all samples.

Sample	T_{Onset} (°C)	T_{Peak} (°C)	H_2 (wt%)	Theoretical H_2 (wt%)
As-received MgH_2	418	434	7.1	7.69
20 h milled MgH_2/TiC (95 : 5 atomic %)	239	290	6.5	6.86
95% 20h milled MgH_2/TiC + 5% Plasma C	200	312	6.4	6.51
50% 20h milled MgH_2/TiC + 50 % Plasma C	180	285	3.6	3.43

CONCLUSIONS

MgH_2 milled with catalyst TiC was mixed with plasma carbon. The onset and peak temperatures of H_2 desorption of the milled MgH_2 are substantially reduced with the addition of TiC, and further decreased to 180 °C and 285 °C by the additive of 50 wt% plasma carbon. Plasma carbon shows a good effect on H_2 sorption of Mg/MgH_2 with TiC, which is stable during H_2 uptake and release with no reaction with Mg or MgH_2. 50% MgH_2/TiC+50% plasma carbon shows good H_2 uptakes compared with theoretical H_2 content of it. The H_2 spillover effect mechanism of plasma carbon needs to be further investigated.

ACKNOWLEDGEMENTS

REFERENCES

[1] Zhai D, Du H, Li B, Zhu Y, Kang F. Porous graphitic carbons prepared by combining chemical activation with catalytic graphitization. Carbon.49(2):725-0.
[2] Terrones M, Hsu W, Kroto H, Walton D, Hirsch A. Nanotubes: A Revolution in Materials Science and Electronics Fullerenes and Related Structures. Springer Berlin / Heidelberg;2000:189-234.
[3] Tian M, Shang C. Nano-structured MgH2 catalyzed by TiC nanoparticles for hydrogen storage. Journal of Chemical Technology & Biotechnology;86(1):69-74.